

Summer 1998

Pneumatic fracture propagation and particulate transport in geologic formations

Suresh Puppala

New Jersey Institute of Technology

Follow this and additional works at: <https://digitalcommons.njit.edu/dissertations>



Part of the [Civil Engineering Commons](#)

Recommended Citation

Puppala, Suresh, "Pneumatic fracture propagation and particulate transport in geologic formations" (1998). *Dissertations*. 955.
<https://digitalcommons.njit.edu/dissertations/955>

This Dissertation is brought to you for free and open access by the Theses and Dissertations at Digital Commons @ NJIT. It has been accepted for inclusion in Dissertations by an authorized administrator of Digital Commons @ NJIT. For more information, please contact digitalcommons@njit.edu.

Copyright Warning & Restrictions

The copyright law of the United States (Title 17, United States Code) governs the making of photocopies or other reproductions of copyrighted material.

Under certain conditions specified in the law, libraries and archives are authorized to furnish a photocopy or other reproduction. One of these specified conditions is that the photocopy or reproduction is not to be “used for any purpose other than private study, scholarship, or research.” If a user makes a request for, or later uses, a photocopy or reproduction for purposes in excess of “fair use” that user may be liable for copyright infringement,

This institution reserves the right to refuse to accept a copying order if, in its judgment, fulfillment of the order would involve violation of copyright law.

Please Note: The author retains the copyright while the New Jersey Institute of Technology reserves the right to distribute this thesis or dissertation

Printing note: If you do not wish to print this page, then select “Pages from: first page # to: last page #” on the print dialog screen

The Van Houten library has removed some of the personal information and all signatures from the approval page and biographical sketches of theses and dissertations in order to protect the identity of NJIT graduates and faculty.

INFORMATION TO USERS

This manuscript has been reproduced from the microfilm master. UMI films the text directly from the original or copy submitted. Thus, some thesis and dissertation copies are in typewriter face, while others may be from any type of computer printer.

The quality of this reproduction is dependent upon the quality of the copy submitted. Broken or indistinct print, colored or poor quality illustrations and photographs, print bleedthrough, substandard margins, and improper alignment can adversely affect reproduction.

In the unlikely event that the author did not send UMI a complete manuscript and there are missing pages, these will be noted. Also, if unauthorized copyright material had to be removed, a note will indicate the deletion.

Oversize materials (e.g., maps, drawings, charts) are reproduced by sectioning the original, beginning at the upper left-hand corner and continuing from left to right in equal sections with small overlaps. Each original is also photographed in one exposure and is included in reduced form at the back of the book.

Photographs included in the original manuscript have been reproduced xerographically in this copy. Higher quality 6" x 9" black and white photographic prints are available for any photographs or illustrations appearing in this copy for an additional charge. Contact UMI directly to order.

UMI

A Bell & Howell Information Company
300 North Zeeb Road, Ann Arbor MI 48106-1346 USA
313/761-4700 800/521-0600

NOTE TO USERS

The original manuscript received by UMI contains pages with indistinct and/or slanted print. Pages were microfilmed as received.

This reproduction is the best copy available

UMI

UMI Number: 9906989

**Copyright 1998 by
Puppala, Suresh**

All rights reserved.

**UMI Microform 9906989
Copyright 1998, by UMI Company. All rights reserved.**

**This microform edition is protected against unauthorized
copying under Title 17, United States Code.**

UMI
300 North Zeeb Road
Ann Arbor, MI 48103

**PNEUMATIC FRACTURE PROPAGATION AND PARTICULATE
TRANSPORT IN GEOLOGIC FORMATIONS**

**by
Suresh Puppala**

**A Dissertation
Submitted to the Faculty of
New Jersey Institute of Technology
in Partial Fulfillment of the Requirements for the Degree of
Doctor of Philosophy**

Department of Civil and Environmental Engineering

August 1998

Copyright © 1998 by Suresh Puppala

ALL RIGHTS RESERVED

APPROVAL PAGE

**PNEUMATIC FRACTURE PROPAGATION AND PARTICULATE
TRANSPORT IN GEOLOGIC FORMATIONS**

Suresh Puppala

John R. Schuring Date
Chairperson of Supervisory Committee
Professor of Civil and Environmental Engineering, NJIT

Denis Blackmore Date
Professor of Mathematics, NJIT

Paul C. Chan Date
Professor of Civil and Environmental Engineering, NJIT

Edward G. Dauenheimer Date
Professor of Civil and Environmental Engineering, NJIT

Dorairaja Raghu Date
Professor of Civil and Environmental Engineering, NJIT

ABSTRACT

PNEUMATIC FRACTURE PROPAGATION AND PARTICULATE TRANSPORT IN GEOLOGIC FORMATIONS

by
Suresh Puppala

Pneumatic fracturing is an *in situ* remediation enhancement technology developed to increase the permeability of contaminated geologic formations. This technology can also be used to deliver atomized liquid and particulate supplements to geologic formations, thereby enhancing *in situ* processes such as bioremediation and reactive dechlorination.

The main objective of this study was the development of a mathematical model that simulates the propagation of pneumatic fractures in soil and rock formations. Pneumatic fracture propagation differs from other fluid fracturing phenomena in the propagation velocity (1-3 m/sec) and the viscosity of the fracturing fluid (1.9E-05 Pa·sec). For the purposes of model development, the geologic formation was assumed to be homogenous with regard to composition, anisotropic with respect to pneumatic conductivity, and overconsolidated with respect to geostatic stress.

The propagation model was formulated by coupling equations describing the three physical processes controlling propagation: (i) pressure loss due to frictional effects; (ii) leak-off into the surrounding formation; and (iii) deflection of the overburden. Pressure dissipation was modeled based on Poiseuille's law, and leak-off was modeled using two-dimensional Darcian flow. The deflection of the overlying formation was modeled as a circular plate clamped at its edges and subjected to logarithmically varying load.

The model was solved numerically and the solution was expressed as an algorithm. The algorithm seeks an equilibrium fracture radius and aperture that simultaneously satisfies flow continuity and stress equilibrium criteria at the fracture tip. Different methods of solution convergence were examined and the Bisection Method was found to be the most efficient.

Sensitivity analyses showed that model behavior was dominated by the pneumatic conductivity of the geologic formation since this parameter largely determines leak-off rate. The algorithm was calibrated with field data from six different pneumatic fracturing projects and regressed values of pneumatic conductivity and elastic modulus showed reasonable agreement with field measured values. The most important result of the calibration process was the coincidence between the regressed conductivity ($1.1\text{E-}03$ to $1.8\text{E-}05$) and the post-fracture conductivities measured in the field ($3.1\text{E-}03$ to $1.7\text{E-}05$). This result supported the fundamental thesis that final fracture radius is determined with the geologic formation in a disturbed state.

A separate pneumatic fracture propagation model was developed and solved based solely on the continuity criterion. The solution demonstrated reasonable correlation with field measured radii, although it tended to overestimate fracture radius in soil formations at shallow depths of injection (on an average 15 % more than field measured radius).

As a secondary objective of this study, a methodology to model the mechanism of particulate transport in a fluidized soil formation was proposed. The methodology was tested with field data from a recent case study.

BIOGRAPHICAL SKETCH

Author: Suresh Puppala
Degree: Doctor of Philosophy
Date: August 1998

Undergraduate and Graduate Education:

- Doctor of Philosophy in Civil Engineering,
New Jersey Institute of Technology, Newark, NJ, 1998
- Master of Science in Environmental Engineering,
New Jersey Institute of Technology, Newark, NJ, 1993
- Bachelor of Science in Civil Engineering,
Deccan College of Engineering and Technology,
Osmania University, Hyderabad, India, 1991

Major: Civil and Environmental Engineering

Presentations and Publications:

S. Puppala, J. R. Schuring, and D. Washington, "An Approach for Modeling Pneumatic Fracture Propagation and the Distribution of Injected Amendments," at the 4th International Symposium on Environmental Geotechnology and Global Sustainable Development, Boston, Massachusetts, USA, August 9-13, 1998.

**This dissertation is dedicated to
my parents
Subramanyeswara Rao Puppala and Sita Puppala**

ACKNOWLEDGMENT

I would like to thank my advisor Dr. John R. Schuring, for his input in shaping the developed models and reviewing the drafts several times. His work ethic and optimism have been a source of inspiration during this work.

I appreciate the input from the members of the committee, for their critical reviews of the proposal, and drafts of the final dissertation.

My brother, Goutham Puppala has been a source of constant support, throughout this period.

The data used in calibrating the models was obtained from the work done previously for nearly a decade. I would like to thank the students who worked on the project, whom I do not know personally.

Finally I would like to acknowledge the help of my friends and colleagues in reviewing the drafts and countless other aspects of the work Firoz Ahmed, Thomas Boland, Michael Canino, Yuan Ding, Hugo Fernandez, Conan Fitzgerald, Michael Galbraith, Heather Hall, Trevor King, Sean McGonigal, Deepak Nautiyal, Deborah Schnell and Brian Sielski.

TABLE OF CONTENTS

Chapter	Page
1 INTRODUCTION AND OBJECTIVES	1
1.1 Introduction.....	1
1.2 Research Objectives.....	6
2 LITERATURE REVIEW	10
2.1 Fracture Propagation Models	10
2.1.1 Overview.....	10
2.1.2 Magma Driven Fracture Propagation	13
2.1.3 Hydraulic Fracturing	18
2.1.4 Other Hydraulic Fracturing Investigations	25
2.1.5 Gas-Driven Explosive Fracturing	26
2.2 Particulate Transport.....	27
2.2.1 Overview	27
2.2.2 Interstitial Transport of the Injected Solid Particles.....	30
2.2.3 Particulate Transport in a Discrete Fluidized Zone	31
2.2.4 Particulate Transport in a Discrete Open Fracture	33
2.2.4.1 Proppant Transport in Hydraulic Fracturing Process	37
2.2.4.2 Proppant Transport Using Nitrogen Gas	38
3 MODEL APPROACH.....	41
3.1 Introduction.....	41

TABLE OF CONTENTS
(Continued)

Chapter	Page
3.2 Mechanism of Pneumatic Fracture Propagation	41
3.3 Model Assumptions.....	48
3.3.1 General Assumptions	48
3.3.2 Presumed Fracture Characteristics.....	50
3.4 Mathematical Formulation of the Propagation Problem	52
3.4.1 Pressure Distribution Model	54
3.4.2 Leak-off Model.....	55
3.4.3 Deflection Model	64
3.4.4 Coupling Interaction of Propagation Processes.....	67
4 MODEL DEVELOPMENT	68
4.1 Introduction.....	68
4.2 Conceptual Model Algorithm.....	69
4.2.1 Convergence Methodology	72
4.3 Details of Algorithm Structure	76
4.3.1 Main Routine.....	77
4.3.2 Bisection Method Subroutine	82
4.3.3 Subroutine to Determine Flow and Pressure Variation in the Fracture	85
4.4 Closed Form Solution of Pneumatic Fracture Propagation.....	92

TABLE OF CONTENTS
(Continued)

Chapter	Page
5 VALIDATION AND CALIBRATION OF THE ALGORITHM.....	96
5.1 Overview.....	96
5.2 Algorithm Sensitivity.....	97
5.2.1 Overall Behavior and Sensitivity of the Algorithm.....	97
5.2.2 Discussion of Overall Behavior and Sensitivity Results.....	101
5.3 Calibration of the Algorithm	105
5.3.1 Calibration Procedure.....	106
5.3.2 Calibration Results	110
5.4 Validation of the Closed Form Solution	115
5.5 Recommended Parameters for the Algorithm.....	117
5.6 Applications of the Algorithm.....	119
6 A METHODOLOGY TO MODEL PARTICULATE TRANSPORT.....	124
6.1 Overview	124
6.2 Outline of a Methodology for Modeling Particulate Transport in a Fluidized Soil Formation.....	125
6.3 Application of the Particulate Transport Methodology - A Case Study	131
6.3.1 Hanford Site Background.....	132
6.3.2 Results	135
6.3.3 Model Validation	139

TABLE OF CONTENTS
(Continued)

Chapter	Page
7 CONCLUSIONS AND RECOMMENDATIONS	141
7.1 Conclusions.....	141
7.2 Recommendations	147
APPENDIX A DEFLECTION OF A CIRCULAR PLATE CLAMPED AT THE EDGES AND SUBJECTED TO A LOGARITHMICALLY VARYING LOAD.....	151
APPENDIX B CLOSED FORM SOLUTION FOR CALCULATING EXTENT OF FRACTURE PROPAGATION (cubic pressure distribution within the fracture).....	159
APPENDIX C LEAK-OFF ESTIMATION BY FLOWNET METHOD-II	163
APPENDIX D CLOSED FORM SOLUTION FOR CALCULATING EXTENT OF FRACTURE PROPAGATION (linearly varying pressure within the fracture)	165
APPENDIX E FRACTURE PROPAGATION MODEL (Mathcad Version)	
E-1 Input Parameters for the Model	169
E-2 Three Different Approaches Investigated to Solve for the Roots of the Model.....	170
E-3 Predicting the Steady State Fracture Dimensions (Analytical Method)	171
E-4 Predicting the Steady State Fracture Dimensions (using flow net to estimate leak-off).....	173
E-5 Predicting the Steady State Fracture Dimensions (Constant Width Fractures).....	176

TABLE OF CONTENTS
(Continued)

Chapter	Page
APPENDIX F PARTICULATES TRANSPORT IN A FLUIDIZED SOIL FORMATION.....	178
F-1 Extent of Particulate Transport (360 Nozzle Setting).....	180
F-2 Extent of Particulate Transport (North - Quad Nozzle Setting).....	181
F-3 Extent of Particulate Transport (South - Quad Nozzle Setting).....	182
F-4 Extent of Particulate Transport (East - Quad Nozzle Setting).....	183
F-5 Extent of Particulate Transport (West - Quad Nozzle Setting).....	184
APPENDIX G SHAPE FACTORS OF FLOWNETS FOR DIFFERENT FRACTURE GEOMETRIES	185
APPENDIX H FORMATION PARAMETERS.....	192
H-1 Fluid Conductivities of Rocks and Soils	192
H-2 Anisotropic Fluid Conductivities of Rocks And Soils	201
H-3 Young's Modulii of Rocks and Soils	203
REFERENCES.....	211

LIST OF TABLES

Table	Page
1.1 Summary of Pneumatically Fractured Sites.....	4
3.1 Pneumatic Fracture Propagation Velocities	46
5.1 Range of Parameter Variation	98
5.2 Accuracy of Parameter Determination	101
5.3 Data Used to Calibrate and Validate the Model.....	107
5.4 Algorithm Input Parameters for Soil and Rock Formations.....	118
6.1 Summary of Soil Index Properties-Hanford Soils	134
6.2 Calculated and Measured Values of Extent of Fluidization.....	140

LIST OF FIGURES

Figure	Page
1.1 Pneumatic Fracturing Process	3
1.2 Different Aspects of the Pneumatic Fracturing Problem.....	7
2.1 Fracture Propagation Phenomena in Geologic Media.....	11
2.2 Magma Driven Fracture Propagation	14
2.3 Fracture Configurations for Theoretical Models	19
2.4 Mechanisms of Particle Transport.....	29
2.5 Different Regions of Proppant Transport in Hydraulic Fractures	39
2.6 Proppant Banking for Different Treatment Conditions	39
3.1 Pressure Variation During a Typical Pneumatic Injection	43
3.2 Pressure Contours During a Typical Pneumatic Injection.....	43
3.3 Temporal Variation of Ground Surface Heave Contours During Injection.....	47
3.4 Effect of Pressure and Gradient Variation on Leak-off Distribution.....	57
3.5 Cross-Section of a Radially Propagating Horizontal Fracture.....	59
3.6 Effect of Formation Anisotropy on Flow Pattern	60
3.7 Effect of Formation Anisotropy and Change in Fracture Extent on Shape Factor	63
4.1 Conceptual Flow Chart of the Propagation Model.....	70
4.2 Pressure and Flow Determination in a Segmented Fracture.....	71

**LIST OF FIGURES
(Continued)**

Figure	Page
4.3 Case I - Pressure and Flow Behavior in an Underestimated Fracture.....	74
4.4 Case II - Pressure and Flow Behavior in an Overestimated Fracture	75
4.5 Main Routine	78
4.6 Bisection Subroutine	81
4.7 Deflection, Pressure and Flow Subroutine	86
4.8 Different Fracture Geometries that can be Modeled by the Algorithm	90
4.9 Region of Leak-off Estimation ‘G’	93
5.1 Variation of Fracture Dimensions for the Range of Parameter Variation	99
5.2 Model Sensitivity to Error in Parameter Estimation.....	103
5.3 Procedure for Calibrating the Fracture Propagation Model.....	109
5.4 Sites Calibrated for Conductivities Using Different Methods of Leak-off Estimation (Soil Formations).....	112
5.5 Sites Calibrated for Conductivities Using Different Methods of Leak-off Estimation (Rock Formations).....	112
5.6 Comparison of Derived and Field Measured Conductivities	114
5.7 Radii Predicted by the Closed Form Solution	116
5.8 Algorithm Example in the “Forward Mode”	121
5.9 Algorithm Example in the “Backward Mode”	122
6.1 Conceptual Diagram of Integrated PF/ISV Process	133
6.2 Resistance Measurements - 360 ⁰ Nozzle.....	136

LIST OF FIGURES
(Continued)

Figure	Page
6.1 Extent of Graphite Lens - 360 ⁰ Nozzle Setting.....	137
6.2 Extent of the Graphite Lens - Quad Nozzle Setting	138

LIST OF SYMBOLS

A	=	area of one fracture face
b	=	width of the fracture at a distance from wellbore
b_w	=	maximum fracture aperture at the wellbore
b_{we}	=	fracture width at the wellbore after the pump stops
C	=	fracturing fluid coefficient
C_D	=	coefficient of drag
D_t	=	diameter of the tube
D	=	flexural rigidity
d	=	particle diameter
d_m	=	diameter of the coarser media (filter media)
$d_{m,15}$	=	diameter at which 15% by weight of the coarser media had a smaller diameter
$d_{p,85}$	=	diameter at which 85% by weight of the finer media had a smaller diameter
d_p	=	diameter of the finer media (particles moving through the filter)
E	=	Young's modulus
f_l	=	normalized fracture length
G	=	rigidity modulus
g	=	acceleration due to gravity
h	=	height of the vertical fracture
h_p	=	distance between the parallel plates
H	=	height of the fracture
H_{mf}	=	bed height at incipient fluidization point
i	=	hydraulic gradient
K	=	hydraulic conductivity
K_{ic}	=	fracture toughness of the formation
K_{air}	=	pneumatic conductivity
K_{h-air}	=	horizontal pneumatic conductivity

LIST OF SYMBOLS
(Continued)

K_{v-air}	=	vertical pneumatic conductivity
l	=	distance from the particles source
l_{grad}	=	length of the flow path along which the pressure is dissipated
$2L$	=	fracture length(linear fracture)
n'	=	non-Newtonian fluid constant
N_A	=	airborne concentration of particles at a distance from the source
N_P	=	airborne concentration of particles at the source
N_d	=	number of potential drops in the flow net
N_f	=	number of flow tubes present in flow net
p	=	pressure inside the fracture
p_d	=	driving pressure or overpressure at wellbore
p_m	=	maintenance pressure
p_{tip}	=	pressure at the tip of the fracture
p_{prop}	=	propagation pressure
p_w	=	pressure at wellbore
Δp_B	=	pressure drop across fluidized bed
Q_{in}	=	fracturing fluid injection flow rate
Q_{leak}	=	fracturing fluid leak-off rate
Q_{res}	=	residual flow in the fracture
R	=	maximum radial extent of the fracture
Re_g	=	grain Reynolds number
r	=	variable fracture radius
r_w	=	well radius
S_p	=	Spurt loss
t	=	time
T_{\perp}	=	tensile strength perpendicular to the bedding plane

LIST OF SYMBOLS (Continued)

T_{\parallel}	=	tensile strength parallel to the bedding plane
U^*	=	friction velocity
u	=	velocity of the fluid
u_{mf}	=	minimum fluidizing velocity
V_{leak}	=	volume of fluid lost to the formation as leak-off
V_{frac}	=	volume of the fracture
V_{res}	=	residual fluid volume
V_{cr}	=	critical velocity for initiation of particle movement
v_s	=	terminal settling velocity of the particles
w	=	deflection of formation due to the pressure in the fracture
z	=	depth of fracture from surface
z_w	=	piezometric level of the ground water

Greek Letters

γ	=	specific weight of the formation
γ_f	=	specific weight of the fluid
γ_p	=	specific weight of the particles
γ_w	=	specific weight of water
δ	=	deflection of the formation overlying the fracture
ϵ_i	=	deposition efficiency for a given particle size
ϵ_{mf}	=	bed voidage at incipient fluidization point
μ_{air}	=	dynamic viscosity of air
ν	=	Poisson's ratio
ν_{kin}	=	kinematic viscosity
ρ_{air}	=	density of air

LIST OF SYMBOLS
(Continued)

ρ_f	=	density of fluid
$\sigma_x, \sigma_y, \sigma_z,$	=	in situ stresses
σ_{ta}	=	apparent tensile strength of the formation
τ^*	=	dimensionless shear stress
τ_0	=	boundary shear stress

CHAPTER 1

INTRODUCTION AND OBJECTIVES

1.1 Introduction

When remediating sites containing contaminated soil and ground water, the “*in situ*” treatment approach is preferred, i.e., remove or treat the contaminants in place without excavation and disturbance of the site. In most cases, the *in situ* approach is the most economical alternative, and a number of these technologies have emerged over the last decade with varying degrees of success. The major obstacle to *in situ* remediation technologies such as vapor extraction, bioremediation, and pump and treat, is the low permeability of some geologic formations. If the site contains fine-grained soils such as silt or clay, or dense bedrock such as shale or siltstone, *in situ* technologies are generally not effective. The hydraulic conductivity limit below which current *in situ* technologies are not normally applicable is 1×10^{-4} cm/sec.

In order to overcome the retarding effect of low formation permeability, a number of enhancement technologies are now under development. *In situ* enhancement approaches include fracturing, electrokinetics and ultrasound techniques. Of interest in the present study is enhancement by fracturing, which may be generally divided into three categories: pneumatic fracturing, hydraulic fracturing and explosive fracturing. The principal objective of all three techniques is similar, i.e., creation of an artificial fracture network in the geologic formation.

The primary focus of the present study is the pneumatic fracturing technology, which is a patented process [U.S. Patent #5,032,042] developed at the Hazardous Substance

Management Research Center (HSMRC) at New Jersey Institute of Technology (NJIT). The process involves injecting high pressure air or other gas into contaminated geologic formations at a pressure that exceeds the *in situ* stresses, and at a flow rate that exceeds the permeability of the formation. Figure 1.1 shows the major components of the current pneumatic fracturing system.

The pneumatic fracturing process was first demonstrated in the field at a contaminated site in Richmond, Virginia in 1990 [Schuring *et al.*, 1991]. Since this first demonstration, the technology has been successfully applied in a number of projects. A partial list of the sites fractured to date and their site characteristics are given in Table 1.1. It is noted that two of these demonstrations (indicated with an asterisk) were conducted under the United States Environmental Protection Agency (US EPA) Superfund Innovative Technologies Evaluation (SITE) Program, including one at a contaminated industrial site in New Jersey to enhance soil vapor extraction [US EPA, 1993], and the other at a contaminated site in Pennsylvania to enhance *in situ* bioremediation [US EPA, 1995]. As indicated in the table, the *in situ* remediation technologies which have been integrated with pneumatic fracturing are vapor extraction, bioremediation, pump and treat, *in situ* vitrification, and reactive dechlorination. The projects have comprised a variety of geologic formations including three different rock formations and fourteen different soil formations.

Although the principal application of pneumatic fracturing is to increase formation permeability, the process can also deliver gaseous, liquid and granular supplements into the subsurface. For example, when applied to bioremediation, pneumatic fracturing can seed the formation by injecting microbes and nutrients during fracture injection.

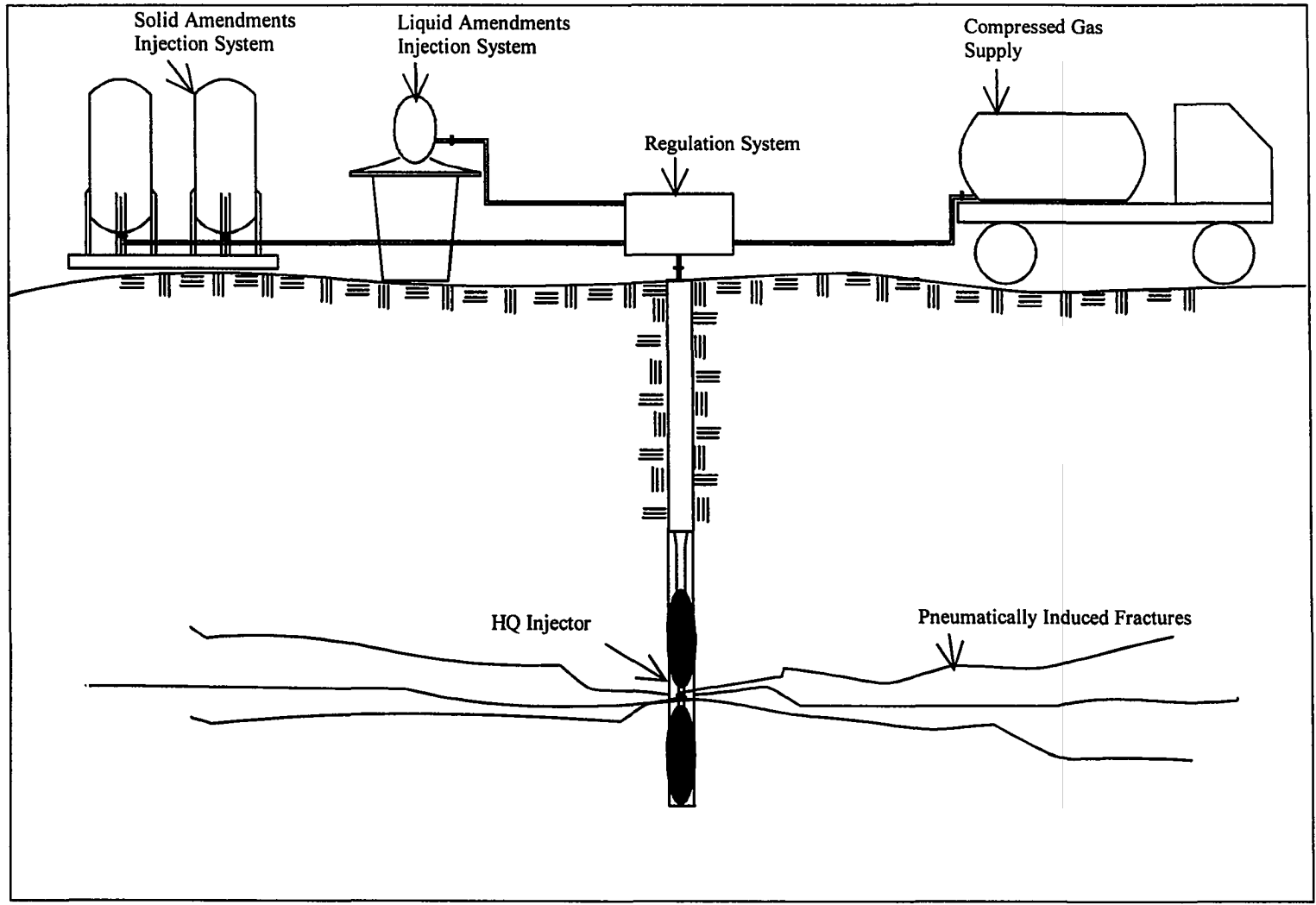


Figure 1.1 Pneumatic Fracturing Process

Table 1.1 Summary of Pneumatically Fractured Sites

Location	Textural Description	USCS	Fracture Injection Depth (ft)	Estimated Radius of Influence (ft)	Target Contaminant	Integrated <i>In situ</i> Technology
AL-1 Huntsville	Sandy gravel	GP	34-36.3	49	VOCs	Pump & Treat
CA-1 Santa Clara	Silty Clay/ Sandy Clay	CH	-	-	Chlorinated Solvents	Soil Vapor Extraction
CAN-1 Toronto	Clayey Silt	CL,ML	-	11-56	VOCs	Soil Vapor Extraction
LA-1 Shreveport	Clayey Silt	CL,ML	9.1-11.6	-	TCE	Soil Vapor Extraction
NJ-1 Frelinghuysen	Clayey Silt/ Sandy Silt	CL,ML	5-7	9	Clean Site	Soil Vapor Extraction
NJ-2 Newark-NJIT	Sandstone	NA	9-11	>10	Clean Site	Soil Vapor Extraction
NJ-3 Roseland	Clayey Sand/ Silty Sand	SC,SM	4-6	9	Chlorinated Solvents	Soil Vapor Extraction
NJ-4 * Hillsborough	Siltstone	NA	9.1-11.1	>20	Chlorinated Solvents	Soil Vapor Extraction / Hot Gas Injection
NJ-5 Newark- Chem Fleur	Sandy Silt	SM,ML	5.3-7.3	-	Miscellaneous VOCs	Soil Vapor Extraction
NJ-6 East Orange	Sand/Sandy Silt	SM,ML	-	-	Petroleum Hydrocarbons	Soil Vapor Extraction
NJ-7 Highland Park	Siltstone with Carbonate	NA	14-16.5	35	Chlorinated Solvents	Soil Vapor Extraction
NJ-8 Flemington	Siltstone	NA	14.5-16.7	40	Chlorinated Solvents	Bioremediation
OH-1 Piketon	Silty Clay	CH,MH	30-32.3	-	Clean Site	Pump & Treat
OK-1 Oklahoma City	Clayey Silt	CL,ML	7-9	23	Chlorinated Solvents & Petroleum Hydrocarbons	Soil Vapor Extraction
PA-1 * Marcus Hook	Clayey Silt	CL,ML	3-5	15	Petroleum Hydrocarbons	Bioremediation
VA-1 Richmond	Silty Clay	CH,MH	7.1-8.8	9	Chlorinated Solvents	Soil Vapor Extraction
WA-1 Richland	Sandy Gravel	GP	14	10	Clean Site	<i>In Situ</i> Vitrification

(* conducted under U.S.EPA SITE program) (VOCs Volatile Organic Compounds) (- Not Available)

Pneumatic fracturing is also being used with *in situ* vitrification (ISV) to create an electrically conductive starter path between the system electrodes, and with *in situ* reactive barriers for injection of iron powder to create a permeable reactive cell.

Another approach to formation fracturing is hydraulic fracturing which uses water as the injection fluid instead of air. The hydraulic fracturing process has been studied and used extensively for enhancing the permeability of oil-bearing formations [e.g., Gidley *et al.*, 1989; Howard and Fast, 1970], and more recently has been applied to the remediation of sites contaminated with hazardous waste [Murdoch, 1992]. One of the disadvantages of hydraulic fracturing is the large quantity of water used, which has the potential to mobilize and spread the contaminants when used in the vadose zone. Other advantages of pneumatic fracturing over hydraulic fracturing include beneficial aeration and air sparging occurring during fracture injection which enhance both stripping and biodegradation of volatile organic compounds (VOCs). Also, since pneumatic fracturing utilizes air as an injection fluid and is a relatively rapid process (< 20 seconds), the risk of contaminant mobilization is greatly reduced.

Explosive fracturing has also been used for permeability enhancement of petroleum and gas reservoirs [Druet and O'Connor, 1991] and its application to the remediation of contaminated sites is now being explored. Some obvious limitations of using explosives for *in situ* remediation are chemical residues, vibration during detonation, and permitting and perception problems.

Although pneumatic fracturing is operationally quite different from either hydraulic fracturing or explosive fracturing, there are similarities in the way a geologic formation responds to all three technologies. Throughout the present study, available knowledge from

these related fracturing technologies will be used to analyze the pneumatic fracturing process.

1.2 Research Objectives

In order to improve the understanding of the pneumatic fracturing process and broaden its engineering applications, a number of fundamental questions must be addressed. These research needs are outlined in Figure 1.2. As indicated, the problems under study have been divided into two general groups: “Fracture Mechanism” and “Formation Response.” Studies of fracture mechanism focus on the actual fracture event with the goal of controlling and optimizing the process. Studies of formation response deal with the behavior of the geologic formation after fracturing, on both a short-term and long-term basis.

Some aspects of the pneumatic fracturing process have already been studied. For example, the mechanism of fracture initiation was investigated by King [1993] and post-fracturing gas flow in pneumatically-fractured formations was studied by Nautiyal [1994]. Ding [1995] developed and validated a convection-diffusion model describing contaminant transport out of a discrete fracture. A study of fracture behavior in clay by Hall [1995] identified key geologic and environmental factors related to fracture longevity. Canino [1997] studied the effects of fracturing on overlying structures and developed a model to predict ground deformation. Ongoing research activities include studying the effectiveness of ultrasound enhanced contaminant removal in pneumatically-fractured formations as well as the development of a comprehensive computer model to aid in site screening and preliminary remediation design [Sielski, in progress].

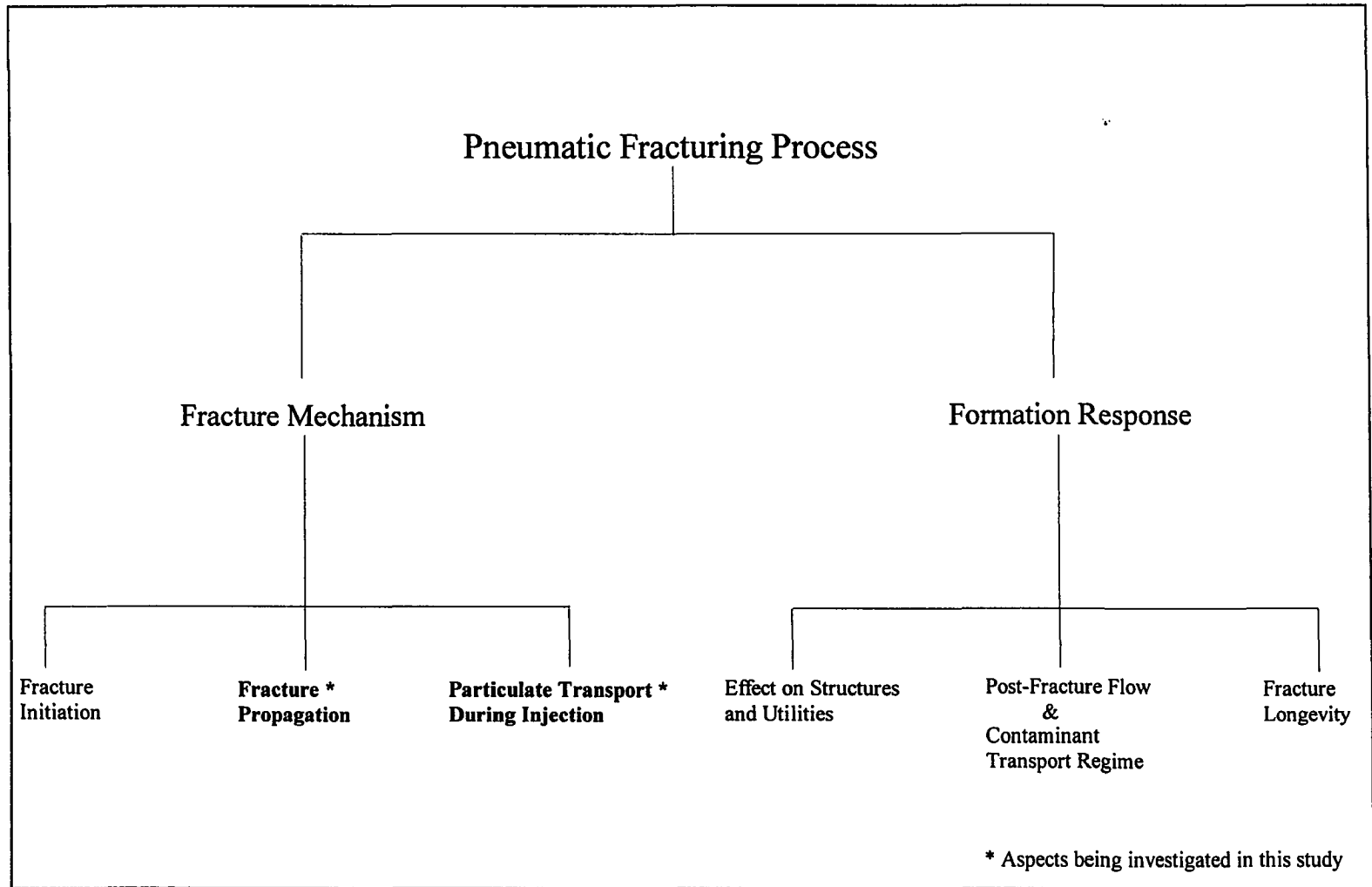


Figure 1.2 Different Aspects of the Pneumatic Fracturing Problem

A key aspect of the pneumatic fracturing mechanism which has not yet been studied is the propagation of pneumatic fractures in geologic media. Prediction of the geometry and extent of propagating fractures is important in the design of pneumatic fracturing projects. It will also be useful in assessing formation response. While some limited analyses of fracture propagation have been conducted, there is still no constitutive, theoretically-based model. The development of a mathematical model simulating fracture propagation and formation response for the pneumatic fracturing process is therefore the primary focus of this dissertation. It is noted that a considerable database of fracture propagation data has now accumulated from field tests, which will be used to calibrate and validate the propagation model.

A problem which is auxiliary to the propagation phenomenon is injection of particulate media into the fracture network. Supplements in both a liquid and solid form are often injected into the fracture network to enhance remediation processes such as bioremediation and *in situ* vitrification. A secondary objective of this study, then, will be to investigate the transport of the supplemental solid media into fractured formations and predict its distribution.

In summary, the objectives of this research study are:

1. To formulate a mathematical model of pneumatic fracture propagation in geologic formations. Both soil and rock formations will be addressed, and the model will be related to geotechnical properties typically determined during the site evaluation phase of a project.

2. To solve the problem of pneumatic fracture propagation. Both analytical and numerical solutions will be investigated. The model will predict the equilibrium fracture geometry including radius and aperture.
3. To validate and calibrate the developed model with field data from past projects involving pneumatic fracturing.
4. To summarize the particulate media transport mechanisms that might occur in geologic formations during pneumatic injection. Also, a methodology will be developed to predict the extent of soil fluidization and media transport distance.

This dissertation will begin with a review and summary of related literature on fracture propagation and particulate transport (Chapter 2). This is followed by a presentation of the assumptions and formulation of the propagation problem (Chapter 3). The solution to the propagation problem and the details of the model implementation are presented next (Chapter 4). The subsequent chapter calibrates the model and checks its validity using data collected during previous field investigations (Chapter 5). In the next chapter, the methodology for predicting the transport of injected particulate media is described and validated with data from a case study of the phenomena (Chapter 6). Finally, the study conclusions are presented along with recommendations for future study (Chapter 7).

CHAPTER 2

LITERATURE REVIEW

2.1 Fracture Propagation Models

2.1.1 Overview

The phenomenon of fracture propagation in geologic formations has been studied in a wide range of industrial applications. Most investigators have focused on intentionally creating new fractures in geologic media and maximizing their effects [e.g., Howard, & Fast, 1970; Wolff *et al.*, 1975; Nemat-Nasser *et al.*, 1983]. However, some studies have addressed preventing rather than propagating fractures, as in earth dam failures [Vallejo, 1993].

Figure 2.1 is presented in an attempt to classify the fracture propagation phenomena studies which are available in the literature. The basic distinguishing characteristic of the various fracture phenomena is the rheology of the fracturing fluid, which ranges from molten solids to gases. The other important characteristic is the rate of pressurization and resultant fracture propagation velocity. As indicated, fracture tip velocities for the various phenomena range from low subsonic to supersonic velocities.

At the low end of the velocity spectrum, fractures are propagated by magma during the natural emplacement of igneous sills, dikes and laccoliths. The fracturing fluid in this case is a molten solid, and the fracture tip velocity is relatively low at 0.5 m/sec. This phenomenon has received a moderate amount of attention by investigators in the geological sciences [e.g., Pollard and Johnson, 1973; Spence and Turcotte, 1985].

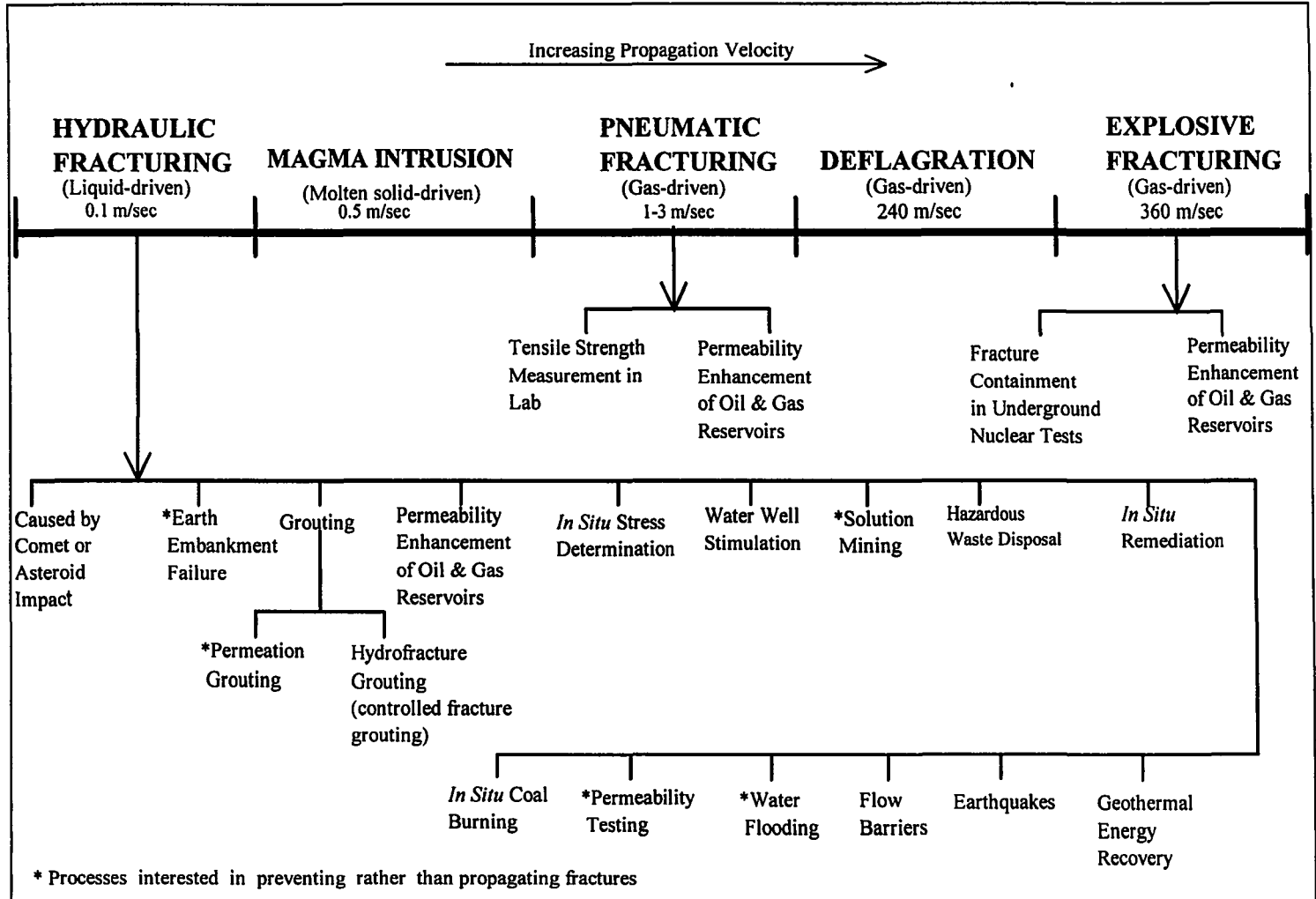


Figure 2.1 Fracture Propagation Phenomena in Geologic Media

Fracture tip velocities in the hydraulic fracturing process are comparable to those of magma-driven fracture propagation. Considerable work has been done on analysis of hydraulic fracture propagation because of its economic importance in the petroleum industry. A number of mathematical models have been developed over the last few decades for predicting the fracture dimensions [e.g., Perkins and Kern, 1961; Geertsma and de Klerk, 1969].

At the high end of the velocity spectrum, fractures have been propagated by explosives and deflagration (e.g., High Energy Gas Fracturing - HEGF). Such fractures propagate at approximately the velocity of sound (330 m/sec) and are driven by expanding gases generated from extremely rapid chemical oxidation reactions. Explosive fracturing and deflagration have been applied to enhance permeabilities of oil, gas and geothermal wells [e.g., Nilson *et al.*, 1985].

The fracture phenomena which has received the least attention are fractures propagated by the rapid injection of a gas. Pneumatic fracturing, which is the focus of the present study, falls into this category. Data collected from field demonstrations over the last several years indicate the propagation velocity of pneumatic fractures is in the range of 2-5 m/sec. This velocity is intermediate between the slower liquid-driven fractures and the more rapid explosive fracturing. Since investigations of fracture propagation phenomena have clearly shown that fracture behavior is strongly dependent on propagation velocity and fracturing fluid properties, there is a clear need for further investigation of pneumatic fracturing phenomena.

The sections that follow are a review of the various propagation phenomena and associated models which are available in the literature. They are presented as background

for development of the pneumatic fracture propagation model presented in Chapters 3 and 4.

2.1.2 Magma Driven Fracture Propagation

Geologic features such as sills and laccoliths are created by igneous intrusions into rock formations. The overlying geologic strata arch upwards as a result of these magmatic intrusions. Investigators have analyzed the response of the overlying strata assuming that the formation behaves like an elastic plate with a uniformly distributed load acting upon it.

A. M. Johnson (1970) applied elasticity theory to determine the geometry of a concordant sill intrusion in two dimensions. The key assumptions of this model are that the overlying lithosphere behaves as a fixed elastic beam (Figure 2.2(a)), the pressure is constant throughout the intrusion, and the strata below the plane of injection do not deflect due to the magmatic over-pressure. The maximum displacement, b_w , occurs at the center of the intrusion and is given by:

$$b_w = \frac{p_d R}{32Gz^3} \quad (2.1)$$

where p_d is the magmatic overpressure, R is the fracture radius, z is the fracture depth and G is the shear modulus. This equation assumes that the flexing overburden is very thin relative to the length of the intrusion, i.e. the ratio of the length to depth, R/z , is greater than 10:1.

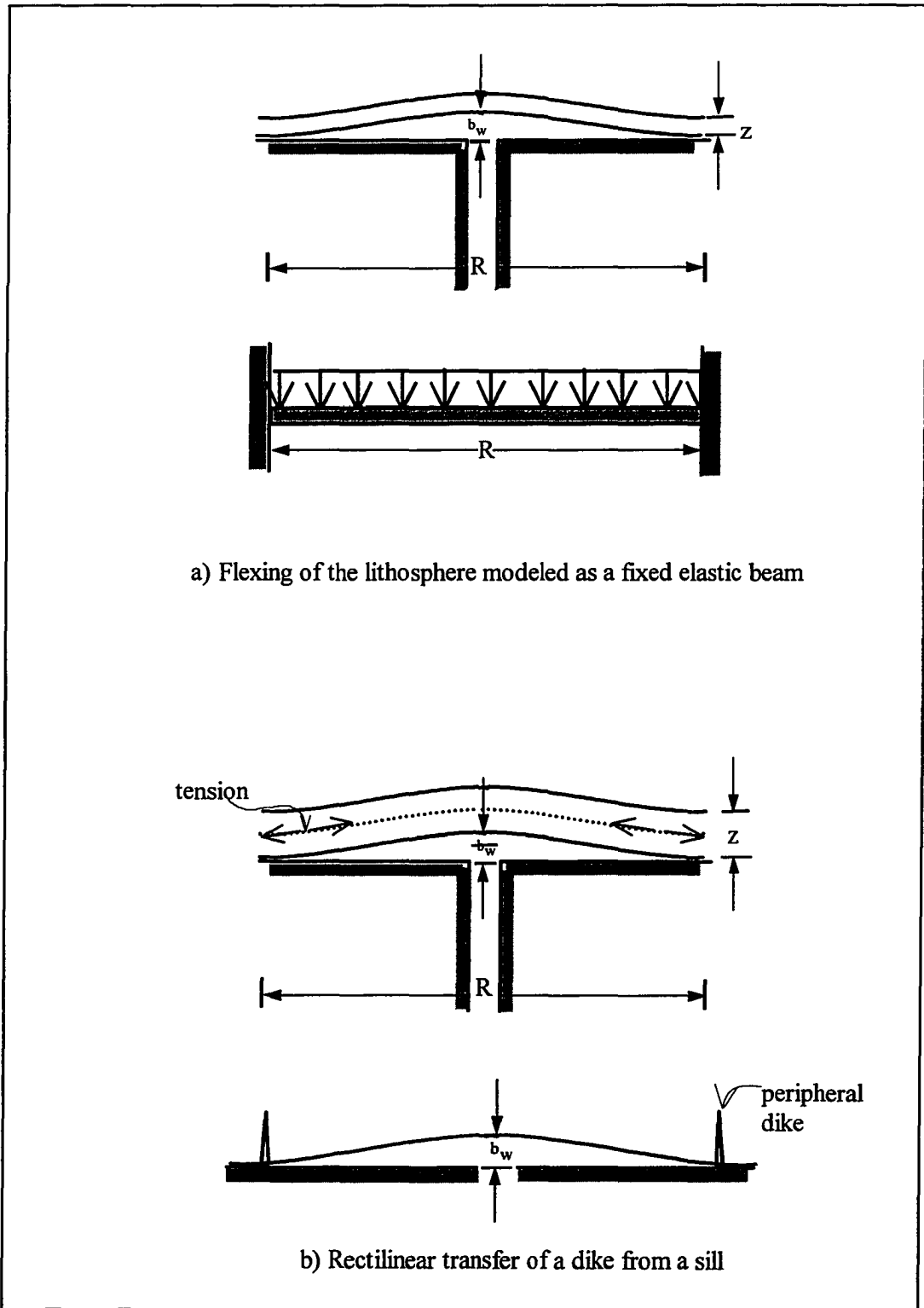


Figure 2.2 Magma-Driven Fracture Propagation

Laccoliths are concordant intrusions where the overburden is thick with respect to its length with $R/z < 10:1$. For laccoliths, the relation for maximum displacement, b_w , is given by:

$$b_w = \frac{p_d R^4}{2Gz^3} \left(0.3125 - \frac{1}{R^2} \right) \quad (2.2)$$

An examination of the preceding two solutions reveals that they are of the same form as plate-bending analysis in structural engineering [Timoshenko and Goodier, 1951].

Johnson also studied the conditions conducive to emplacement of dikes. Figure 2.2(b) shows the stresses developed by flexing an elastic plate and peripheral dike development. The mechanics of the rectilinear transfer from a sill to a dike would provide insight into conditions that might influence “daylighting” of pneumatic fractures. Fracture “daylighting” occurs when propagating fractures deviate from a horizontal plane of propagation and intersect the ground surface.

D. D. Pollard and A. M. Johnson (1973) used the theory of elasticity, to analyze the deformation of sedimentary rocks in the Henry Mountains during a magma intrusion. They derived theoretical models for laccolithic and sill intrusions.

The effect of the host rocks on the form and growth of the laccoliths was analyzed as the bending of a stack of thin elastic plates. They assumed that the area over which the magma was spread is elliptical in plan. By varying the axis length of the ellipse, plan shapes of intrusions varying from a rectangular strip (anticlinal plan) to circular were

examined. Three different load distributions, a point load, a uniform distribution and a triangular distribution of load, were considered. The following are the equations for overburden deflection with terms as previously defined:

$$w = \frac{P_d(1-\nu^2)}{2Ez^3}(R^2 - 2R^2r^2 + R^4)(\text{anticlinal plan - uniform pressure distribution}) \quad (2.3)$$

$$w = \frac{3P_d(1-\nu^2)}{16Ez^3}(R^2 - 2R^2r^2 + r^4)(\text{circular plan - uniform pressure distribution}) \quad (2.4)$$

$$w = \frac{P_d(1-\nu^2)}{20Ez^3}\left(10r^4 - \frac{2|r|^5}{R} - 15R^2r^2 + 7R^4\right)(\text{circular plan - triangular load distribution}) \quad (2.5)$$

As seen from the above equations, the overburden deflection due to magma intrusion is affected more by the extent and the depth of the magma intrusion than any other parameters.

The modeling of the overburden deflection above the sills was based on the assumption that the cross-section of the intrusion is elliptical and the pressure is uniform throughout the fracture. The following is the elastic solution for the deflection of the overburden, overlying a sill with an anticlinal plan:

$$w = \frac{P_d f}{4G} \left[(3 - 4\nu) \sin \eta (\cosh \xi - \sinh \xi) - \frac{I \sinh 2\xi + J \sin 2\eta}{\cosh 2\xi - \cos 2\eta} + I + \frac{L \cosh 2\xi_{50}}{K^2 + L^2} \right] \quad (2.6)$$

where $I = \sinh\xi \sin\eta$, $J = \cosh\xi \cos\eta$, $K = \sinh\xi \cos\eta$, $L = \cosh\xi \sin\eta$, of the elliptical coordinate system (ξ, η) , f is the focal length of the ellipsoidal sill contact, and G is the Shear modulus.

D. A. Spence and D. L. Turcotte (1985) analyzed the behavior of magma-driven cracks using techniques developed to study the propagation behavior of hydraulically-induced fractures (see Section 2.1.3 “Hydraulic Fracturing”). They analyzed the crack geometry of an expanding two-dimensional crack in an impermeable elastic medium. Assuming a constant injection rate and laminar flow conditions, a similarity solution containing fracture toughness was derived. It was also assumed that the fracture was deep within the formation so that there was no interaction with the surface. The analytical solution for predicting the aperture of a propagating fracture was determined to be:

$$b_w = 2kA_0Q^{1/2} \left[\frac{3\mu(1-\nu)}{G} \right]^{1/6} t^{1/3} \quad (2.7)$$

where Q is the flow rate, μ is the dynamic viscosity, ν is Poissons ratio, t is the time, A_0 and k are coefficients.

A significant finding of the study was the dependence of fracture aperture on fluid viscosity. It was also determined that the fracture toughness of the elastic medium can be neglected in magma-driven fracture propagation problems.

It is noted that deflection of the geologic formation has been studied in the related phenomena of cover subsidence over sinkholes [**Habibagahi, 1981**]. The principal

difference is that the formation is analyzed as a uniformly loaded fixed beam which deflects downward over a subterranean cavity.

2.1.3 Hydraulic Fracturing

Because of its economic importance, hydraulic fracturing has received considerable study, particularly in the petroleum industry. The following is a summary of the chronological development of hydraulic fracture propagation models as they increase in complexity.

R. D. Carter (1957) was the first investigator to develop a solution for estimating the extent of hydraulic fracture propagation in geologic media. His model was the basis for design of a large number of fracturing treatment projects in the petroleum industry. Due to its simplicity, the model was widely used as it requires only fluid loss data which are easily obtainable from simple laboratory experiments. Figure 2.3(a) is a schematic of the fracture geometry assumed for the Carter model. It takes into consideration the strong dependence of fracture propagation on leak-off, as well as the time duration over which the fracture surface has been exposed to the fracturing fluid. Carter's model assumes that initial leak-off velocities are high (called the "spurt loss"), but decrease gradually with time due to the wall building effects of the fracturing fluid. Based on this work the equation for estimating the extent of the fractured area, A , as a function of time, t , in terms of the treatment conditions is:

$$A(t) = \frac{Qb_w}{4C^2\pi} \left\{ e^{\left[\frac{2C\sqrt{\pi t}}{b_w} \right]} \operatorname{erfc} \left[\frac{2C\sqrt{\pi t}}{b_w} \right] + \frac{4C\sqrt{t}}{b_w} - 1 \right\} \quad (2.8)$$

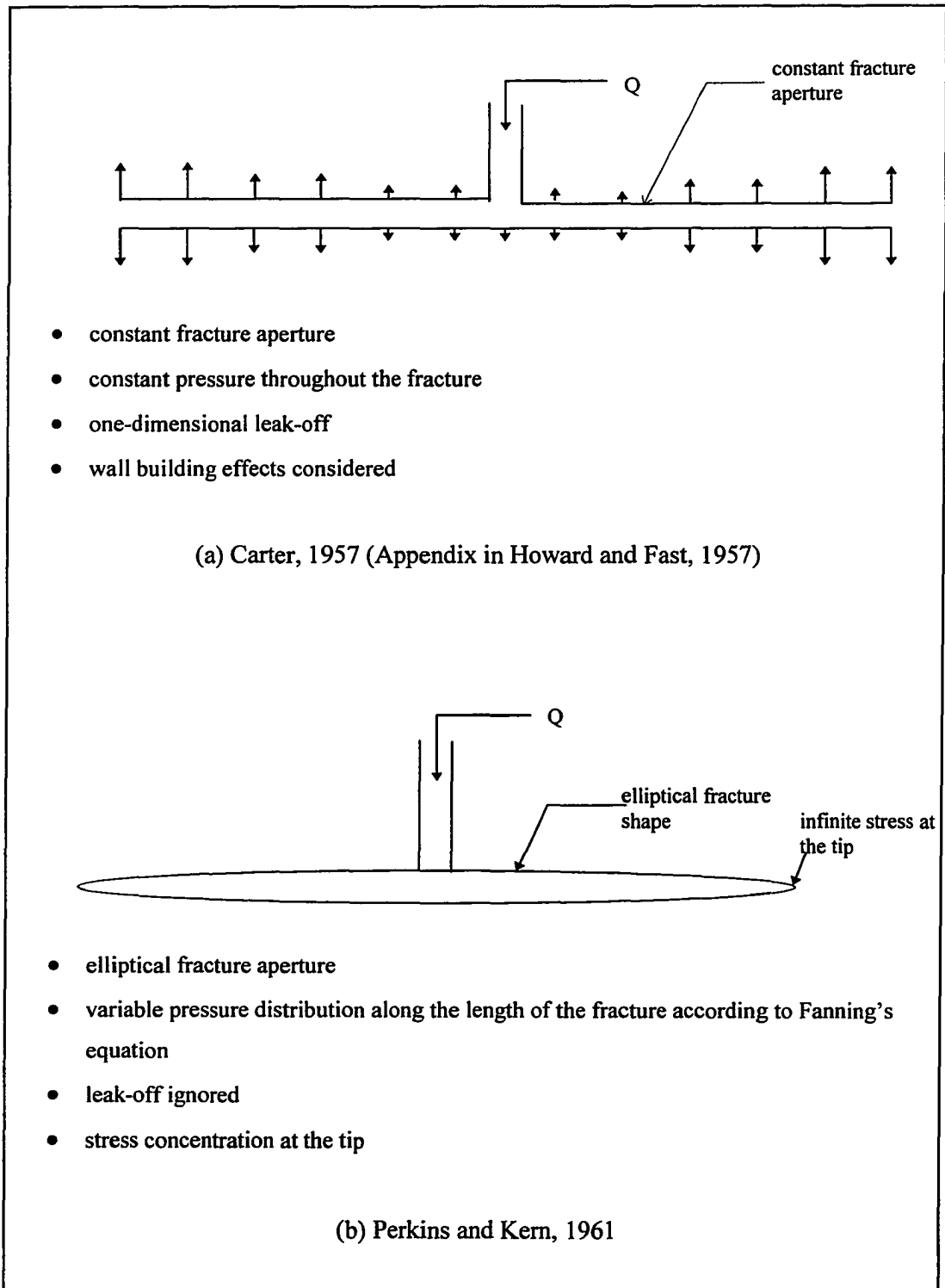


Figure 2.3 Fracture Configurations for Theoretical Models

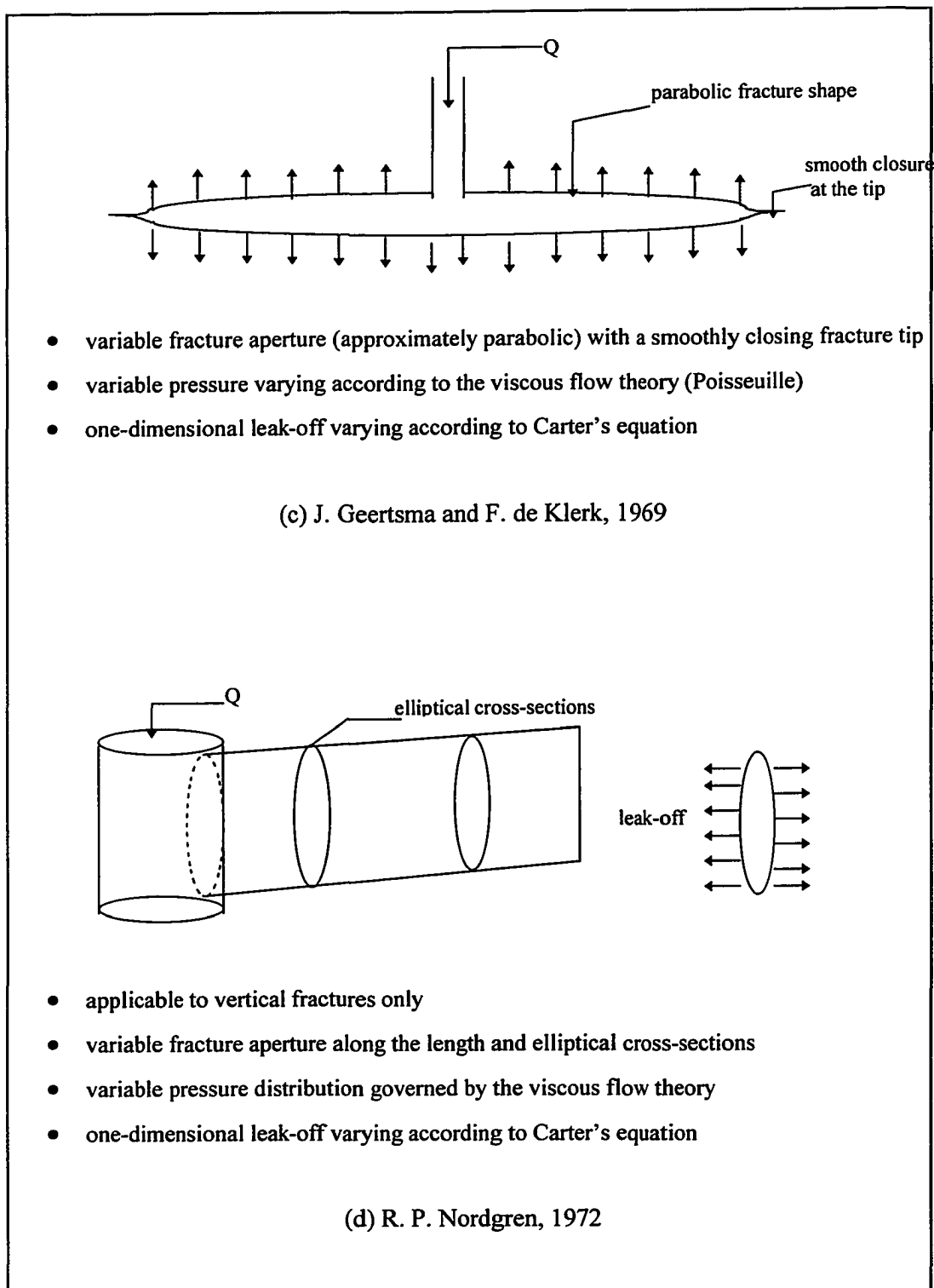


Figure 2.3 (cont.) Fracture Configurations for Theoretical Models

where C is the fracturing fluid coefficient. One limitation of the Carter model is that it does not take into account the effect of the fracturing fluid shear on filter cake buildup at the fracture surface (static fluid leak-off). Additionally, it does not consider the effect of reservoir fluid pressure, or variations in fracture aperture and pressure along the length of the fracture.

T. K. Perkins and L. R. Kern (1961) presented a closed-form solution for estimating fracture aperture for varying conditions of fracturing fluid rheology and fracture orientation. The model was an improvement over the Carter model in that it used a more realistic elliptical geometry (shown in Figure 2.3(b)). Also, the pressure variation within the fracture was considered in calculating the aperture of the fracture. Some key assumptions made by Perkins and Kern include: (i) formation is homogeneous, isotropic, brittle and elastic; (ii) a pressure drop along the length of the fracture defined by Fanning's equation; and (iii) plane strain conditions. In development of the model, the authors acknowledged that the aperture of horizontal fractures results only from compression of surrounding rock when the fractures are deep ($L < 4/3z$, where L is extent of the fracture and z is the depth of the fracture), but included both compression and flexing/lifting of overburden when the fractures are shallow ($L > 4/3z$).

The Perkins and Kern solution for fracture aperture, b_w , of horizontally propagating fractures for Newtonian fluids with laminar flow takes the form:

$$b_w = 0.0765 \left\{ \frac{Q\mu L \left[\frac{4}{\pi} + \frac{3}{16} \left(\frac{L}{z} \right)^3 \right]^4}{E \left[\frac{4}{3\pi} + \frac{1}{32} \left(\frac{L}{z} \right)^3 \right]} \right\}^{1/4} \quad (\text{shallow fractures}) \quad (2.9)$$

$$b_w = 0.22 \left[\frac{(Q)(\mu)(L)}{E} \right]^{1/4} \text{ (deep fractures)} \quad (2.10)$$

where E is the Young's modulus. An important result of the Perkins and Kern solution is that fracture aperture is not sensitive to the rock properties, since typical rock moduli do not vary more than 10 to 20 fold. However, aperture is sensitive to the pumping rate and viscosity of the fracturing fluid since these are much more variable. Therefore, operating conditions which cause a high pressure drop along the fractures (such as high injection rates and/or viscous fluids) will lead to relatively wide fractures, and vice versa.

A severe limitation of the Perkins and Kern model is that it does not consider the effect of leak-off on fracture dimensions. Also, because of the assumed elliptical fracture shape, an anomaly of infinite stress exists at the fracture tip.

J. Geertsma and F. de Klerk (1969) developed a model to predict the dimensions of both linear and radially propagating fractures around a well bore. This model was a significant improvement over previous models as it considered the effect of both the fluid leak-off and the pressure variation within the fracture, which had been addressed separately by Carter and 'Perkins and Kern,' respectively.

The model was based on Barenblatt's [1962] treatment of an infinite homogeneous, isotropic and elastic solid containing a crack which was subjected to plane strain conditions in a plane perpendicular to the well bore. As indicated in Figure 2.3(c), the crack has a

smoothly closing tip so that a finite stress exists just beyond the crack tip (equilibrium crack).

The solution for fracture aperture is obtained using Poisseuille's equations for the pressure drop within a fracture, Sneddon's equation of a radially propagating fracture [Sneddon, 1946] and the Barrenblatt's boundary condition [Barenblatt, 1962]. The leak-off model was the same as that developed by Carter [1957]. For calculating the extent of fracture propagation, a material balance equation was utilized. Laplace transforms and convolution theory were applied to the material balance equation to obtain a closed-form solution for the fracture extent. The resulting equations for the aperture, b_w , and the extent, R , of a radially-propagating fracture are similar to those developed by Carter and 'Perkins and Kern,' are shown below:

$$b_w = 2^4 \sqrt{\frac{\mu QL}{G}} \quad (2.11)$$

$$L^2 = \frac{Q}{30\pi^2 C^2} (4b_w + 15S_p) \left(\frac{2\alpha_R}{\pi} - 1 + e^{\alpha_R^2} \operatorname{refc}(\alpha_R) \right) \quad (2.12)$$

$$\text{where, } \alpha_L = \frac{8C\sqrt{\pi t}}{\pi b_w + 8S_p}, \quad \alpha_R = \frac{15C\sqrt{\pi t}}{4b_w + 15S_p},$$

S_p is the spurt loss and b_w is the fracture width near the well bore at the time the pump stops. It is noted that the effects of leak-off were considered only for calculation of fracture extent. The effect of leak-off on the fracture aperture was ignored as it had a negligible influence.

R. P. Nordgren (1972) analyzed hydraulic fractures of limited vertical extent and elliptical cross-section (Figure 2.3(d)), thus extending the ‘Perkins and Kern’ model to include fluid leak-off and the effect of change in fracture aperture with time. Assumptions include a homogeneous, isotropic, elastic and brittle formation. In addition, plane strain conditions and Newtonian behavior of the fracturing fluid were assumed.

Nordgren established a continuity equation for fluid flow in the fracture and solved for the boundary conditions numerically. Approximate solutions were also obtained by neglecting the leak-off and fracture volume change for small and large times, respectively. The large and small times in the fracture propagation correspond to the no fluid loss and large fluid loss conditions. For the case of large fluid loss (large time approximation):

$$L(t) = \frac{Qt^{1/2}}{\pi Ch} \quad (2.13)$$

$$b_w = 4 \left[\frac{2(1-\nu)\mu Q^2}{\pi^3 GCh} \right]^{1/4} t^{1/8} \quad (2.14)$$

where h is the height of the fracture. For the case of no fluid loss (small time approximation):

$$L(t) = 0.68 \left[\frac{GQ^3}{(1-\nu)\mu h^4} \right]^{1/5} t^{4/5} \quad (2.15)$$

$$b_w = 2.5 \left[\frac{(1-\nu)\mu Q}{Gh} \right]^{1/5} t^{1/5} \quad (2.16)$$

This model, also known as the “PKN Model,” is one of the two “first generation” two-dimensional fracture propagation models currently in wide use within the petroleum industry [Mendelsohn, 1984]. The other model currently being used was developed by Geertsma and de Klerk and modified by Daneshy [1973] to account for non-Newtonian fluids. It is referred to as the “CGDD Model,” named after the principal developers.

2.1.4 Other Hydraulic Fracturing Investigations

Hydraulic fracture propagation is critical to the success of other subsurface processes and has been studied by a number of investigators. For example, hydraulic fractures caused by deep well injection of hazardous waste have been analyzed, since it is critical to avoid contact with nearby permeable formations [Wolff *et al.*, 1975]. Hydraulic fracturing has also proven to be a useful tool for measuring *in situ* stress [Abou-Sayed *et al.*, 1978], recovering geo-thermal energy from hot, dry rock masses [Nemat-Nasser *et al.*, 1983], fracture grouting [Zhang, 1989], constructing flow barriers [Huck *et al.*, 1980], solution mining [Haimson and Stahl, 1970], *in situ* coal burning [Nilson, 1981], water well stimulation [e.g., Stewart, 1974; Hurlburt, 1989] and treatment of sites contaminated with hazardous wastes [Murdoch, 1992].

Avoidance of hydraulic fracture propagation becomes important in processes such as permeation grouting [Wong and Farmer, 1973], permeability testing [Bjerrum *et al.*, 1972], enhanced oil and gas recovery by water flooding [Yuster and Calhoun, 1945], air

sparging of contaminated ground water [Johnson *et al.*, 1993] and earth embankment failure [Vallejo, 1993].

Hydraulic fracturing has also been studied as a dominant process following an earthquake [Holzer *et al.*, 1989] and during an asteroid/comet impact [Huntoon and Shoemaker, 1995]. In both of these situations, the excess pore fluid pressures created by the sudden terrestrial deformation leads to widespread propagation of hydraulic fractures.

2.1.5 Gas-Driven Explosive Fracturing

The propagation of explosively-driven fractures is important in a number of applications: containment of underground nuclear tests, explosive stimulation of oil, gas and geothermal wells, and permeability enhancement of oil shale and coal prior to *in situ* combustion. Subsonic gas-driven fractures and liquid-driven fractures have similar solid mechanics in that the induced fracture tip velocity is generally small compared to the velocity of stress waves, but do differ from a fluid mechanics perspective. In hydraulic fracturing, the driving pressure is only slightly greater than the confining tectonic stress, and the fluid pressure is nearly uniform along the fracture. In explosive fracturing, the driving pressure greatly exceeds the resisting compressive stress, and the fluid pressure varies considerably along the fracture.

A comprehensive numerical solution of gas-driven explosive fractures was developed by Nilson [1981]. He assumed the formation to be elastic and impermeable, and the gas to behave ideally and isothermally. His approach to the problem was similar to that of Geertsma and de Klerk by assuming the fracture shape to be functionally related to pressure distribution by linear elasticity. The application of the boundary condition of a

smoothly closing fracture tip, as addressed by Barenblatt's theory of equilibrium fracture, is also similar to the above referenced liquid-driven fracture propagation investigations.

The analysis was performed by establishing ordinary differential equations for fracture aperture using variable pressure distribution, elasticity theory, conservation of mass and momentum within the fracture, and viscous shear stress during laminar and turbulent flow conditions. The differential equations were solved using numerical techniques for laminar and turbulent flow regimes satisfying the Barrenblatt's boundary conditions, i.e., the stress is finite at the tip of a fracture which is in mobile equilibrium.

Some interesting observations follow from Nilson's analysis. The flow experiences a diverging/converging channel because the fracture aperture increases with time and decreases with distance from the point of initiation. The injected gas accelerates through three different flow regimes: laminar, turbulent and inviscid. The flow at the tip of the fracture is always laminar and a vacuum exists at the tip of the fracture either in an impermeable medium or in a permeable medium at later times. The model also considered seepage interactions of the gas in a permeable formation and showed that the leak-off effects become less important as the fracture length increases. The physical explanation for this is that as aperture increases, the longitudinal through-flow is enhanced more rapidly than the corresponding increase in fracture length enhancing the leak-off.

2.2 Particulate Transport

2.2.1 Overview

Study of particulate transport is of interest in a wide range of phenomena and processes. The aim of the present literature survey is to collect relevant work from the various fields in

preparation for formulation of the particulate flow problem in the pneumatic fracturing process. The fundamental aspects of the particulate flow phenomena are dealt with in detail in a number of texts [e.g., Brodkey, 1967; Soo, 1967].

During the pneumatic fracturing injection process, the state of the injected dry media can best be described as a “polydispersed primary aerosols.” Aerosols, by definition, are particulate suspensions in gases and are formed either by disintegration of liquids/solids introduced into the transporting fluid (primary particulates), or by the gas-to-particle conversion (secondary particulates). The term “polydisperse” is used to describe a distribution of particle sizes, as opposed to “monodisperse” in which all particles are of the same size.

Previous investigations by the HSMRC research group have tentatively identified three fundamental mechanisms by which particles can be transported in the subsurface during pneumatic fracturing injection:

- (a) interstitial transport;
- (b) transport in a discrete fluidized zone; and
- (c) transport within an open, discrete fracture.

These three transport mechanisms are shown conceptually in Figure 2.4. It is hypothesized that the particular mechanism which dominates is expected to be a function of the formation properties (e.g., permeability) and the injection system parameters (e.g., flow rate, rate of injection). Related background studies for each of these mechanisms are presented in the following sections.

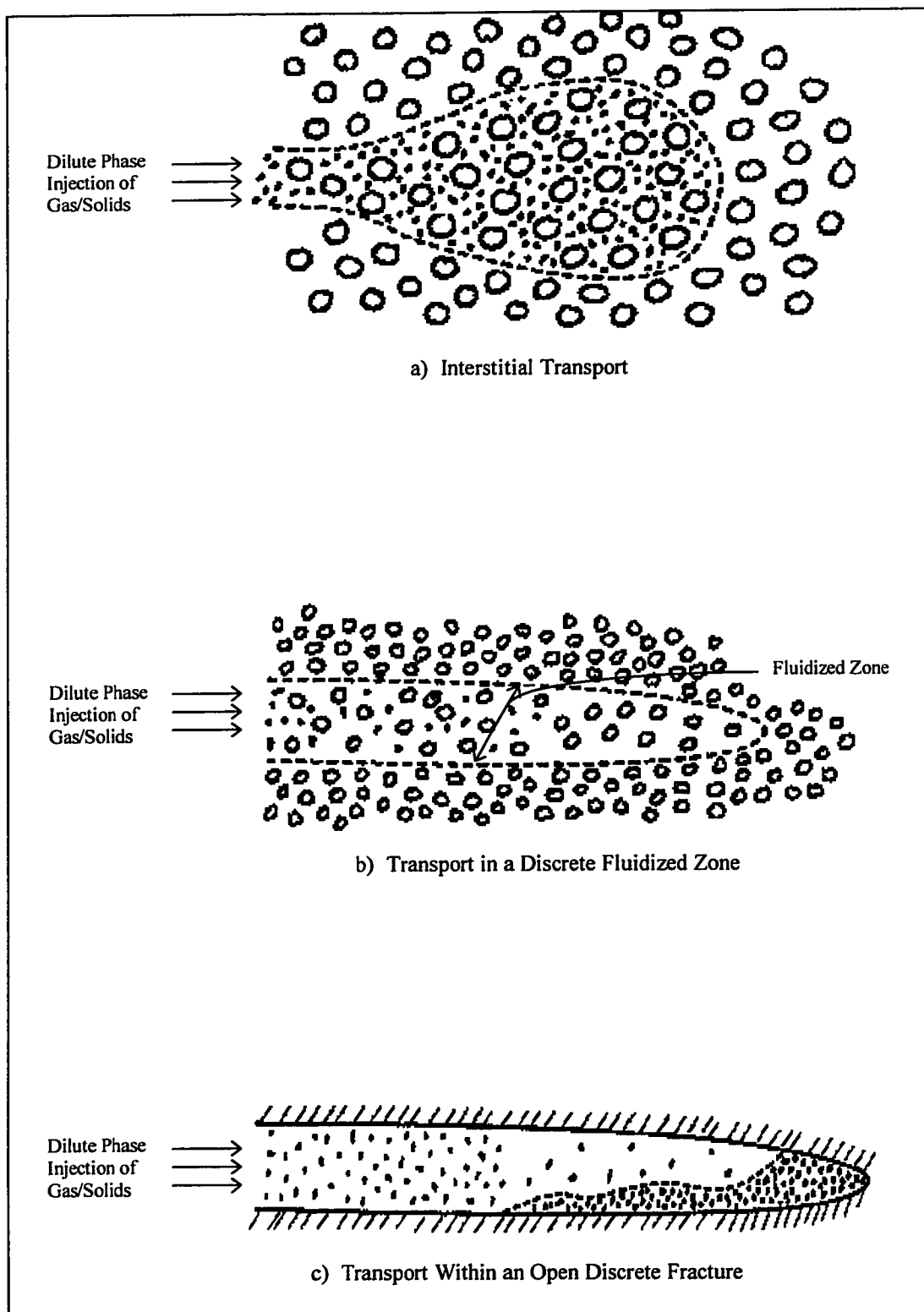


Figure 2.4 Mechanisms of Particulate Transport

2.2.2 Interstitial Transport of the Injected Solid Particles

Transport of the suspended particulate matter through the interstices of a porous media is an established phenomenon [McDowell-Boyer *et al.*, 1986]. For particles whose grain size is close to that of the porous media, a cake or a surface mat will form preventing any particle penetration. This surface caking is associated with a significant decrease in the permeability of the media. Particles which are slightly smaller than the media grain size penetrate the soil for some distance, but are eventually halted by mechanical straining. Straining near the surface of the porous media aids in the build up of a surface mat. Only particles which are substantially smaller than the media can penetrate substantial distances into the matrix.

Whether or not particle caking or straining occurs is determined by the ratio of media diameter to particle diameter. Shakthivadivel [1969] found that finer particles would not penetrate coarser particles if the following condition is satisfied:

$$\frac{d_m}{d_p} < 10 \quad (2.17)$$

where d_m is the diameter of the coarser media, and d_p is the diameter of the finer media.

If the ratio of the media diameter to particle diameter is less than 10, severe caking can be expected. When the ratio falls in the range $10 < d_m/d_p < 20$, a permeability reduction of 7-15 times is typically observed, accompanied by an approximate 30% reduction in the pore volume occupied by the deposited particles. When the size of the injected media particles is small ($d_m/d_p > 20$), permeability reduction of 10-50% of the clean porous media value may be expected with particle deposition in only 2-5% of the pore volume. Shakthivadivel further observed that particles, once deposited, cannot be dislodged by an

increased flow rate. However, flow reversal can resuspend deposited particles. When there is a size distribution of particles both in the injected media and the coarser geological media, the criteria developed by Sherard *et al.* [1984] for geotechnical filter materials can be applied as follows:

$$\frac{d_{m,15}}{d_{p,85}} < 9 \quad (2.18)$$

where $d_{m,15}$ is the diameter at which 15% by weight of the coarser media had a smaller diameter, and $d_{p,85}$ is the diameter at which 85% by weight of the finer media had a smaller diameter. This is a more simplified criteria and can be considered as the transition between caking and straining. Note that the value ratio of nine is almost the same as the previous criteria of ten for uniform particle sizes.

2.2.3 Particulate Transport in a Discrete Fluidized Zone

The mechanism of particulate transport through a fluidized aggregate zone or lens occurs when the treated formation is cohesionless and the injected gas velocities are sufficient to suspend the individual soil particles in the fluid. This situation is similar to the condition existing within a “fluidized bed reactor.”

The minimum gas velocity for particle fluidization is a function of soil porosity, shape and size range of the particles, and the viscosity of the injection fluid. The pressure drop-velocity relation for a fluidized bed at the stage of incipient fluidization has the following form [Ergun, 1952]:

$$\frac{\Delta p_B}{H_{mf}} = 150 \frac{(1 - \epsilon_{mf}) U_{mf} d \rho_f}{\epsilon_{mf}^3 \mu_{air}} + \frac{1.75}{\epsilon_{mf}^3} \left(\frac{U_{mf} d \rho_f}{\mu_{air}} \right)^2 \quad (2.19)$$

where Δp_B is the pressure drop across the fluidized bed, H_{mf} is the bed height at incipient fluidization, U_{mf} is the minimum fluidizing velocity, ρ_f is the fluid density, d is the particle diameter, and ϵ_{mf} is the bed voidage at incipient fluidization. Gas-solid systems (aggregate fluidization) in general exhibit characteristics that are significantly different than liquid-solid systems (particulate fluidization) when fluidized.

Particles in a fluidized bed tend to segregate. It is hypothesized that the particle transport during pneumatic injection of particles in a fluidized formation occurs through this mechanism. Mathematical models that describe patterns of segregation were first described by Gibilario and Rowe [1974].

Fluid-particle interactions in a fluidized bed are different from the fluidization which occurs during pneumatic injection. The direction of the fluid flow in the former is in the same plane as the gravitational forces, while in the latter the flow is perpendicular to gravity. The fluid-particle interactions of gas jets in fluidized beds, discharging in the horizontal direction, provide a close parallel to the fluidized state during a pneumatic injection. Penetration length studies of the gas jets and related correlations for horizontal discharges are available in the literature [Shakhova, 1968; Merry, 1971].

2.2.4 Particulate Transport in a Discrete Open Fracture

Particle dynamics differ depending on the size of the particulates. From the largest to the smallest, the following regimes will govern: continuum flow/Stoke's regime ($> 1.3 \mu\text{m}$), slip flow/Cunningham regime ($1.3\text{-}0.4 \mu\text{m}$), transition flow regime ($0.01\text{-}0.4 \mu\text{m}$) and free molecule regime ($<0.01 \mu\text{m}$). The particle size of the liquid/solid supplements injected by pneumatic fracturing are predominantly greater than $1 \mu\text{m}$. This is true since there is a lower physical limit beneath which liquid and solid particles can be broken down with the available equipment. This places particle transport in pneumatically fractured formations within the continuum flow regime, where the particle behavior is governed by Stoke's law.

The transport of particulates in a discrete fracture can be described using basic sediment transport theory [Boggs, 1987]. All particles are transported either in suspension or by saltation/rolling along the boundary. Important properties of the sediment that affect its transport are individual grain properties such as size, shape (sphericity and shape factor) and specific gravity, as well as the bulk properties of the particles including grain size distribution, bulk unit weight and porosity.

The problem of particulate transport in pneumatically fractured formations is similar to that of mobile boundary channels in hydraulics. Studies on conditions critical to the initiation of particle movement can be classified as: (1) methods based on drag; (2) methods based on shearing force; and (3) methods based on lift.

According to the first method, particle movement occurs when the drag exerted on the particle by the moving water is sufficient to overcome the frictional resistance between the particle and the bed. According to Brahms and Airy [1936], who based their derivation

on this principle, the critical velocity for initiation of particle movement, V_{cr} , may be computed by:

$$V_{cr}^2 = \frac{4}{3} \frac{dg}{\alpha C_D} (s-1) \tan \theta \quad (2.20)$$

where d is the particle diameter, g is the acceleration due to gravity, C_D is the coefficient of drag, θ is angle of friction, while s and α are coefficients.

The shearing force method, also known as the tractive force method, is a second approach for describing the initiation of sediment motion. An important development in the tractive force approach was made by Shields [1936]. He stated that the critical condition for sediment motion is a function of the Reynolds number and developed a diagram to determine whether or not initiation of particle movement has occurred. This diagram is known as Shields diagram which is a plot of two dimensionless ratios: τ^* , which is the dimensionless shear stress, and R_{eg} , the grain Reynolds number. These are defined as follows:

$$\tau^* = \frac{\tau_0}{(\gamma_p - \gamma_f)} \quad (2.21)$$

$$R_{eg} = \frac{U^* d}{v_{kin}} \quad (2.22)$$

where τ_0 is the boundary shear stress, γ_p is the specific gravity of the particles, γ_f is the

specific weight of the fluid, U^* is the friction velocity, and ν is the kinematic viscosity of the fluid. By plotting these parameters for the particles under consideration on the diagram, it can be determined whether or not the particles would be set in motion.

The third method considers the lift force caused by velocity shear. The critical condition is obtained from a balance of the lift force and particle weight. The lift forces are caused by the velocity gradients across the particles and the instantaneous velocity differences accompanying turbulent fluctuations. Thomas [1961] developed an equation for this mechanism by considering two different conditions depending upon whether or not a particle is inside the laminar sublayer. The equation for the case where the particle diameter is larger than the laminar sublayer is given by:

$$\frac{v_{f0}}{v_{s0}^*} = 4.9 \left(\frac{v_{s0}^* \rho_f d}{\mu} \right) \left(\frac{v_{s0}^* \rho_f D}{\mu} \right) \left(\frac{\rho_p - \rho_f}{\rho_f} \right)^{0.23} \quad (2.23)$$

where, v_{f0} is the terminal settling velocity, v_{s0}^* is the friction velocity at infinite dilution, ρ_f is the density of the fluid, ρ_p is density of the particles, μ is the dynamic viscosity, D is pipe inner diameter and d is particle diameter. For the case when particle diameter is smaller than the laminar sublayer, it becomes

$$\frac{v_{f0}}{v_{s0}^*} = 0.01 \left(\frac{v_{s0}^* \rho_f d}{\mu} \right) \quad (2.24)$$

Correlations also exist which address the problem of particle deposition from an air stream. The fraction of particles that are deposited under laminar flow conditions while being transported between parallel plates was given by Fuchs [1964]:

$$\varepsilon_i = \frac{v_s l}{uh_p} \quad (2.25)$$

where ε_i is the deposition efficiency for a given particle size, v_s is the terminal settling velocity of the particles, l is the distance from the source, u is the velocity of the fluid and h_p is the distance between the parallel plates. A similar relation for horizontal pipes was developed by Thomas [1958]:

$$\varepsilon_i = \frac{2}{\pi} \left(2C_2 \sqrt{1 - C_2^{2/3}} + \sin^{-1} C_2^{1/3} - C_2^{1/3} \sqrt{1 - C_2^{2/3}} \right) \quad (2.26)$$

where $C_2 = (3v_s l)/(4D_t u)$ and D_t is the diameter of the tube.

The deposition of particles is affected by the nature of the flow regime. In flow systems which contain considerable turbulent mixing, the rate of particle settling decreases. The concentration of particles at a distance from the source, N_A , in a horizontal rectangular duct with turbulent flow is given by Davies [1966]:

$$N_A = N_p \exp\left(-\frac{v_s l}{uh}\right) \quad (2.27)$$

where N_p is airborne concentration of particles at source.

2.2.4.1 Proppant Transport in Hydraulic Fracturing Process: Additional insight into particulate transport mechanisms during pneumatic fracturing is available from studies of proppant transport during hydraulic fracturing. One of the factors influencing the success of a hydraulic fracturing operation is the proper placement of proppant within the created fractures. Methods for predicting behavior of particles in liquid systems are similar to those used for gases, and substitution of the proper physical constants is normally all that is required to switch from one fluid to the other. Hence, a review of the existing literature on proppant transport in hydraulic fractures is relevant.

A number of laboratory investigations of proppant transport during hydraulic fracturing have been carried out [e.g., Kern *et al.*, 1958; Lowe and Huitt, 1965; Babcock *et al.*, 1967]. The following is a collective summary of the important observations from these studies:

1. Sand injected during the early part of the treatment tended to deposit close to the well bore, while that injected during the later part was deposited farther from the well bore.
2. Equilibrium velocity is relatively insensitive to fluid viscosity, particle size, particle injection rate and particle concentration. Density differences between particles and fluid were found to be an important parameter affecting the equilibrium velocity.
3. In vertical fractures, a gradient of proppant concentration exists, which is a continuous function of height. Four distinct zones can be identified. These include a stationary bank of packed particles, a saltation zone, a zone of well-dispersed particles and a zone of zero particle concentration.

4. For horizontal fractures there are three different types of particle transport mechanisms that occur within the fracture as function of the distance from the well bore. These are illustrated in Figure 2.5 and can be described as follows:

Region I: Particles are transported individually in suspension.

Region II: The particles aggregate and travel in bulk amounts. Particles roll and bounce along the surface of the fracture while being transported.

Region III: As the fluid velocity becomes too low or the concentration too high to keep the mutually interfering particles moving, particle deposition or dune formation begins.

2.2.4.2 Proppant Transport Using Nitrogen Gas: Proppant transport using nitrogen gas is occasionally used in the petroleum industry to avoid problems with water and oil emulsions, clay swelling, clay migration and water sensitive shales. Gottschling *et al.*, [1985] performed a series of lab experiments to investigate the ability of nitrogen gas to transport the proppant. They constructed a physical model to demonstrate, qualitatively, the involved transport mechanisms (see Figure 2.6).

The following is a summary of their experimental observations made over a wide range of gas and proppant flow rates:

1. Proppant is initially deposited in the well, the proppant level in the well rises until it reaches the lower perforations connecting the well bore to the fracture. Only now does the proppant start to enter the fracture.

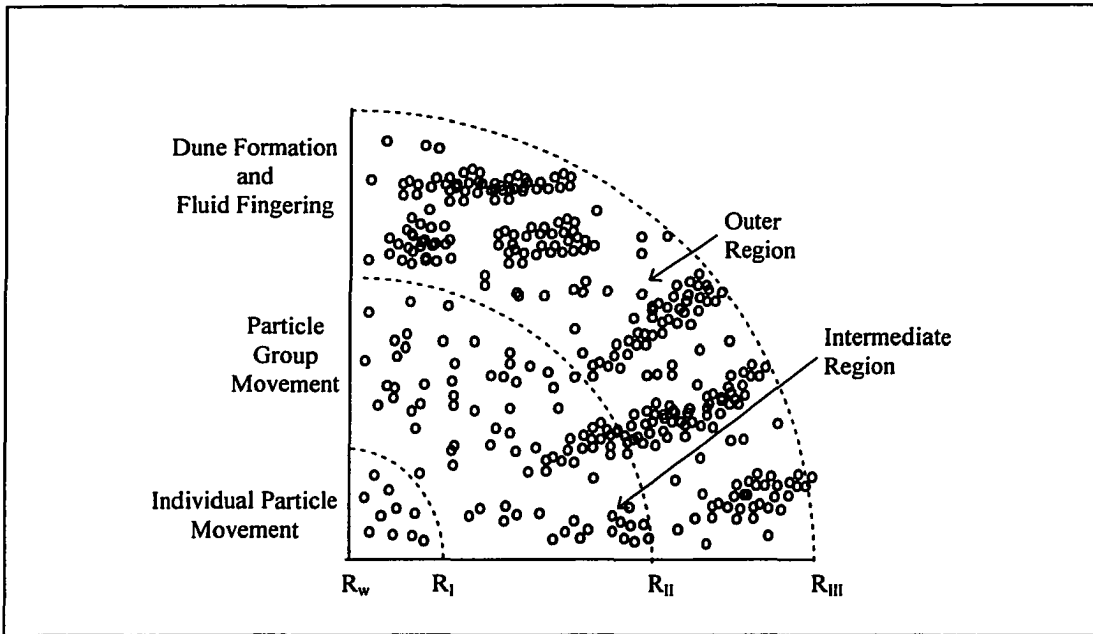


Figure 2.5 Different Regions of Proppant Transport in Hydraulic Fractures

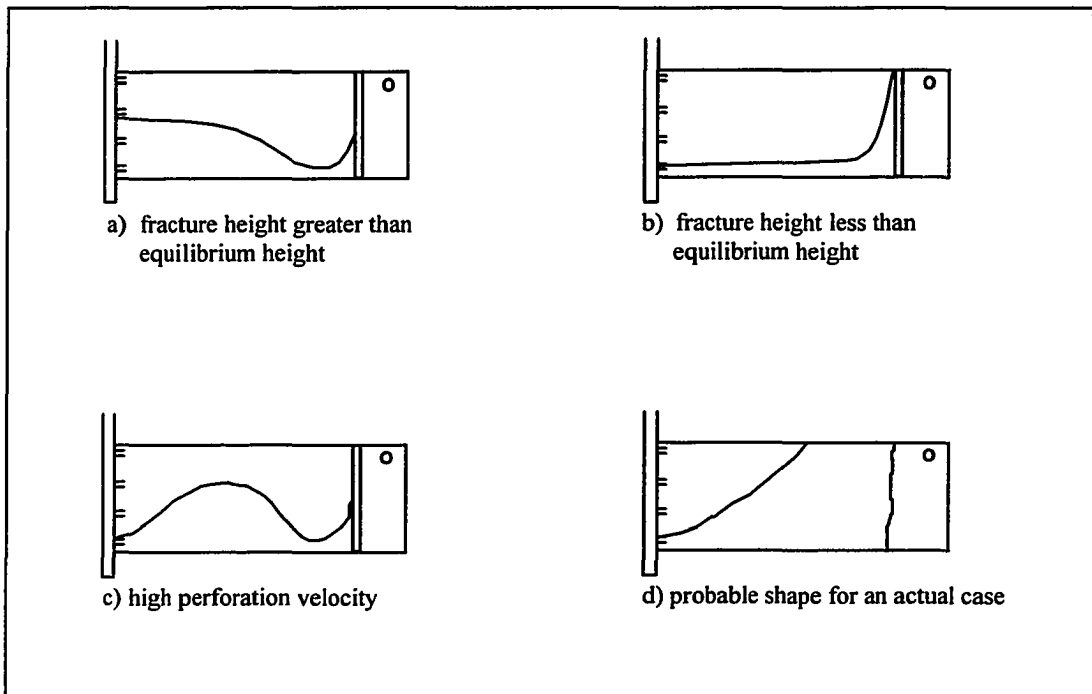


Figure 2.6 Proppant Banking for Different Treatment Conditions

2. When the fracture height was greater than the equilibrium bank height, proppant was deposited inside the fracture closer to the well bore until the bank height exceeded the equilibrium bank height (Figure 2.6b). When the equilibrium bank height is exceeded, the velocity of the gas passing over the proppant bank is high enough to carry the particles in suspension. Just beyond the proppant bank, the velocity of the gas decreases because of the greater flow cross-sectional area, and the proppant is deposited here.
3. When the fracture height was less than the equilibrium height of the proppant bank, the gas velocities were greater than the critical velocity required to carry the proppant in suspension. All the proppant was consequently transported to the fracture tip.
4. When the gas velocities were much greater than the critical velocity for carrying the proppant in suspension, all the proppant in the fracture was carried away from around the well bore. This resulted in a reduced fracture conductivity closer to the well bore.

CHAPTER 3

MODEL APPROACH

3.1 Introduction

This chapter describes the approach taken to model the propagation of pneumatically induced fractures. The motivation for development of the current model is the uniqueness of the pneumatic fracture propagation phenomena. Pneumatic fracture propagation differs from other fracture propagation phenomena in both the rate of pressurization and the propagation velocity. Another important distinction is the low viscosity of the fracturing fluid (air or other gas), which results in a high rate of leak-off into the surrounding geologic formation.

The chapter begins with a physical description of the mechanism of pneumatic fracture propagation based on field observations made over the last several years. Next, the assumptions with regard to the formation and fracture characteristics will be concisely stated. Finally, mathematical statements will be formulated describing the physical processes involved in the fracture propagation mechanism.

3.2 Mechanism of Pneumatic Fracture Propagation

For the past several years field observations of pneumatic fracture propagation have been well studied and documented [e.g. Schuring et al., 1992]. These studies have provided considerable insight into the mechanism of pneumatic fracturing, as well as the factors affecting initiation, orientation and extent of propagation. This section provides a summary of the current understanding of the pneumatic fracture propagation mechanism.

To initiate and propagate fractures in a geologic formation, there are two basic conditions that must be satisfied. First, gas must be injected into the formation at a rate that exceeds the natural permeability of the formation. Second, the injection pressure must exceed the minimum *in-situ* stresses present in the formation surrounding the injection point. When these two basic conditions are satisfied simultaneously, a pneumatic fracture will initiate and propagate from the point of injection.

The direction of the fracture propagation is controlled by the magnitude and direction of the *in situ* stresses present at the depth of fracturing. In overconsolidated formations where the least principal stress is vertical, fractures tend to propagate horizontally. Conversely, in normally consolidated soils where the least principal stress is horizontal, fractures will propagate in the vertical direction. Since a majority of soil formations encountered near the earth's surface are overconsolidated, the predominant direction of pneumatic fracture propagation has been horizontal. Some vertical fracture propagation has been observed when fracturing in poorly consolidated fill soils, or at very shallow fracturing depths (< 2.4 meters / 8 feet). In these cases, fractures were observed to curve upwardly and intersect or "daylight" the ground surface.

During a typical pneumatic injection event a two foot interval is sealed at the desired depth within an injection well, and this zone is then pressurized. Insight into the mechanism of pneumatic fracturing can be gained by examining the pressure variation in the sealed zone during injection. Pressure is recorded by an electronic pressure transducer connected to a data logging system. Figure 3.1 is typical of the numerous pressure data recorded during field applications of pneumatic fracturing. The pressure-time history reveals four distinct stages of the fracturing process:

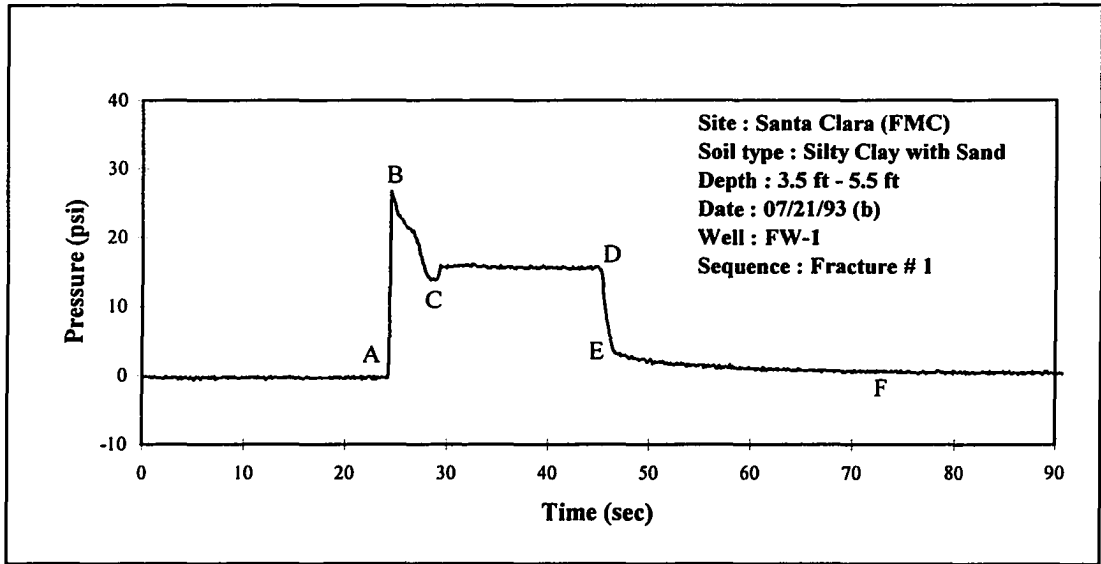


Figure 3.1 Pressure Variation During a Typical Pneumatic Injection

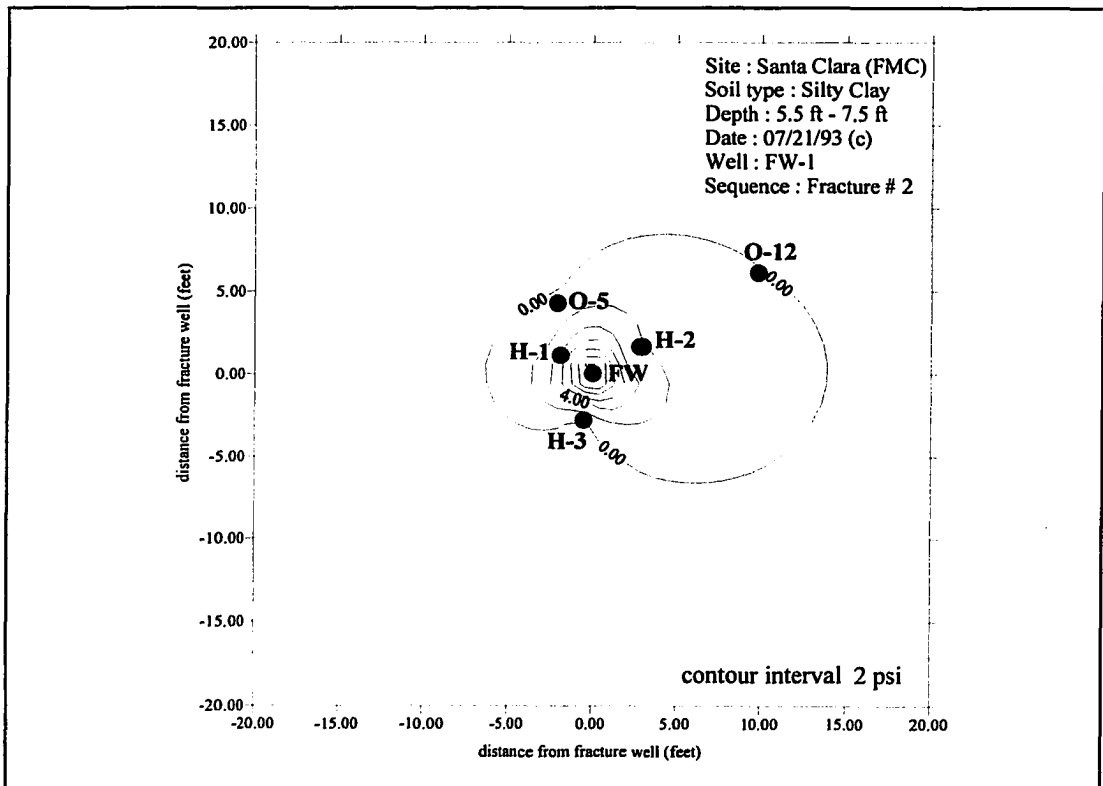


Figure 3.2 Pressure Contours During a Typical Pneumatic Injection

- pressure build-up leading to fracture initiation or formation breakdown (A-B);
- pressure drop during fracture extension (B-C);
- fracture maintenance pressure after propagation has ceased (C-D);
- pressure decline after termination of gas injection (D-F).

Each of these stages will now be briefly discussed.

The fracture event begins with a rapid build-up of pressure during the first two to three seconds of gas injection (segment AB in Figure 3.1). During this period the borehole expands elastically, until the breakdown pressure of the formation is reached (point B in Figure 3.1). At this point a fracture nucleates and begins to propagate away from the borehole. The magnitude of the breakdown pressure depends on both the overburden pressure (the minimum in situ stress in overconsolidated formations) and the natural cohesion of the formation [King, 1993]. As the fracture propagates away from the borehole, the effect of the natural cohesion (fracture toughness) becomes less significant and the fracture propagation pressure is dominated by the overburden [Spence & Turcotte, 1985].

Immediately following fracture initiation, gas rushes into the newly created fracture, resulting in a pressure drop at the borehole (segment BC). Gas now leaks off into the formation through the newly created fracture surfaces. After some time delay, points away from the borehole and at the tip of the propagating fracture will experience a pressure variation similar to that shown in Figure 3.1.

At some point in time fracture propagation will cease even though injection of gas is continued. This is due to the equilibrium that has been established between the amount of injected gas and the gas lost to the formation as leak-off. The formation is now

literally “floating” on a cushion of gas which will continue until the injection of gas is stopped. This stage corresponds to the pressure plateau (segment CD) in Figure 3.1 and is referred to as the “maintenance pressure” [King, 1993]. It is noted that it is the equilibrium fracture dimension which is the focus of the proposed model.

Once the gas injection is stopped, the pressure in the injection well decreases and the fractures begin to constrict. Closure is not complete, however, because of the self-propping nature of the fractures resulting from asperities and shifting of soil blocks along the fracture surfaces [Hall, 1995]. During this stage the pressure first decreases quickly (segment DE), and then more gradually (segment EF).

During some field operations of pneumatic fracturing the outlying monitoring wells are sealed and outfitted with pressure gauges. The pressure gauges record the maximum pressure in the monitoring well which occurs when the fracture has reached its equilibrium radius. Figure 3.2 is a contour diagram generated from the pressures recorded at the monitoring wells during an injection. The contour diagram provides an indication of the extent of fracture propagation, and also shows that pressure within the fracture decreases as one moves away from the injection well.

Additional insight into the pneumatic fracturing mechanism is provided by ground surface deformation. During injection, the ground surface heaves considerably, and at relatively shallow injection depths (< 3 meters / 10 feet) it may even be perceptible to the naked eye. Electronic tiltmeters are used to record the change in ground surface slope at various locations around the fracture well, and these recordings are used to generate contours of ground surface heave. Because the tiltmeters sample data several times a second for the entire duration of the injection, a time history of fracture

propagation can be generated. Figure 3.3 shows the temporal ground surface behavior during a typical pneumatic injection. A review of the heave contours at various times indicate that the fracture had reached its maximum extent somewhere between five to eight seconds after injection began, as there is no discernible difference between the contours at eight seconds and those at 14 seconds.

In order to determine the typical range of pneumatic fracture propagation velocities, heave contours from a number of sites were analyzed and the results are summarized in Table 3.1. As indicated the average propagation velocities range from 0.85 m/sec (2.8 ft/sec) to 3.5 m/sec (11.6 ft/sec). This velocity range, while faster than hydraulic fracturing, is clearly still in the low subsonic range. This has led to pneumatic fracturing being classified as a quasi-static rather than a dynamic phenomena.

Table 3.1 Pneumatic Fracture Propagation Velocities

Site Name	Geology	Average Maximum Radius meters (feet)	Time to Attain Maximum Radius (secs)	Average Propagation Velocity m/sec (ft/sec)
Flemington, NJ	Siltstone	7.5 (24.5)	5	1.5 (4.9)
Highland Park, NJ	Siltstone	6.4 (21.1)	5	1.3 (4.3)
Hillsborough, NJ	Siltstone	8.3 (27.2)	9	0.9 (3.0)
Huntsville, AL	Gravelly Clay	10.6 (34.8)	3	3.5 (11.6)
Marcus Hook, PA	Clayey Silt	3.6 (11.7)	4	0.9 (2.9)
Tinker, OK	Clayey Silt	5.0 (16.5)	6	0.9 (2.8)

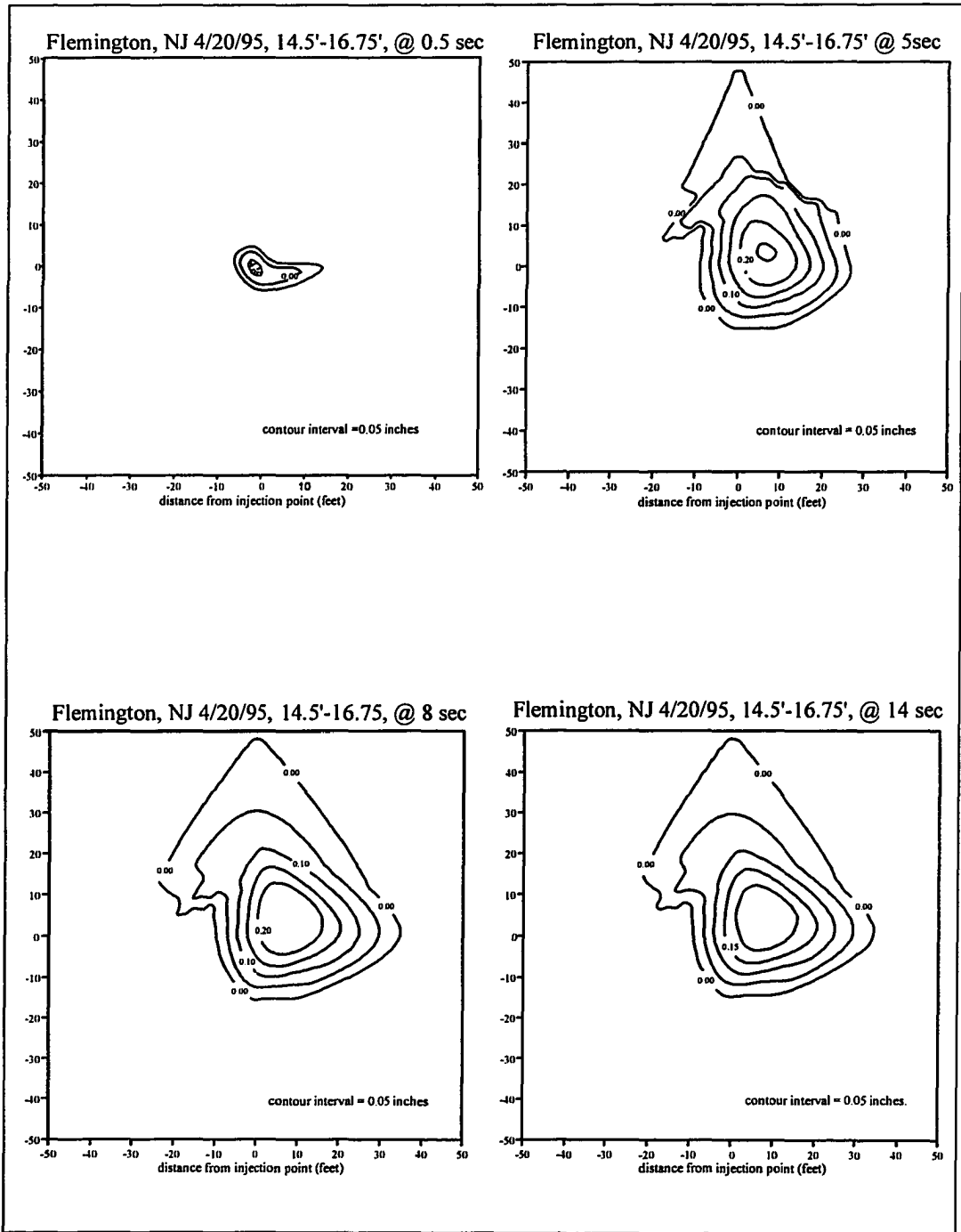


Figure 3.3 Temporal Variation of Ground Surface Heave Contours During Injection

3.3 Model Assumptions

The modeling of pneumatic fracture propagation is a complex task as it involves the coupling of phenomena from the fields of fluid mechanics, solid mechanics, rheology and heat transfer. In order to solve a problem of this complexity, it is necessary to establish a basic set of assumptions. The assumptions have been chosen to reflect as closely as possible the physical phenomenon of pneumatic fracturing, yet permit enough simplicity so that a solution is possible. The following section summarizes the assumptions for the proposed propagation model. The assumptions have been grouped into “General Assumptions” and “Presumed Fracture Characteristics.”

3.3.1 General Assumptions

1. *The geologic media is elastic, and will undergo brittle failure.*

Justification: Bedrock formations and stiff soil formations have been shown to exhibit brittle, elastic behavior [Wuerker, 1956]. Even formations which are less stiff such as weathered bedrock or plastic soils will tend towards brittle, elastic behavior due to the dynamic nature of the load imparted by pneumatic fracturing.

2. *The geologic formation is homogeneous with regard to elastic properties.*

Justification: Due to the relatively local extent of the fracture network (typically < 10 m radius), homogeneity will be assumed. This is a necessary simplifying assumption due to the complexity of the various interacting physical processes of the model.

3. *From a perspective of geostatic stress, the soil formations are considered to be anisotropic and overconsolidated.*

Justification: Numerous geologic investigations have shown that near surface deposits of soil are overconsolidated due to desiccation, overburden erosion and other natural phenomena. In overconsolidated deposits the minimum principal stress is in the vertical direction.

4. *In rock formations, an analogous state of stress is assumed to exist, i.e. the minimum in situ stress is in vertical direction and the maximum stress in the horizontal direction.*

Justification: Numerous geologic investigations have shown that geostatic horizontal stresses exceed vertical stresses in near surface rock formations (< 100 m depth) due to tectonic activity.

5. *The formation is stratified, which results in the presence of horizontal or nearly horizontal planes of weakness in the formation.*

Justification: Stratification is a common occurrence, as a majority of geologic formations at shallow depths are of sedimentary origin.

6. *The pneumatic conductivity of the formation is anisotropic, i.e. the horizontal pneumatic conductivity (K_h) is not the same as vertical pneumatic conductivity (K_v).*

Justification: Most geologic formations have greater conductivity in the horizontal direction due to their stratified origin [Harr, 1962]. In rock formations, this anisotropy may also be related to fractures caused by exfoliation or tectonic movements.

7. *Leak-off of gas from the fracture into the formation will occur as Darcian flow, and can be defined by a two-dimensional flow function.*

Justification: This approach will permit due consideration of the effects of conductivity anisotropies and successive fracture injections.

8. *The fracturing fluid behaves as an ideal gas.*

Justification: Since the pressures are relatively low and the temperature of the gas used in fracturing operations is well above its critical temperature, the fracturing fluid is considered to behave ideally.

9. *The thermodynamic state during pneumatic fracture propagation is considered to be adiabatic.*

Justification: The heat transfer is important when the temperature difference between the gas and the surrounding formation is high and the contact times are large [e.g., in explosive fracturing, Nilson,1981]. Pneumatic fracturing process is too rapid for any significant amount of heat transfer between the injected gas and the formation.

3.3.2 Presumed Fracture Characteristics

1. *The fracture propagates radially from the injection well, and is approximately horizontal and circular in shape.*

Justification: In their work on hydraulic fracturing, Hubbert and Willis [1957] established the relationship between direction of fracture propagation and principal stress orientation. The presumed condition of overconsolidation (see General Assumption 3 above) leads to horizontal fracture orientation. Though individual fractures maybe asymmetric due to geologic heterogeneities, field observations made at numerous sites suggests that the shape can best be described as approximately circular. Also the circular shape is a consequence of the homogeneity assumption.

- 2. *The fractures are created at shallow depths so the aperture is primarily a consequence of deflection of the overburden. Elastic compression of the surrounding formation is small and is ignored.***

Justification: This is consistent with analytical models and field observations by previous investigators in hydraulic fracturing [Perkins and Kern, 1961]. Data collected from numerous field demonstrations of pneumatic fracturing for this project show that significant surface heave is observed for shallow fractures (due to the deflection of the overburden) and little heave was observed for deeper injections.

- 3. *Early time phenomenon in the immediate vicinity of the borehole in conjunction with fracture initiation are ignored.***

Justification: The original state of geostatic stress is disturbed during the process of drilling a borehole. Studies have shown that this altered state of stress has little effect on the final orientation of the fractures [Murdoch, 1991]. Additionally, the high velocity of the injected gas (≥ 91.5 m/sec or 300 ft/sec) effectively “pre-notches” the geologic formation which de-emphasizes the importance of the fracture mechanism in the immediate vicinity of the borehole.

- 4. *Fracture propagation is dynamic but occurs at low subsonic speeds. Maximum radius is attained within several seconds and the process may be considered as “quasi-static.”***

Justification: Observations of ground surface heave during shallow fracturing operations indicate typical fracture tip velocities of 0.9-3.7 m/sec (3-12 ft/sec) which is well below fracture tip velocities in supersonic gas-driven (explosive) fracturing.

3.4 Mathematical Formulation of the Propagation Problem

Once a fracture has been initiated it will continue to propagate as long as the injected flow rate exceeds the rate of gas leak-off into the formation, and the pressure at the fracture tip is greater than the propagation pressure. At the instant when the fracture attains maximum radius, the following two conditions are simultaneously satisfied:

- fluid continuity
- stress equilibrium at the fracture tip

These two conditions will now be stated mathematically.

The condition for fluid continuity begins with the overall mass-balance of flow within the fracture which is given by:

$$Q_{in} = \frac{dV_{leak}}{dt} + \frac{dV_{frac}}{dt} + \frac{dV_{res}}{dt} \quad (3.1)$$

where Q_{in} is the injected flow, V_{leak} is the volume of fluid lost to the formation as leak-off, V_{res} is the residual fluid volume and V_{frac} is the volume of the fracture. If we ignore fracture volume, V_{frac} , which is negligible, and express the above equation in terms of flow, the following is obtained:

$$Q_{res} = Q_{in} - Q_{leak} \quad (3.2)$$

where Q_{res} is the residual flow left to propagate the fracture and Q_{leak} is the flow lost as leak-off. Fracture propagation continues until the injected flow exactly equals the leak-

off into the formation. The continuity criterion for the equilibrium fracture radius may therefore be stated as:

$$Q_{res} = 0 \quad (3.3)$$

The second simultaneous condition occurring at maximum radius is stress equilibrium at the fracture tip. During propagation the pressure at the tip, p_{tip} , exceeds the propagation pressure, p_{prop} . That is,

$$P_{tip} > P_{prop} \quad (3.4)$$

When the fracture reaches its equilibrium radius, the pressure at the tip must equal the propagation pressure. This is designated as the stress equilibrium criterion which may be expressed as:

$$P_{tip} = P_{prop} \quad (3.5)$$

Now that the two basic criteria for final fracture radius have been defined, the processes that control propagation will be examined. The discussion in Section 3.2 has established that pneumatic fracturing involves three distinct physical processes:

- pressure dissipation of injected gas as it flows through the fracture;
- leak-off of injected gas into the surrounding formation;

- deflection of the over-burden causing a discrete open fracture.

In the following sections the governing equations for each of these processes will be detailed. The final model solution presented in Chapter 4 will require that these equations be coupled and solved simultaneously to attain the required mass balance of the injected gas and stress equilibrium at the fracture tip

3.4.1 Pressure Distribution Model

The first physical process controlling the fracture propagation is pressure dissipation within the fracture. Pressure in the fracture decreases with increasing distance from the injection well on account of fluid friction, and this has in fact been observed in the field (Section 3.2; Figure 3.2). Previous investigators at NJIT [Nautiyal, 1994] have developed an analytical solution to account for the loss in the pressure head due to the frictional effects of the fracture wall. The model is based on Poiseuille flow between two infinite, smooth parallel plates. The flow equation is given by:

$$\frac{d\phi}{dx} = \frac{\mu_{\text{gas}}}{g\rho_{\text{gas}}} \frac{d}{dy} \left(\frac{du}{dy} \right) \quad (3.6)$$

where ϕ is the potential function and u is the velocity of the fluid in the radial direction. Taking gas compressibility effects into account and solving the above differential equation yields:

$$p_{n+1} = \sqrt{p_n^2 - \frac{12p_n Q \mu_{\text{gas}} \ln\left(\frac{r_{n+1}}{r_n}\right)}{\pi g \rho_{\text{gas}} b^3}} \quad (3.7)$$

where p_n and p_{n+1} are pressures at a distance r_n and r_{n+1} respectively, Q is the flow between r_n and r_{n+1} , b is the fracture aperture, μ_{gas} is the dynamic viscosity of the fluid, ρ_{gas} is the density of the injected gas, and g is the acceleration due to gravity.

3.4.2 Leak-off Model

The second of the three physical processes affecting fracture propagation is leak-off. Previous investigators in hydraulic and explosive fracturing modeled leak-off one-dimensionally and assumed a uniform leak-off distribution along the fracture length. These models also ignored formation anisotropy with respect to conductivity, as well as fluid losses from the fracture tip. The leak-off model proposed in this section is an improvement over previous approaches since it models leak-off two dimensionally and considers a variable distribution of leak-off (varying with distance from injection well). In addition, the effects of formation anisotropy and fluid losses occurring from the fracture tip will be taken into account.

As stated above, leak-off from the fracture varies as a function of radial distance, and it also differs between the top and the bottom fracture faces. The factors responsible for these variations are:

- pressure variation with radial distance;
- gradient variation due to differing flowpaths; and

- formation anisotropy with respect to conductivity.

As illustrated in Figure 3.4b, the pressure within the fracture decreases with increasing radius. Since, leak-off is directly proportional to the pressure within the fracture, this results in a general trend of decreasing leak-off with increasing distance from the well. The effects of pressure on leak-off are the same for both the upper and lower faces of the fracture.

The gradient driving the leak-off is also variable, as it depends on the length of the flow paths of exiting gas. The gradients along the top fracture face are higher since the flow path to atmospheric pressure boundary (ground surface) are shorter (see Figure 3.4c). The gradients along the bottom fracture face are correspondingly lower, and the lowest gradient occurs on the bottom face closer to the well.

Anisotropy also significantly influences the distribution of leak-off from a fracture (Figure 3.4d). Close to the injection well where flow lines are predominantly perpendicular to the fracture face, leak-off is most influenced by the vertical conductivity of the formation. As the fracture tip is approached, however, the effect of the horizontal conductivity becomes more and more dominant. It is important to note that the percentage of leak-off at the fracture tip increases with increasing anisotropy.

If the cumulative effects of pressure variation, gradient and anisotropy are superimposed, the final distribution of leak-off from a pneumatic fracture can be determined. The pattern of leak-off which results is shown conceptually in Figure 3.4e which differs notably from a one-dimensional, constant leak-off pattern. This difference has been the main impetus for improving leak-off analysis in the present model. An

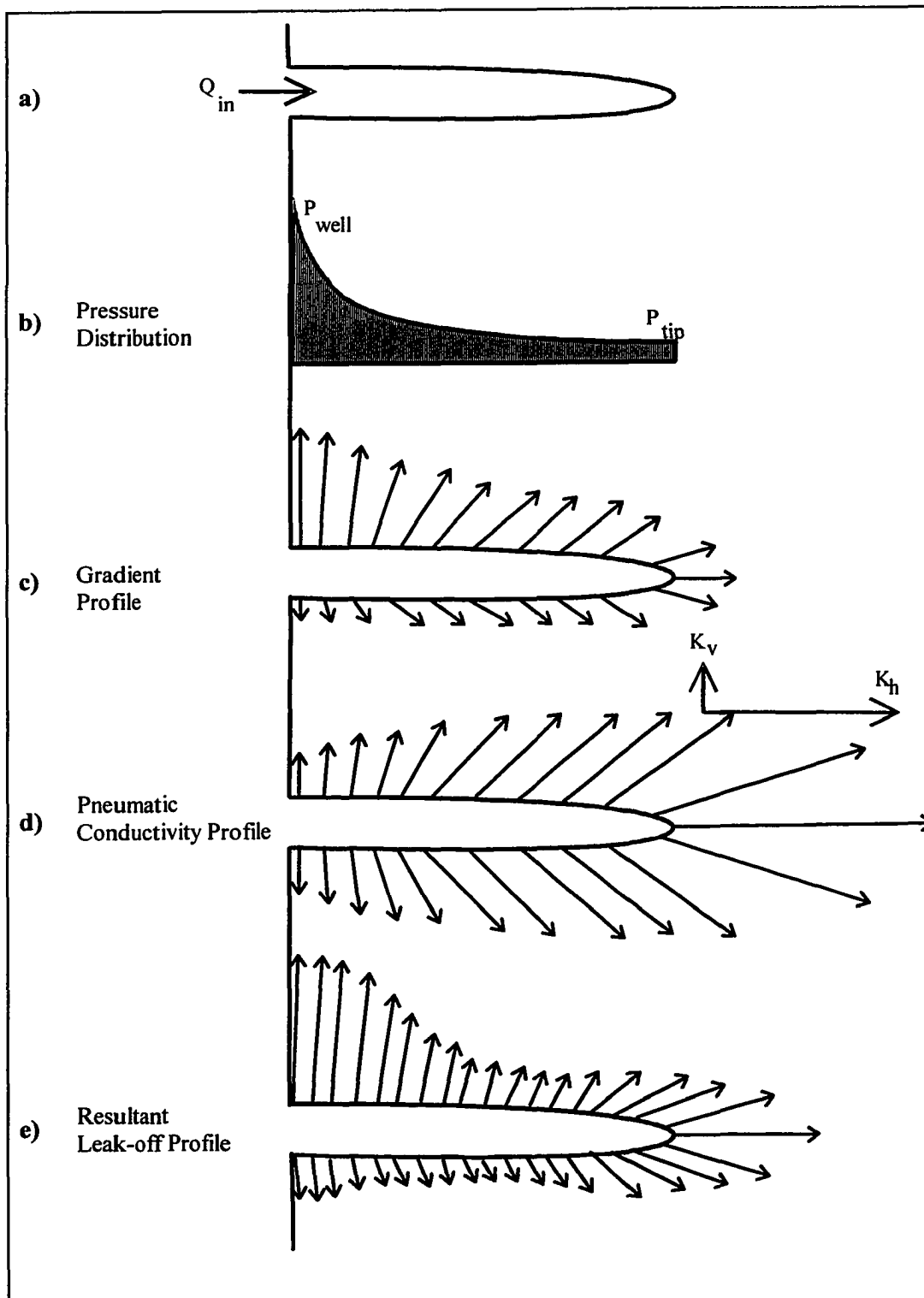


Figure 3.4 Effect of Pressure and Gradient Variation on Leak-off Distribution

axisymmetric version of the leak-off surrounding a pneumatic fracture is shown conceptually in Figure 3.5.

The best way to calculate leak-off is to construct a flownet with the appropriate boundary conditions. Figure 3.6 depicts the equipotential lines and streamlines for leak-off occurring from a fracture (two-dimensional) for isotropic conditions and for two cases of anisotropy. On comparing Figure 3.4e and Figure 3.6, the correlation between the pattern of leak-off distribution and the distribution of the streamlines is clearly evident. Therefore the model will utilize potential theory to account for the complex pattern of leak-off occurring from the fracture.

Three different approaches for estimating the leak-off for a three-dimensional radial fracture were developed. The first two are based on the flownet approach, and the last method was purely analytical. All approaches begin initially utilizing a two-dimensional expression. Which is then extended to the three-dimensions by rotation about an axis passing through the center of the injection well. Since flownets were traditionally hand drawn in the past, the two flownet methods of leak-off estimation will be referred to in the remainder of the study as the “graphical methods.”

In the first flownet method, Darcy’s law for a two-dimensional flownet is modified to account for the variation of leak-off with fracture radius. The Darcy’s equation being given by:

$$Q_{\text{leak}} = K_{\text{gas}} H \left(\frac{N_f}{N_d} \right) \quad (3.8)$$

where Q_{leak} is total discharge across the entire fracture surface, H is the total head driving

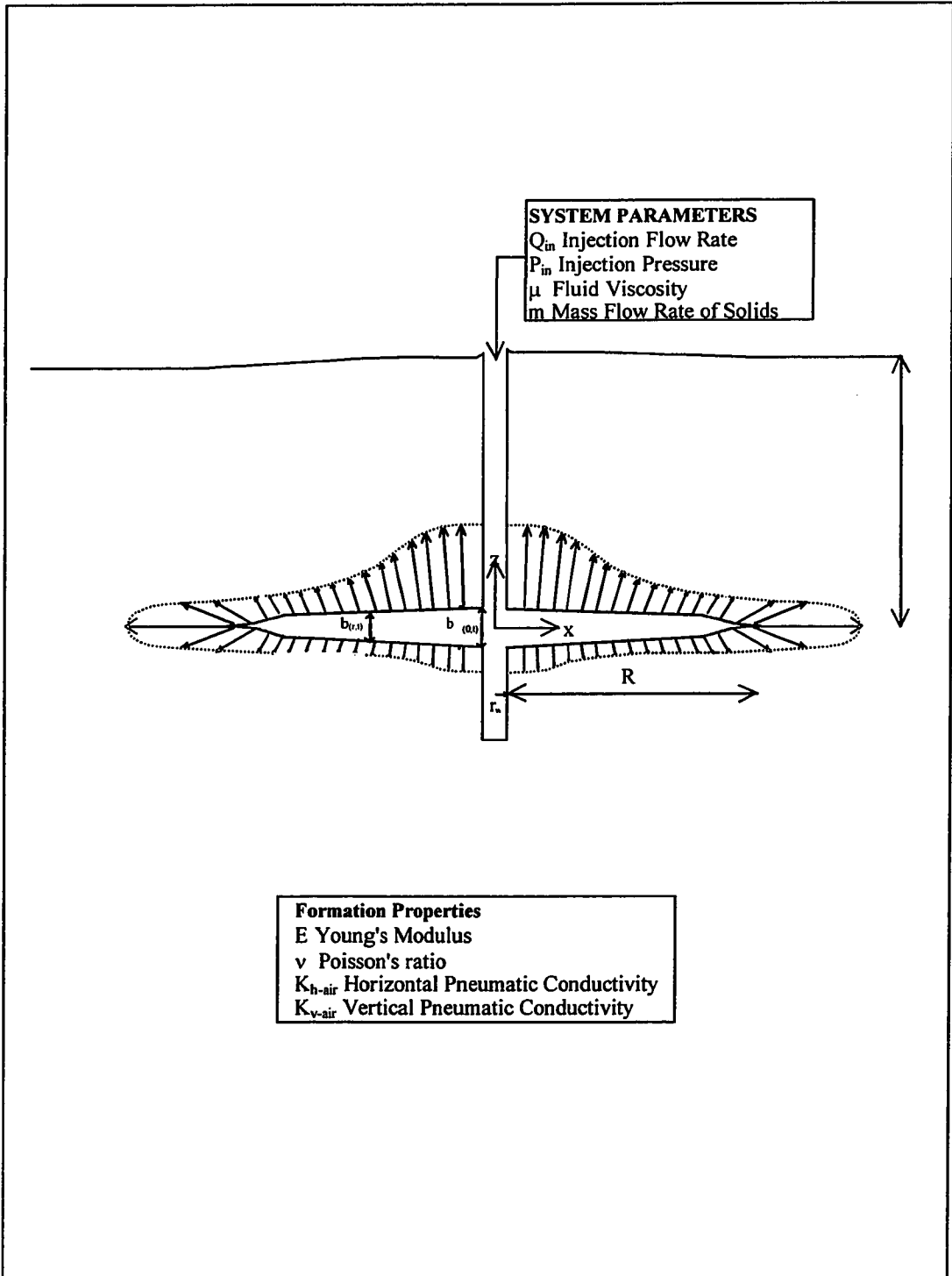


Figure 3.5 Cross-Section of a Radially Propagating Horizontal Fracture

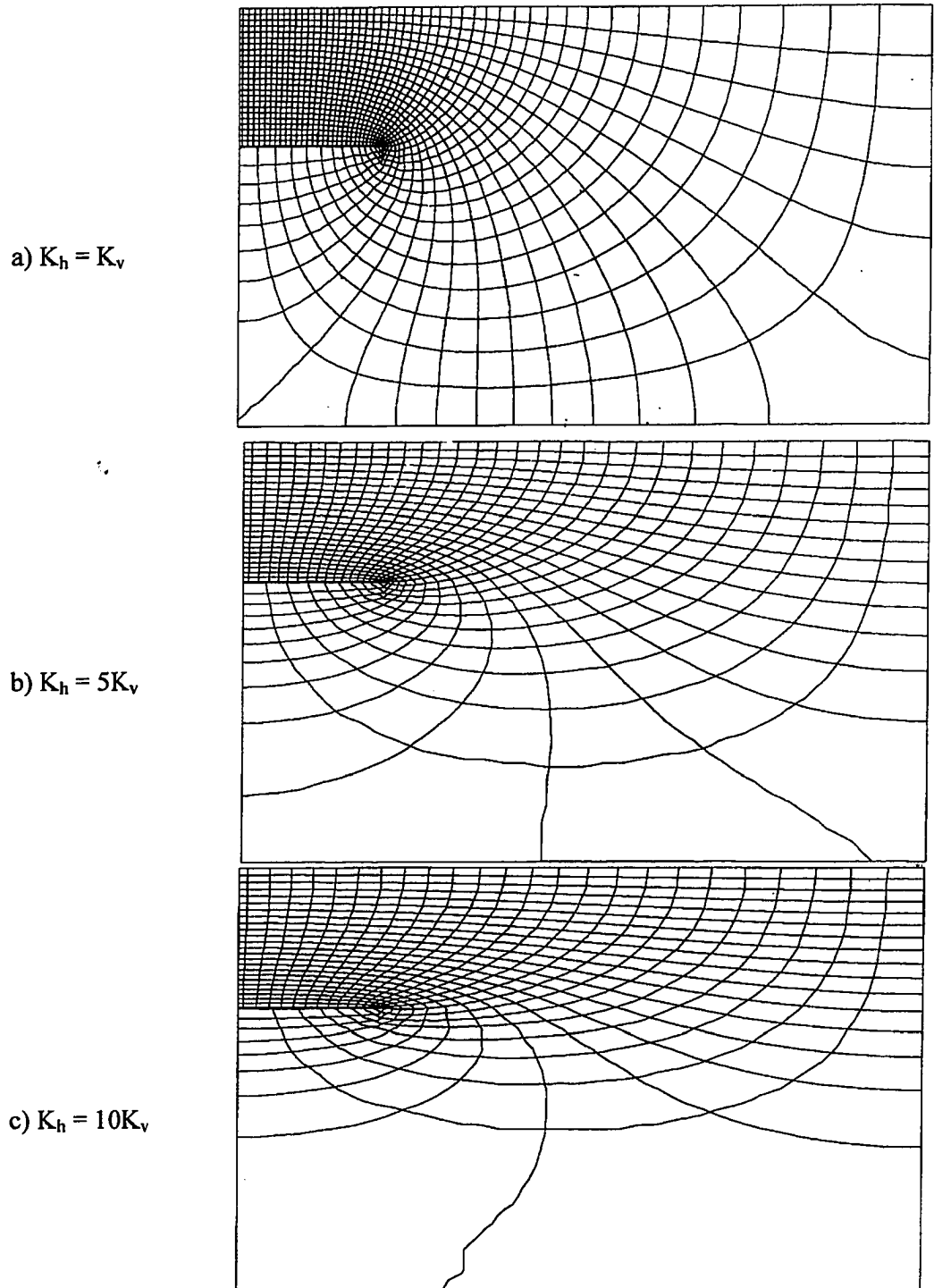


Figure 3.6 Effect of Formation Anisotropy on Flow Pattern

the flow, K_{gas} is the effective pneumatic conductivity of the formation, N_f is the number of flow tubes, and N_d is the number of potential drops.

To calculate the variation in the leak-off with radial distance, the extent of fracture length must be discretized into 'n' segments. The number of flow tubes leaving each segment are counted, and the leak-off occurring through each segment is computed as follows:

$$Q_{\text{leak}} = \sum_{r_0=r_w}^{r_n=R} K_{\text{gas}} H_n \left(\frac{N_f}{N_d} \right)_n \quad (3.9)$$

where H_n is the total head driving the flow in the n^{th} segment.

Extending the discretized two-dimensional fracture into three dimensions requires that the radial fracture be segmented into concentric annular rings. The total leak-off is a summation of gas lost through each of the annular rings. The formula for total leak-off then becomes:

$$Q_{\text{leak}} = \sum_{r_0=r_w}^{r_n=R} K_{\text{gas}} H_n \left(\frac{N_f}{N_d} \right)_n \pi (r_{n-1} + r_n) \quad (3.10)$$

where r_n and r_{n+1} are the inner and outer radial distances of the annular ring.

It is apparent in the previous equation which will henceforth be referred to as "flownet method-I," the variation in leak-off is directly dependent on the variation in shape factor. Figure 3.7 illustrates the effects of formation anisotropy and the fracture

size on the shape factors. As indicated, the higher values of the shape factor at the fracture tip are due to the increased number of flow tubes present at the tip of the fracture. An inspection of the figure suggests that anisotropy is more important early in the fracture propagation, at lower injection flow rates, and for deeper fractures. A more comprehensive compilation of variation in shape factors corresponding to different fracturing depths and fracture radii for isotropic and anisotropic formations are contained in Appendix G.

A second method using flownets for estimating leak-off from a three dimensional fracture was also investigated, which will be referred to as the “flownet method - II.” The main difference with respect to the previous method of leak-off estimation lies in the approach taken in deriving the formulae. In flownet method - II the leak-off is initially calculated over a plan area which is a square encompassing the fracture extent and then it is corrected for the differences in the plan surface areas. The equation for determining leak-off by this second method, which is also based on flownet theory, is given by:

$$Q_{\text{leak}} = \sum_{n=1}^{n=R/\delta r} \frac{\pi}{2} RK_{\text{gas}} H_n \left(\frac{N_f}{N_d} \right)_n \quad (3.11)$$

where R is the equilibrium fracture radius, and δr is the width of the annular ring. The complete derivation of the equation has been presented in Appendix C.

The last method of leak-off estimation uses a purely analytical approach. The analytical method involves calculating leak-off from successive annular rings of the fracture surface, using the following flow function:

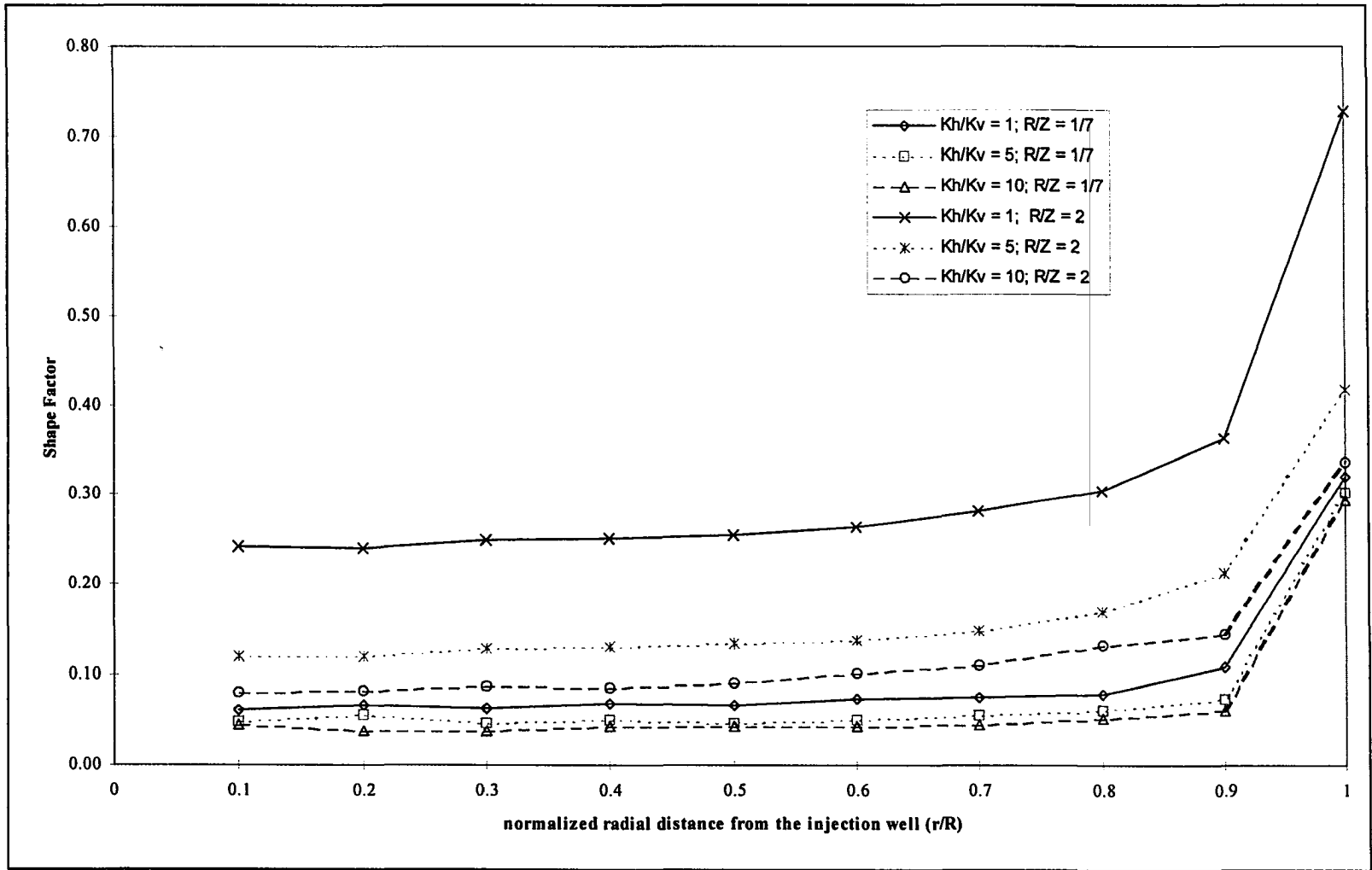


Figure 3.7 Effect of Formation Anisotropy and Change in Fracture Extent on Shape Factor

$$Q_{\text{leak}} = \sum_{r_0=r_w}^{r_n=R} \sqrt{(K_{h\text{-gas}} K_{v\text{-gas}})} \left(\frac{P_d}{l_{\text{grad}}}_n \right) \pi (r_n^2 - r_{n-1}^2) \quad (3.12)$$

where $K_{h\text{-gas}}$ and $K_{v\text{-gas}}$ are the horizontal and vertical pneumatic conductivities of the formation, respectively and l_{grad} is length of the flow path along which the pressure is dissipated. The length of the flow path is of course dependent on the depth of the fracture.

3.4.3 Deflection Model

The last of the three processes controlling fracture propagation to be modeled is deflection of the overburden. When a pneumatic fracture is created, the resulting fracture aperture is assumed to be a consequence of the overburden deflection. Therefore a model for overburden deflection effectively predicts the fracture form.

The form of the deflecting overburden is a function of the pressure distribution within the fracture. Most previous investigators have used simplified uniform or linear pressure distributions (Chapter 2). The present model attempts to use a non-linear distribution which is clearly more realistic for a tapering fracture.

The overburden can be modeled as the bending of a circular elastic plate clamped at the edges. This is consistent with numerous field observations of ground surface heave contours which were approximately circular, in shape. The overburden deflection for this case can be obtained by solving the following differential equation [Timoshenko and Woinowsky-Krieger, 1959].

$$\frac{d^3b}{dr^3} + \frac{1}{r} \frac{d^2b}{dr^2} - \frac{1}{r^2} \frac{db}{dr} = \frac{S}{D} \quad (3.13)$$

where r is the radial distance from the center of the plate, b is the deflection of the plate (fracture aperture), S is the magnitude of the shear force, and D is the flexural rigidity.

If it is assumed that the over-pressure at the tip of the fracture is zero, the following approximate pressure distribution can be used which closely approximates the “cubic law” distribution of pressure believed to exist in pneumatic fractures:

$$P = P_w - k \ln\left(\frac{r}{r_w}\right) \quad (3.14)$$

$$\text{where } k = \frac{P_w}{\ln\left(\frac{R}{r_w}\right)}$$

such that $P = P_w$ when $r = r_w$

and $P = 0$ when $r = R$

The magnitude of the shearing force S can then be determined by the following equation:

$$S = \frac{P_w r}{2} - \frac{k}{2} r \ln\left(\frac{r}{r_w}\right) + \frac{k}{4r} (r^2 - r_w^2) \quad (3.15)$$

Substituting S in equation 3.13, the following relation between pressure and aperture can be obtained:

$$\frac{d}{dr} \left[\frac{1}{r} \frac{d}{dr} \left(r \frac{db}{dr} \right) \right] = \frac{P_w r}{2D} - \frac{k}{2D} r \ln \left(\frac{r}{r_w} \right) + \frac{k}{4D} \frac{(r^2 - r_w^2)}{r} \quad (3.16)$$

The complete solution to the above equation has been presented in Appendix A.

The resulting solution is given by:

$$\begin{aligned} b = & \frac{r^4}{128D} \left[2p_d + 3k - 2k \ln \left(\frac{r}{r_w} \right) \right] \\ & + \frac{r^2}{256D} \left[R^2 (8kp_d - 8p_d - 10k) + r_w^2 \left(8k + 16p_d - 16k \ln \left(\frac{r}{r_w} \right) \right) \right] \\ & + \frac{kR^4}{64D} - \frac{kr_w^2}{32D} R^2 \end{aligned} \quad (3.17)$$

$$\text{where, } k = \frac{P_d}{\ln \left(\frac{R}{r_w} \right)}, \quad D = \frac{Ez^3}{12(1-\nu^2)}$$

b is the fracture aperture at a distance r from the well, R is the radial extent of the fracture, r_w is radius of the well, p_d is the driving pressure at the injection well, E being the Young's Modulus of the formation, ν is Poisson's ratio and z is the depth of fracturing.

It is noted that the above deflection equation (equation 3.17) is a fourth degree polynomial which matches with a previous study [Canino, 1997] that the ground surface above a pneumatic fracture conforms to a fourth degree polynomial.

3.4.4 Coupling Interaction of Propagation Processes

The final radius of a pneumatic fracture will depend on the coupling of the three processes just discussed and on their mutual interaction. For example, any change in the pressure distribution will affect leak-off since, by Darcy's law, leak-off is proportional to pressure within the fracture. This new leak-off distribution will necessitate a change in the extent of fracture surface area and radius. Based on the deflection model, a revised radius will correspond to a new fracture aperture. A change in the fracture aperture will in turn directly affect the pressure distribution. Thus, we have come a full circle, implying that a change in any one of these individual processes will affect the rest of the processes, as well as the process itself.

In summary then, the physical processes governing the propagation of a pneumatic fracture expressed as a function of the formation and system parameters are:

$$p_r = f(Q_{res}, \mu_{gas}, \rho_{gas}, r, b, p_w) \quad (3.18)$$

$$Q_{leak} = f(R, p_r, K_{h-gas}, K_{v-gas}, z, N_f/N_d, t) \quad (3.19)$$

$$b = f(R, E, \nu, p_r, z, t) \quad (3.20)$$

The coupling of the above equations is apparent since each of the dependent variables on the left hand side of the equations appear within the list of independent variable parameters on the right hand side of the other equations. This level of coupling is severe, and will play a major role in the solution of the model.

CHAPTER 4

MODEL DEVELOPMENT

4.1 Introduction

This chapter develops an algorithm for modeling propagation of pneumatically induced fractures. The principal function of the algorithm is to couple the solutions presented in the previous chapter for pressure dissipation, leak-off and overburden deflection, and then solve them to obtain the dimensions of the fracture. The algorithm may be classified as a numerical solution since it performs tasks such as discretization, iteration and convergence. For the purposes of the current study the algorithm has been implemented in “Mathcad 7.0” to permit testing and calibration. It can be easily coded in any other computer language.

The algorithm has some unique features compared with past fracture propagation models that are noteworthy. First, gas leak-off from the fracture into the formation is modeled using two-dimensional Darcian flow. This approach provides a higher degree of accuracy which is crucial in view of the low viscosity of air and consequent high potential for leak-off. A second unique feature of the algorithm is it considers formation anisotropy with regard to conductivity. This permits a more realistic representation of actual field conditions since most geologic formations tend to exhibit some amount of anisotropy. Finally, the algorithm is capable of utilizing a number of overburden deflection models. These include models for a linearly tapering fracture, fracture with an anticlinal plan subjected to uniform pressure, fractures with circular plan subjected to a

uniform pressure, and fractures with a circular plan subjected to a logarithmically varying pressure.

During the course of the study attempts were made to obtain a closed form solution incorporating the models of pressure dissipation, leak-off, and overburden deflection, while satisfying the residual flow and stress criteria. These attempts were not successful because of the severe coupling interaction among these processes. However, a limited analytical solution based solely on the principle of fluid continuity was successfully developed, and will be presented. The continuity solution is useful for obtaining rough estimates of the fracture radius as well as for checking the full algorithm.

In the sections to follow, the conceptual framework of the algorithm will be presented first (Section 4.2). This is followed by a detailed step by step discussion of the routines and subroutines that make up the algorithm (Section 4.3). Finally, the closed form solution for fracture propagation based on the continuity principle will be given (Section 4.4).

4.2 Conceptual Model Algorithm

The algorithm is based on the presumption that for a given set of injection and formation parameters, there exists a unique fracture radius that satisfies the continuity and pressure conditions at the tip of the fracture simultaneously. A conceptual flow chart of the algorithm depicting its execution control and the component models is shown in Figure 4.1. After the formation and injection parameters are entered, the algorithm starts with an assumed “equilibrium fracture radius.” The algorithm has been structured to divide the assumed radius into small segments as shown in Figure 4.2. The size of the segments can

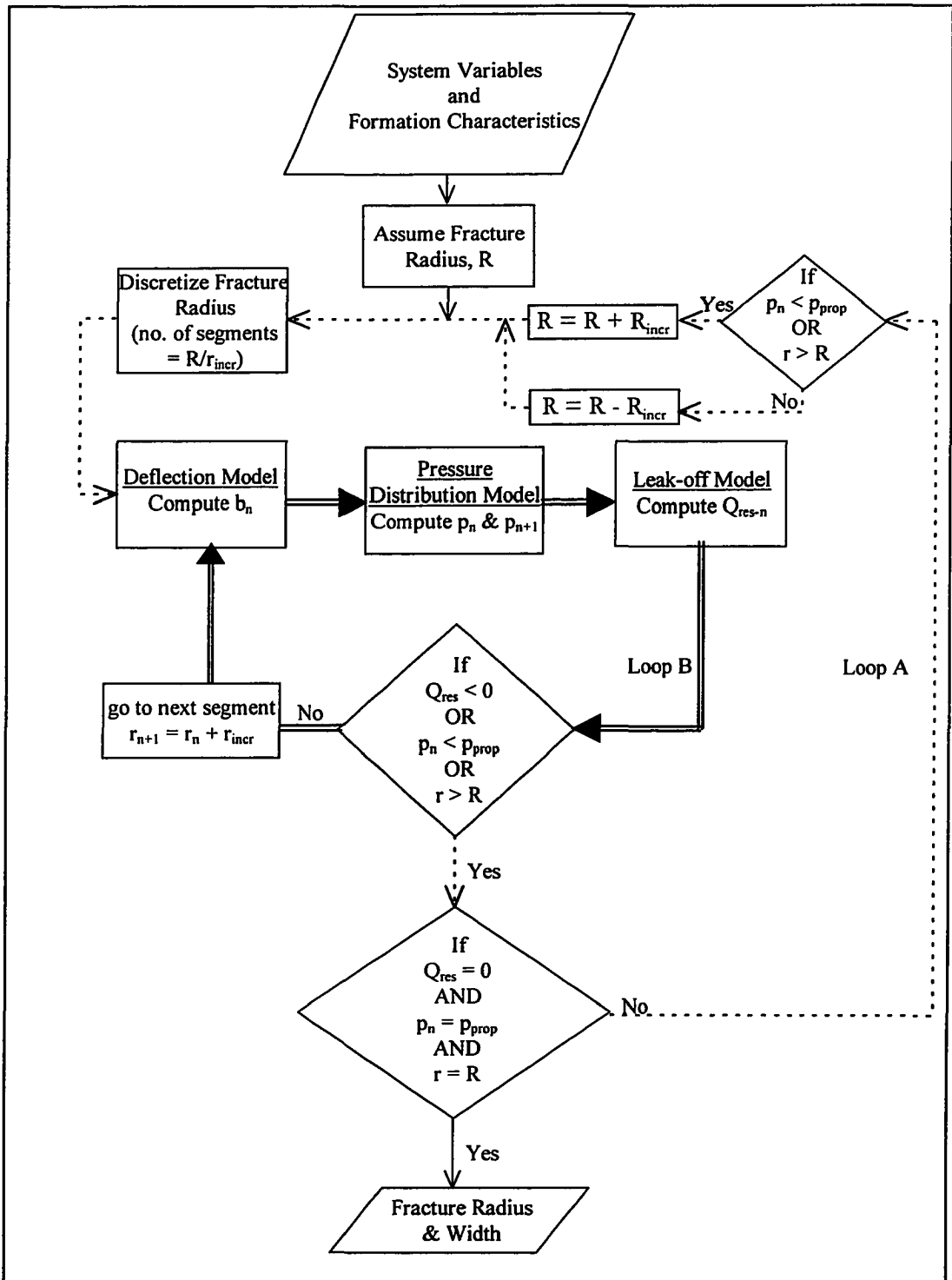


Figure 4.1 Conceptual Flow Chart of the Propagation Model

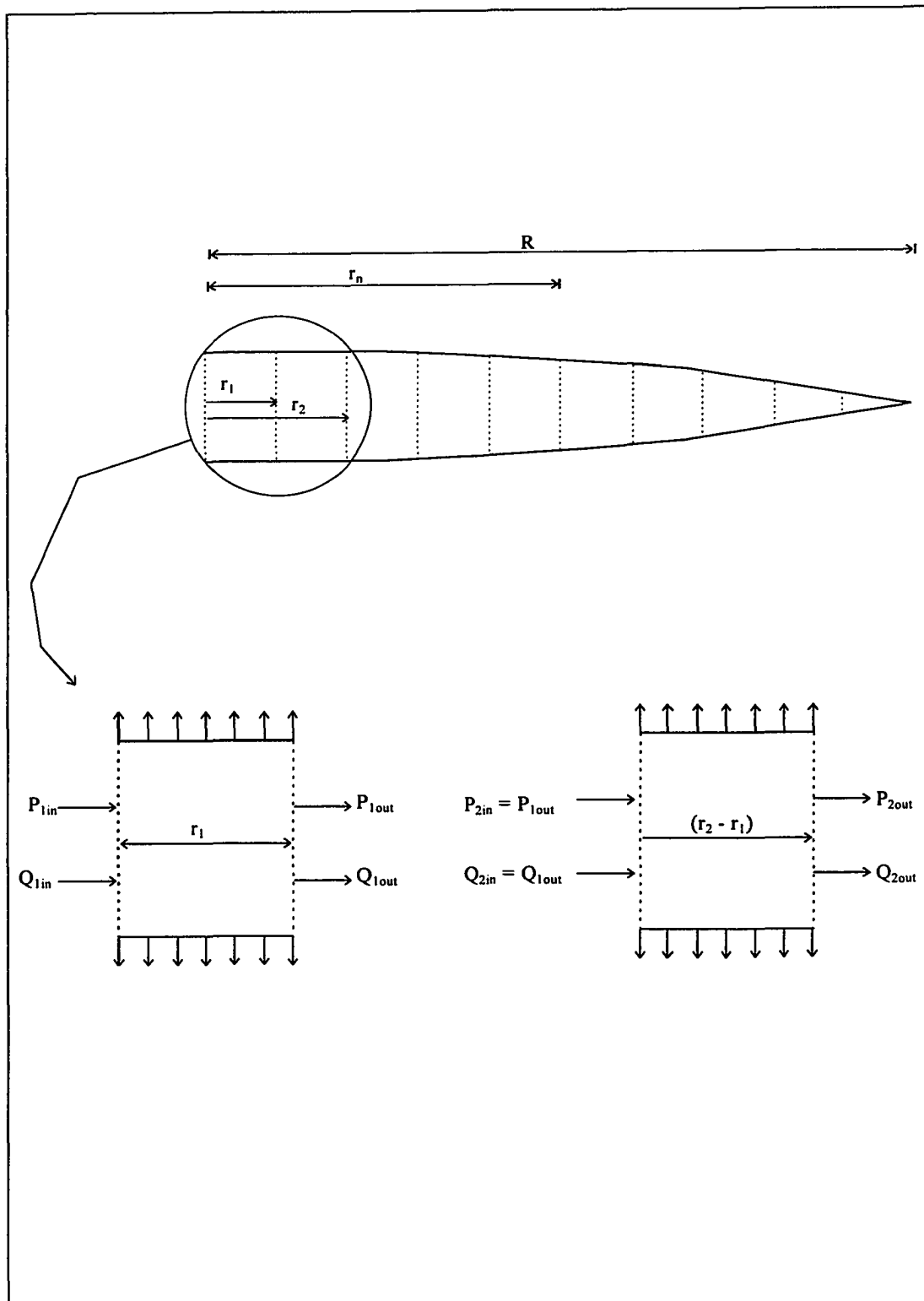


Figure 4.2 Pressure and Flow Determination in a segmented fracture

be chosen to be arbitrarily small. The accuracy of the algorithm improves with decreasing size of the segments, but this obviously lengthens execution time of the algorithm.

For each of the segments, starting from the injection well, the deflection model computes the magnitude of the fracture aperture. The pressure distribution model, which is a function of the fracture aperture, computes pressure drop within the segment due to frictional effects. Next the leak-off model calculates the magnitude of fluid lost to the formation, which is a function of the back-pressure within the fracture. Finally the residual flow is calculated by conducting a mass balance of the fluid entering and exiting the segment. The pressure and flow at the end of the current segment are used as the input values for the next segment.

The process (inner loop B, Fig 4.1) is repeated until one of the criteria (equation 3.3 or 3.5) for termination of a propagating fracture is met. If both the propagation criteria are satisfied simultaneously in the same segment at the fracture tip, the assumed fracture radius is the true “equilibrium fracture radius.” When both the criteria are not satisfied the fracture radius in the outer loop A is either increased or decreased to converge on the “equilibrium fracture radius.”

4.2.1 Convergence Methodology

Three different methods, the incrementing method, decrementing method, and the Bisection Method were investigated to determine the most efficient method of converging to the solution, i.e., “the equilibrium fracture radius.” Computation times for each of the

methods to arrive at the “equilibrium radius” were compared, and the method with minimum execution time was selected for the algorithm.

The incrementing method starts with an obviously undersized fracture radius. In this case the fracture surface area is too small to account for the loss of all the injected air. Thus, the fracture radius is incremented until the pressure and the continuity conditions for the termination of a propagating fracture are satisfied simultaneously at the fracture tip. The behavior of this convergence methodology is illustrated in Figure 4.3a. As indicated, the iterative process (inner loop B, Figure 4.1) initially terminates when the over-pressure in the fracture drops below the propagation pressure as the segmental fracture radius, “ r_n ” increases. The continuity criterion is not satisfied, however, since the residual flow is not zero. Therefore, the current fracture radius is not the “equilibrium fracture radius.” At this stage the algorithm increments the radius of the fracture and the process (loop A, Fig 4.1) is iterated until both the pressure and flow criteria are satisfied simultaneously in the same segment. A plot of the residual flow at the termination of the iterative process for increasing fracture radius is depicted in Figure 4.3b. The point of intersection of the curve with the x-axis represents the equilibrium fracture radius.

In the decrementing method, the algorithm begins with an obviously overestimated fracture radius. As seen in Figure 4.4a, an overestimated fracture fails the criteria because residual flow reaches zero before the pressure criterion is satisfied. The dimensions of the fracture are successively reduced until the fracture dimensions that satisfy the conditions for a fracture in equilibrium are reached. A plot of the over-pressure for this convergence method is shown in Figure 4.4b. The point of intersection of the curve with the x-axis representing the equilibrium fracture radius.

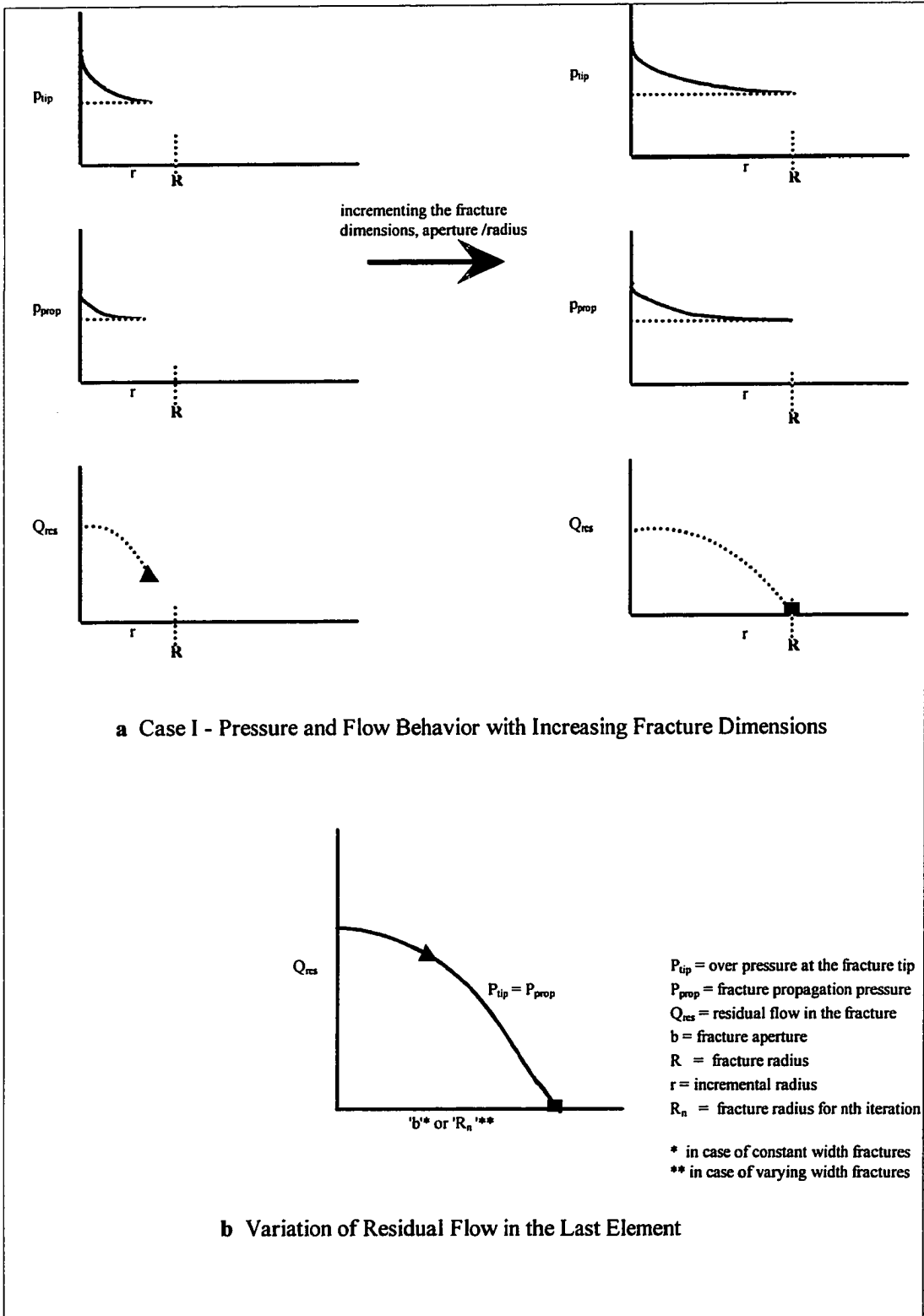


Figure 4.3 Case I - Pressure and Flow Behavior in an Underestimated Fracture

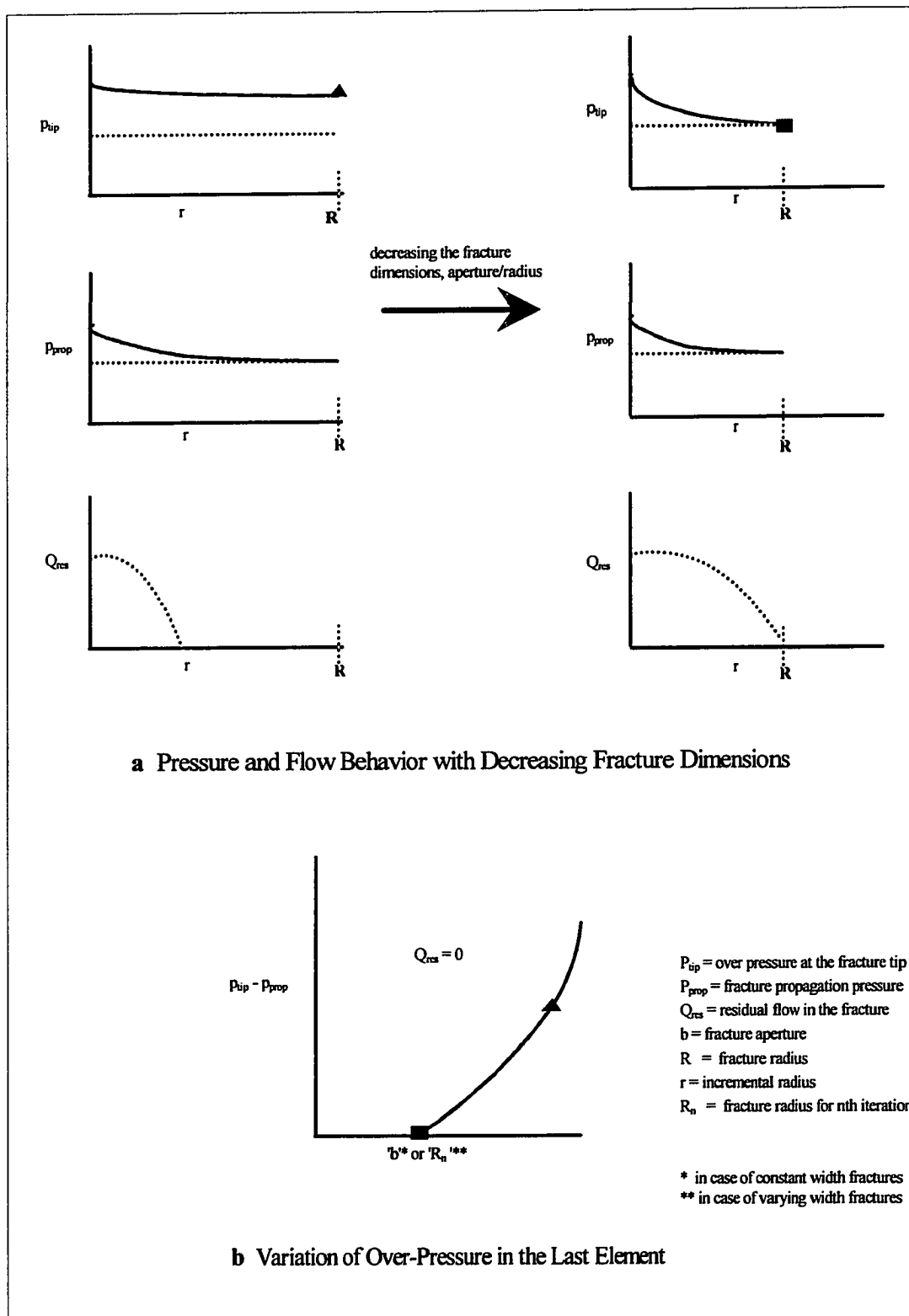


Figure 4.4 Case II - Pressure and Flow Behavior in an Overestimated Fracture

Since it is clear from the plots in Figures 4.3b and 4.4b that the solution has only one root, a root finding convergence method known as the Bisection Method was investigated. The Bisection Method is based on the fact that a curve will change sign in the neighborhood of its root. The method requires an initial estimate of the interval bracketing the root. The interval bounding the root is divided into half and the location of the root within these two intervals is determined. The interval bracketing the root is retained and the other half discarded. The process is repeated to obtain refined values of the root. Further details of the Bisection Method are discussed in Section 4.3.2.

Converging towards the solution by fixed increments/decrements is tedious, and the process becomes more labored as the accuracy requirements increase. For example, it typically took about 4 minutes of the CPU time (100 MHz, Pentium processor) for the algorithm to converge to the solution to obtain a radius accuracy of 0.1 feet. Using the bisection method, CPU time was reduced to about 30 seconds for the same accuracy level. Eventually it was decided to implement the “bisection method” [Chapra and Canale, 1988] of convergence.

4.3 Details of Algorithm Structure

This section details the algorithm introduced in the previous section. Basically, the algorithm has two nested loops as shown in the conceptual flow chart in Figure 4.1. Loop A, which is the outer loop, invokes the convergence subroutine (incrementing radius method vs. decrementing radius method vs. Bisection Method, discussed in Section 4.2.1). While the convergence subroutine is being implemented, the subroutine for

determining the flow and pressure variations within the fracture is “invoked dynamically.”

The detailed flow charts for the algorithm routines and subroutines are presented in Figures 4.5 through 4.7. The “Mathcad” version of the full algorithm is given in Appendix E. Each of the algorithm steps will now be described in more detail.

4.3.1 Main Routine

The Main Routine shown in Figure 4.5 handles the input and output of the algorithm, selects the deflection model to use, selects the method of leak-off estimation and invokes the convergence subroutine.

Step 1 – Input. The parameters required by the algorithm as input are those related to the geology at the site and the injection system parameters for a given injection event. The formation characteristics that impact the extent of fracture propagation are site specific. The parameter values to be inputted with respect to the formation characteristics and the injection event can be gathered from the data collected during the preliminary site characterization studies.

The following parameters are required by the algorithm: depth of fracturing, z , injection flow rate, Q_{in} , pneumatic conductivity of the formation, K_{h-gas} , and K_{v-gas} , formation modulus, E , Poisson’s ratio, ν and formation density, γ .

Step 2 - Selecting Fracture Geometry. The selected deflection model has a significant effect on the predicted extent of fracture propagation. Fracture geometry is a function of the pressure distribution, plan shape of the fracture and assumed

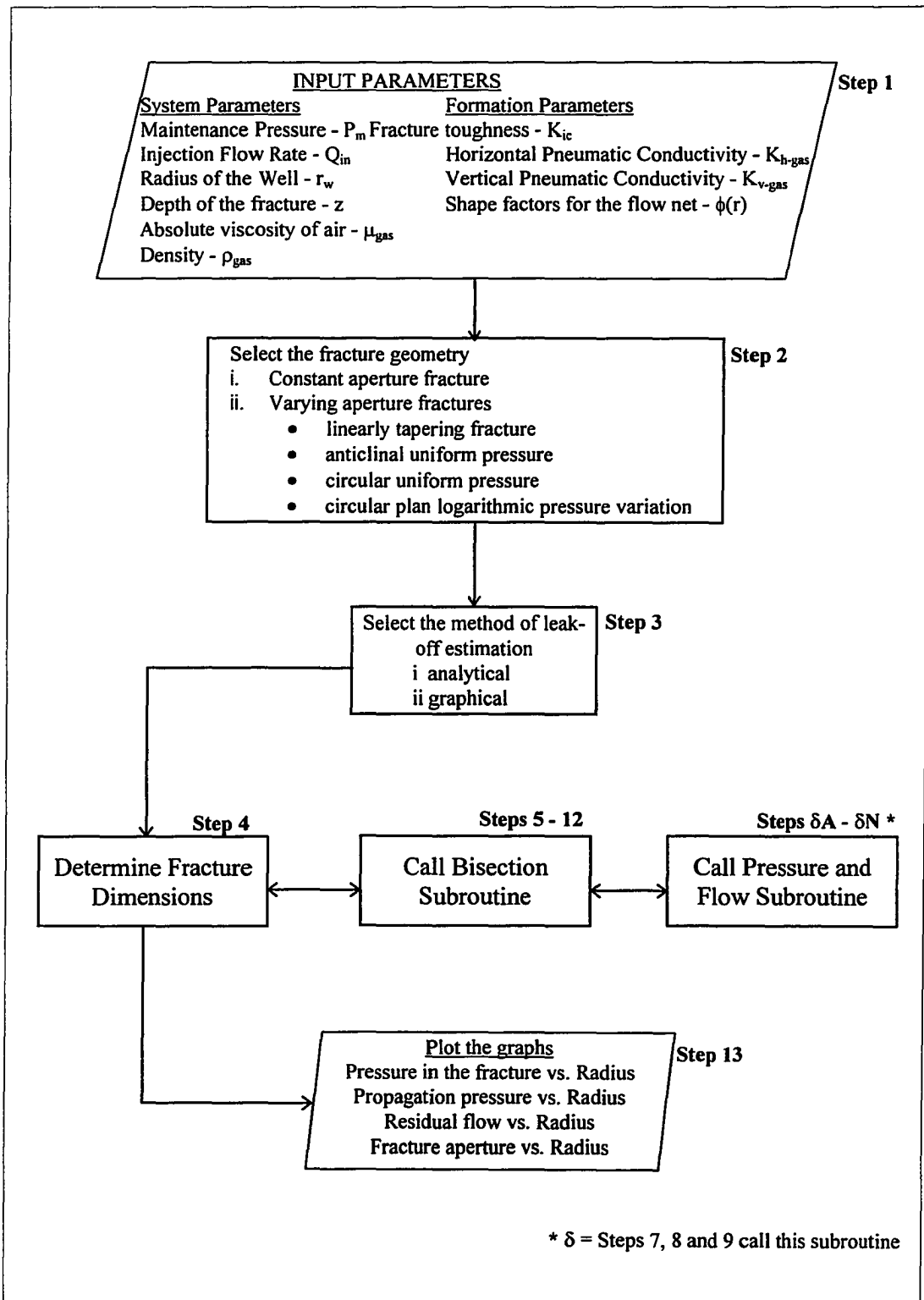


Figure 4.5 Main Routine

fixity conditions. The algorithm has been designed with the following options:

- a) Constant aperture fracture, the fracture shape assumed by Carter [1957].
- b) Varying aperture fractures including,
 - linearly tapering fractures;
 - anticlinal plan fracture subjected to uniform pressure;
 - circular plan fracture subjected to uniform pressure;
 - circular plan fracture subjected to logarithmically varying pressure.

Based on earlier studies [Canino, 1997] the deflection model which appears to provide the best fit with field measured ground surface heave data is the bending of a circular plate fixed at its edges. This is considered the default choice for deflection model, although others may be applicable for special cases.

Step 3 - Selecting the Method of Leak-off Estimation. Due to the relatively low viscosity of air, leak-off has a considerable influence on the dimensions of the predicted fracture. A precise estimation of the magnitude and distribution of leak-off along the length of the fracture is critical to an accurate prediction of the extent of fracture propagation. The algorithm provides the following two options for estimating the leak-off which are both based on Darcy's law:

- a) The first option is the graphical method (equation 3.10) that computes leak-off. It is based on obtaining the "shape factor" after constructing a flow net for the given boundary conditions of a propagating fracture. This method of estimating leak-off is believed to best represent the actual distribution of leak-off from the fracture.

- b) The second option is an analytical method (equation 3.12) that calculates leak-off through the successive annular rings of the fracture surface. When calculating leak-off in anisotropic formations, an “effective” conductivity must be used. This method is less complicated than the graphical method, but is not considered as accurate since it does not account for variation in gradient and formation anisotropy.

Step 4 - Determine Fracture Dimensions. The equilibrium fracture dimensions for the given Input Parameters and the selected deflection and leak-off models are computed. This is achieved by invoking two nested subroutines. The first is the “Bisection Subroutine” which corresponds to loop A in Figure 4.1. The other is the “Pressure and Flow Subroutine” corresponding to loop B of the conceptual flow chart shown in Figure 4.1.

Steps 5-12 - Bisection Subroutine. The execution control passes onto the “Bisection Subroutine”. Figure 4.6 is a flow chart of the Bisection Method algorithm. Usually the Bisection Method is used to determine the roots of an analytical function, but in the present case, the subroutine (Figure 4.7 Deflection, Pressure and Flow Subroutine) behaves as a virtual function. As shown in Figure 4.7 the fracture radius (input to the subroutine) is the independent variable and the subroutine returns the magnitude of the residual flow/over-pressure (output of the subroutine) which are dependent variables. More details of the Bisection Subroutine Loop are presented in the next section 4.3.2 “Bisection Method Subroutine.”

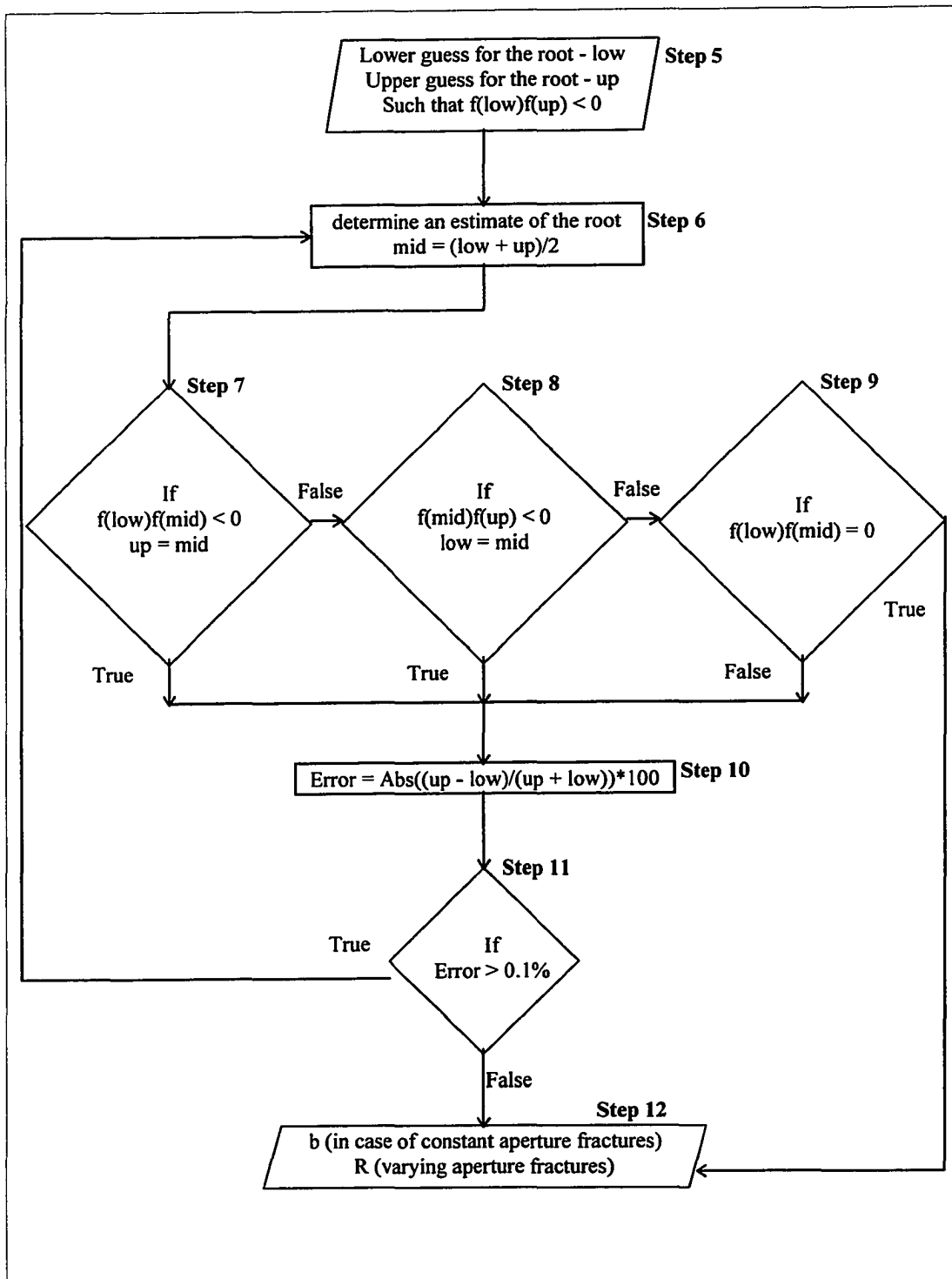


Figure 4.6 Bisection Subroutine

Steps δA - δN - Pressure and Flow Subroutine. This subroutine discretizes the extent of fracture radius and determines the pressure and flow variation within the fracture.

Details of this subroutine are presented in Section 4.3.3

Step 13 - Output. In this final step, the fracture dimensions that satisfy the pressure and flow conditions for a fracture in equilibrium are outputted. The pressure and residual flow distribution within the fracture as a function of the radial distance from the well are plotted.

4.3.2 Bisection Method Subroutine.

The Bisection Method, also known as binary chopping, interval halving, or Bolzano's method, is a root finding method based on the fact that a curve will change sign in the neighborhood of its root. The method requires an initial estimate of the interval bracketing the root, which are designated as a lower boundary, x_l , and an upper boundary, x_u . This can be accomplished by plotting the curve and noticing where it intercepts the x -axis. If the curve is continuous in the interval (x_l, x_u) , and $f(x_l)$ and $f(x_u)$ have opposite signs, then there is at least one real root between x_l and x_u . The interval bounding the root is divided into half at x_r (where $x_r = (x_l + x_u)/2$) and the location of the root within these two intervals is determined. The interval bracketing the root is retained and the other half discarded. The process is repeated to obtain refined values of the root. The iterations are terminated when the error with respect to the true root reaches a pre-specified value. Since the true root is not known, an approximate relative error will be used as the termination criterion. The approximate relative error is calculated as:

$$|\varepsilon_a| = \left| \frac{x_r^{\text{new}} - x_r^{\text{old}}}{x_r^{\text{new}}} \right| 100\% \quad (4.1)$$

$$\text{since } x_r^{\text{new}} = \frac{(x_u + x_l)}{2} \quad \text{and} \quad (x_r^{\text{new}} - x_r^{\text{old}}) = \frac{(x_u - x_l)}{2}$$

$$|\varepsilon_a| = \left| \frac{x_u - x_l}{x_u + x_l} \right| 100\% \quad (4.2)$$

where x_r^{new} is the estimate of the root for the present iteration and x_r^{old} is the estimate of the root from the previous iteration.

Step 5 - The initial estimates of the upper and the lower bounds for the root (i.e., dimensions of the fracture) used by the Bisection Method are chosen such that the function changes sign within the interval. From experience, the lower limit for fracture dimensions are chosen as 1.5E-01 m (0.5 ft) and 3.0E-04 m (0.001 ft) for the radius and aperture, respectively. For upper limits, a radius and aperture of 6.1E+01 m (200 ft) and 6.0E-02 m (0.2 ft) are adequate to bracket the solution.

Step 6 - Next an approximation of the root is computed, which is the mid-point of the interval bracketing the root. This is given by:

$$x_r = \frac{x_l + x_u}{2} \quad (4.3)$$

Two new intervals are now created, (x_l, x_r) and (x_r, x_u) , and the root lies within one of them.

Step 7, 8 & 9 - The location of the root within the two intervals created in the previous step is determined, the interval bracketing the root is retained while the other discarded.

$$\text{If } f(x_l)f(x_r) < 0, \text{ root lies in the lower subinterval, set } x_u = x_r, \quad (4.4)$$

$$\text{if } f(x_l)f(x_r) > 0, \text{ root lies in the upper subinterval, set } x_l = x_r, \text{ and} \quad (4.5)$$

$$\text{if } f(x_l)f(x_r) = 0, \text{ root equals } x_r, \text{ terminate the computation.} \quad (4.6)$$

The function $f(x)$ is not an analytical function, but a subroutine behaving as a virtual function (shown in Figure 4.7, detailed in Section 4.3.3). Given the fracture radius, the subroutine returns the residual flow/over-pressure within the fracture, at the end of an iterative loop when one of the conditions for terminating a propagating fracture are met.

Step 10 - The estimated error between the real root and the current estimate of the root is computed. The error calculated depends on the interval boundaries for the current iteration, as given in equation 4.1.

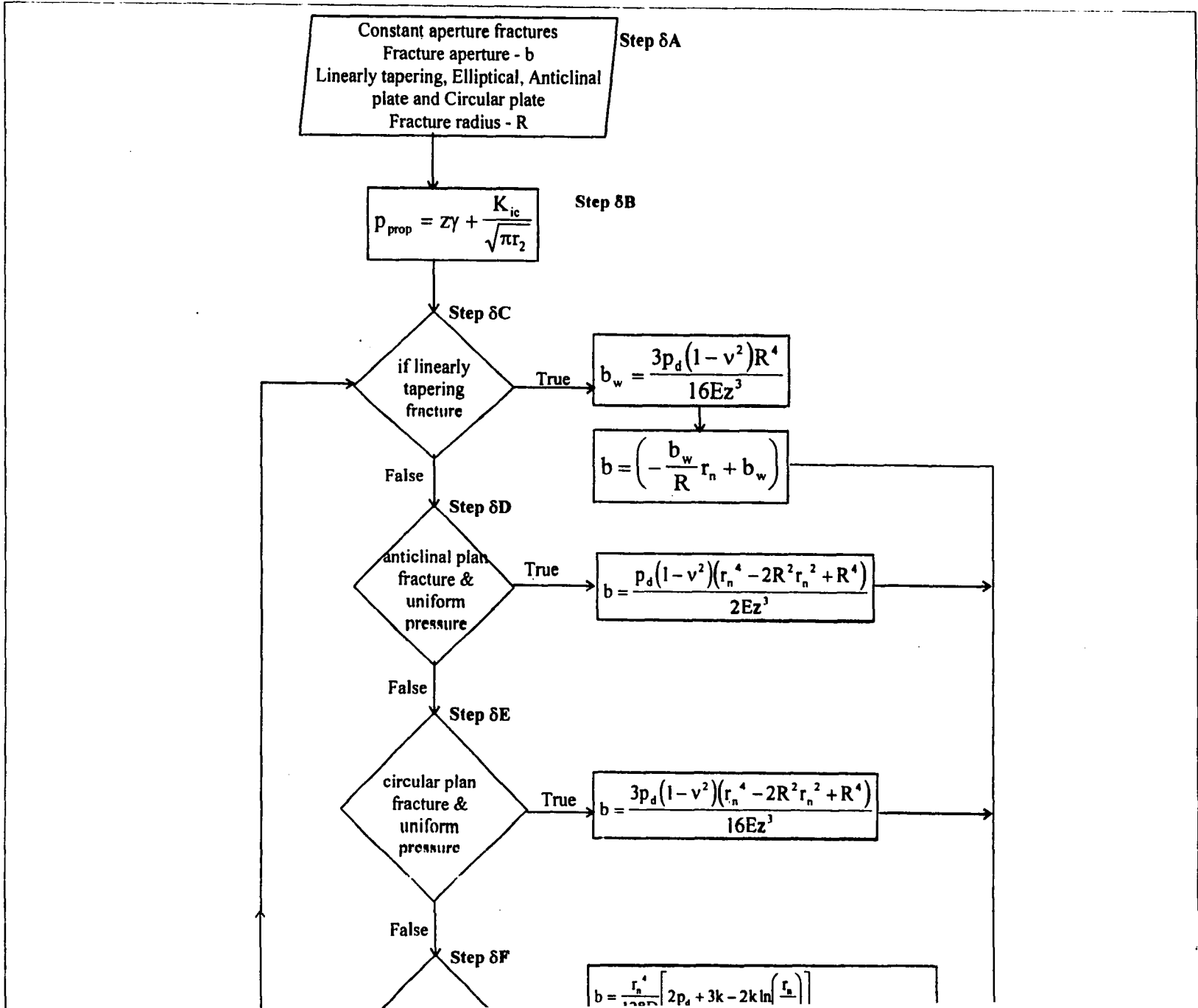
Step 11 - The algorithm enters a loop to converge towards the solution. The loop is not exited as long as the estimated percent error is greater than the specified termination criterion given by the following equation:

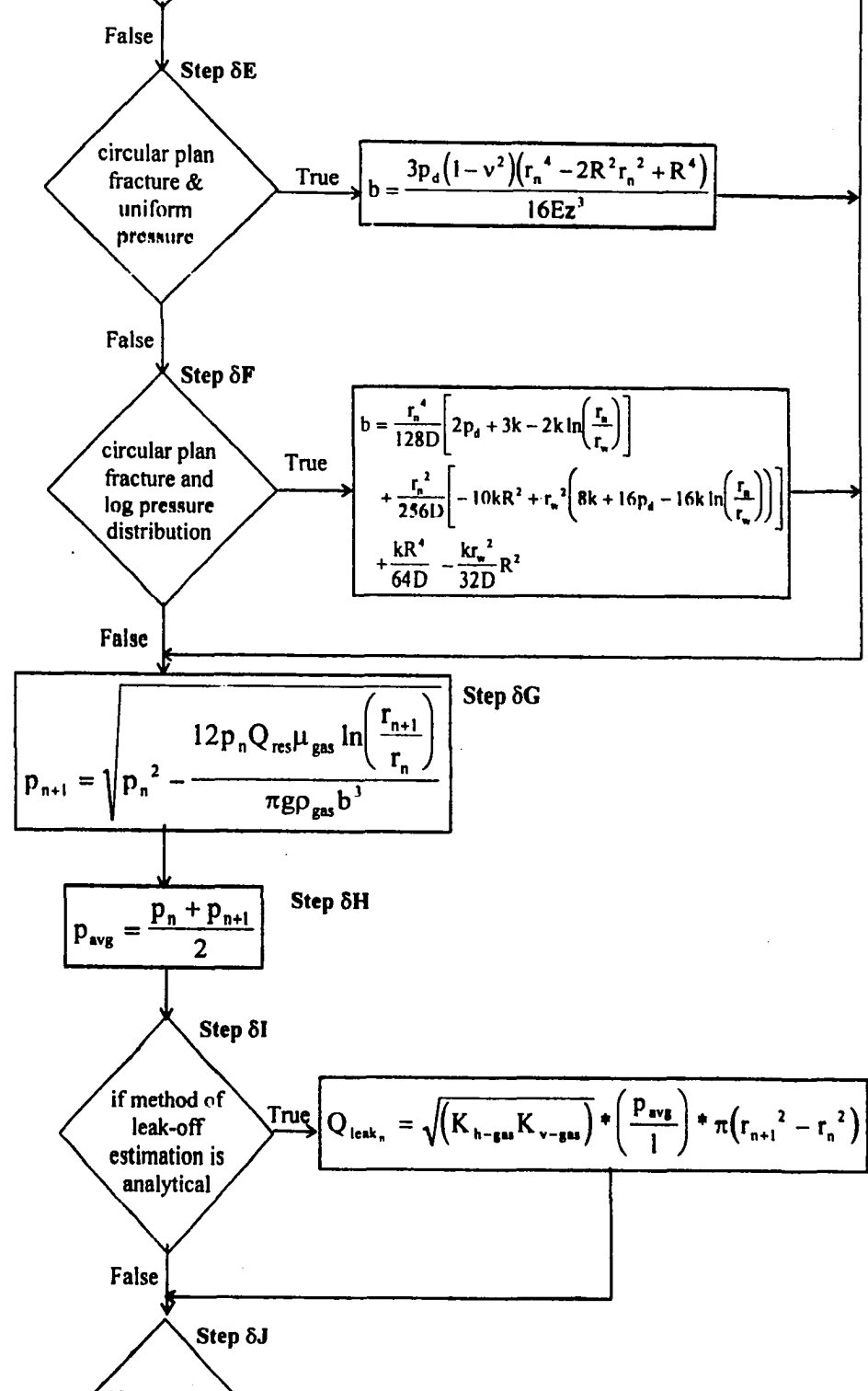
$$\varepsilon_a > 0.1\% \quad (4.7)$$

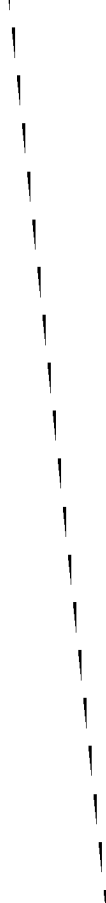
Step 12 - The root of the function is outputted and the execution control of the algorithm is returned to the main routine. The root outputted is the fracture aperture when a constant aperture fracture geometry is being analyzed, and fracture radius when a varying aperture fracture geometry is being analyzed.

4.3.3 Subroutine to Determine Flow and Pressure Variation in the Fracture.

This subroutine is invoked by the “Bisection Method Subroutine” in Steps 7, 8 and 9. It returns the values of residual-flow/over-pressure for a given fracture radius when the conditions for the termination of a propagating fracture are met. For a given fracture radius passed on by the “Bisection Method Subroutine,” the fracture extent is discretized into small segments, and a computation of pressure and residual flow within the first segment is made. The segmental radius is incremented and new calculations performed using the flow and pressure conditions at the boundary of the previous segment (Figure 4.2). This process is repeated until the residual flow reaches zero or the over pressure is less than the propagation pressure. Since this subroutine can be invoked in three different steps of the “Bisection Method Subroutine,” a common prefix ‘ δ ’ has been assigned to the algorithm steps where $\delta = 7, 8$ and 9 .







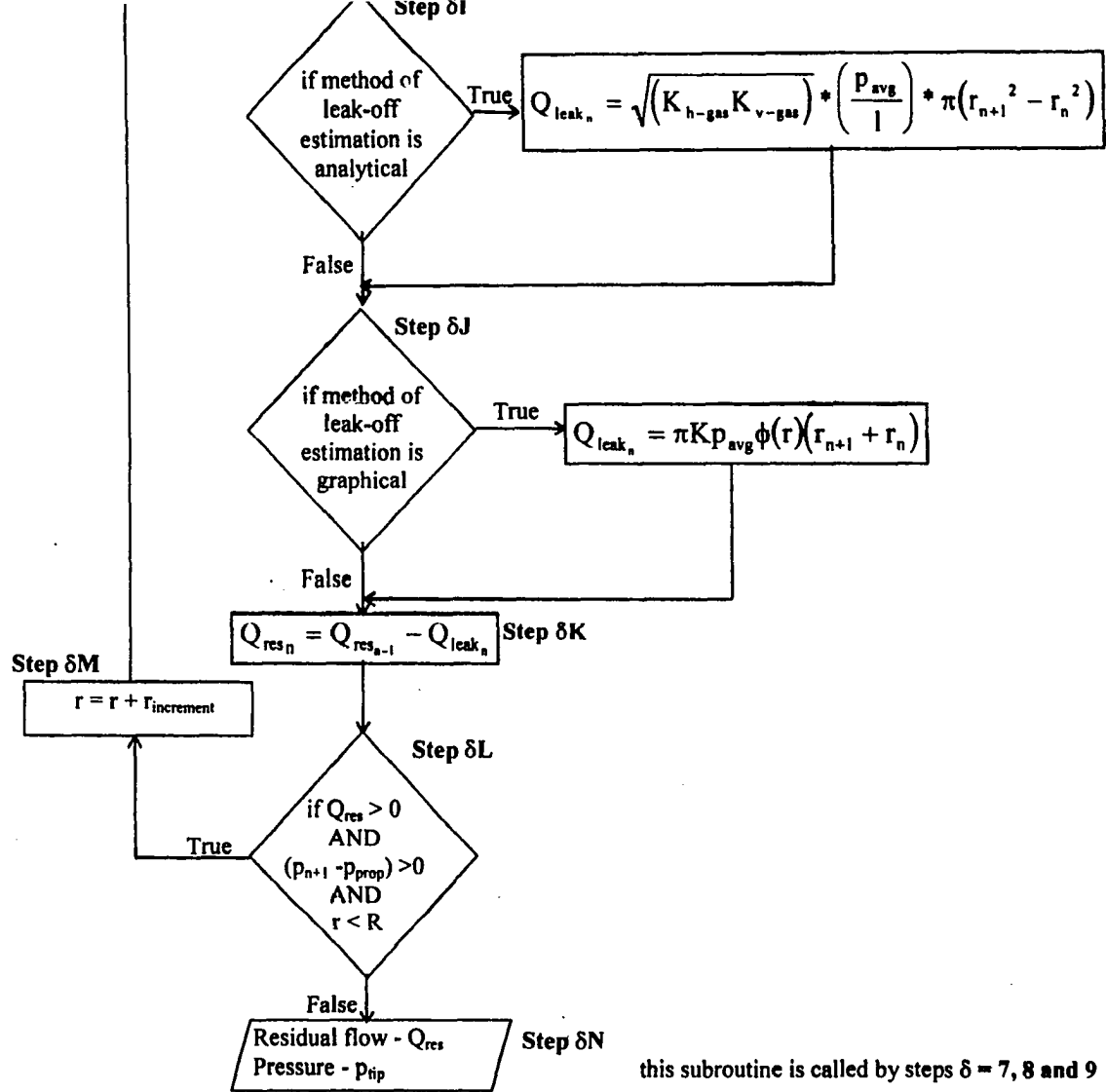


Figure 4.7 Deflection, Pressure and Flow Subroutine

Step δA - Input. The fracture radius 'R' is the input to the subroutine passed on by the "Bisection Method Subroutine." This value is the upper or lower bound of an interval being investigated for the presence of the root by the Bisection Method.

Step δB - Determining fracture maintenance and propagation pressures. A semi-empirical relation is available for estimating the fracture maintenance pressure [King, 1993]. Fracture maintenance pressure is a function of the geology of the formation, depth of fracturing and location of the water table. The fracture maintenance pressure, p_m , in the saturated zone is given by:

$$p_m = [\lambda_1 * (z - z_w) * \gamma] + [\lambda_1 * z_w * (\gamma - \gamma_w)] + [z_w * \gamma_w] \quad (4.8)$$

where z is the depth of the fracture, z_w is the piezometric level of the ground water above the zone of consideration, γ is bulk weight of the formation, γ_w is specific weight of water and λ_1 is a coefficient. The above equation for the case of fracturing in the vadose zone reduces to

$$p_m = \lambda_1 z \gamma \quad (4.9)$$

which is the method of maintenance pressure determination currently being used in the "Mathcad" version of the Algorithm.

In order for the fracture to propagate, the pressure at the tip of the fracture must exceed the weight of the overburden. Fracture propagation pressure may

also be affected by the fracture toughness of the material. The amount of pressure, p_k required to overcome the fracture toughness of a circular crack was given by Sneddon [1946] as:

$$p_k = \frac{K_{ic}}{\sqrt{\pi r}} \quad (4.10)$$

where K_{ic} is the fracture toughness of the formation and r is the radius of the fracture. The pressure required to propagate a fracture, p_{prop} , will thus have two components, maintenance pressure, p_m and the pressure required to overcome fracture toughness, p_k which can be written as.

$$p_{prop} = p_m + p_k \quad (4.11)$$

Some investigators [e.g., Spence and Turcotte, 1985] have suggested that fracture toughness can be ignored in most situations involving fracture propagation in geologic media. The effect of fracture toughness on propagation pressure, decreases with increasing fracture radius and depth of fracturing. For example, for a fracture propagating in a medium stiff clay to a radius of 15 ft, at a depth of 20 feet below the ground surface fracture toughness contributes only 10 % to the total propagation pressure.

Steps δC to δF - Fracture Dimensions. At this stage the algorithm enters an iterative loop which is exited only when any one of the conditions for terminating a

propagating fracture are met. A fracture geometry corresponding to that selected in 'Step 2' of the 'Main Routine,' is used by the algorithm to calculate fracture aperture.

The different fracture geometries that can be analyzed by the algorithm are summarized in Figure 4.8. Based upon experience to date with the model, it is believed that circular clamped plate subjected to a logarithmic variation in the pressure best represents the actual pressure distribution within the fracture. In all the relations in Figure 4.8, p_d is the driving pressure or over-pressure, and the other terms are as defined previously. It is noted that the plate bending equations only take into account the flexure of the overburden since calculations have shown that the elastic compression of the formation (both from downward compression and Poisson shortening of the flexed overburden) are negligible.

Step δG and δH - Pressure Distribution. Once the magnitude of the fracture aperture has been determined, the pressure dissipation within each segment due to frictional wall effects is computed. The modified Poiseuille's relation [Nautiyal, 1994] for radial flow of compressible fluids between impermeable parallel plates as previously presented in Chapter 3 is:

$$p_{n+1} = \sqrt{p_n^2 - \frac{12p_n Q \mu_{\text{air}} \ln\left(\frac{r_{n+1}}{r_n}\right)}{\pi g \rho_{\text{air}} b^3}} \quad (3.7)$$

where p_n and p_{n+1} are pressures at a distance r_n and r_{n+1} , respectively, Q is the flow between r_n and r_{n+1} , b is the fracture aperture, μ_{air} is the dynamic viscosity


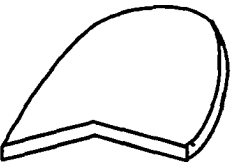
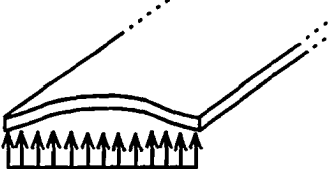
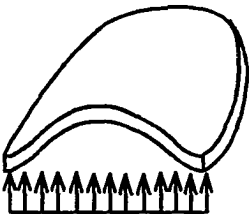
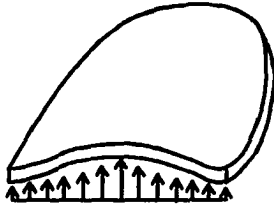
Fracture Geometry and Fixity	Assumed Pressure Distribution	Figure	Aperture Relationship
Linearly Tapering			$b = b_w \left(1 - \frac{r}{R} \right)$
Anticlinal Plan with Fixed Edges	Uniform		$b = \frac{p_d (1 - \nu^2) (r^4 - 2R^2 r^2 + R^4)}{2Ez^3}$
Circular Plan with Fixed Edges	Uniform		$b = \frac{3p_d (1 - \nu^2) (r^4 - 2R^2 r^2 + R^4)}{16Ez^3}$
Circular Plan with Fixed Edges	Logarithmic		$b = \frac{r^4}{128D} \left[2p_w + 3k - 2k \ln \left(\frac{r}{r_w} \right) \right]$ $+ \frac{r^2}{256D} \left[-10kR^2 + r_w^2 \left(8k + 16P_w - 16k \ln \left(\frac{r}{r_w} \right) \right) \right]$ $+ \frac{kR^4}{64D} - \frac{kr_w^2}{32D} R^2$ $k = \frac{P_w}{\ln \left(\frac{R}{r_w} \right)}$ $D = \frac{Ez^3}{12(1 - \nu^2)}$

Figure 4.8 Different Fracture Geometries Available that can be Modeled by the Algorithm

of the fluid, ρ_{air} is the density of the injected gas, and g is the acceleration due to gravity. The magnitude of pressure at the exit end of the segment is used as the input pressure for the adjoining element during the next iteration (Figure 4.2).

Steps δI to δK - Estimating Leak-off. The leak-off from the fracture, which is a function of the pressure distribution, gradient and formation anisotropy, will be calculated next. Leak-off is calculated either analytically or graphically depending on the option chosen. Recalling the equations for estimating leak-off from Chapter 3:

$$\text{(graphical method)} \quad Q_{\text{leak}} = \sum_{r_0=r_w}^{r_n=R} K_{\text{air}} H_n \left(\frac{N_f}{N_d} \right)_n \pi (r_{n-1} + r_n) \quad (3.10)$$

$$\text{(analytical method)} \quad Q_{\text{leak}} = \sum_{r_0=r_w}^{r_n=R} \sqrt{(K_{h\text{-gas}} K_{v\text{-gas}})} \left(\frac{P_d}{I_{\text{grad}}} \right)_n \pi (r_n^2 - r_{n-1}^2) \quad (3.12)$$

Once the amount of leak-off has been determined, an overall mass-balance of flow in the fracture is undertaken and the residual flow computed. If fracture volume is ignored, the following is obtained:

$$Q_{\text{res}_n} = Q_{\text{res}_{n-1}} - Q_{\text{leak}_n} \quad (4.12)$$

where Q_{res} is the residual flow left in the current segment after leak-off, $Q_{\text{res}(n-1)}$ is the flow entering the current segment being analyzed and $Q_{\text{leak}(n)}$ is the leak-off flow loss.

Step δL - Loop termination criteria. At this point the residual flow and pressure at the exit end of the segment are compared to the conditions of flow and pressure that would exist at the tip of a fracture in equilibrium. If none of the conditions are satisfied the execution control is handed to Step 13. On the other hand, if any one of the conditions is satisfied, the algorithm execution is passed onto Step 14.

Step δM - The ‘segmental fracture radius, r_n ,’ is incremented and the residual flow and pressure at the exit end of the segment in the previous iteration are used as the input for the new segment (Figure 4.2)

$$r_{n+1} = r_n + r_{incr} \quad (4.13)$$

where r_n is the segmental radius for the current iteration, r_{incr} is the size of the fracture segment and r_{n+1} is the segmental fracture radius for the next iteration.

Step δN - Output. The values returned by this subroutine are the magnitude of residual-flow/over-pressure when the loop was terminated at step δL . These values are returned to the Bisection Method subroutine.

4.4 Closed Form Solution of Pneumatic Fracture Propagation

This section outlines the approach taken to develop a closed form solution for predicting the extent of fracture propagation based on the principle of flow continuity. The reader is referred to Appendix D for the complete derivation.

The problem begins by considering a region G of the fracture surface (see Figure 4.9). The leak-off over this region can be readily determined using the Darcy’s law.

Leak-off is not constant over the entire region, but is a function of the varying pressure head distribution within the region. If region G is divided into very small parts and the leak-off is assumed constant in each part, the total fluid leak-off for the region can be represented by the following integral expression:

$$Q_{\text{leak}} = \iint_G f(x,y) dx dy \quad (4.14)$$

where $f(x,y)$ is the intensity of leak-off which varies over the surface G.

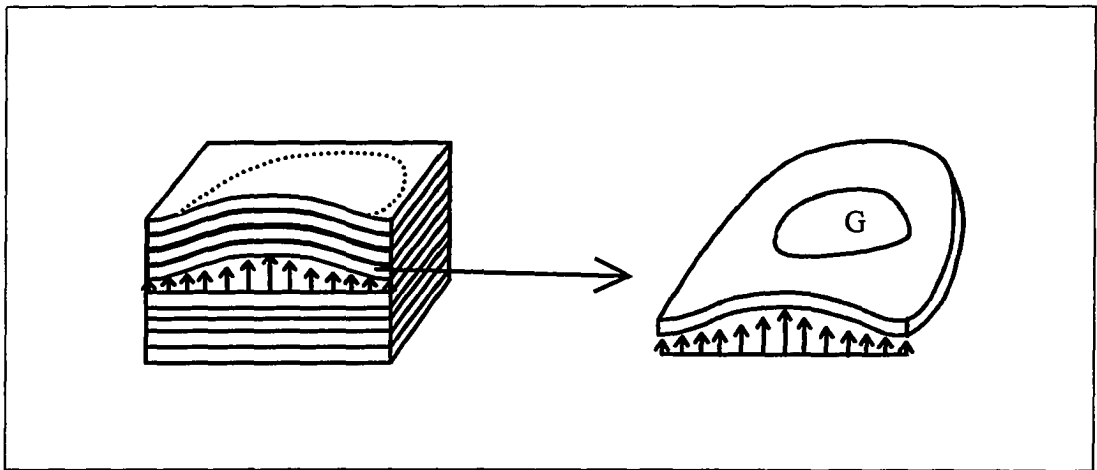


Figure 4.9 Region of Leak-off Estimation 'G'

If it is now assumed that the pressure within the fracture decreases as the cube of the distance from the injection well, and leak-off is occurring through both fracture faces, the following equation is obtained:

$$Q_{\text{leak}} = 2 \left[4 \int_0^R \int_0^{\sqrt{R^2-y^2}} k \frac{p_w}{z} \left[\frac{R^3 - (\sqrt{x^2+y^2})^3}{R^3} \right] dx dy \right] \quad (4.15)$$

Integration of the above equation (see appendix B for full solution) yields the following expression for total leak-off:

$$Q_{\text{leak}} = 3.53K_{\text{air}} \frac{p_w}{z} R^2 \quad (4.16)$$

Since the continuity criterion requires that total leak-off equal injected flow, the above equation can be solved for the maximum radius, R , to which the fracture has propagated:

$$R = \sqrt{\frac{Q_{\text{in}} z}{3.53K_{\text{gas}} p_w}} \quad (4.17)$$

Once the maximum radius, R , has been determined it can be used to ascertain the complete fracture geometry, since the fracture aperture depends on the extent of fracture propagation. The fracture aperture can be easily calculated using equation 3.13 which was previously developed in Chapter 3.4.3. This equation which is repeated here for convenience, models the deflection of a circular plate clamped at the edges and subjected to a logarithmically varying load.

$$\begin{aligned}
b = & \frac{r^4}{128D} \left[2p_d + 3k - 2k \ln \left(\frac{r}{r_w} \right) \right] \\
& + \frac{r^2}{256D} \left[-10kR^2 + r_w^2 \left(8k + 16p_d - 16k \ln \left(\frac{r}{r_w} \right) \right) \right] \\
& + \frac{kR^4}{64D} - \frac{kr_w^2}{32D} R^2
\end{aligned} \tag{3.13}$$

where, $k = \frac{P_d}{\ln \left(\frac{R}{r_w} \right)}$, $D = \frac{Ez^3}{12(1-\nu^2)}$,

w is the width of the fracture at a distance r from the well, R is the radial extent of the fracture, r_w is the radius of the well, p_w is the over-pressure at the injection well, E being the Young's Modulus of the formation, ν is the Poisson's ratio and z is the depth of fracturing.

CHAPTER 5

VALIDATION AND CALIBRATION OF THE ALGORITHM

5.1 Overview

Before a mathematical model can be used to solve engineering problems, it must undergo two essential procedures. The first is validation, which confirms whether or not the model reasonably represents the target phenomena. The second procedure is calibration, which establishes the necessary coefficients for proper functioning of the model.

The algorithm developed in the previous chapter was subjected to both procedures. Validation and calibration of the algorithm were greatly facilitated by the availability of field data from the more than 35 sites which have been pneumatically fractured to date. Although the quality of the data varies, it is believed to be sufficient for the first calibration of the algorithm. Calibration of the algorithm will of course continue for several more years as new data become available.

The validation and calibration procedures were affected by formation heterogeneities, which are inevitably present in all natural geologic formations, and will limit the predictive ability of any subsurface model. In essence, heterogeneities present a two-fold problem. First, if heterogeneities are known to exist, a deviation from predicted behavior may be expected since the actual conditions do not coincide with the original assumptions of the algorithm. The second problem occurs when heterogeneities are present but not detected. Once again, actual field behavior will deviate from model predictions. In spite of these limitations, the current algorithm is expected to serve as a valuable tool for estimating the dimensions of pneumatic fractures.

Validation of the pneumatic fracturing propagation algorithm begins with a sensitivity analysis to check overall behavior of the algorithm, and also to identify the most critical input parameters. Model sensitivity to errors in parameter estimation are also assessed (Section 5.2). Following this, the algorithm is calibrated with data from actual field operations using regression methods (Section 5.3). The predictive ability of the closed form solution is similarly examined (Section 5.4). Next, recommendations are made for input parameters for various kinds of geologies (Section 5.5). Finally, the practical uses of the algorithm and its limitations are discussed (Section 5.6).

5.2 Algorithm Sensitivity

This section describes the sensitivity analysis employed to examine the overall behavior of the algorithm. The basic approach of the sensitivity analysis was to vary each parameter individually while holding the others constant. The first analysis varied the input parameters over a relatively large range of values to check overall model behavior.

The sensitivity of the algorithm to errors in parameter estimation was also examined. The range of parameter variation for this second analysis was considerably smaller, and was intended to reflect the typical range of field error.

5.2.1 Overall Behavior and Sensitivity of the Algorithm

To assure realism, the constant parameters were selected from an actual pneumatic fracturing injection event in the field which was considered typical. Table 5.1 lists the constants as well as the range over which each parameter was varied.

The results of the this analysis are shown in Figure 5.1. In each case, both the fracture radius, R , and the maximum fracture aperture, b , were computed over the full parametric range. It is noted that all the graphs show a non-linear dependence of the fracture dimensions on the algorithm parameters. Overall, two different trends can be distinguished. The first is where the fracture radius and aperture increase or decrease together. In the second trend the fracture radius and aperture show an inverse relationship, one decreasing while the other is increasing. The results of the overall behavior analysis are discussed further in Section 5.2.3.

Table 5.1 Range of Parameter Variation

Parameter	“Constant” Parameter Value	Range of Variation
E	688 psi	500 psi – 10^6 psi
K	2.0 ft/day ($7.1 \cdot 10^{-4}$ cm/sec)	28.4 ft/day - $28.4 \cdot 10^{-6}$ ft/day (10^{-2} cm/sec - 10^{-8} cm/sec)
ν	0.4	0.1 – 0.5
z	8.3 ft	1 ft – 100 ft
Q	1500 scfm	100 scfm – 3000 scfm
P_w	18 psi	5 psi – 100 psi
γ	105 lb/ft ³	80 lb/ft ³ - 170 lb/ft ³

The sensitivity analysis with respect to field errors in parameter estimation was performed for two different geologic conditions, one for a soil formation, and the other for a rock formation. The test parameters and their assumed accuracies are summarized

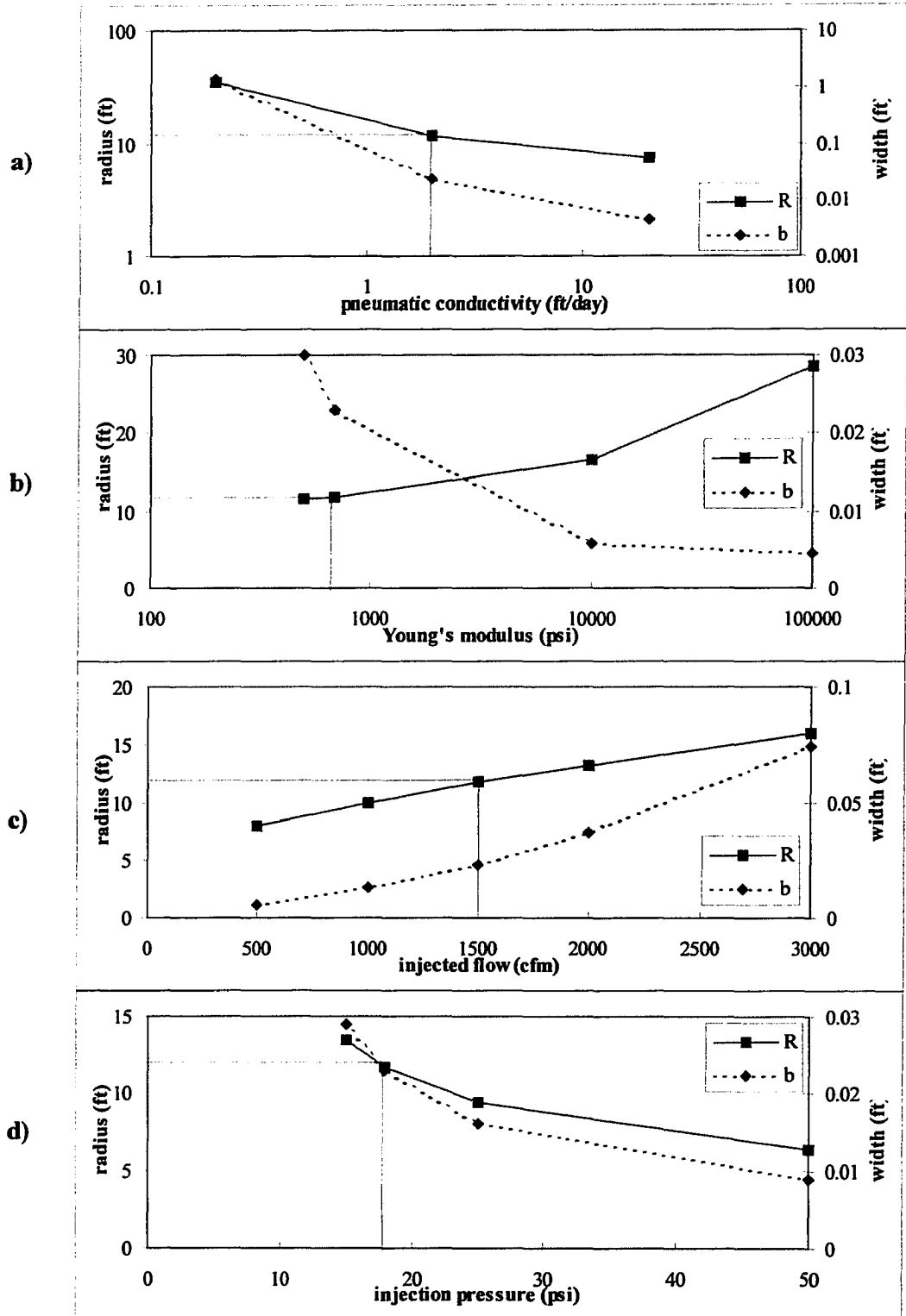


Figure 5.1 Variation of Fracture Dimensions for the Range of Parameter Variation

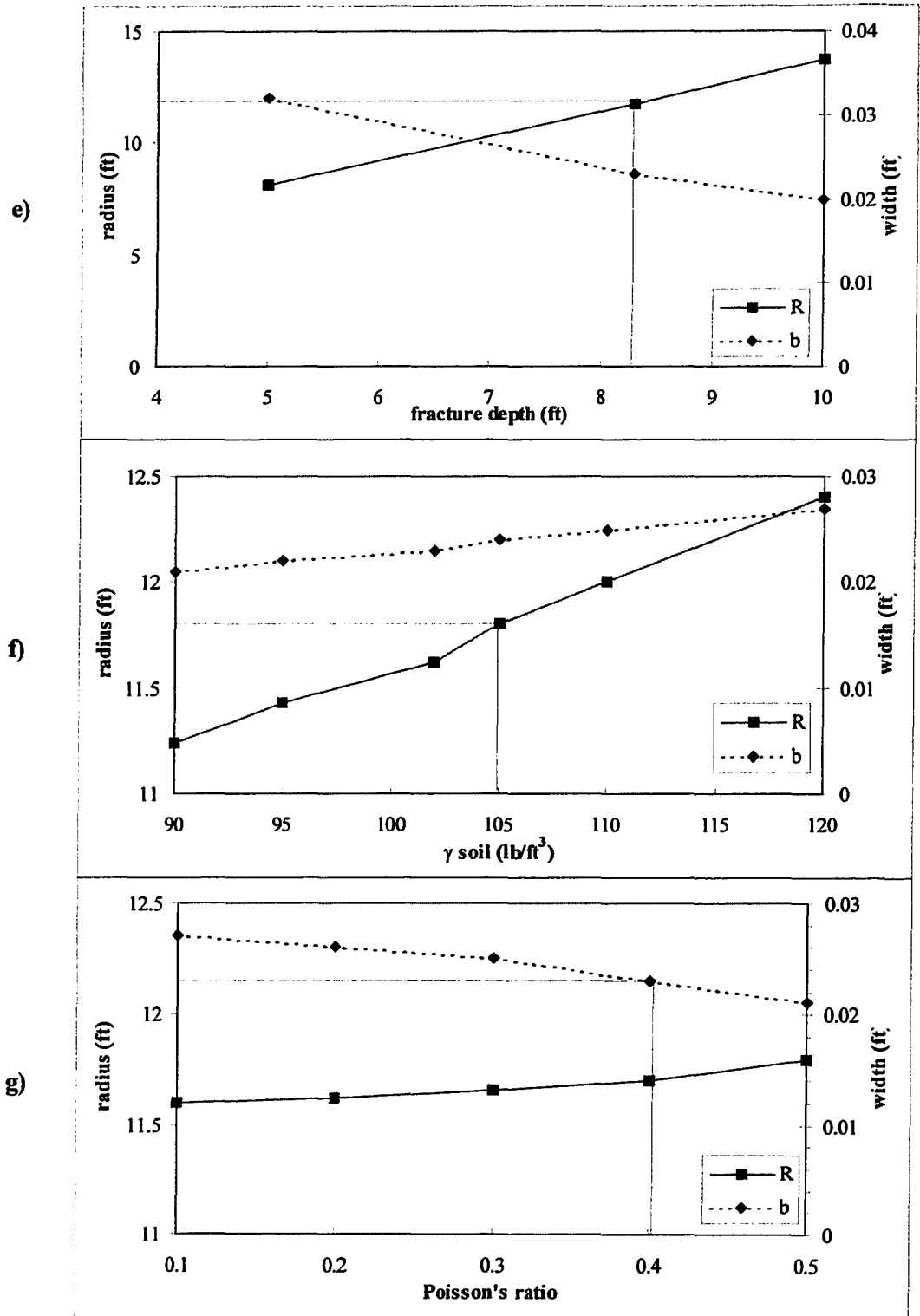


Figure 5.1 cont. Variation of Fracture Dimensions for the Range of Parameter Variation

in Table 5.2. As in the previous analysis, the “constant” parameters were taken from actual injection events.

The results of the error sensitivity analysis are summarized in Figure 5.2, which shows the ratio of predicted fracture radius to actual fracture radius for the assumed variation of each input parameter. As seen in the figure, both the soil and rock formation exhibit a similar trend in terms of relative sensitivity. The algorithm is most sensitive to the pneumatic conductivity of the formation. The other parameters in the decreasing order of their relative importance are injection pressure, fracturing depth, injection flow rate, unit weight of the formation, formation modulus, and Poisson’s ratio.

Table 5.2 Accuracy of Parameter Determination

Parameter	Injection in Soil	Injection in Rock	Accuracy with which Parameters can be Determined in the Field
E	688 psi	27835 psi	±20 %
K	2.0 ft/day (7.1×10^{-4} cm/sec)	0.228 ft/day (5.2×10^{-9} cm/sec)	one order of magnitude
v	0.4	0.25	±0.1
z	8.3 ft	10 ft	±0.5 ft
Q	1500 scfm	1500 scfm	±200 scfm
P _w	18 psi	21 psi	± 2 psi
γ	105 lb/ft ³	140 lb/ft ³	±10 lb/ft ³

5.2.2 Discussion of Overall Behavior and Sensitivity Results

Algorithm Sensitivity to Varying Formation Conductivity: A review of Figure 5.1a and Figure 5.2 clearly shows that the algorithm is more sensitive to pneumatic

conductivity than any other parameter. The relation is one of inverse proportionality, with fracture dimensions decreasing as pneumatic conductivity increases. This behavior can be explained by Darcy's law, since pneumatic conductivity has a substantial effect on formation leak-off, which in turn controls final radius.

Unfortunately, the determination of pneumatic conductivity is often difficult since laboratory tests are not representative of field values, and field tests are expensive. In most cases during preliminary design, pneumatic conductivity is only known to an accuracy of one order of magnitude. Thus, it is obvious from these results that the accuracy of this parameter will largely control the reliability of the algorithm predictions.

Algorithm Sensitivity to Varying Formation Modulus: The algorithm is very sensitive to formation modulus if the entire possible range of this parameter variation is considered (Figure 5.1b). However, if the typical error range for modulus is examined ($\pm 20\%$), the model is much less sensitive (Figure 5.2). Thus, the potential error introduced by this parameter is considered to be low to moderate.

The general trend is that when the modulus is increased, the fracture aperture decreases and the radius increases. This behavior can be explained by the fact that when the formation modulus is increased, its rigidity increases, thereby resulting in a reduced deflection and aperture. A smaller aperture will increase the rate of pressure loss within the fracture which in turn leads to a decrease in the leak-off. The surplus air left due to lower leak-off requires additional fracture surface area (and fracture radius) to satisfy the continuity criteria.

Algorithm Sensitivity to Varying Injection Flow Rate: The algorithm is moderately sensitive to varying the injection flow rate. As expected, an increase in the rate of

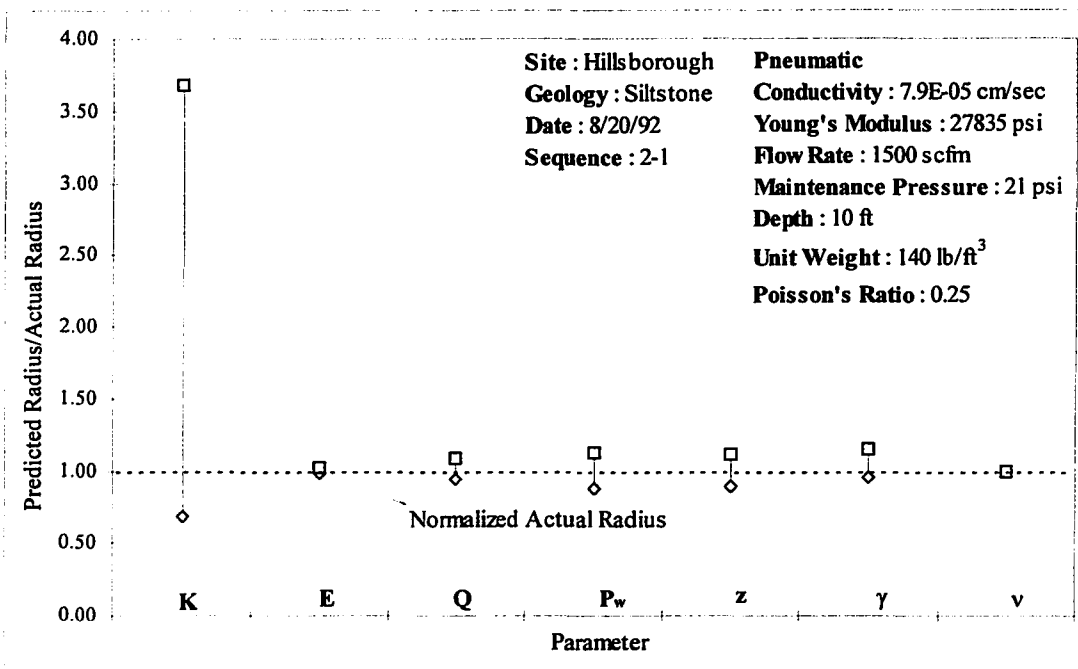
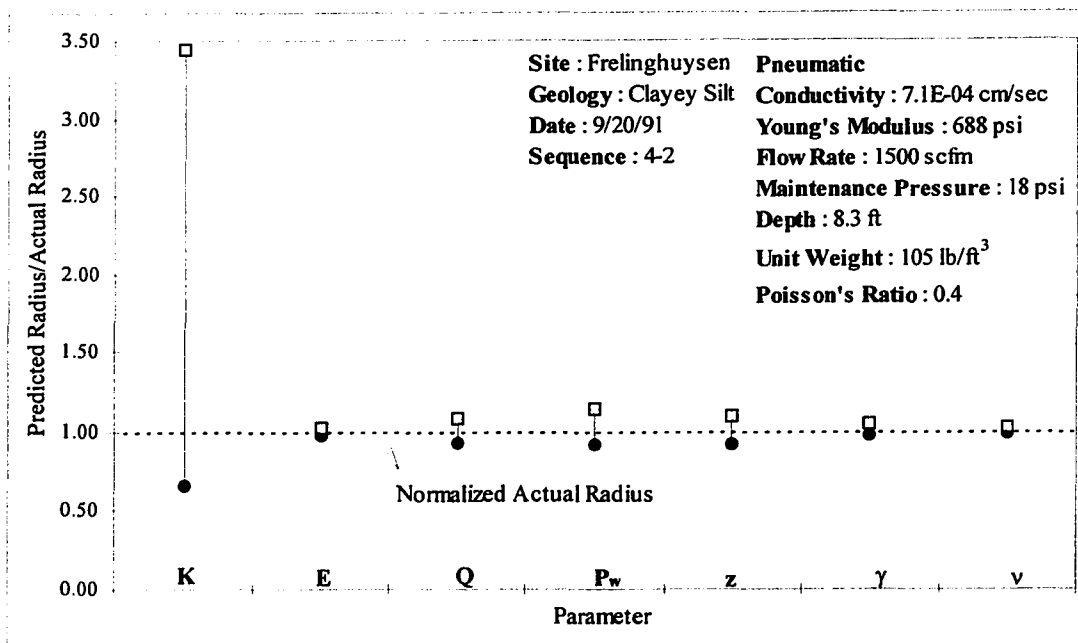


Figure 5.2 Model Sensitivity to Error in Parameter Estimation

injection flow causes a corresponding increase in fracture radius and aperture. This occurs simply because the additional volume of injected air needs a larger fracture surface area (and fracture radius) to satisfy the fluid continuity criteria of the algorithm. A larger radius thus produces a greater deflection and fracture aperture. Since the injection flow rates can be controlled reasonably well in the field, usually to within 200 scfm, the errors introduced by this parameter to the algorithm results are not expected to be significant.

Algorithm Sensitivity to Varying Injection Pressure: The algorithm is moderately sensitive to varying the injection pressure. The fracture dimensions decrease for increasing injection pressures. An increase in the injection pressure leads to an increase in leak-off velocity based on Darcy's law. This increment in the leak-off velocity results in a smaller fracture surface area (and fracture radius), since fracture surface area is inversely proportional to leak-off velocity. Field methods of recording injection pressure are generally accurate to within a few 'psi.' It can be seen from Figure 5.2, that this degree of uncertainty does not produce a large variation in the predicted fracture dimensions.

It is noted that in the field, injection pressure and the injection flow rate are coupled to some extent, since injection pressures have to be increased to attain higher injection flow rates and vice versa. The opposing effects increasing injection pressure and injection flow rate on the fracture dimensions are expected to cancel each other out to some degree.

Algorithm Sensitivity to Varying Fracturing Depth: The algorithm is moderately sensitive to variations in the fracturing depth. When depth is increased, predicted fracture radius increases and fracture aperture decreases. This is attributed to increased flexural

rigidity of the overburden. Fortunately, the depth of fracturing can be accurately determined in the field, usually to within ± 0.5 ft. It is apparent from Figure 5.1e that this amount of depth variation will not produce a significant error when predicting fracture dimensions.

Algorithm Sensitivity to Varying Formation Density: The algorithm is relatively insensitive to any change in the formation density. Fracture dimensions increase with increasing formation density. This formation index property does not vary significantly within a given geology, and can be usually be estimated with sufficient accuracy.

Algorithm Sensitivity to Varying Poisson's Ratio: The algorithm is not sensitive to variation in Poisson's ratio. As shown in Figure 5.1 when the Poisson's ratio is increased, the algorithm predicts a slightly larger fracture radius and a slightly smaller fracture aperture.

In summary, sensitivity of the algorithm to a particular parameter depends on the range of its variation. When the entire range through which the parameters can be varied are considered, in the decreasing order of sensitivity, the algorithm is most sensitive to, pneumatic conductivity, elastic modulus, injection flow rate, injection pressure, depth of fracturing, formation density and Poisson's ratio. When the typical range of field errors is considered, pneumatic conductivity singularly dominates model performance.

5.3 Calibration of the Algorithm

After establishing algorithm sensitivity, the next step was to calibrate the algorithm with data collected from past pneumatic fracturing operations. The objectives of the calibration step were two-fold:

- i) to compare derived parameters with field measured and literature values.
- ii) to check the predictive ability of the algorithm;

The model calibration also provided additional validation of the algorithm.

5.3.1 Calibration Procedure

Data from 35 different sites were initially reviewed for algorithm calibration. A screening procedure was applied to assure that only data of acceptable quality were used in the calibration process. The following criteria were adhered to in the screening process:

- Only sites with sufficient geologic reconnaissance data available were considered;
- Sites with overlying fill materials were not used;
- Injections with abnormal equipment operation were not considered; and
- Only injections that produced a maximum surface heave of at least 0.003 meters (1/8 inch) at the injection point were considered. Injections with smaller surface heaves do not allow development of reliable ground surface heave contours.

After evaluation of all available data, six different sites were chosen for calibration purposes including three sites involving fracturing of soil formations and three sites involving rock formations. The field data from each of these sites are listed in Table 5.3 which will serve as input parameters for the algorithm calibration (shown shaded).

The sensitivity analysis in the preceding section clearly established that the algorithm was most sensitive to the pneumatic conductivity. A low to moderate sensitivity was also exhibited for modulus of elasticity. Since these two parameters are among the more difficult to determine for a given field site, it was decided to calibrate the

Table 5.3 Data used to calibrate and validate the Algorithm

Site Name	Date	Geology	Inj no	Field Data used as Input for the Algorithm							P _a driving pressure (psi)	E Young's modulus (psi)
				Z	γ _{sat}	v	Q	P _m	b	R _{field}		
				fracture depth (ft)	formation density (pcf)	Poisson's ratio	injection flow rate (ccfs)	maintenance pressure (psi)	maximum measured Heave (ft)	average measured radius (ft)		
Frelinghuysen, Phase 1	18-Apr-90	Clayey Silt	1-1	3.5	105	0.4	300	10	0.0792	4.2	7.4	38
	18-Apr-90	CL-ML	1-3	3.5	105	0.4	300	10	0.0533	4.2	7.4	56
	27-Apr-90	CL-ML	1-7	3.5	105	0.4	300	7	0.0208	4.2	4.4	86
	27-Apr-90	CL-ML	1-8	3.5	105	0.4	300	8	0.0317	4.2	5.4	69
Frelinghuysen, Phase 2	24-May-91	CL-ML	3-1	6	105	0.4	715	13	0.0342	8.5	8.6	272
	24-May-91	CL-ML	3-2	6	105	0.4	1227	13	0.0367	8.5	9.6	283
	20-Sep-91	CL-ML	4-1	6	105	0.4	1157	13	0.0075	5.7	10.6	347
	20-Sep-91	CL-ML	4-2	8.3	105	0.4	1500	13	0.0233	11.7	11.9	688
	20-Sep-91	CL-ML	5-1	6	105	0.4	1500	17	0.0375	8.6	12.6	379
	20-Sep-91	CL-ML	5-3	8.6	105	0.4	1339	17	0.0390	11.3	10.7	291
Frelinghuysen, Phase 3	29-May-92	CL-ML	5-1	6	105	0.4	857	15	0.0167	4.2	10.6	51
	29-May-92	CL-ML	5-2	6	105	0.4	964	14	0.0275	12.6	7.0	1197
	29-May-92	CL-ML	5-3	6	105	0.4	1000	11	0.0250	9.6	6.6	449
	29-May-92	CL-ML	5-4	9	105	0.4	943	16.5	0.0183	14.1	9.9	1149
	29-May-92	CL-ML	5-5	9	105	0.4	1114	14.7	0.0150	16.1	8.1	1890
	03-Jun-92	CL-ML	6-1	6	105	0.4	722	12.5	0.0275	11.7	8.1	1049
	03-Jun-92	CL-ML	6-2*	8.3	105	0.4	984	17	0.0158	11.4	10.9	843
site average												
Tinker AFB, OK	08-Jul-93	Clayey Silt	SWT-5	8	105	0.4	1716	31	0.0417	19	25.2	5585
	09-Jul-93	Clayey Silt	SWT-6	19	105	0.4	1759	130	0.0125	30.8	116.1	39881
	12-Jul-93	Clayey Silt	NTA-5	8	105	0.4	1716	12	0.1000	23	22.2	4219
site average												
Marcus Hook, PA	21-Oct-92	Clayey Silt	1-1	6	105	0.4	1200	12	0.0500	16.2	7.6	1835
	22-Oct-92	Clayey Silt	1-3	6	105	0.4	1276	19	0.0500	15.8	14.6	3204
	22-Oct-92	Clayey Silt	1-4	6	105	0.4	1400	14	0.0700	15.1	9.6	1270
site average												
Hillsborough Phase 2	20-Aug-92	Siltstone	2-1	10	140	0.25	1500	21	0.0320	27.9	11.3	7960
	20-Aug-92	Siltstone	2-2	12	140	0.25	1607	25	0.0258	29.4	13.3	8238
	20-Aug-92	Siltstone	2-3	14	140	0.25	1886	30	0.0317	27.7	16.4	4141
Hillsborough Phase 3	06-Apr-93	Siltstone	3-1	14	140	0.25	1029	28	0.0333	30	14.4	4683
site average												
Newark, NJIT	19-Nov-90	Sandstone	1-1	10	140	0.25	771	37.5	0.0133	25	27.8	31135
	19-Nov-90	Sandstone	1-2	16	140	0.25	857	53	0.0108	30	37.4	25171
site average												
Flemington, NJ Phase 1	20-Apr-95	Siltstone	1-8	16	140	0.25	2286	35	0.0260	24.5	19.4	2522
	20-Apr-95	Siltstone	6-8	27	140	0.25	1886	75	0.0104	33	48.8	10166
site average												

Algorithm		P _d driving pressure (psi)	E Young's modulus (psi)	R/z ratio	b _{strain} aperture due to strain shortening of over-burden (ft)	b maximum predicted fracture aperture (ft)	R _{model} predicted fracture radius (ft)	R _{model} R _{field}	R _{model-cd} closed form solution (ft)	R _{model-cd} R _{field}	K permeability conductivity-isotropic conditions (cm/sec)		
b	R _{field}										based on analytical method of leak-off estimation	based on flownet method -I of leak-off estimation	based on flownet method -II of leak-off estimation
circum	average												
measured	measured												
leave	radius												
(ft)	(ft)												
0792	4.2	7.4	38	1.2	1.13E-05	0.070	4.2	1.0	5.4	1.3	4.94E-04	2.65E-04	6.52E-04
0533	4.2	7.4	56	1.20	3.43E-06	0.050	4.2	1.0	5.3	1.3	4.94E-04	2.72E-04	6.63E-04
0208	4.2	4.4	86	1.20	2.04E-07	0.019	4.1	1.0	4.8	1.2	7.76E-04	4.66E-04	1.02E-03
0317	4.2	5.4	69	1.20	7.22E-07	0.034	4.3	1.0	5.1	1.2	6.35E-04	3.70E-04	8.64E-04
0342	8.5	8.6	272	1.42	2.21E-07	0.033	8.4	1.0	9.4	1.1	3.95E-04	2.72E-04	6.10E-04
0367	8.5	9.6	283	1.42	2.74E-07	0.034	8.3	1.0	9.3	1.1	6.35E-04	4.41E-04	9.80E-04
0075	5.7	10.6	347	0.95	5.19E-09	0.008	5.7	1.0	5.5	1.0	1.59E-03	1.09E-03	1.98E-03
0233	11.7	11.9	688	1.41	3.7E-08	0.024	11.8	1.0	12.2	1.0	4.59E-04	3.36E-04	7.14E-04
0375	8.6	12.6	379	1.43	2.85E-07	0.038	8.6	1.0	9.4	1.1	6.17E-04	4.37E-04	7.81E-04
0390	11.3	10.7	291	1.31	1.86E-07	0.040	11.4	1.0	12.9	1.1	4.59E-04	2.93E-04	6.56E-04
0167	4.2	10.6	51	0.70	1.06E-07	0.016	4.2	1.0	5.4	1.3	1.83E-03	8.47E-04	1.83E-03
0275	12.6	7.0	1197	2.10	5.24E-08	0.027	12.6	1.0	13.2	1.0	2.84E-04	2.12E-04	4.40E-04
0250	9.6	6.6	449	1.60	6.78E-08	0.024	9.6	1.0	11.4	1.2	5.29E-04	3.04E-04	6.35E-04
0183	14.1	9.9	1149	1.57	1.23E-08	0.019	14.3	1.0	13.7	1.0	2.41E-04	1.98E-04	4.16E-04
0150	16.1	8.1	1890	1.79	5.21E-09	0.015	16.0	1.0	17.0	1.1	2.54E-04	1.72E-04	3.32E-04
0275	11.7	8.1	1049	1.95	6.08E-08	0.028	11.8	1.0	12.9	1.1	2.25E-04	1.50E-04	3.19E-04
0158	11.4	10.9	843	1.37	1.21E-08	0.016	11.4	1.0	11.7	1.0	3.44E-04	2.54E-04	5.29E-04
											6.04E-04	3.75E-04	7.89E-04
0417	19	25.2	5585	2.38	8.03E-08	0.042	19.0	1.0	19.8	1.0	1.06E-04	8.23E-05	1.81E-04
0125	30.8	116.1	39881	1.62	8.24E-10	0.012	30.7	1.0	36.0	1.2	2.47E-05	1.44E-05	2.96E-05
0100	23	22.2	4219	2.88	7.56E-07	0.100	23.0	1.0	22.6	1.0	7.76E-05	6.95E-05	1.59E-04
											6.94E-05	5.54E-05	1.23E-04
0500	16.2	7.6	1835	2.70	1.91E-07	0.050	16.2	1.0	15.7	1.0	1.98E-04	1.77E-04	3.88E-04
0500	15.8	14.6	3204	2.63	2E-07	0.042	15.8	1.0	15.7	1.0	1.38E-04	1.18E-04	2.61E-04
0700	15.1	9.6	1270	2.52	6.02E-07	0.049	15.8	1.0	15.5	1.0	2.22E-04	1.81E-04	4.06E-04
											1.86E-04	1.59E-04	3.52E-04
0320	27.9	11.3	7960	2.79	1.05E-08	0.032	27.9	1.0	25.8	0.9	8.18E-05	7.76E-05	1.64E-04
0258	29.4	13.3	8238	2.45	4.97E-09	0.028	29.5	1.0	29.0	1.0	8.08E-05	6.63E-05	1.43E-04
0317	27.7	16.4	4141	1.98	1.04E-08	0.033	27.6	1.0	30.5	1.1	1.02E-04	6.84E-05	1.44E-04
0333	30	14.4	4683	2.14	1.03E-08	0.036	29.9	1.0	32.7	1.1	5.00E-05	3.50E-05	7.76E-05
											7.87E-05	6.18E-05	1.32E-04
0133	25	27.8	31135	2.50	9.41E-10	0.013	25.0	1.0	23.4	0.9	3.05E-05	2.72E-05	5.57E-05
0108	30	37.4	25171	1.88	3.5E-10	0.011	30.0	1.0	32.0	1.1	2.72E-05	1.83E-05	3.70E-05
											2.89E-05	2.28E-05	4.64E-05
0260	24.5	19.4	2522	1.53	7.32E-09	0.027	24.5	1.0	25.1	1.0	1.55E-04	1.20E-04	2.58E-04
0104	33	48.8	10166	1.22	2.58E-10	0.010	33.0	1.0	35.0	1.1	6.10E-05	4.02E-05	8.04E-05
											1.08E-04	8.01E-05	1.69E-04

conditions (cm/sec)	K pneumatic conductivity - anisotropic conditions (cm/sec)						R _{model-cd} closed form solution (R) (flownet isotropic)	R _{model-cd} R _{field} (flownet isotropic)	R _{frwd_model} (R) (flownet isotropic)	R _{frwd_model} R _{field}	
	K _{horizontal} = 5 x K _{vertical}			K _{horizontal} = 10 x K _{vertical}							
	K _{horizontal}	K _{vertical}	K _{effective}	K _{horizontal}	K _{vertical}	K _{effective}					
based on flownet method -II of leak-off estimation	based on flownet method-I for calculating leak-off			based on flownet method-I for calculating leak-off							
6.52E-04	9.35E-04	1.87E-04	4.18E-04	1.69E-03	1.69E-04	5.34E-04	5.4	1.3	2.5	0.6	
6.63E-04	9.70E-04	1.94E-04	4.34E-04	1.72E-03	1.72E-04	5.44E-04	5.3	1.3	2.6	0.6	1 st Refracture
1.02E-03	1.72E-03	3.46E-04	7.71E-04	2.99E-03	2.99E-04	9.46E-04	4.8	1.2	3.9	0.9	2 nd Refracture
8.64E-04	1.36E-03	2.72E-04	6.08E-04	2.37E-03	2.37E-04	7.49E-04	5.1	1.2	3.3	0.8	3 rd Refracture
6.10E-04	9.70E-04	1.94E-04	4.34E-04	1.75E-03	1.75E-04	5.53E-04	9.4	1.1	5.9	0.7	
9.80E-04	1.59E-03	3.18E-04	7.11E-04	2.85E-03	2.85E-04	9.01E-04	9.3	1.1	7.2	0.8	Refracture
1.98E-03	3.92E-03	7.83E-04	1.75E-03	7.02E-03	7.02E-04	2.22E-03	5.5	1.0	7.1	1.2	
7.14E-04	1.23E-03	2.45E-04	5.49E-04	2.19E-03	2.19E-04	6.93E-04	12.2	1.0	9.4	0.8	
7.81E-04	1.57E-03	3.14E-04	7.02E-04	2.82E-04	2.82E-05	8.92E-05	9.4	1.1	7.2	0.8	
6.56E-04	1.07E-03	2.13E-04	4.77E-04	1.88E-03	1.88E-04	5.95E-04	12.9	1.1	8.4	0.7	
1.83E-03	3.03E-03	6.07E-04	1.36E-03	5.38E-03	5.38E-04	1.70E-03	5.4	1.3	4.9	1.2	
4.40E-04	8.56E-04	1.71E-04	3.83E-04	1.69E-03	1.69E-04	5.34E-04	13.2	1.0	8.9	0.7	1 st Refracture
6.35E-04	1.22E-03	2.43E-04	5.44E-04	2.43E-03	2.43E-04	7.68E-04	11.4	1.2	7.7	0.8	2 nd Refracture
4.16E-04	1.45E-04	7.23E-04	3.24E-04	1.30E-03	1.30E-04	4.11E-04	13.7	1.0	10.5	0.7	
3.32E-04	7.09E-04	1.42E-04	3.17E-04	1.39E-03	1.39E-04	4.40E-04	17.0	1.1	13.2	0.8	Refracture
3.19E-04	6.13E-04	1.23E-04	2.75E-04	1.19E-03	1.19E-04	3.76E-04	12.9	1.1	7.5	0.6	
5.29E-04	9.35E-04	1.87E-04	4.18E-04	1.69E-03	1.69E-04	5.34E-04	11.7	1.0	8.9	0.8	
7.89E-04	1.34E-03	3.10E-04	6.16E-04	2.34E-03	2.34E-04	7.41E-04					
1.81E-04	3.33E-04	6.66E-05	1.49E-04	6.39E-04	6.39E-05	2.02E-04	19.8	1.0	29.5	1.6	
2.96E-05	5.82E-05	1.16E-05	2.60E-05	1.10E-04	1.10E-05	3.48E-05	36.0	1.2	20.3	0.7	
1.59E-04	2.79E-04	5.57E-05	1.25E-04	5.29E-04	5.29E-05	1.67E-04	22.6	1.0	15.3	0.7	
1.23E-04	2.23E-04	4.46E-05	9.99E-05	4.26E-04	4.26E-05	1.35E-04					
3.88E-04	7.14E-04	1.43E-04	3.20E-04	1.37E-03	1.37E-04	4.33E-04	15.7	1.0	16.8	1.0	
2.61E-04	4.80E-04	9.60E-05	2.15E-04	9.23E-04	9.23E-05	2.92E-04	15.7	1.0	12.0	0.8	Refracture
4.06E-04	7.18E-04	1.44E-04	3.22E-04	1.39E-03	1.39E-04	4.40E-04	15.5	1.0	15.8	1.0	Refracture (
3.52E-04	6.37E-04	1.28E-04	2.85E-04	1.23E-03	1.23E-04	3.88E-04					
1.64E-04	3.14E-04	6.28E-05	1.40E-04	6.10E-04	6.10E-05	1.93E-04	25.8	0.9	36.4	1.3	
1.43E-04	2.79E-04	5.57E-05	1.25E-04	5.37E-04	5.37E-05	1.70E-04	29.0	1.0	30.7	1.0	
1.44E-04	2.76E-04	5.52E-05	1.23E-04	5.31E-04	5.31E-05	1.68E-04	30.5	1.1	28.0	1.0	
7.76E-05	1.39E-04	2.79E-05	6.23E-05	2.74E-04	2.74E-05	8.66E-05	32.7	1.1	23.8	0.8	
1.32E-04	2.52E-04	5.04E-05	1.13E-04	4.88E-04	4.88E-05	1.54E-04					
5.57E-05	1.11E-04	2.20E-05	4.94E-05	2.17E-04	2.17E-05	6.86E-05	23.4	0.9	28.4	1.1	Radius Estim
3.70E-05	7.57E-05	1.51E-05	3.38E-05	1.50E-04	1.50E-05	4.74E-05	32.0	1.1	17.4	0.6	Radius Estim
4.64E-05	9.34E-05	1.86E-05	4.16E-05	1.84E-04	1.84E-05	5.80E-05					
2.58E-04	4.41E-04	8.82E-05	1.97E-04	7.75E-04	7.75E-05	2.45E-04	25.1	1.0	23.4	1.0	
8.04E-05	1.50E-04	3.00E-05	6.71E-05	2.62E-04	2.62E-05	8.29E-05	35.0	1.1	28.0	0.8	
1.69E-04	2.96E-04	5.91E-05	1.32E-04	5.19E-04	5.19E-05	1.64E-04					

$\mu = 10 \times K_{\text{vertical}}$		$R_{\text{model-cd}}$	$R_{\text{model-cd}}$	$R_{\text{fwd_mode}}$	$R_{\text{fwd_mode}}$	Remarks
K_{vertical}	$K_{\text{effective}}$	closed form solution (ft) (flownet isotropic)	R_{field} (flownet isotropic)	(ft) (flownet isotropic)	R_{field} R_{field}	
.69E-04	5.34E-04	5.4	1.3	2.5	0.6	
.72E-04	5.44E-04	5.3	1.3	2.6	0.6	1 st Refracture
.99E-04	9.46E-04	4.8	1.2	3.9	0.9	2 nd Refracture
.37E-04	7.49E-04	5.1	1.2	3.3	0.8	3 rd Refracture
.75E-04	5.53E-04	9.4	1.1	5.9	0.7	
.85E-04	9.01E-04	9.3	1.1	7.2	0.8	Refracture
.02E-04	2.22E-03	5.5	1.0	7.1	1.2	
.19E-04	6.93E-04	12.2	1.0	9.4	0.8	
.82E-05	8.92E-05	9.4	1.1	7.2	0.8	
.88E-04	5.95E-04	12.9	1.1	8.4	0.7	
.38E-04	1.70E-03	5.4	1.3	4.9	1.2	
.69E-04	5.34E-04	13.2	1.0	8.9	0.7	1 st Refracture
.43E-04	7.68E-04	11.4	1.2	7.7	0.8	2 nd Refracture
.30E-04	4.11E-04	13.7	1.0	10.5	0.7	
.39E-04	4.40E-04	17.0	1.1	13.2	0.8	Refracture
.19E-04	3.76E-04	12.9	1.1	7.5	0.6	
.69E-04	5.34E-04	11.7	1.0	8.9	0.8	
.34E-04	7.41E-04					
.39E-05	2.02E-04	19.8	1.0	29.5	1.6	
.10E-05	3.48E-05	36.0	1.2	20.3	0.7	
.29E-05	1.67E-04	22.6	1.0	15.3	0.7	
.26E-05	1.35E-04					
.37E-04	4.33E-04	15.7	1.0	16.8	1.0	
.23E-05	2.92E-04	15.7	1.0	12.0	0.8	Refracture
.39E-04	4.40E-04	15.5	1.0	15.8	1.0	Refracture (Directional Nozzle)
.23E-04	3.88E-04					
.10E-05	1.93E-04	25.8	0.9	36.4	1.3	
.37E-05	1.70E-04	29.0	1.0	30.7	1.0	
.31E-05	1.68E-04	30.5	1.1	28.0	1.0	
.74E-05	8.66E-05	32.7	1.1	23.8	0.8	
.88E-05	1.54E-04					
.17E-05	6.86E-05	23.4	0.9	28.4	1.1	Radius Estimated
.50E-05	4.74E-05	32.0	1.1	17.4	0.6	Radius Estimated
.84E-05	5.80E-05					
.75E-05	2.45E-04	25.1	1.0	23.4	1.0	
.62E-05	8.29E-05	35.0	1.1	28.0	0.8	
.19E-05	1.64E-04					

algorithm in a “backward” mode to these two parameters. That is, the observed field radius was used to back calculate modulus and then pneumatic conductivity for a given site. This allowed a comparison of the regressed formation properties with both field measured values as well as those reported in the literature. It is important to note that in actual practice the algorithm will most often be used in a “forward” mode, i.e., input the operational and formation parameters in order to estimate the fracture radius and aperture.

Figure 5.3 illustrates the procedure followed to calibrate the algorithm. First, those parameters which are either reliably known or exhibited low sensitivity were used to determine elastic modulus. This was achieved by a regressional form of equation 3.3 which describes overburden deflection assuming it is a circular plate that is clamped at its edges and subjected to a logarithmically varying load distribution. Solving for elastic modulus, E , based on maximum radius, R , and maximum heave at the well, b_w , the following is obtained:

$$E = \frac{12(1 - \nu^2)p_m \left[\left(\frac{R^4}{64} \right) - \left(\frac{r_w^2 R^2}{32} \right) \right]}{\ln \left(\frac{R}{r_w} \right) b_w z^3} \quad (5.1)$$

Once the modulus was determined, the algorithm was used in a “backward” mode to determine pneumatic conductivity. In this mode it was necessary to use a trial and error procedure until there was agreement between the field measured and calculated values of fracture radius.

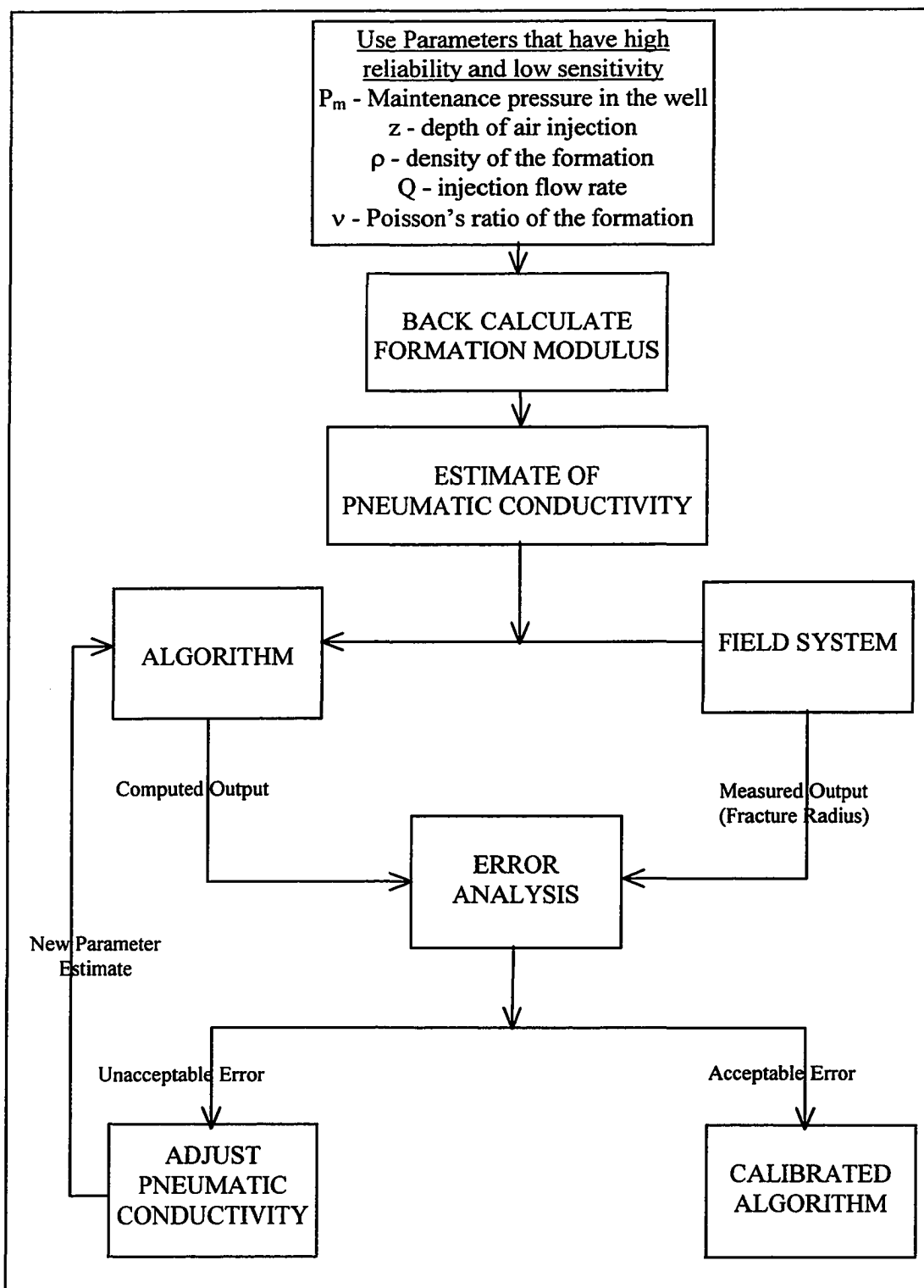


Figure 5.3 Procedure for Calibrating the Fracture Propagation Model

5.3.2 Calibration Results

The first part of the calibration compared the five different methods of leak-off estimation (Chapter 3.4.2). These results are presented in Figures 5.4 and 5.5 for soil and rock formations, respectively. For each site, the maximum, minimum, and average conductivity values are shown for the various methods of leak-off estimation. It can be seen that the variation of regressed conductivity values for a particular site ranged up to approximately one order of magnitude. The minimum variation in conductivity was observed at Newark and was attributed to the fact that fracturing at this site involved only two injections in a single well. Thus, the subsurface conditions were relatively homogeneous leading to a small variation in computed conductivity values. In contrast, the largest variation was observed at the Frelinghuysen site where the injections were carried out in three phases in different wells and at different locations. Thus, the propagating fractures likely encountered different geologic conditions, leading to a wider variation in the conductivity values.

A review of the conductivity values in Figure 5.4 and 5.5 also shows that the flownet method-I of leak-off estimation consistently yielded conductivity values which were lower than the analytical method. This appears to confirm the original hypothesis that the flownet method-I senses greater leak-off at the fracture tip and is therefore more realistic than the analytical method. It is further noted that the conductivity values obtained using the flownet method-II were higher than those obtained by all the other methods. The reason for this lies in the approach taken in deriving the equation, which is more approximate with respect to fracture geometry (Appendix B). Based on these

results it can be concluded that the flownet method-I seems to be the most representative of actual leak-off and is therefore the preferred method of estimation.

Figures 5.4 and 5.5 also compare the effective conductivity values obtained by assuming the formation is anisotropic. Conductivity ratios (K_h/K_v) of five and ten times were investigated, since such variations are typical of those encountered in the field. The plotted results suggest that effective conductivity of the formation increases or decreases by about half an order of magnitude for a conductivity ratio of ten (depending on whether horizontal conductivity is increased by ten times or vertical conductivity is decreased by ten times, respectively).

The most important objective of the calibration process was to compare the back-calculated values of pneumatic conductivity with field measured values. This comparison is presented in Figure 5.6 which juxtaposes the derived conductivity values on the field permeability test results for each site. A majority of the field permeability tests were performed upon the entire well screen with the outlying monitoring well sealed (sealed inlet condition), although selected tests were performed with the outlying monitoring well open (passive inlet condition). Also, some tests were also conducted on a discrete interval of the well with the outlying monitoring wells sealed. For every field test, both pre-fracture and post-fracture permeabilities are shown.

The first significant trend shown in Figure 5.6 is the close agreement between the conductivity values back-calculated by the algorithm and the post-fracture field test results. This is consistent with the fundamental thesis that final equilibrium fracture radius is determined with the geologic formation in a disturbed state. As discussed previously, the primary and secondary fractures caused by pneumatic injection increase

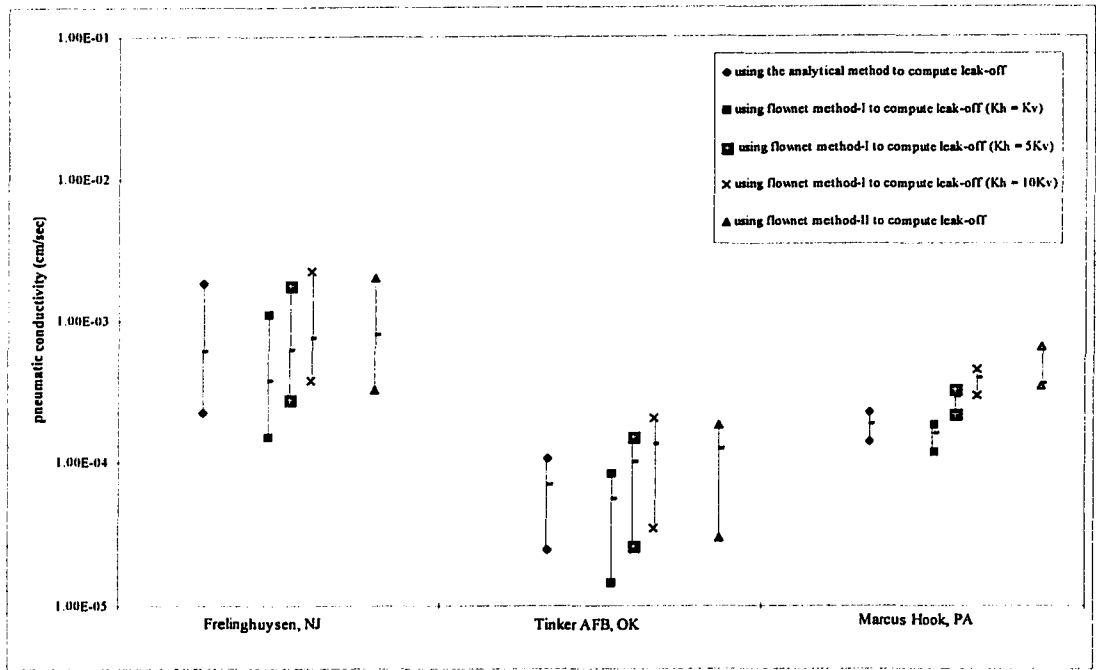


Figure 5.4 Sites Calibrated for Conductivities Using Different Methods of Leak-off Estimation (Soil Formations)

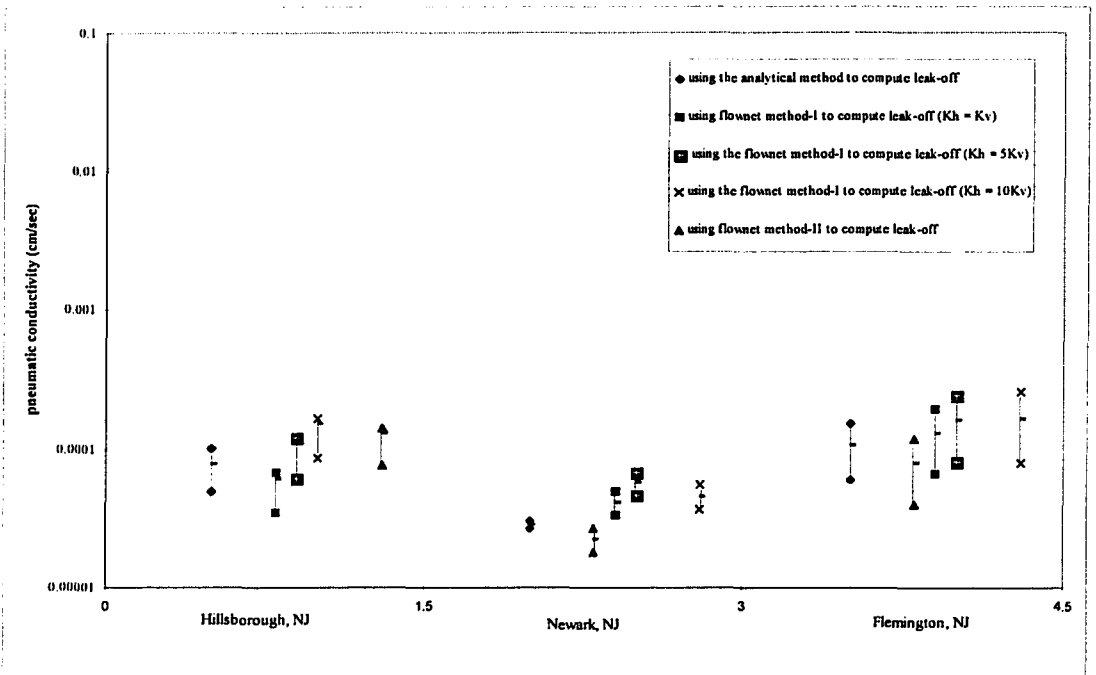


Figure 5.5 Sites Calibrated for Conductivities Using Different Methods of Leak-off Estimation (Rock Formations)

the conductivity of the formation which in turn increases leak-off. It is further observed that at some of the sites the derived conductivity values ranged even higher which probably reflects the dilated state of the formation during the injection event.

As seen in the figure, the calibrated values of conductivity varied within about one order of magnitude irrespective of the geology, thus suggesting that there is an “upper limit” above which conductivity enhancement is not possible with pneumatic fracturing. The existence of an upper limiting conductivity was in fact hypothesized early in the research [Schuring and Chan, 1992], and the results of the current study are consistent with this concept.

The calibration results in Figure 5.6 clearly indicate that it is not appropriate to input into the algorithm values of pneumatic conductivity taken directly from pre-fracture field permeability tests. Rather, the model requires post-fracture values which are typically one to three orders of magnitude higher. Similar caution should be exercised when using conductivity values directly from the literature.

A review of the computed modulus values in Table 5.3 indicate reasonable agreement with literature values, although they tended towards the lower end of published ranges. The probable reason for this deviation is that the modulus values cited in the literature are often “intact moduli,” and do not take into account the effect of secondary structures and discontinuities present in geologic formations. Pneumatic fracture injections flex a large portion of the formation, so the effects of discontinuities become quite significant.

For relatively deep injections, modulus values were sometimes lower compared with shallow injections in the same well. This is attributed to the fact that the vertical

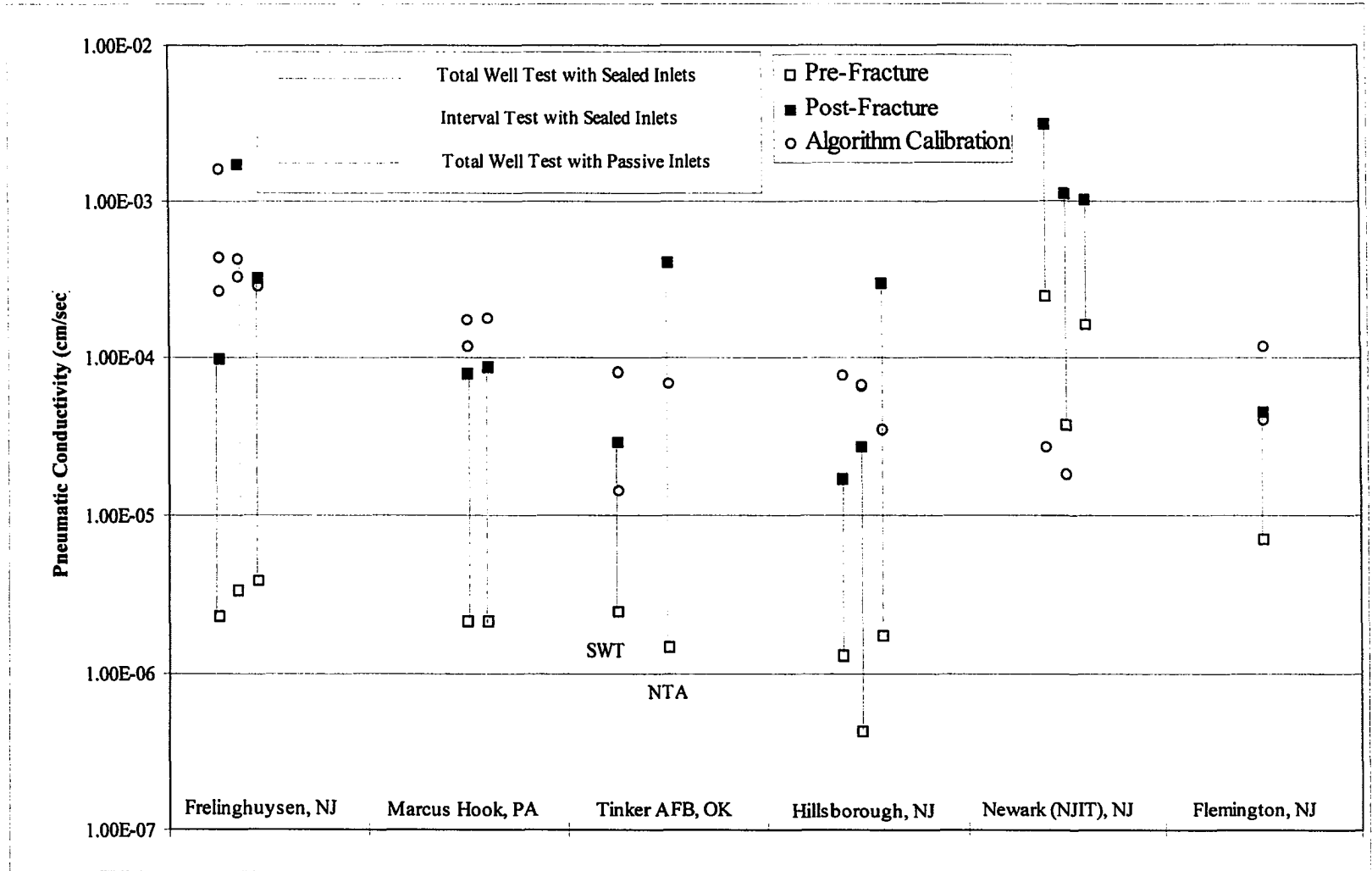


Figure 5.6 Comparing Derived and Field Measured Conductivities

strain of the deeper fractures is masked to some degree by the loosened overburden above. Evidence of strain absorption has in fact been observed during packer permeability testing of fracture wells. Since strain absorption reduces surface heave which translates to an artificially lowered E value, it may be concluded that the model will be most applicable for the first injection in a given well.

5.4 Validation of the Closed Form Solution

The closed form solution presented in Chapter 4.4 was also validated with field data. The solution, expressed as equation 4.17, is solely a function of pneumatic conductivity of the formation. The solution was checked with conductivity values determined during the calibration procedure (Table 5.3).

The results of the validation are presented in Figure 5.7 which shows the ratio of predicted radius to field measured radius for each site. As seen from the plot the agreement is reasonably good for all the sites except Frelinghuysen, where the closed form solution tended to overestimate the fracture dimensions. It is noted that the fracturing depth at this site was relatively shallow which increases the potential for fractures to intersect the ground surface. It is hypothesized that fracture “daylighting” may have reduced the actual fracture radius due to premature gas escape.

In summary, it is believed that the closed form solution will be useful for obtaining rough estimates of fracture radius at sites. Validation will continue as more field data become available.

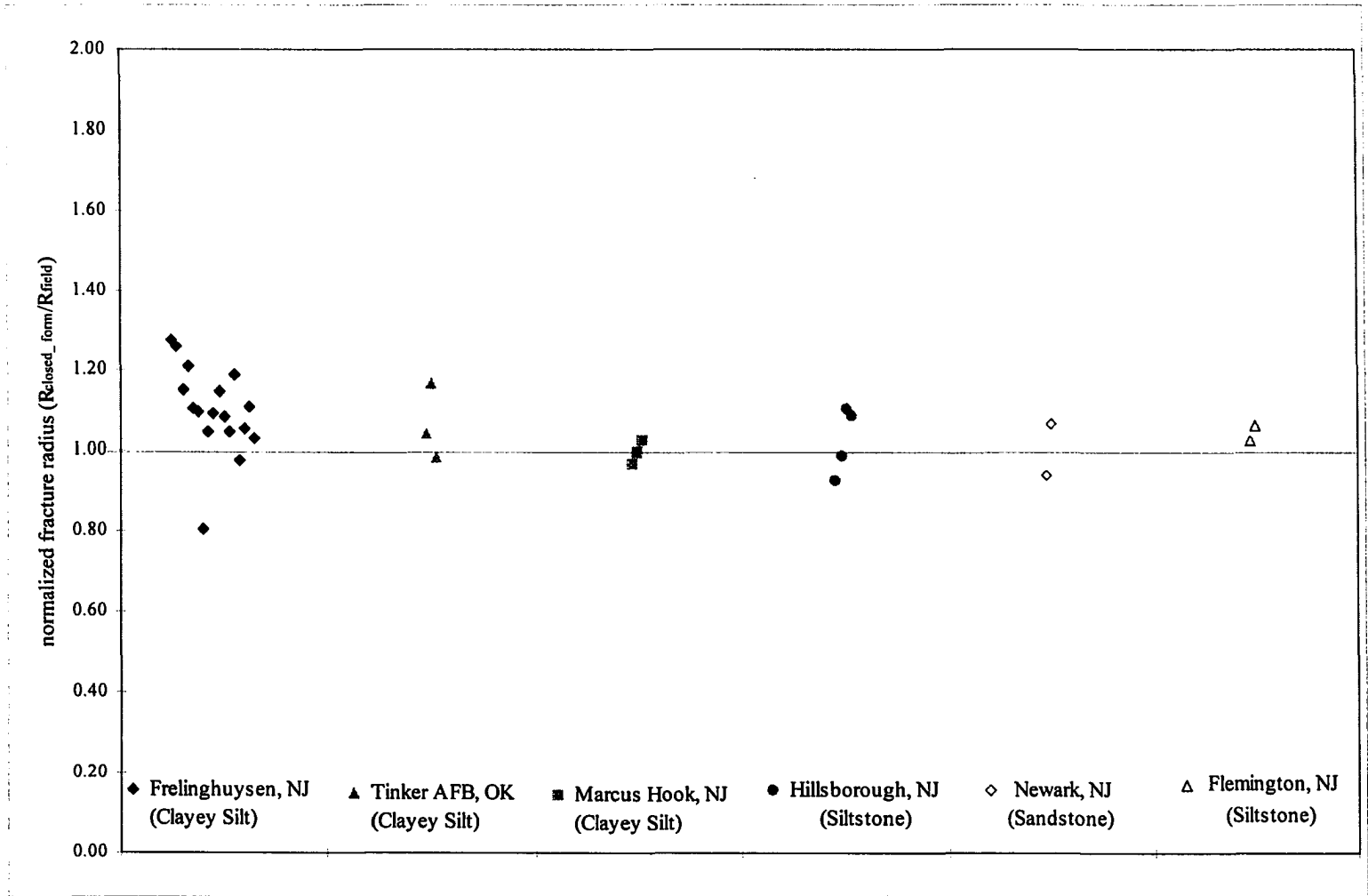


Figure 5.7 Radii Predicted by the Closed Form Solution

5.5 Recommended Parameters for the Algorithm

This section contains guidelines for selecting formation parameters and operational parameters when using the algorithm. Recommended parameter values are summarized in Table 5.4, and are also discussed below. These are considered tentative, and will be refined as more field data becomes available.

The calibration results established that the algorithm is more sensitive to pneumatic conductivity than any other parameter. Therefore, care must be exercised in selecting this parameter. The recommended conductivity values shown in Table 5.4 are based upon regressed values from actual field sites as well as data from other sources. It is noted that if conductivity values are obtained from either pre-fracture field tests or published estimates, the conductivity must be increased by one to three orders of magnitude to reflect the disturbance caused by fracturing.

The values of elasticity moduli in Table 5.4 are also based upon regressed values from actual field sites and as well as data modified from other sources. It is cautioned that if modulus is selected from the literature, *in situ* values are preferred over results from intact laboratory specimens.

The overall behavior of the algorithm has shown that it is relatively insensitive to variations in unit weight and Poisson's ratio. Table 5.4 gives typical ranges for these parameters for various generic geologic descriptions.

The injection flow rate will depend on the injection pressure and the pneumatic conductivity of the formation. A injection flow rate in the range of 500 scfm - 3000 scfm is typically used during field injections. The pressure required to propagate and sustain a fracture is a function of unit weight of the formation and depth of fracturing. The depth

Table 5.4 Algorithm Input Parameters for Soil and Rock Formations (Tentative)

Geology		Pneumatic Conductivity K_{air} SI: (cm/sec)	Young's Modulus E U.S: (psi)	Dry Unit Weight $\gamma_{dmin} - \gamma_{dmax}$ (lb/ft ³)	Poisson's ratio ν
Formation Parameters*					
SOILS:					
Clayey Silt:	Soft to Medium	4.0E-04	100 - 300	95 - 120	0.3 - 0.35
	Medium to Stiff	2.0E-04	300 - 1,000	95 - 120	0.3 - 0.35
	Stiff to Hard	9.0E-05	1,000 - 5,000	95 - 120	0.3 - 0.35
Sandy Clay / Clayey Sand:	Stiff to very Stiff	7.0E-05	4,000	112 - 137	0.3 - 0.4
Silty Sand: (residual soil derived from fine-textured Sandstone)	Extremely Dense (weathered rock)	1.5E-05	40,000	102 - 121	0.2 - 0.4
SEDIMENTARY ROCK :					
Mudstone / Siltstone:	slightly weathered, closely jointed	7.0E-05	5,000 - 10,000	120 - 150	0.1 - 0.15
Fine Sandstone / Coarse Siltstone	unweathered, medium jointed	2.0E-05	20,000 - 30,000	165	0.05 - 0.45
Operational Parameters					
Parameter			Remarks		
Depth of Fracturing			must be accurate to within 0.5 feet		
Injection Pressure			Use Equation 4.16		
Injection Flow rate			1000 - 3000 scfm (typically - 2000 scfm)		

* Values of 'K' and 'E' regressed from actual field data of Pneumatic Fracturing.

† Parameter values obtained from the literature, formation conductivity being corrected for presence of heterogeneities and effects of Pneumatic Fracturing.

** Conversion: $K_{hydraulic} \times \text{cm/sec} = 15.24 \times K_{pneumatic} \times \text{cm/sec} (@ 20 \text{ } ^\circ\text{C or } 68 \text{ } ^\circ\text{F}) = 9.80\text{E}+04 \times k_{intrinsic} \times \text{cm}^2$

of fracturing depends on the distribution of the contamination and the remediation technology being employed. Injection pressure can be estimated using equation 4.9.

5.6 Applications of the Algorithm

It is envisioned that the algorithm will be applied in two different modes. The first is when it is necessary to estimate the dimensions of a pneumatic fracture for preliminary design purposes, i.e. radius and aperture. In this mode the user will input basic geologic data as well as operational parameters. When the algorithm is operated in this fashion, it is referred to as the “forward mode.”

The second mode of application will be as a part of a field pilot test, when actual fracture dimensions have been measured at a particular site for a known set of operational parameters. In this application the algorithm is essentially a calibration tool which will be extended to design production fracturing for the remainder of the site. This is referred to as the “backward mode” of algorithm operation, and is quite similar to the calibration procedure described in the previous section. In the backward mode, the algorithm will yield values of formation modulus and pneumatic conductivity which can then be used to design future fracture injections in the forward mode.

Regarding the expected accuracy of predictions by the algorithm, it is clear that it will be most accurate when used in the backward mode since it will be simulating the behavior of a specific geologic formation. The accuracy in this mode is expected to fall within an accuracy range of $\pm 10\%$. Larger deviations may be expected for sites which have a high degree of heterogeneity.

In the forward mode of application, the algorithm is expected to provide less accurate predictions, due mainly to the difficulty in obtaining reliable values for pneumatic conductivity and elastic modulus for a particular geologic formation. In this mode, the accuracy of the algorithm predictions are expected to decline to an estimated range of $\pm 25\%$. In general, accuracy of the algorithm in the forward mode will be directly related to the accuracy with which the formation properties are known.

To illustrate algorithm usage, an example of both modes of operation will now be presented. In both examples, the following options were selected:

- flownet method-I to estimate leak-off;
- isotropic formation with respect to conductivity; and
- overburden deflection modeled as a circular plate fixed at the edges subjected to a logarithmically varying load.

Figure 5.8 presents the input parameters and resulting output in the “forward mode.” Formation parameters such as E , K , γ , and ν were selected based on recommendations in Section 5.5 (Table 5.4). Alternatively, values can be selected from the literature. When the conductivity values are obtained from the literature they should be adjusted to account for heterogeneities and the effects of pneumatic fracturing. The depth of injection and injection flow rates are selected next. Based on the depth of injection, the injection pressure is calculated using equation 4.8. Once these parameters are entered into the algorithm, the algorithm can be executed to obtain the fracture dimensions.

Figure 5.9 shows an example of the “backward mode” usage of the algorithm. The input data for the “backward mode” should be obtained from a pilot test of

ALGORITHM EXAMPLE IN THE “FORWARD MODE”

Applicability: In the “forward mode” the algorithm is used to predict fracture dimensions (radius and aperture) for a site by inputting geologic and operational parameters. It is useful for preliminary design purposes, and the accuracy of the predictions will largely depend on the accuracy to which the formation properties are known, especially K and E.

Hints for Input:

- Care must be exercised when selecting the values of gas conductivity. The values in Section 5.5 (Table 5.4) are recommended unless post-fracture field permeability test results are available.
- The remaining formation properties should be selected from site characterization results when available. Formation parameters may also be selected from values in section 5.5 (Table 5.4), or alternatively from the literature.
- The traditional range of operational parameters for Pneumatic Fracturing are given in Table 5.4. In lieu of other information, use 2000 scfm for flow rate and the pressure as determined by equation 4.8.

Example Problem *

Input Parameters	
<u>Formation Properties</u>	
E - formation modulus	10,000 psi
K _{gas} - gas conductivity	0.0001 cm/sec
γ - unit weight	105 lb/ft ³
ν - Poisson's ratio	0.4
<u>Operational parameters</u>	
z - depth of gas injection	8 ft.
Q _{in} - injection flow rate	2000 scfm
P _{inj} - injection pressure	31 psi
Output	
b - fracture aperture	0.024 ft
R - fracture radius	23 ft

* Calculations done using the flownet method-I of leak-off estimation for isotropic conditions. The overburden deflection was modeled as a circular plate clamped at the edges and subjected to a logarithmic pressure distribution.

Figure 5.8 Algorithm Example in the “Forward Mode”

ALGORITHM EXAMPLE IN THE “BACKWARD MODE”

Applicability: The “backward mode” of the algorithm is used to support field production operations of Pneumatic Fracturing. The model is calibrated using field test results to determine the actual formation properties. Once calibrated to a site, the algorithm is used in the forward mode to design fracture well spacing and to help predict ground surface heave.

Hints for Input:

- When using equation 3.17 in Step 1, use the maximum heave at the well for fracture aperture, b .
- When back calculating the formation conductivity by trial and error (Figure 5.3), start with a conductivity value selected from Section 5.5 (Table 5.4).
- Optional parameters in Step 3 are varied to attain a desired radius.
- The traditional range of operational parameters for Pneumatic Fracturing are given in Table 5.4. In lieu of other information, use 2000 scfm for flow rate and the pressure as determined by equation 4.8.

Example Problem *

Step 1: Back calculate E by substituting the aperture ‘ b ’ and fracture radius ‘ R ’ in equation 3.17.

Step 2: Use back calculated E along with the algorithm to find K_{gas} .

Input Parameters	
E	2000 psi
Q_{in}	1200 scfm
P_{inj}	12 psi
z	6 ft
γ	105 lb/ft ³
ν	0.4
R	16 ft
Output	
K_{gas}	2.9×10^{-4} cm/sec

Step 3: Use back calculated E and K_{gas} along with the algorithm in the “forward mode” to predict fracture dimensions for new injections.

Input Parameters	
E	1800 psi
	← variable
	← variable
	← variable
γ	105 lb/ft ³
ν	0.4
K_{gas}	2.9×10^{-4} cm/sec
Output	
R	17.2 ft

* Calculations done using the flownet method-I of leak-off estimation for isotropic conditions. The overburden deflection was modeled as a circular plate clamped at the edges and subjected to a logarithmic pressure distribution.

Figure 5.9 Algorithm Example in the “Backward Mode”

pneumatic fracturing at a site. All the input parameters except formation modulus and conductivity are generally known or can be estimated fairly accurately. The formation modulus is back calculated first using the surface heave data and equation 3.17. Next, the formation conductivity is obtained in a manner similar to the calibration procedure previously described in Section 5.3. At this point all parameters are known and can be used to run the algorithm in the “forward mode,” to design other injections at the site (see Figure 5.8). It is noted that the conductivity value obtained in Step 2 becomes a constant input parameter, while the injection pressure, injection flow rate, and depth of fracturing are varied to obtain the desired fracture radius and injection well spacing.

CHAPTER 6

A METHODOLOGY TO MODEL PARTICULATE TRANSPORT

6.1 Overview

A secondary objective of the study was to develop a methodology for analyzing transport of dry particulate media in pneumatic fractures. Such media are introduced after a pneumatic fracture has been propagated, and can supplement a variety of *in situ* processes such as bioremediation and reactive dechlorination, as well as serving as a fracture proppant. The three fundamental mechanisms of particulate transport in the geologic formations during pneumatic fracture injections are interstitial transport, transport within a discrete fracture and transport in a fluidized lens (Figure 2.4), and these have been previously discussed in Section 2.2.1.

From the perspective of field operations, interstitial transport is not expected to be an important mechanism for introducing media into pneumatic fractures since the mean diameter of the injected particles is typically larger than the effective pore spaces of the geologic formation. Interstitial transport may be an important secondary transport mechanism, however, as the injected media penetrates and/or cakes on the surface boundaries of the fracture. Under these conditions, it can have a significant effect on gas leak-off into the formation, and therefore can affect both particle transport and fracture propagation.

The mechanics of the second fundamental mechanism, particulate transport in a discrete fracture, has been studied by investigators in the field of hydraulic fracturing. These studies have focused on proppant transport by both liquids and gases, and a

moderate amount of guidance is available in the literature for modeling this mode of transport (see Section 2.2.4).

It was decided to focus the current study on the third mechanism, transport within a fluidized lens, since this has received the least attention in past investigations. The importance and relevance of this transport mechanism was confirmed by exploratory excavations made at two sites where solid media were pneumatically injected. The first project was at the Hanford site and involved injections of graphite/glass frit to enhance *in situ* vitrification. The second project was performed in Kansas City and consisted of injecting iron powder into an aquifer for the purposes of reactive dechlorination. At both of these sites the excavations showed that fluidization of cohesionless sands present was the principal transport mechanism.

6.2 Outline of a Methodology for Modeling Particulate Transport in a Fluidized Soil Formation

The methodology for modeling particulate transport through fluidized soil (Figure 2.4b) is based upon the following assumptions with regard to the properties of the formation and the injected media:

- i) the formation is cohesionless;
- ii) the density of the formation is less than the maximum density for the soil medium;
- iii) the injected gas pressures exceed the *in situ* stresses of the formation;
- iv) the formation surrounding the fluidized zone experiences a minimal amount of dilation and deformation;

- v) the particles carried in the injection air stream are in a dilute suspension;
- vi) the pore fluid velocities exceed the critical entrainment velocity for the media particles being transported in the formation; and
- vii) the particles are not transported beyond the zone of fluidization.

Based on these assumptions, a general methodology for modeling this transport phenomena will now be outlined:

Determination of Pressure Distribution in the Formation

The first step in modeling particulate transport through a fluidized bed of soil is to determine the pressure distribution in the formation during the injection event. The approach for determining the pressure regime has been adopted from a model developed for soil-vapor extraction by Shan *et al* [1992]. The continuity equation for gas flow in a homogenous, isotropic soil formation is given by:

$$\frac{\phi\mu}{p} \frac{\partial p^2}{\partial t} = \nabla \cdot (\tilde{k} \nabla p^2) \quad (6.1)$$

where ϕ is the gas-filled porosity, p is the gas pressure in the formation and \tilde{k} is the permeability tensor. For steady state conditions, the above equation reduces to:

$$\nabla \cdot (\tilde{k} \nabla p^2) = 0 \quad (6.2)$$

This equation can be solved to obtain the pressure distribution around the injection well.

Equation 6.2 can be written in terms of the variable 'u' defined as

$$u = p_a^2 - p^2 \quad (6.3)$$

$$\nabla \cdot (\tilde{k} \nabla u) = 0 \quad (6.4)$$

When the above relation is solved for the case of a point source in an infinite anisotropic medium [Shan *et al*, 1992], the following equation is obtained:

$$u = \frac{-q}{4\pi\alpha_r [\bar{r}^2 + (z - z')^2]^{1/2}} \quad (6.5)$$

$$\text{where } q = \frac{2p_a RTM}{\phi M_{wt}}, \quad \alpha_r = \frac{k_r p_a}{\phi \mu}, \quad \bar{r} = \left(\frac{k_z}{k_r} \right)^{1/2} r,$$

q is the source strength located at a radial distance $r = 0$ and depth $z = z'$, M is the mass removal rate, M_{wt} is the average gas molecular weight, p_a is the ambient air pressure, R is the universal gas constant, T is the temperature in degrees Rankine. Substituting equation 6.5 in 6.3 results in:

$$p = \sqrt{p_a^2 - \frac{-q}{4\pi\alpha_r [\bar{r}^2 + (z - z')^2]^{1/2}}} \quad (6.6)$$

which gives the pressure distribution around the well at steady state conditions for a gas injection.

Determination of Gas Velocities

Once the pressure distribution in the formation has been established, the pore fluid velocities may be calculated by applying Darcy's law :

$$v_x = Ki_x = K \frac{\Delta p_x}{l_x} \quad (6.7)$$

$$v_y = Ki_y = K \frac{\Delta p_y}{l_y} \quad (6.8)$$

$$v = \sqrt{v_x^2 + v_y^2} \quad (6.9)$$

where v_x and v_y are the components of the air velocities in x and y directions, respectively, V is the resultant velocity, Δp_x and Δp_y are the differences in pore pressures of two points located along the direction of the reference axes and separated by distances l_x and l_y respectively.

Criteria for Fluidization and Entrainment

In order for the soil to become fluidized, fluid velocities be high enough to overcome the weight of the soil particles. The 'Shield's' criteria for entrainment of particles which are at rest, into a moving fluid, will be used to calculate the critical velocities for the soil

fluidization. The Shield's method is also known as the shearing force method, or the tractive force method, is an approach for describing the initiation of sediment motion. He stated that the critical condition for sediment motion is a function of the Reynolds number and developed a diagram to determine whether or not initiation of particle movement has occurred.

The Shield's method requires determination of the dimensionless shear stress, τ^* and the dimensionless grain Reynold's number, R_{eg} at different velocities of air through the soil. These values are then plotted on the Shield's diagram, the air velocity corresponding to the intersection of the plotted curve and the Shield's curve is the critical entrainment velocity for the given conditions. The dimensionless shear stress is given by:

$$\tau^* = \frac{\tau_0}{(\gamma_p - \gamma_{air})d_p} \quad (6.10)$$

where τ_0 , is the boundary shear stress, γ_p is the specific weight of the particles, γ_{air} is the specific weight of air and d_p is the diameter of the particles. The grain Reynold's number is given by:

$$R_{eg} = \frac{U^* d_p}{\nu_{air}} \quad (6.11)$$

where U^* is the friction velocity of the fluid, defined as

$$U^* = \sqrt{\frac{\tau_0}{\rho_{\text{air}}}} \quad (6.12)$$

The boundary shear stress term occurring in the above equations is defined as

$$\tau_0 = \mu_{\text{air}} \frac{dV_{\text{air}}}{dy} \quad (6.13)$$

where μ_{air} is the dynamic viscosity of air and V_{air} is the velocity of air in the soil.

Separating the variables, integrating and applying the limits

$$\begin{aligned} \text{at } y=0 & \quad V_{\text{air}} = 0 \\ y = d_{\text{pore}}/2 & \quad V_{\text{air}} = V \end{aligned} \quad (6.14)$$

$$\int_0^{b/2} \tau_0 dy = \int_0^V \mu dV \quad (6.15)$$

where d_{pore} is the diameter of the soil pores through which air is flowing. The above equation reduces to:

$$\tau_0 = \frac{2\mu V}{d_{\text{pore}}} \quad (6.16)$$

The boundary shear stress τ_0 can now be substituted in equation 6.12 to determine the friction velocity of the fluid, which in turn is used in equation 6.11 to find out the grain

Reynolds number R_{eg} . The value of the boundary shear stress is also used in equation 6.10 to determine the boundary shear stress τ^* . As described previously the grain Reynolds number and the boundary shear stress can now be plotted on the Shield's diagram to find the critical entrainment velocity.

The most critical input parameters when applying the methodology are the formation porosity, mean pore diameter, anisotropy of formation conductivity and the grain size of the injected supplements for which the critical entrainment velocities are computed. These parameters generally vary over a range and the selection of a particular value critically influences the predictions of the extent of particulate transport within the formation.

6.3 Application of the Particulate Transport Methodology - A Case Study

The particulate transport methodology outlined in the previous section was used to analyze field data collected at a recent project at the Hanford Site as a first test of the concept. The Hanford site seemed ideal since field observations confirmed that the primary transport mechanism was by fluidization of the formation. Interstitial transport of the injected particles beyond the zone of fluidization was minimal as indicated by the tests in the laboratory. The sections to follow present the site background, the general results of the field demonstration and finally the calculated results with the proposed methodology.

6.3.1 Hanford Site Background

The Hanford Site located in Richland, WA was the former production facility of Plutonium for fission based atomic weapons throughout World War II and the Cold War. During operation of these facilities by the Department of Energy (DOE) large amounts of liquid radioactive waste was generated which subsequently contaminated the soil and groundwater beneath portions of the Hanford Site.

In situ Vitrification (ISV) was developed by the DOE initially to treat soil contaminated with radioactive wastes like those occurring at the Hanford Site. More recently, it has been used to treat other difficult mixed wastes like those occurring in industrial landfills. ISV is a thermal treatment process that converts contaminated soil to a chemically inert substance that is physically and compositionally close to Obsidian. The process utilizes “Joule” resistance heating of the soil between two electrodes connected to a power source. A conductive starter path of graphite and glass-frit must be placed between the electrodes to initiate the melt due to the low conductance of the natural soil. The ISV process has a limitation with respect to the depth to which it can vitrify soil. The maximum effective depth varies from 5 to 6 meters at present.

The purpose of integrating pneumatic fracturing with ISV is to overcome this depth limitation. With pneumatic fracturing, the starter path can be placed at any selected depth which greatly improves the versatility of ISV. The first field demonstration of pneumatic fracturing integrated with ISV was performed at the Hanford Site. Figure 6.1 is a conceptual schematic of pneumatic fracturing integrated with ISV.

The Hanford Site is underlain by coarse gravel sediments of Pleistocene age deposited by the cataclysmic Missoula floods. The Hanford formation extends to an

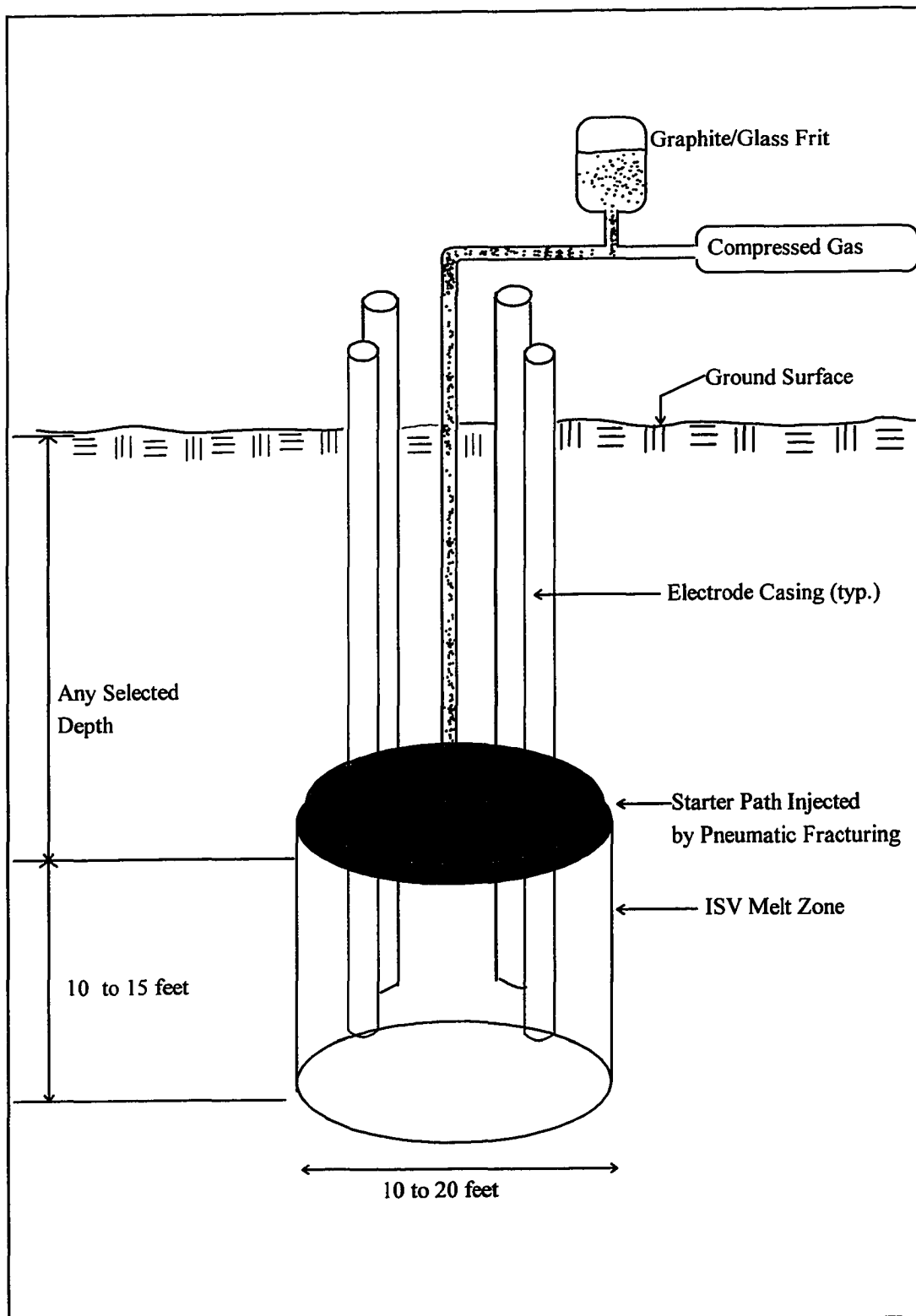


Figure 6.1 Conceptual Diagram of Integrated PF/ISV Process

average depth of 40-50 ft and consists of predominantly sand with some gravel and occasional cobbles. On account of the rapid deposition and relatively young geologic age of the formation, the hydraulic conductivity of the Hanford formation is very high (1,000 - 10,000 ft/day) and it has a low bulk density (100 lb/ft³). The depth to the water table at the location of the pilot scale test was 33-49 ft below the ground surface. A summary of the soil index properties of the Hanford soils is presented in Table 6.1.

Table 6.1 Summary of Soil Index Properties-Hanford Soils

Index Property	Results	Remarks
Moisture	1 wt%-5 wt%	Bjornstad(1994)
Bulk Density	103 lb/ft ³	Last and Rohay(1993)
Hydraulic Conductivity	1,000-10,000 ft/day	
Liquid and Plastic Limits	Non-plastic	ASTM D 2217-85 ASTM D 4318-84
Organic Content	0.12 wt%	ASTM D 854-92
Specific Gravity	2.82	ASTM D 854-92
USCS Classification	GP	ASTM D 2487-93
Color	Batch 1--10YR 5/6: Yellowish Brown Batch 2--10YR 4/2: Dark Grayish Brown	Munsell® Soil Color Charts (air dry soil)

Two different injection nozzle configurations were evaluated to inject the starter path with pneumatic fracturing and are henceforth referred to as the '360 Nozzle' and 'Quad Nozzle' reflecting the geometry of the injections. These two configurations were tested at different locations on the site, and were removed far enough from each other to discount any interference between each other. Four electrodes were placed inside wells

around each of the injection nozzles, extending to the depth of the injection nozzle. At each of the locations the injection nozzle was at the center of a square with the four electrodes as its vertices. The distance between any two electrodes (discounting the diagonal distances), was one meter. An array of monitoring points were located in the vicinity of the injections to measure any variations in resistance and ambient temperatures of the soil.

The injections of the starter path material were carried out at a depth of 14 ft. During injection, air pressure at the well head, injection air flow rate, mass flow rate of the graphite/glass-frit powder and resistance variations within the subsurface were monitored. The site was subsequently excavated and the extent and thickness of the starter paths around the injection wells were mapped.

6.3.2 Results

Following the injection of the starter path, electrical resistance was measured between the electrode casings and the outlying instrument conduits. The resistance results, which are shown in Figure 6.2, showed that the injections were effective since the resistance of the path between the electrodes was reduced from > 500,000 ohms (natural soil resistance) to 50-104 ohms, thus satisfying the criteria for initiating a successful melt. An initial attempt was made to vitrify the soil, but was unsuccessful. The failure was attributed to insufficient power and the poor contact between the electrodes and injected starter path [Luey *et al.*, 1995b]. It was therefore decided to excavate both settings to delineate and map the starter path.

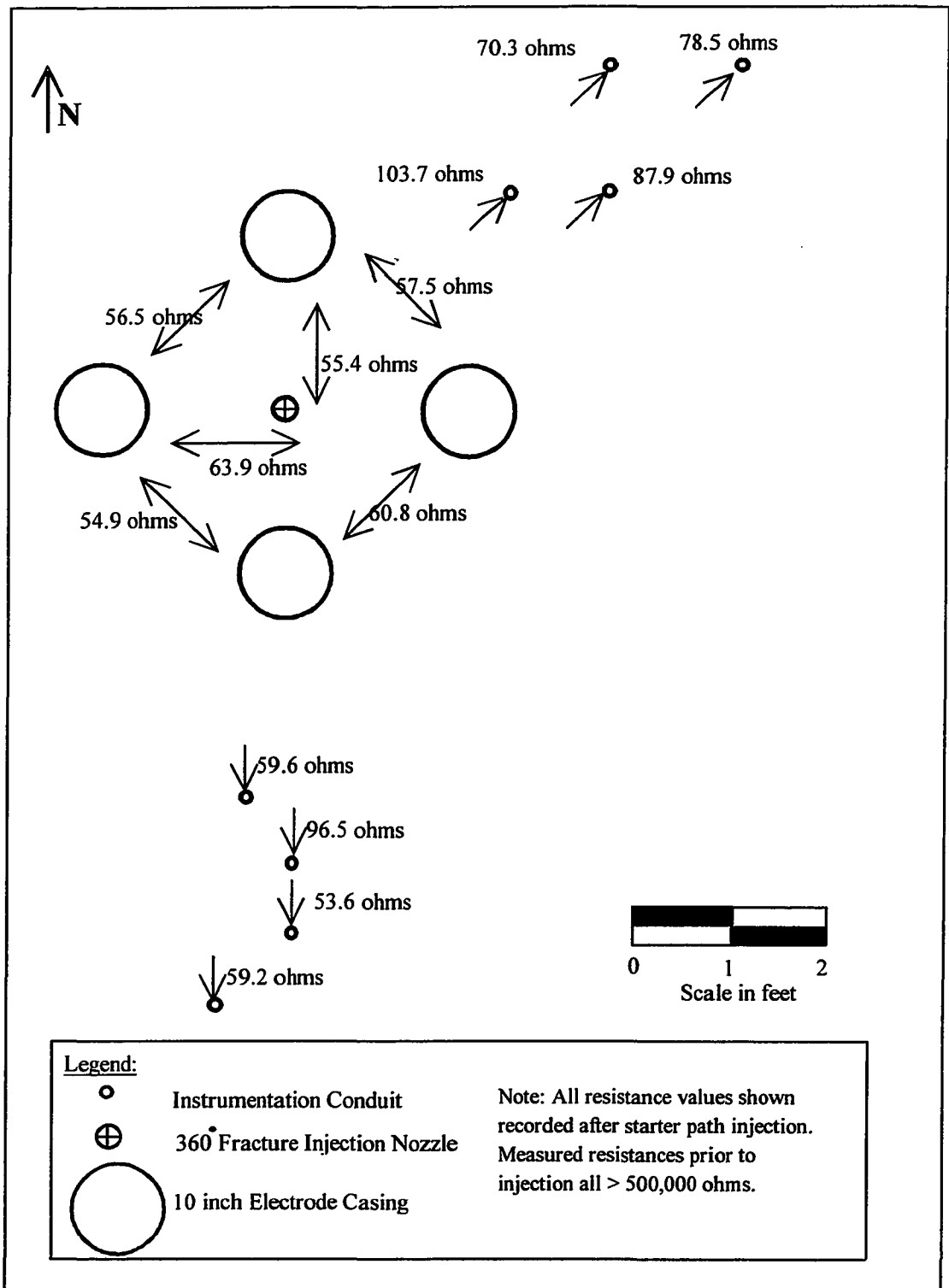


Figure 6.2 Resistance Measurements - 360° Nozzle

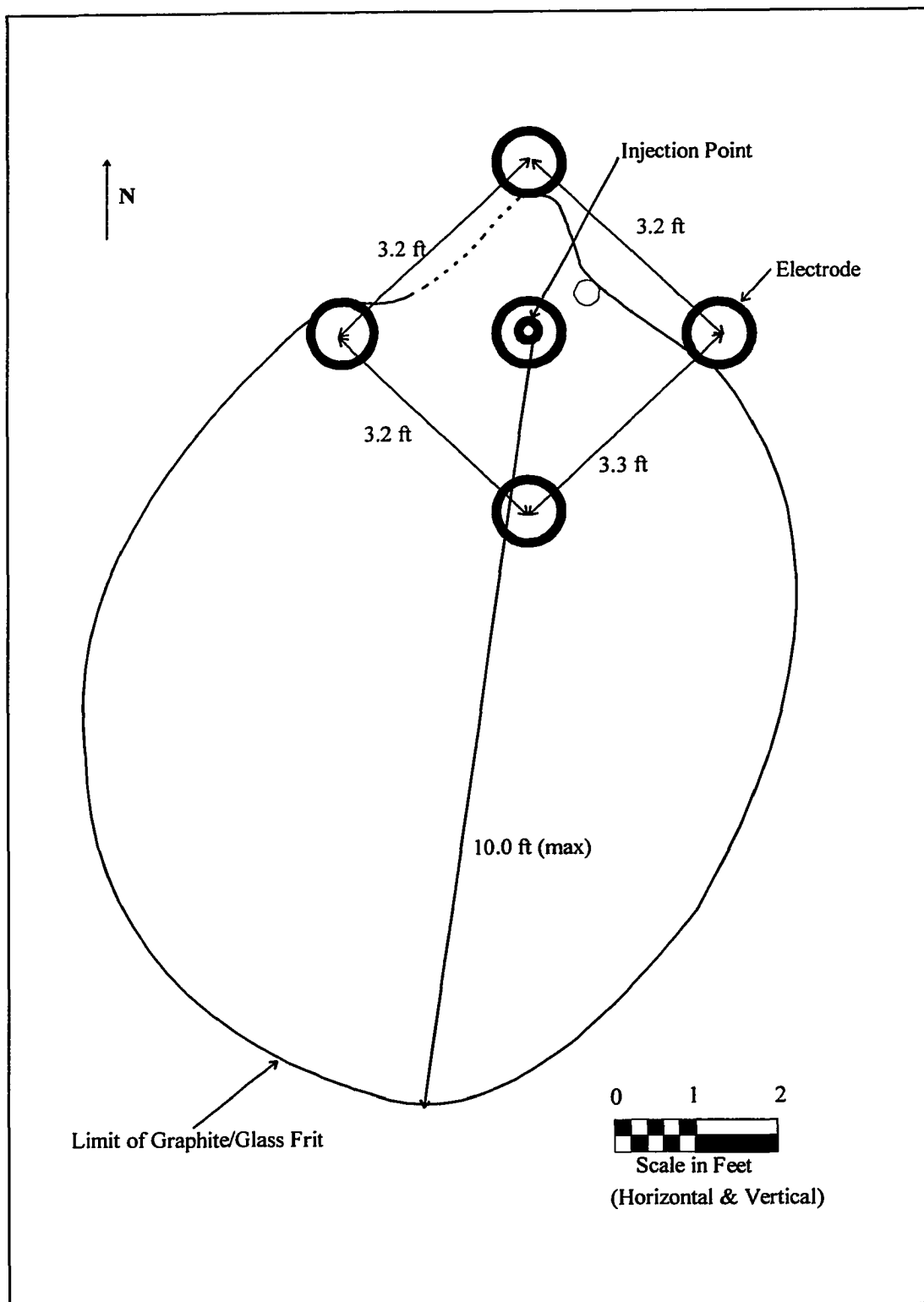


Figure 6.3 Extent of the Graphite Lens - 360° Nozzle Setting

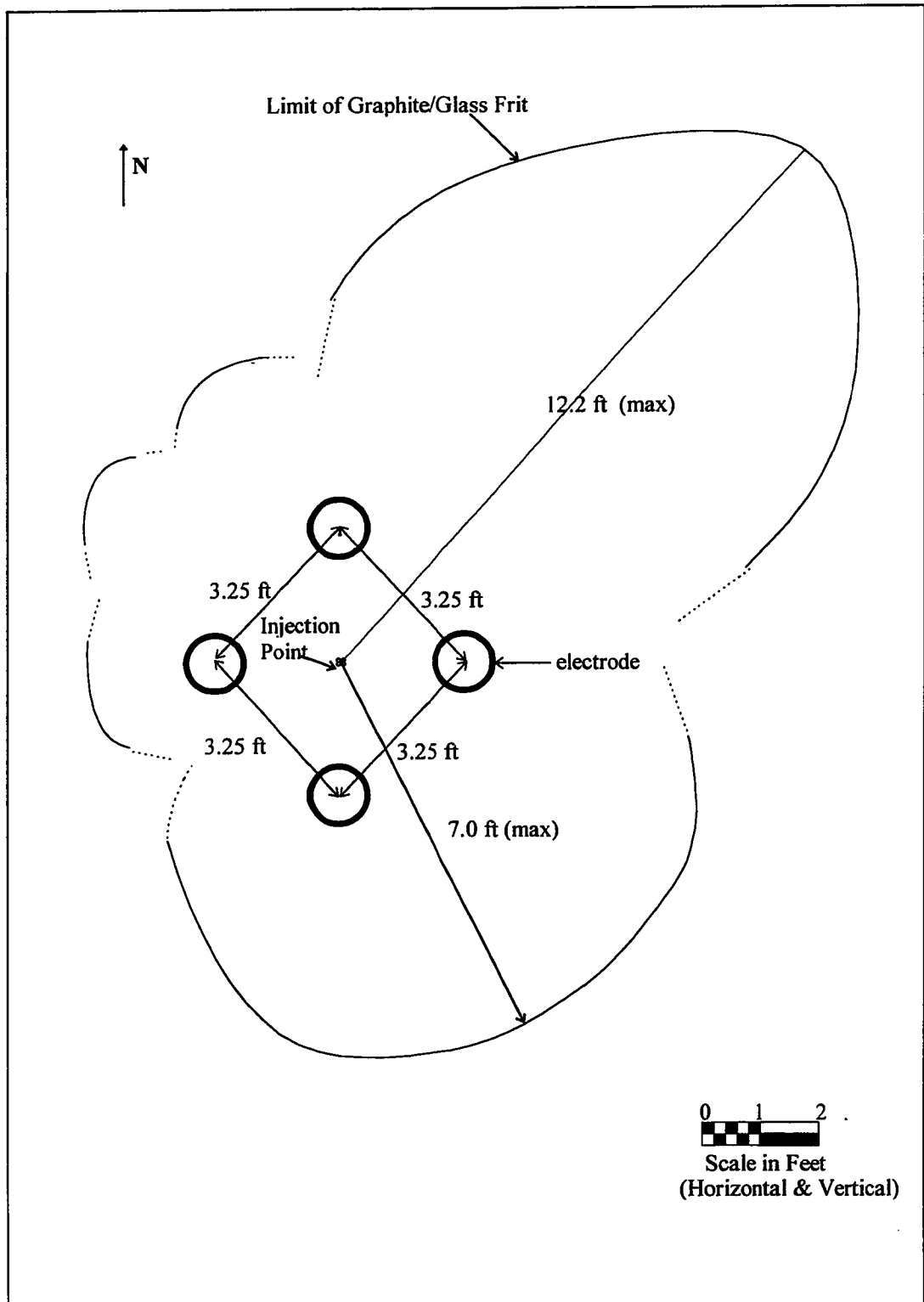


Figure 6.4 Extent of the Graphite Lens - Quad Nozzle Setting

The results of the excavations are shown in Figure 6.3 and 6.4 which depicts the extent and the orientation of the injected graphite/glass frit mixture. In both the settings, a lens of well mixed soil/starter path material (graphite/glass-frit) was observed suggesting that a local fluidization of soil occurred during injection.

A review of Figures 6.3 and 6.4 reveals that the maximum distance traveled by the injected particles was greater for the quad nozzle setting (12 ft) compared with the 360° nozzle setting (10 ft). This was attributed to the flow concentration into a 90° sector at the well instead of a 360° sweep for the other setting. The preferential southerly orientation of the 360° nozzle setting was due to obstructions (instrument probe and lost tool inside the well) on the north side of the injection well.

Subsequently, a second attempt to initiate the melt was made after backfilling the site. The melt was successfully initiated and sustained for a nine hour duration. Subsequent excavation revealed a coherent vitrified soil mass weighing two tons. A significant result of the test was the power requirement of 0.7 kW/kg, which was 30% less than that required for surface melts. This was attributed to the insulating effect of the surrounding soil. Since the power represents a significant portion of the cost of ISV technology, it appears that subsurface initiation may have cost advantages over surface initiated melts.

6.3.3 Computational Results

This section describes the application of the methodology developed in Section 4.2. The general approach was to calculate the critical fluidization velocities, estimate the extent of

fluidization and then compare the calculated results with the field observations made during the Hanford Site test.

The calculations were performed in Mathcad 6.0 and are contained in Appendix F. The input parameters were based on a combination of field measurements during previous site investigations and values extracted from the literature. The results of the computations using the proposed methodology are summarized in Table 6.2 which compares the predicted and measured values of the fluidized lens. It is noted that, for the quad-nozzle setting, since the flow was concentrated in a 90° sector, the flow values used in the calculations have been increased four fold. As seen in the table some nozzle settings show relatively good agreement between the measured and predicted extent of fluidization, while others vary by as much as a factor of two. The computational results are of course greatly influenced by certain formation parameters which were estimated and vary over a range. Nevertheless, the results in Table 6.2 are encouraging and the general modeling approach of the methodology seems to have some merit. Continued development of the general approach is recommended, and calibration with new field data as it becomes available should be accomplished.

Table 6.2 Calculated and Measured Values of Extent of Fluidization

Nozzle Setting	Measured Extent of Fluidization	Calculated Extent of Fluidization	
		$K_h/K_v = 10$	$K_h/K_v = 100$
360°	10 feet	4.5 feet	10.5 feet
quad - North	12.2 feet	7 feet	22 feet
quad - South	7 feet	7 feet	21 feet
quad - East	5 feet	8 feet	24 feet

CHAPTER 7

CONCLUSIONS AND RECOMMENDATIONS

7.1 Conclusions

Pneumatic fracturing is an *in situ* technology that can enhance the permeability of geologic formations by creating an artificial network of fractures. Although the principal application is to increase permeability, the process can also deliver gaseous, liquid, and granular supplements into the subsurface. In order to improve the understanding of the pneumatic fracturing process and broaden its engineering applications, a number of fundamental questions are under study.

The current study has focused on the mechanism and propagation of pneumatic fractures in geologic formations. Prediction of the geometry and extent of propagating fractures is important in the design of pneumatic fracturing projects. While some limited analyses of pneumatic fracture propagation had been previously reported in the literature, a constitutive, theoretically-based model was not available. Therefore, the overall objective of this study was to develop a pneumatic fracture propagation model and validate it with field data.

The following has been concluded from the current study:

1. Pneumatic fracture propagation differs from other fracturing phenomena in geologic formations with respect to rheology of the fracturing fluid and rate of pressurization. This gives rise to some peculiarities that are characteristic of pneumatic fracture propagation, including a high rate of gas leak-off owing to the low viscosity of the

fracturing fluid ($1.9\text{E-}05$ Pa.sec), and an intermediary propagation velocity (~ 3 m/sec).

2. A basic set of model assumptions were established to reflect as closely as possible the physical phenomenon of pneumatic fracturing. First, the formation was assumed to be homogenous with regard to composition and anisotropic with respect to pneumatic conductivity. Also, since most geologic formations are overconsolidated with respect to geostatic stress, the pneumatic fractures were assumed to propagate radially in a horizontal direction. Leak-off of gas from a fracture into the surrounding geologic formation was assumed to be Darcian and gradient driven. Finally, owing to the intermediate propagation velocity, the overall phenomena was categorized as quasi-static.
3. There are two fundamental criteria for the propagation of a pneumatic fracture. First, the injected flow rate must exceed the rate of gas leak-off into the formation (continuity criterion). Second, the pressure at the fracture tip must be greater than the minimum propagation pressure (stress equilibrium criterion). The “equilibrium radius” for a pneumatic fracture is achieved when these two propagation criteria are simultaneously satisfied, i.e. injected flow equals leak-off and fracture tip pressure equals propagation pressure.
4. The propagation model was formulated by mathematically expressing the three physical processes controlling fracture propagation: i) pressure loss due to frictional wall effects and the resulting pressure distribution within the fracture; ii) the leak-off

distribution from the fracture; and iii) the deflection of the overburden which creates the fracture aperture.

Pressure loss within the fracture was modeled as Poiseuille flow between two radial, parallel plates taking into account the compressibility effects of the injected gas. The rate of pressure dissipation within the fracture was influenced significantly by the fracture aperture, as pressure drop is inversely proportional to the cube of the aperture.

Leak-off had a significant influence on fracture propagation owing to the low viscosity of gases used in pneumatic fracturing. It varied with radial distance from the injection well, and also between the top and the bottom fracture faces. This is due to the decreasing pressure, varying gradient along the fracture length and anisotropy of the formation. Different methods of leak-off estimation were developed using both potential theory (flownets) and analytical approaches, all of which were based on Darcy's law.

Deflection of the overburden, which is the last of the three processes controlling fracture propagation, was modeled as the bending of a circular elastic plate clamped at the edges. A logarithmic pressure distribution was assumed for overburden loading which approximates the actual cubic pressure distribution.

5. A numerical solution for fracture propagation problem was developed which couples processes of pressure dissipation, leak-off and overburden deflection, and then solves them to obtain the dimensions of the fracture. The solution (developed algorithm) is based on the presumption that for a given set of injection and formation parameters,

there exists a unique fracture radius that satisfies the continuity and stress equilibrium criteria at the tip of the fracture simultaneously.

6. The algorithm requires an input of geologic and operational parameters and is structured in two loops. The outer loop varies the fracture dimensions until they satisfy the continuity and stress equilibrium criteria at the fracture tip. The inner loop discretizes the extent of the fracture into small segments, and analyzes each segment to determine size of the fracture aperture, pressure drop and fluid losses into the formation. Pressure and flow at the end of the current segment are used as the input for the next segment, and the inner loop is exited when the criteria for the termination of a propagating fracture are met.
7. Three different methods of converging to the solution, i.e. “the equilibrium fracture radius,” were examined. The first two methods start with a grossly underestimated or overestimated radius which is incremented or decremented, respectively, until the pressure and the continuity conditions are satisfied simultaneously at the fracture tip. The third method is the Bisection Method which converges to the solution by halving the interval bounding the solution and then retaining the half that contains the solution. The process is repeated to converge to the solution. The Bisection Method proved to be more efficient than the aforementioned methods.
8. The algorithm was validated and calibrated with field data from actual pneumatic fracturing sites. Data from 35 different sites were evaluated and six sites were selected for calibration purposes. The first part of the validation procedure examined

the sensitivity of the algorithm to the various input parameters. Also, the algorithm was calibrated with respect to pneumatic conductivity and elastic modulus of the formation, since these two parameters are among the more difficult to determine in the field. This allowed a comparison of the regressed formation properties with both field measured values, as well as those reported in the literature.

9. The sensitivity analysis showed that the most critical input parameter was the pneumatic conductivity of the formation. There was also a low to moderate algorithm sensitivity to formation modulus if the entire range of parameter variation was considered. If the field errors that occur during parameter determination are considered, then the relative importance of the parameters in decreasing order are injection pressure, fracturing depth, injection flow rate, unit weight of the formation, formation modulus, and Poisson's ratio.
10. The most important result of the calibration process was the close agreement between the conductivity values back-calculated with the algorithm and the post-fracture field conductivities. This is consistent with the fundamental thesis that the final equilibrium fracture radius is determined with the geologic formation in a disturbed state. In other words, the primary and secondary fractures caused by the pneumatic injection increase the conductivity of the formation which in turn increases leak-off.
11. A comparison of the different methods of leak-off estimation showed that the flownet method-I of leak-off estimation consistently yielded lower conductivity values than the other methods. This appears to confirm the original hypothesis that the flownet

method-I senses greater leak-off at the fracture tip, and is therefore the preferred method of estimation.

12. The results of the calibration emphasize the sensitivity of the algorithm to conductivity, and care must be exercised in selecting this parameter. The calibration results also indicate that it is not appropriate to input values of pneumatic conductivity into the algorithm which are taken directly from pre-fracture field permeability tests. The model requires post-fracture values which are typically one to three orders of magnitude higher. Similar caution should be exercised when using conductivity values directly from the literature.
13. A closed form solution to predict the extent of fracture propagation was developed based solely on the principle of fluid continuity. The closed form solution appears useful for obtaining rough estimates of fracture radius at sites, as well as for checking the algorithm. The solution demonstrated reasonable correlation with field measured radii.
14. Three possible mechanisms of dry particulate transport during pneumatic injections were identified including i) interstitial transport, ii) transport with an open discrete fracture; and iii) transport in a discrete fluidized lens. A methodology was proposed to predict the transport radius of the injected particulate media within the fluidized zone.
15. The developed methodology for particulate transport was applied to field data from a recent project at the Hanford Site involving injection of powdered graphite in support

of the *in situ* vitrification (ISV) process. Methodology predictions in general compared well with the field measurements, though this involved a critical judgement of some input parameters with respect to the formation properties.

7.2 Recommendations

Algorithm Proofing: The algorithm should be used in support of actual field operations for pneumatic fracturing so that predictions can be compared with field measurements of the fracture dimensions. Field data can also be used to calibrate the algorithm with respect to formation conductivity and modulus. Every opportunity should be taken to calibrate the model for new and different geologic formations.

Algorithm Refinement: The algorithm developed in this study can be further refined by implementing the following suggestions:

- The propagation model developed in this study predicts the “equilibrium fracture dimensions” and is not capable of predicting the variation in fracture dimensions with time after its initiation. Therefore there is a clear need for a model that predicts the temporal variation of fracture dimensions.
- The present algorithm is based on overburden bending and is therefore capable of handling shallow fracturing injections only. It should be extended to model deep fractures as well, where the elastic compression of the formation will be the principal source of the deflection.

- The pressure at which the formation fractures not only depends on the depth of fracturing and *in situ* stresses present, but also on fluctuations in the gas-reservoir pressure in the fracturing equipment. The propagation algorithm could be improved by incorporating a predictive model that simulates this behavior.
- In the current algorithm injection flow rate and injection pressure are independent input variables. A relation that correlates these two parameters based on the pipe flow analysis of the fracturing system and reservoir pressure would be desirable since field experience has suggested that these two variables are coupled to some extent.
- When the algorithm is executed using the flownet method-I to estimate leak-off, it depends upon a database of shape factors for its computations. This part of the algorithm can be made more eloquent by developing a closed form expression to estimate the shape factors for the various boundary conditions.
- A root finding method that converges faster than the Bisection Method should be sought to improve the overall efficiency of the algorithm.

Theoretical Investigations:

- During the course of this study it has been firmly established that pneumatic fracture propagation is a complex phenomena involving the coupling of various physical processes. Work should continue to investigate the feasibility of developing a comprehensive closed form solution incorporating all the physical processes. The partial closed form solution based on continuity developed during this study can serve as a first step in this search.

- When air is injected into the formation one of the following three phenomena occurs, aeration of the subsurface, fluidization of the soil surrounding the injection well, or initiation and propagation of a discrete fracture. At present there are no criteria based on which one can predict the particular mechanism that might occur. A closed form solution that can determine for the given set of operational and formation parameters which one of these phenomenon occurs is therefore desirable.

Field Instrumentation:

- Continued calibration of the algorithm will require surface heave monitoring to determine fracture radius and aperture. Electronic tiltmeters are preferred but, then cost is usually not justified on production projects. Some minimal amount of monitoring using optical levels or LVDT's would still be valuable for continued calibration and validation of the algorithm.
- Alternative methods of monitoring ground surface heave such as using the Global Positioning System (GPS) should be investigated.
- During pneumatic fracture injections the flow rate is assumed constant, although in reality it fluctuates. It is difficult to record this behavior since flow measuring devices in the required range are either inaccurate or cause disturbance to the gas flow. It is recommended that this problem be revisited periodically so that any improvements in flow measuring technology can be accessed.

- Connection of the pressure transducers, tiltmeters and flow measuring devices to a common timer will permit better study of the transient propagation behavior of pneumatic fractures.

Field Tests:

- More field tests involving injection of a traceable dye or particulate supplements should be performed. This could be followed by excavation of the site to map fracture dimensions. Such direct evidence greatly supplements surface heave measurements which are only an indirect indication of fracture propagation.
- The algorithm has not been validated with respect to formation anisotropy. This could be accomplished by running both horizontal and vertical permeability tests during site characterization to determine the direction and magnitude of any major anisotropies.

Final Comment: As the production use of pneumatic fracturing continues to expand, there is an increasing tendency to minimize the amount of field monitoring for field projects. While this is complimentary in the respect that process enhancements no longer have to be proven, the disadvantage is that there is less usable data for research. If the technology is to reach full maturity, a continued effort of field monitoring coupled with mathematical modeling will be essential.

APPENDIX A

DEFLECTION OF A CIRCULAR PLATE CLAMPED AT THE EDGES AND SUBJECTED TO A LOGARITHMICALLY VARYING LOAD

The formation overlying the fracture can be modeled as the bending of an elastic plate. The expression for the deflection of circular plate clamped at the edges, can be obtained by solving the following differential equation [Timoshenko and Woinowsky-Krieger, 1959].

$$\frac{d^3b}{dr^3} + \frac{1}{r} \frac{d^2b}{dr^2} - \frac{1}{r^2} \frac{db}{dr} = \frac{S}{D} \dots\dots\dots(1)$$

which can be written as

$$\frac{d}{dr} \left[\frac{1}{r} \frac{d}{dr} \left(r \frac{db}{dr} \right) \right] = \frac{S}{D} \dots\dots\dots(2)$$

where r is the radial distance from the center of the plate, b is the deflection of the plate (fracture aperture), S is the magnitude of the shear force, and D is the flexural rigidity. The particular solution can be determined by applying the boundary conditions to the general solution and finding the integration constants.

The deflection of the plate is a function of the magnitude and distribution of the load it is subjected to. Existing propagation models assume that the pressure within the fracture to be either constant throughout the fracture [Carter, 1957], linear pressure gradient [Pollard and Johnson, 1973], or an average of the existing pressure distribution [Perkins and Kern, 1961].

The pressure distribution within the fracture is given by:

$$P = \sqrt{P_w^2 - \frac{12P_w Q_{in} \mu \ln\left(\frac{r}{r_w}\right)}{\pi g \rho b^3}}$$

where P_w is the over-pressure at the well, Q_{in} is the air injection flow rate, μ is dynamic viscosity of the air, r is radial distance from the well, r_w is the radius of the well, P and b are the pressure and fracture aperture at a radial distance r from the well respectively.

As can be seen from the above equation the pressure distribution is a function of fracture aperture. Therefore the equation for the deflection of the plate and the pressure distribution are coupled. Assuming that the over-pressure at the tip of the fracture is zero, an approximate pressure distribution that could be used is given by:

$$P = P_w - k \ln\left(\frac{r}{r_w}\right), \quad \text{where } k = \frac{P_w}{\ln\left(\frac{R}{r_w}\right)}$$

$$\text{such that } P = P_w \text{ when } r = r_w$$

$$\text{and } P = 0 \text{ when } r = R$$

for a fracture with constant fracture aperture and flow without leak-off.

In the figure A.1, the circular plate of radius R is subjected to a load of intensity P_w at the center that is decreasing exponentially with radius. The magnitude of the shear force at a radial distance ' r ,' is equal to the total load within this circle of radius ' r ' divided by its circumference. The total load within the circle is equal to the sum of the volumes of the cylinder and the volume of revolution of the curve above the cylinder, as shown in the figure A.1.

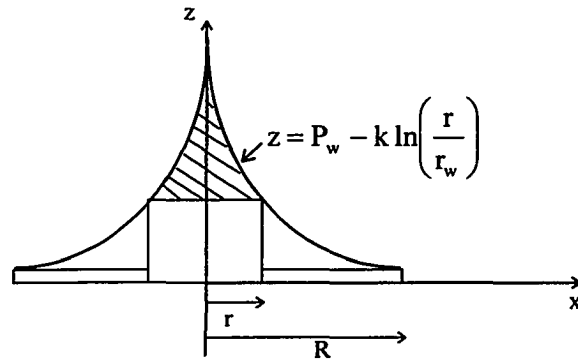


Figure A.1 Circular Plate Subjected to an Exponentially Varying Pressure

Volume of the cylinder

$$\begin{aligned}
 &= \pi r^2 z \\
 &= \pi r^2 \left[P_w - k \ln \left(\frac{r}{r_w} \right) \right]
 \end{aligned}$$

Volume generated by the revolution of the curve

$$\begin{aligned}
 &= \int_{\left[P_w - k \ln \left(\frac{r}{r_w} \right) \right]}^{P_w} \pi r^2 dz \\
 &= \int_{\left[P_w - k \ln \left(\frac{r}{r_w} \right) \right]}^{P_w} \pi [g(z)]^2 dz
 \end{aligned}$$

$$\text{where } z = P_w - k \ln \left(\frac{r}{r_w} \right)$$

$$k \ln \left(\frac{r}{r_w} \right) = P_w - z$$

$$\begin{aligned}
 \ln\left(\frac{r}{r_w}\right) &= \frac{(P_w - z)}{k} \\
 r &= r_w e^{\frac{(P_w - z)}{k}} \\
 \therefore g(z) &= r_w e^{\frac{(P_w - z)}{k}} \\
 &= \int_{\left[P_w - k \ln\left(\frac{r}{r_w}\right)\right]}^{P_w} \pi \left[r_w e^{\frac{(P_w - z)}{k}} \right]^2 dz \\
 &= \pi r_w^2 \int_{\left[P_w - k \ln\left(\frac{r}{r_w}\right)\right]}^{P_w} e^{\frac{2(P_w - z)}{k}} dz \\
 &= \pi r_w^2 \left[-\frac{k}{2} e^{\frac{2(P_w - z)}{k}} \right]_{\left[P_w - k \ln\left(\frac{r}{r_w}\right)\right]}^{P_w} \\
 &= \pi r_w^2 \left[-\frac{k}{2} e^{\frac{2(P_w - P_w)}{k}} + \frac{k}{2} e^{\frac{2\left[P_w - P_w + k \ln\left(\frac{r}{r_w}\right)\right]}{k}} \right] \\
 &= \pi r_w^2 \left[-\frac{k}{2} + \frac{k}{2} e^{\ln\left(\frac{r}{r_w}\right)^2} \right] \\
 &= \frac{k}{2} \pi (r^2 - r_w^2)
 \end{aligned}$$

total load = volume of the cylinder + volume of revolution of the curve

$$= \pi r^2 \left[P_w - k \ln \left(\frac{r}{r_w} \right) \right] + k \frac{\pi}{2} (r^2 - r_w^2)$$

The magnitude of the shearing force Q is determined by the equation

$$2\pi r Q = \text{total load within the circle described by radius } r$$

$$2\pi r Q = \pi r^2 \left[P_w - k \ln \left(\frac{r}{r_w} \right) \right] + k \frac{\pi}{2} (r^2 - r_w^2)$$

$$Q = \frac{r}{2} \left[P_w - k \ln \left(\frac{r}{r_w} \right) \right] + \frac{k}{4r} (r^2 - r_w^2)$$

$$Q = \frac{P_w r}{2} - \frac{k}{2} r \ln \left(\frac{r}{r_w} \right) + \frac{k}{4r} (r^2 - r_w^2)$$

Substituting Q in equation (2)

$$\frac{d}{dr} \left[\frac{1}{r} \frac{d}{dr} \left(r \frac{db}{dr} \right) \right] = \frac{P_w r}{2D} - \frac{k}{2D} r \ln \left(\frac{r}{r_w} \right) + \frac{k}{4D} \frac{(r^2 - r_w^2)}{r}$$

Integrating

$$\frac{1}{r} \frac{d}{dr} \left(r \frac{db}{dr} \right) = \frac{P_w r^2}{4D} - \frac{k}{2D} \left[\frac{r^2}{2} \ln \left(\frac{r}{r_w} \right) - \frac{r^2}{4} \right] + \frac{k}{4D} \left[\frac{r^2}{2} - r_w^2 \ln \left(\frac{r}{r_w} \right) \right] + C_1$$

$$\frac{d}{dr} \left(r \frac{db}{dr} \right) = \frac{P_w r^3}{4D} - \frac{k}{2D} \left[\frac{r^3}{2} \ln \left(\frac{r}{r_w} \right) - \frac{r^3}{4} \right] + \frac{k}{4D} \left[\frac{r^3}{2} - r_w^2 r \ln \left(\frac{r}{r_w} \right) \right] + C_1 r$$

$$\frac{d}{dr} \left(r \frac{db}{dr} \right) = \left(\frac{P_w}{4D} + \frac{k}{4D} \right) r^3 - \frac{k}{4D} r^3 \ln \left(\frac{r}{r_w} \right) - \frac{k r_w^2}{4D} r \ln \left(\frac{r}{r_w} \right) + C_1 r$$

Integrating

$$r \frac{db}{dr} = \left(\frac{P_w}{4D} + \frac{k}{4D} \right) \frac{r^4}{4} - \frac{k}{4D} \left[\frac{r^4}{4} \ln \left(\frac{r}{r_w} \right) - \frac{r^4}{16} \right] - \frac{kr_w^2}{4D} \left[\frac{r^2}{2} \ln \left(\frac{r}{r_w} \right) - \frac{r^2}{4} \right] + C_1 \frac{r^2}{2} + C_2$$

$$\frac{db}{dr} = \left(\frac{P_w}{4D} + \frac{5k}{16D} \right) \frac{r^3}{4} - \frac{k}{16D} r^3 \ln \left(\frac{r}{r_w} \right) - \frac{kr_w^2}{8D} r \ln \left(\frac{r}{r_w} \right) + \frac{kr_w^2}{16D} r + C_1 \frac{r}{2} + \frac{C_2}{r} \dots \dots \dots (3)$$

Integrating

$$b = \left(\frac{P_w}{4D} + \frac{5k}{16D} \right) \frac{r^4}{16} - \frac{k}{16D} \left[\frac{r^4}{4} \ln \left(\frac{r}{r_w} \right) - \frac{r^4}{16} \right] - \frac{kr_w^2}{8D} \left[\frac{r^2}{2} \ln \left(\frac{r}{r_w} \right) - \frac{r^2}{4} \right] + \frac{kr_w^2}{16D} \frac{r^2}{2} + C_1 \frac{r^2}{4} + C_2 \ln \left(\frac{r}{r_w} \right) + C_3$$

$$b = \left(\frac{P_w}{4D} + \frac{3k}{8D} \right) \frac{r^4}{16} - \frac{k}{64D} r^4 \ln \left(\frac{r}{r_w} \right) - \frac{kr_w^2}{16D} r^2 \ln \left(\frac{r}{r_w} \right) + \frac{kr_w^2}{16D} r^2 + C_1 \frac{r^2}{4} + C_2 \ln \left(\frac{r}{r_w} \right) + C_3 \dots \dots \dots (4)$$

applying the following boundary conditions to equation (3)

at radial distances $r = 0, R$

the slope of the plate $\frac{db}{dr} = 0$

$\therefore C_2 = 0$

and

$$\left(\frac{P_w}{4D} + \frac{5k}{16D} \right) \frac{R^3}{4} - \frac{k}{16D} R^3 \ln \left(\frac{R}{r_w} \right) - \frac{kr_w^2}{8D} R \ln \left(\frac{R}{r_w} \right) + \frac{kr_w^2}{16D} R + C_1 \frac{R}{2} = 0$$

$$\left(\frac{P_w}{4D} + \frac{5k}{16D} \right) \frac{R^2}{2} - \frac{k}{8D} R^2 \ln \left(\frac{R}{r_w} \right) - \frac{kr_w^2}{4D} \ln \left(\frac{R}{r_w} \right) + \frac{kr_w^2}{8D} + C_1 = 0$$

$$\therefore C_1 = \frac{kr_w^2}{4D} \left[\ln\left(\frac{R}{r_w}\right) - \frac{1}{2} \right] - \frac{R^2}{2} \left(\frac{P_w}{4D} + \frac{5k}{16D} \right) + \frac{k}{8D} R^2 \ln\left(\frac{R}{r_w}\right)$$

substituting the values of constants C_1 and C_2 in equation (4)

$$b = \left(\frac{P_w}{4D} + \frac{3k}{8D} \right) \frac{r^4}{16} - \frac{k}{64D} r^4 \ln\left(\frac{r}{r_w}\right) - \frac{kr_w^2}{16D} r^2 \ln\left(\frac{r}{r_w}\right) + \frac{kr_w^2}{16D} r^2 + \frac{r^2}{4} \left\{ \frac{kr_w^2}{4D} \left[\ln\left(\frac{R}{r_w}\right) - \frac{1}{2} \right] - \frac{R^2}{2} \left[\frac{P_w}{4D} + \frac{5k}{16D} \right] + \frac{k}{8D} R^2 \ln\left(\frac{R}{r_w}\right) \right\} + C_3 \dots\dots\dots(5)$$

applying the following boundary conditions to equation (5)

$$\text{at a radial distance} \quad r = R$$

$$\text{the displacement} \quad b = 0$$

$$\begin{aligned} & \left(\frac{P_w}{4D} + \frac{3k}{8D} \right) \frac{R^4}{16} - \frac{k}{64D} R^4 \ln\left(\frac{R}{r_w}\right) - \frac{kr_w^2}{16D} R^2 \ln\left(\frac{R}{r_w}\right) + \frac{kr_w^2}{16D} R^2 \\ & + \frac{R^2}{4} \left\{ \frac{kr_w^2}{4D} \left[\ln\left(\frac{R}{r_w}\right) - \frac{1}{2} \right] - \frac{R^2}{2} \left(\frac{P_w}{4D} + \frac{5k}{16D} \right) + \frac{k}{8D} R^2 \ln\left(\frac{R}{r_w}\right) \right\} + C_3 = 0 \\ & \left(\frac{P_w}{4D} + \frac{3k}{8D} - \frac{P_w}{2D} - \frac{5k}{8D} \right) \frac{R^4}{16} + \frac{k}{D} R^4 \ln\left(\frac{R}{r_w}\right) \left(-\frac{1}{64} + \frac{1}{32} \right) \\ & + \frac{kr_w^2}{D} R^2 \left(\frac{1}{16} - \frac{1}{32} \right) + C_3 = 0 \end{aligned}$$

$$C_3 = \left(\frac{P_w}{4D} + \frac{k}{4D} \right) \frac{R^4}{16} - \frac{k}{64D} R^4 \ln\left(\frac{R}{r_w}\right) - \frac{kr_w^2}{32D} R^2$$

substituting the value of C_3 in equation (5)

$$\begin{aligned} b = & \left(\frac{P_w}{4D} + \frac{3k}{8D} \right) \frac{r^4}{16} - \frac{k}{64D} r^4 \ln\left(\frac{r}{r_w}\right) - \frac{kr_w^2}{16D} r^2 \ln\left(\frac{r}{r_w}\right) + \frac{kr_w^2}{16D} r^2 \\ & + \frac{r^2}{4} \left[\frac{kr_w^2}{4D} \left(\ln\left(\frac{R}{r_w}\right) - \frac{1}{2} \right) - \frac{R^2}{2} \left(\frac{P_w}{4D} + \frac{5k}{16D} \right) + \frac{k}{8D} R^2 \ln\left(\frac{R}{r_w}\right) \right] \\ & + \left(\frac{P_w}{4D} + \frac{k}{4D} \right) \frac{R^4}{16} - \frac{k}{64D} R^4 \ln\left(\frac{R}{r_w}\right) - \frac{kr_w^2}{32D} R^2 \end{aligned}$$

$$\begin{aligned}
b &= \frac{r^4}{128D} \left[2P_w + 3k - 2k \ln\left(\frac{r}{r_w}\right) \right] \\
&+ \frac{r^2}{256D} \left[8kr_w^2 - 8P_w R^2 - 10kR^2 - 16kr_w^2 \ln\left(\frac{r}{r_w}\right) + 16kr_w^2 \ln\left(\frac{R}{r_w}\right) + 8kR^2 \ln\left(\frac{R}{r_w}\right) \right] \\
&+ \frac{R^4}{64D} \left[P_w + k - k \ln\left(\frac{R}{r_w}\right) \right] \\
&- \frac{kr_w^2}{32D} R^2
\end{aligned}$$

$$\text{since } k = \frac{P_w}{\ln\left(\frac{R}{r_w}\right)}$$

$$\begin{aligned}
b &= \frac{r^4}{128D} \left[2P_w + 3k - 2k \ln\left(\frac{r}{r_w}\right) \right] \\
&+ \frac{r^2}{256D} \left[-10kR^2 + r_w^2 \left(8k + 16P_w - 16k \ln\left(\frac{r}{r_w}\right) \right) \right] \\
&+ \frac{kR^4}{64D} \\
&- \frac{kr_w^2}{32D} R^2
\end{aligned}$$

APPENDIX B

**CLOSED FORM SOLUTION FOR CALCULATING
EXTENT OF FRACTURE PROPAGATION
(Cubic Pressure Distribution Pressure within the Fracture)**

An equation for estimating the extent of fracture propagation based on the principle of fluid continuity for a non linear (cubic) variation of pressure distribution within the fracture has been presented in this section.

The total amount of air being lost to the formation as leak-off over a region of the fracture surface G is given by

$$Q_{leak} = \iint_G f(x,y) dx dy$$

$$f(x,y) - \text{intensity of leak-off} = Ki = K \frac{p(r)}{z}$$

$$\begin{aligned} P(r) - \text{pressure head} &= p_w \left(1 - \frac{r^3}{R^3} \right) \\ &= p_w \left(1 - \frac{(\sqrt{x^2 + y^2})^3}{R^3} \right) \\ &= p_w \left(\frac{R^3 - (\sqrt{x^2 + y^2})^3}{R^3} \right) \end{aligned}$$

$$\begin{aligned} Q_{leak} &= 2 \left[4 \int_0^R \int_0^{\sqrt{R^2 - y^2}} k \frac{p_w}{z} \left(\frac{R^3 - (\sqrt{x^2 + y^2})^3}{R^3} \right) dx dy \right] \\ &= \frac{8kp_w}{zR^3} \int_0^R \int_0^{\sqrt{R^2 - y^2}} \left(R^3 - (\sqrt{x^2 + y^2})^3 \right) dx dy \dots\dots\dots(1) \end{aligned}$$

Integrating

$$\int_0^{\sqrt{R^2-y^2}} \left(R^3 - (\sqrt{x^2+y^2})^3 \right) dx = R^3 x - \left[\frac{1}{4} x(x^2+y^2)^{\frac{3}{2}} + \frac{3}{8} y^2 x \sqrt{x^2+y^2} + \frac{3}{8} y^4 \ln(x + \sqrt{x^2+y^2}) \right]$$

and applying the limits

$$= R^3 \sqrt{R^2-y^2} - \left[\frac{3}{8} y^2 R \sqrt{R^2-y^2} + \frac{1}{4} R^3 \sqrt{R^2-y^2} + \frac{3}{8} y^4 \ln(\sqrt{R^2-y^2} + R) - \frac{3}{8} y^4 \ln(y) \right]$$

$$= \frac{3}{4} R^3 \sqrt{R^2-y^2} - \frac{3}{8} y^2 R \sqrt{R^2-y^2} - \frac{3}{8} y^4 \ln(\sqrt{R^2-y^2} + R) + \frac{3}{8} y^4 \ln(y) \dots \dots \dots (2)$$

substituting (2) in equation (1)

$$Q_{\text{leak}} = \frac{8kp_w}{zR^3} \int_0^R \left(\frac{3}{4} R^3 \sqrt{R^2-y^2} - \frac{3}{8} y^2 R \sqrt{R^2-y^2} - \frac{3}{8} y^4 \ln(\sqrt{R^2-y^2} + R) + \frac{3}{8} y^4 \ln(y) \right) dy$$

$$= \frac{8kp_w}{zR^3} \left[\int_0^R \left(\frac{3}{4} R^3 \sqrt{R^2-y^2} \right) dy - \int_0^R \left(\frac{3}{8} y^2 R \sqrt{R^2-y^2} \right) dy \right. \\ \left. - \int_0^R \left(\frac{3}{8} y^4 \ln(\sqrt{R^2-y^2} + R) \right) dy + \int_0^R \left(\frac{3}{8} y^4 \ln(y) \right) dy \right]$$

$$= \frac{8kp_w}{zR^3} \left[\int_0^R \left(\frac{3}{4} R^3 \sqrt{R^2-y^2} \right) dy - \int_0^R \left(\frac{3}{8} y^2 R \sqrt{R^2-y^2} \right) dy \right. \\ \left. + \int_0^R \left(\frac{3}{8} y^4 \ln(y) \right) dy - \ln(\sqrt{R^2-y^2} + R) \int_0^R \left(\frac{3}{8} y^4 \right) dy \right. \\ \left. + \int_0^R \left(\frac{d}{dy} (\ln(\sqrt{R^2-y^2} + R)) \right) \int_0^R \left(\frac{3}{8} y^4 \ln(y) \right) dy \right]$$

$$= \frac{8kp_w}{zR^3} \left[\int_0^R \left(\frac{3}{4} R^3 \sqrt{R^2-y^2} \right) dy - \int_0^R \left(\frac{3}{8} y^2 R \sqrt{R^2-y^2} \right) dy \right. \\ \left. + \int_0^R \left(\frac{3}{8} y^4 \ln(y) \right) dy - \ln(\sqrt{R^2-y^2} + R) \int_0^R \left(\frac{3}{8} y^4 \right) dy \right. \\ \left. + \int_0^R \left(\frac{-1}{\sqrt{R^2-y^2}} \frac{y}{(\sqrt{R^2-y^2} + R)} \int_0^R \left(\frac{3}{8} y^4 \ln(y) \right) dy \right) dy \right]$$

Integrating

$$= \frac{8k p_w}{z R^3} \left[\begin{aligned} & \frac{3}{4} \left(\frac{1}{2} y \sqrt{R^2 - y^2} + \frac{1}{2} R^2 \sin^{-1} \left(\frac{y}{R} \right) \right) R^3 \\ & - \frac{3}{8} \left(-\frac{1}{4} y (R^2 - y^2)^{\frac{3}{2}} + \frac{1}{8} R^2 \left(y \sqrt{R^2 - y^2} + R^2 \sin^{-1} \left(\frac{y}{R} \right) \right) \right) R \\ & + \left[\left(\frac{3}{40} y^5 \ln(|y|) \right) - \frac{3}{200} y^5 \right] \\ & \left[-\ln \left(\sqrt{R^2 - y^2} + R \right) \left(\frac{3}{40} y^5 \right) + \int \left(\frac{-1}{\sqrt{R^2 - y^2}} \frac{y}{\left(\sqrt{R^2 - y^2} + R \right)} \left(\frac{3}{40} y^5 \right) \right) dy \right] \end{aligned} \right]$$

$$= \frac{8k p_w}{z R^3} \left[\begin{aligned} & \frac{3}{4} \left(\frac{1}{2} y \sqrt{R^2 - y^2} + \frac{1}{2} R^2 \sin^{-1} \left(\frac{y}{R} \right) \right) R^3 \\ & - \frac{3}{8} \left(-\frac{1}{4} y (R^2 - y^2)^{\frac{3}{2}} + \frac{1}{8} R^2 \left(y \sqrt{R^2 - y^2} + R^2 \sin^{-1} \left(\frac{y}{R} \right) \right) \right) R \\ & + \left[\left(\frac{3}{40} y^5 \ln(|y|) \right) - \frac{3}{200} y^5 \right] - \ln \left(\sqrt{R^2 - y^2} + R \right) \left(\frac{3}{40} y^5 \right) \\ & + \left(-\frac{3}{40} \left[-\frac{1}{4} \sqrt{R^2 - y^2} y^3 + \frac{3}{4} R^2 \left(-\frac{1}{2} y \sqrt{R^2 - y^2} + \frac{1}{2} R^2 \sin^{-1} \left(\frac{y}{R} \right) \right) \right] - \frac{3}{200} y^5 \right) \end{aligned} \right]$$

Applying the limits

$$= \frac{8k p_w}{z R^3} \left[\begin{aligned} & \left(\frac{3}{16} R^5 \pi \right) - \left(\frac{3}{64} R^5 \sin^{-1} \left(\frac{R}{R} \right) \right) \\ & - \left[\left(\frac{3}{40} R^5 \ln(|R|) \right) - \left(-\frac{9}{320} R^5 \sin^{-1} \left(\frac{R}{R} \right) - \frac{3}{200} R^5 \right) \right] \\ & + \left(-\frac{3}{200} R^5 + \frac{3}{40} R^5 \ln(|R|) \right) \end{aligned} \right]$$

$$= \frac{8k p_w}{z R^3} \left(\frac{3}{16} R^5 \pi - \frac{3}{40} R^5 \sin^{-1} \left(\frac{R}{R} \right) - \frac{3}{100} R^5 \right)$$

$$= \frac{8k p_w}{z R^3} \left(\frac{3}{16} R^5 \pi - \frac{3}{40} R^5 \frac{\pi}{2} - \frac{3}{100} R^5 \right)$$

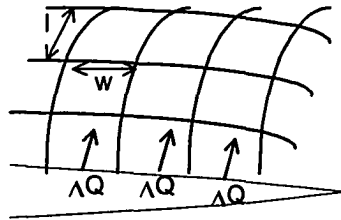
$$= \frac{8k p_w}{z R^3} \left(\frac{3}{20} R^5 \pi - \frac{3}{100} R^5 \right)$$

$$Q_{\text{leak}} = 3.528k \frac{P_w}{z} R^2$$

APPENDIX C

LEAK-OFF ESTIMATION BY FLOWNET METHOD - II

The derivation presented in this section calculates the leak-off occurring from a radial fracture based on potential theory. The leak-off equation derived here forms the basis for one of the methods by which the algorithm calculates leak-off, which will be referred to as “flownet method-II.”



According to Darcy's law

$$Q = KiA$$

$$\Delta Q = K \frac{\Delta h}{l} (w * dL)$$

$$\Delta Q = K \frac{H}{N_d} \frac{w}{l} dL \quad \left(\because \Delta h = \frac{H}{N_d} \right)$$

$$\sum \Delta Q = K \frac{H}{N_d} N_f dL \quad (\because w = l)$$

for a rectangular plan area

$$Q_{leak} = 2RKH \frac{N_f}{N_d}$$

Approximating the leak-off for a fracture with circular plan area

$$Q_{leak} = \frac{\pi R^2}{(2R)^2} 2RKH \frac{N_f}{N_d} \quad \left(\begin{array}{l} \text{area of a square} = (2R)^2 \\ \text{area of the circle} = \pi R^2 \end{array} \right)$$

$$Q_{leak} = \frac{\pi}{2} RKH \frac{N_f}{N_d}$$

APPENDIX D
CLOSED FORM SOLUTION FOR CALCULATING
EXTENT OF FRACTURE PROPAGATION
(Linearly Varying Pressure within the Fracture)

A complete solution for estimating the extent of fracture propagation based on the principle of fluid continuity for a simple case of linearly decreasing pressure distribution within the fracture has been presented in this section.

The total amount of air being lost to the formation as leak-off over a region of the fracture surface G is given by

$$Q_{\text{leak}} = \iint_G f(x,y) dx dy \dots\dots\dots (1)$$

where $f(x,y)$ is the intensity of leak-off which according to Darcy's law is given by

$$f(x,y) = Ki = K \frac{p(r)}{z}$$

where $P(r)$ is the driving pressure head, which is decreasing linearly within the fracture

$$\begin{aligned} &= p_w \left(1 - \frac{r}{R}\right) \\ &= p_w \left(1 - \frac{\sqrt{x^2 + y^2}}{R}\right) \\ &= p_w \left(\frac{R - \sqrt{x^2 + y^2}}{R}\right) \dots\dots\dots (2) \end{aligned}$$

substituting equation (2) in equation (1) we obtain

$$\begin{aligned} Q_{\text{leak}} &= \iint_G K \frac{p_w}{z} \frac{(R - \sqrt{x^2 + y^2})}{R} dx dy \\ &= \frac{K p_w}{z R} \iint_G (R - \sqrt{x^2 + y^2}) dx dy \\ &= 4 \frac{K p_w}{z R} \int_0^R \int_0^{\sqrt{R^2 - y^2}} (R - \sqrt{x^2 + y^2}) dx dy \dots\dots\dots (3) \end{aligned}$$

$$\int_0^{\sqrt{R^2-y^2}} (R - \sqrt{x^2+y^2}) dx = \left\{ Rx - \left[\frac{x\sqrt{x^2+y^2} + y^2 \log(x + \sqrt{x^2+y^2})}{2} \right] \right\}_0^{\sqrt{R^2-y^2}}$$

$$\because \int \sqrt{x^2+a^2} = \frac{x}{2}\sqrt{x^2+a^2} + \frac{a^2}{2} \log(x + \sqrt{x^2+a^2})$$

$$= \left[Rx - \frac{x}{2}\sqrt{x^2+y^2} + \frac{y^2}{2} \log(x + \sqrt{x^2+y^2}) \right]_0^{\sqrt{R^2-y^2}}$$

$$= \frac{R}{2}\sqrt{R^2-y^2} - \frac{y^2}{2} \log(\sqrt{R^2-y^2} + R) + \frac{y^2}{2} \log(y) \dots\dots\dots (4)$$

substituting the above equation (4) in (3)

$$= \frac{KP_w}{Rz} \int_0^R \left(\frac{R}{2}\sqrt{R^2-y^2} - \frac{y^2}{2} \log(\sqrt{R^2-y^2} + R) + \frac{y^2}{2} \log(y) \right) dy$$

$$= \frac{KP_w}{Rz} \left[\int_0^R \frac{R}{2}\sqrt{R^2-y^2} dy - \int_0^R \frac{y^2}{2} \log(\sqrt{R^2-y^2} + R) dy + \int_0^R \frac{y^2}{2} \log(y) dy \right] \dots\dots\dots (5)$$

$$\int_0^R \frac{R}{2}\sqrt{R^2-y^2} dy = \frac{R}{2} \left[\frac{y}{2}\sqrt{R^2-y^2} + \frac{R^2}{2} \sin^{-1}\left(\frac{y}{R}\right) \right]_0^R$$

$$= \frac{R}{2} \left(\frac{R^2}{2} * \frac{\pi}{2} \right)$$

$$= \frac{\pi R^3}{8} \dots\dots\dots (6)$$

$$\int_0^R \frac{y^2}{2} \ln(R + \sqrt{R^2-y^2}) dy = \frac{1}{2} \left[\ln(R + \sqrt{R^2-y^2}) \frac{y^3}{3} \right]_0^R + \frac{1}{2} \int_0^R \frac{y^4}{3\sqrt{R^2-y^2}(\sqrt{R^2-y^2} + R)}$$

$$= \frac{1}{6} \ln(R)R^3 + \frac{1}{6} \int_0^R \frac{y^4}{\sqrt{R^2-y^2}(R + \sqrt{R^2-y^2})} dy \dots\dots\dots (7)$$

substituting
 $y = R \sin \theta$
 $dy = R \cos(\theta) d\theta$

$$\begin{aligned}
 \int \frac{y^4}{\sqrt{R^2 - y^2} (R + \sqrt{R^2 - y^2})} dy &= \int \frac{(R \sin^4 \theta)}{\sqrt{R^2 - R^2 \sin^2 \theta} (R + \sqrt{R^2 - R^2 \sin^2 \theta})} (R \cos \theta) d\theta \\
 &= \int \frac{R^5 \sin^4 \theta \cos \theta}{(R \cos \theta) R (1 + \cos \theta)} d\theta \\
 &= R^3 \int \frac{\sin^4 \theta \cos \theta}{\cos \theta (1 + \cos \theta)} d\theta \\
 &= R^3 \int \frac{(\sin^2 \theta)(\sin^2 \theta)}{(1 + \cos \theta)} d\theta \\
 &= R^3 \int \frac{(1 - \cos^2 \theta)(\sin^2 \theta)}{(1 + \cos \theta)} d\theta \\
 &= R^3 \int \frac{(1 - \cos \theta)(1 + \cos \theta)(\sin^2 \theta)}{(1 + \cos \theta)} d\theta \\
 &= R^3 \int (\sin^2 \theta - \sin^2 \theta \cos \theta) d\theta \\
 &= R^3 \int \left(\frac{1 - \cos 2\theta}{2} - \sin^2 \theta \cos \theta \right) d\theta \\
 &= \frac{R^3}{2} \int (1 - \cos 2\theta) d\theta - R^3 \int (\sin^2 \theta \cos \theta) d\theta \\
 &= \frac{R^3}{2} \left(\theta - \frac{\sin 2\theta}{2} \right) - R^3 \int (\sin^2 \theta \cos \theta) d\theta \\
 &= \frac{R^3}{2} \left(\theta - \frac{2 \sin \theta \cos \theta}{2} \right) - \int (R^2 \sin^2 \theta) (R \cos \theta) d\theta \\
 &= \frac{R^3}{2} \left(\theta - \sin \theta \sqrt{1 - \sin^2 \theta} \right) - \int (R^2 \sin^2 \theta) (R \cos \theta) d\theta
 \end{aligned}$$

$$\theta = \sin^{-1} \frac{y}{R}$$

substituting $(R \cos \theta) d\theta = dy$

$$R^2 \sin^2 \theta = y^2$$

$$\begin{aligned}
 &= \frac{R^3}{2} (\theta) - \frac{R^2}{2} \sin \theta \sqrt{R^2 - R^2 \sin^2 \theta} - \int (R^2 \sin^2 \theta) (R \cos \theta) d\theta \\
 &= \frac{R^3}{2} \theta - \frac{R}{2} R \sin \theta \sqrt{R^2 - R^2 \sin^2 \theta} - \int (R^2 \sin^2 \theta) (R \cos \theta) d\theta \\
 &= \frac{R^3}{2} \sin^{-1} \frac{y}{R} - \frac{R}{2} y \sqrt{R^2 - y^2} - \int y^2 dy \\
 &= \frac{R^3}{2} \sin^{-1} \frac{y}{R} - \frac{R}{2} y \sqrt{R^2 - y^2} - \frac{y^3}{3} \dots\dots\dots (8)
 \end{aligned}$$

substituting in equations 8 in equation 7 and applying the limits

$$= \frac{1}{6} \left[\frac{R^3}{2} \sin^{-1} \frac{y}{R} - \frac{R}{2} y \sqrt{R^2 - y^2} - \frac{y^3}{3} \right]_0^R$$

$$= \frac{1}{6} \left[\frac{\pi R^3}{2} - \frac{R^3}{3} \right] = \frac{1}{6} \left[\frac{\pi R^3}{24} - \frac{R^3}{18} \right] \dots\dots\dots(9)$$

Integrating by parts

$$\begin{aligned} \int_0^R \frac{y^2}{2} \ln(y) dy &= \left[\ln(y) \frac{y^3}{6} - \int \frac{1}{y} \frac{y^3}{6} \right]_0^R \\ &= \left[\ln(y) \frac{y^3}{6} - \frac{y^3}{18} \right]_0^R \\ &= \left[\ln(R) \frac{R^3}{6} - \frac{R^3}{18} \right] \dots\dots\dots(10) \end{aligned}$$

substituting equation 6, 9, and 10 in equation 5

$$\begin{aligned} 4 \frac{K P_w}{R d} \int_0^R \int_0^{\sqrt{R^2 - y^2}} (R - \sqrt{R^2 + y^2}) dx dy &= 4 \frac{K P_w}{R z} \left[\frac{\pi R^3}{8} + \frac{\pi R^3}{24} - \frac{R^3}{18} + \frac{R^3}{6} \ln(R) - \frac{R^3}{18} \right] \\ &= 4 \frac{K P_w}{R z} \left[R^3 \left(\frac{\pi}{6} - \frac{R^3}{9} + \frac{R^3}{6} \ln(R) \right) \right] \\ &= 4 \frac{K P_w}{R z} \left[\frac{R^3}{18} (3\pi - 2 + 3 \ln(R)) \right] \\ \therefore Q_{\text{leak-off}} &= \frac{2}{9} \frac{K P_w R^2}{z} [7.4 + 3 \ln(R)] \end{aligned}$$

APPENDIX E-1 INPUT PARAMETERS FOR THE MODEL

SYSTEM PARAMETERS

Injected Flow : (L ³ /T)	$Q = 857 \frac{\text{ft}^3}{\text{min}}$
Maintenance Pressure : (M/LT ²)	$P_m = 15 \frac{\text{lbf}}{\text{in}^2}$
Well Radius : (L)	$r_w = 0.25 \text{ ft}$
Depth of fracturing : (L)	$z = 6 \text{ ft}$
Density of air : (M/L ³)	$\gamma_{\text{air}} = 0.08 \frac{\text{lbf}}{\text{ft}^3}$
Viscosity of air : (MT)	$\mu_{\text{air}} = 4 \cdot 10^{-7} \frac{\text{lbf} \cdot \text{sec}}{\text{ft}^2}$

FORMATION PARAMETERS

Horizontal Pneumatic Conductivity : (L/T)	$K_{h_air} = 5.19 \frac{\text{ft}}{\text{day}}$	$K_{h_air} = 1.831 \cdot 10^{-3} \frac{\text{cm}}{\text{sec}}$
Vertical Pneumatic Conductivity : (L/T)	$K_{v_air} = 5.19 \frac{\text{ft}}{\text{day}}$	$K_{v_air} = 1.8 \cdot 10^{-3} \frac{\text{cm}}{\text{sec}}$
Poisson's Ratio		$\nu = 0.4$
Young's Modulus : (M/LT ²)		$E = 51 \frac{\text{lbf}}{\text{in}^2}$
Distance over which head is lost : (L)		$\delta l = 1.8 \cdot z \text{ ft}$
Formation density : (M/L ³)		$\gamma = 105 \frac{\text{lbf}}{\text{ft}^3}$
Formation Fracture Toughness : (M/L ^{1/2} T ²)		$K_{ic} = 0 \frac{\text{lbf}}{\text{in}^2} \cdot \sqrt{\text{ft}}$

Fracture Geometry

- Case 1. Linearly Tapering
- Case 2. Anticlinal plan and constant pressure distribution
- Case 3. Circular plan and constant pressure distribution
- Case 4. Circular plan and a log pressure distribution

**APPENDIX E-2
THREE DIFFERENT APPROACHES INVESTIGATED TO SOLVE FOR
THE ROOTS OF THE MODEL**

```

Bisection(low, up)  for N ∈ 0..1000
                    error ←  $\left| \frac{up - low}{up + low} \right| \cdot 100$ 
                    middle ←  $\frac{(low + up)}{2}$ 
                    up ← middle if Varying_Width(low, 1) · Varying_Width(middle, 1) < 0
                    low ← middle if Varying_Width(middle, 1) · Varying_Width(up, 1) < 0 otherwise
                    break if Varying_Width(low, 1) · Varying_Width(middle, 1) = 0
                    break if error < 0.01
                    middle

```

I. Bisection Method Subroutine

```

Incrementing_Radius  R ← 1·ft
                    R_incr ← 0.1·ft
                    Q_tip ← 1
                    for N ∈ 1..106
                        R ← R + R_incr
                        Q_tip ← Varying_Width(R, 1)
                        break if Q_tip < 0
                    R

```

II. Incrementing the fracture radius to arrive at the solution

```

Decrementing_Radius  R ← 30·ft
                    R_decr ← 0.1·ft
                    P_tip ← 1
                    for N ∈ 1..106
                        R ← R - R_decr
                        P_tip ← Varying_Width(R, 6)
                        break if P_tip < 0
                    R

```

III. Decreasing the fracture radius to obtain the solution

APPENDIX E-3
PREDICTING THE STEADY STATE
FRACTURE DIMENSIONS (Analytical Method)
VARYING WIDTH FRACTURE GEOMETRY (Mathcad Version)

$$\begin{aligned}
 \text{Varying_Width (Rad, Call)} &= r_{\text{incr}} - 0.1 \\
 R &= \text{Rad} \cdot \text{ft} \\
 \text{for } N \in 1..10^6 & \\
 r_1 &= 0.25 \\
 r_{\text{incr}} &= 0.001 \text{ if } (R - r_N \cdot \text{ft}) < 1 \cdot \text{ft} \\
 P_d &= P_m - \gamma \cdot z \\
 P_i &= \frac{P_m}{\gamma_{\text{air}}} \\
 Q_1 &= Q \\
 r_{N+1} &= r_N + r_{\text{incr}} \\
 x &= \frac{r_{N+1} + r_N \cdot \text{ft}}{2} \\
 b1_N &= \frac{P_d \cdot (1 - \nu^2)}{E} \cdot \frac{8}{\pi} \cdot \sqrt{R^2 - (r_N \cdot \text{ft})^2} \\
 b_w &= \left[\frac{3 \cdot P_d \cdot (1 - \nu^2) \cdot R^4}{16 \cdot E \cdot z^3} \right] \text{ if Case=1} \\
 b2_N &= b_w \cdot \frac{b_w}{R} \cdot r_N \cdot \text{ft} \text{ if Case=1} \\
 b2_N &= \frac{P_d \cdot (1 - \nu^2) \cdot (x^4 - 2 \cdot R^2 \cdot x^2 + R^4)}{2 \cdot E \cdot z^3} \text{ if Case=2} \\
 b2_N &= \frac{3 \cdot P_d \cdot (1 - \nu^2) \cdot (x^4 - 2 \cdot R^2 \cdot x^2 + R^4)}{16 \cdot E \cdot z^3} \text{ if Case=3} \\
 k &= \frac{P_d}{\ln\left(\frac{R}{r_w}\right)} \\
 b2_N &= \frac{x^4}{128 \cdot D} \cdot \left(2 \cdot P_d + 3 \cdot k - 2 \cdot k \cdot \ln\left(\frac{x}{r_w}\right) \right) \dots \text{ if Case=4} \\
 &+ \frac{x^2}{256 \cdot D} \cdot \left[10 \cdot k \cdot R^2 + r_w^2 \cdot \left(8 \cdot k + 16 \cdot P_d - 16 \cdot k \cdot \ln\left(\frac{x}{r_w}\right) \right) \right] \dots \\
 &+ \frac{k \cdot R^4}{64 \cdot D} - \frac{k \cdot r_w^2}{32 \cdot D} \cdot R^2
 \end{aligned}$$

(continued from previous page - same loop)

for $N \in 1..10^6$ $b_N \leftarrow b_{2N}$

$$\text{if } (P_N)^2 \cdot ft^2 < \frac{12 \cdot Q_N \cdot \frac{ft^3}{\text{sec}} \cdot \mu_{\text{air}} \cdot P_N \cdot ft \cdot \ln\left(\frac{r_{N+1}}{r_N}\right)}{\pi \cdot \gamma_{\text{air}} \cdot (b_N)^3 \cdot ft^3}$$

 $N \leftarrow (N - 1)$

break

$$P_{N+1} \leftarrow \sqrt{(P_N)^2 \cdot ft^2 - \frac{12 \cdot Q_N \cdot \frac{ft^3}{\text{sec}} \cdot \mu_{\text{air}} \cdot P_N \cdot ft \cdot \ln\left(\frac{r_{N+1}}{r_N}\right)}{\pi \cdot \gamma_{\text{air}} \cdot (b_N)^3 \cdot ft^3}}$$

$$P_{\text{prop}_{N+1}} \leftarrow \gamma \cdot z + \frac{K_{ic}}{\sqrt{\pi \cdot r_N \cdot ft}}$$

$$P_{\text{prop}_{N+1}} \leftarrow \frac{P_{\text{prop}_{N+1}}}{\gamma_{\text{air}}}$$

$$QL_N \leftarrow \sqrt{K_{h_{\text{air}}} \cdot K_{v_{\text{air}}} \left[\frac{P_{N+1} + P_N}{\delta l} \right] \cdot \left[\pi \cdot \left[(r_{N+1})^2 - (r_N)^2 \right] \right]}$$

$$Q_{N+1} \leftarrow Q_N - 2 \cdot (QL_N)$$

break if $P_{N+1} < P_{\text{prop}_{N+1}}$ break if $Q_{N+1} \leq 0$ break if $r_{N+1} \cdot ft \geq R$ output $\leftarrow Q_{N+1}$ if Cal=1output $\leftarrow Q$ if Cal=2output $\leftarrow 2 \cdot QL$ if Cal=3output $\leftarrow P$ if Cal=4output $\leftarrow P_{\text{prop}}$ if Cal=5output $\leftarrow P_{N+1} - P_{\text{prop}_{N+1}}$ if Cal=6output $\leftarrow b$ if Cal=7output $\leftarrow r$ if Cal=8output $\leftarrow N$ if Cal=9

output

APPENDIX E-4
PREDICTING THE STEADY STATE
FRACTURE DIMENSIONS (Flownet Method)
VARYING WIDTH FRACTURE GEOMETRY (Mathcad Version)

Varying_Width (Rad, Call) $r_{incr} = 0.1$

$R =$ Rad·ft

for $N \in 1..10^6$

$r_1 = 0.25$

$r_{incr} = 0.001$ if $(R - r_N \cdot \text{ft}) < 1 \cdot \text{ft}$

$P_d = P_m - \gamma \cdot z$

$P_l = \frac{P_m}{\gamma_{air}}$

$Q_l = Q$

$r_{N+1} = r_N + r_{incr}$

$x = \frac{r_{N+1} + r_N}{2} \cdot \text{ft}$

$b1_N = \frac{P_d \cdot (1 - \nu^2)}{E} \cdot \frac{8}{\pi} \cdot \sqrt{R^2 - (r_N \cdot \text{ft})^2}$

$b_w = \left[\frac{3 \cdot P_d \cdot (1 - \nu^2) \cdot R^4}{16 \cdot E \cdot z^3} \right]$ if Case=1

$b2_N = b_w - \frac{b_w}{R} \cdot r_N \cdot \text{ft}$ if Case=1

$b2_N = \frac{P_d \cdot (1 - \nu^2) \cdot (x^4 - 2 \cdot R^2 \cdot x^2 + R^4)}{2 \cdot E \cdot z^3}$ if Case=2

$b2_N = \frac{3 \cdot P_d \cdot (1 - \nu^2) \cdot (x^4 - 2 \cdot R^2 \cdot x^2 + R^4)}{16 \cdot E \cdot z^3}$ if Case=3

$k = \frac{P_d}{\ln\left(\frac{R}{r_w}\right)}$

$b2_N = \frac{x^4}{128 \cdot D} \cdot \left(2 \cdot P_d + 3 \cdot k - 2 \cdot k \cdot \ln\left(\frac{x}{r_w}\right) \right) \dots$ if Case=4
 $+ \frac{x^2}{256 \cdot D} \cdot \left(10 \cdot k \cdot R^2 + r_w^2 \cdot \left(8 \cdot k + 16 \cdot P_d - 16 \cdot k \cdot \ln\left(\frac{x}{r_w}\right) \right) \right) \dots$
 $+ \frac{k \cdot R^4}{64 \cdot D} - \frac{k \cdot r_w^2}{32 \cdot D} \cdot R^2$

for $N \in 1..10^6$

$$b_N \leftarrow b_{2N}$$

$$\text{if } (P_N)^2 \cdot ft^2 < \frac{12 \cdot Q_N \cdot \frac{ft^3}{sec} \cdot \mu_{air} \cdot P_N \cdot ft \cdot \ln\left(\frac{r_{N+1}}{r_N}\right)}{\pi \cdot \gamma_{air} \cdot (b_N)^3 \cdot ft^3}$$

$$N \leftarrow (N + 1)$$

break

$$P_{N+1} \leftarrow \sqrt{(P_N)^2 \cdot ft^2 \cdot \frac{12 \cdot Q_N \cdot \frac{ft^3}{sec} \cdot \mu_{air} \cdot P_N \cdot ft \cdot \ln\left(\frac{r_{N+1}}{r_N}\right)}{\pi \cdot \gamma_{air} \cdot (b_N)^3 \cdot ft^3}}$$

$$P_{prop_{N+1}} \leftarrow \gamma \cdot z + \frac{K_{ic}}{\sqrt{\pi \cdot r_N \cdot ft}}$$

$$P_{prop_{N+1}} \leftarrow \frac{P_{prop_{N+1}}}{\gamma_{air}}$$

$$\phi \leftarrow \begin{cases} \frac{2.1}{24} \frac{10}{R} \cdot r_{incr} \cdot ft & \text{if } r_1 \cdot ft < x < 0.1 \cdot R \end{cases}$$

$$\phi \leftarrow \frac{2.16}{24} \frac{10}{R} \cdot r_{incr} \cdot ft \quad \text{if } 0.1 \cdot R < x < 0.2 \cdot R$$

$$\phi \leftarrow \frac{2.11}{24} \frac{10}{R} \cdot r_{incr} \cdot ft \quad \text{if } 0.2 \cdot R < x < 0.3 \cdot R$$

$$\phi \leftarrow \frac{2.32}{24} \frac{10}{R} \cdot r_{incr} \cdot ft \quad \text{if } 0.3 \cdot R < x < 0.4 \cdot R$$

$$\phi \leftarrow \frac{2.32}{24} \frac{10}{R} \cdot r_{incr} \cdot ft \quad \text{if } 0.4 \cdot R < x < 0.5 \cdot R$$

$$\phi \leftarrow \frac{2.61}{24} \frac{10}{R} \cdot r_{incr} \cdot ft \quad \text{if } 0.5 \cdot R < x < 0.6 \cdot R$$

$$\phi \leftarrow \frac{2.57}{24} \frac{10}{R} \cdot r_{incr} \cdot ft \quad \text{if } 0.6 \cdot R < x < 0.7 \cdot R$$

$$\phi \leftarrow \frac{3.34}{24} \frac{10}{R} \cdot r_{incr} \cdot ft \quad \text{if } 0.7 \cdot R < x < 0.8 \cdot R$$

$$\phi \leftarrow \frac{3.98}{24} \frac{10}{R} \cdot r_{incr} \cdot ft \quad \text{if } 0.8 \cdot R < x < 0.9 \cdot R$$

$$\phi \leftarrow \frac{8.57}{24} \frac{10}{R} \cdot r_{incr} \cdot ft \quad \text{if } 0.9 \cdot R < x < R$$

$$QL_N \leftarrow K \cdot P_N \cdot \phi \cdot \pi \cdot r_{N+1} \cdot r_N$$

$$Q_{N+1} \leftarrow Q_N + (QL_N)$$

```

for N ∈ 1..106
  break if PN+1 < PpropN+1
  break if QN+1 ≤ 0
  break if rN+1 · ft ≥ R
output -- QN+1 if Cal=1
output -- Q if Cal=2
output -- QL if Cal=3
output -- P if Cal=4
output -- Pprop if Cal=5
output -- PN+1 - PpropN+1 if Cal=6
output -- b if Cal=7
output -- r if Cal=8
output

```


APPENDIX E-5
PREDICTING THE STEADY STATE FRACTURE DIMENSIONS
(Constant Width Fractures)

```

Constant_Width (Width, Call) = r_incr = 0.5
b = Width
for N = 1..106
  r_1 = 0.25
  P_1 = P_d / γ_air
  Q_1 = Q
  r_{N+1} = r_N + r_incr
  x = (r_{N+1} + r_N) / 2 * ft
  P_{N+1} = sqrt( (P_N)^2 * ft^2 - (Q_N * (ft^3 / sec) * 12 * μ_air * P_N * ft * ln(r_{N+1} / r_N)) / (π * γ_air * (b)^3 * ft^3) )
  P_prop_{N+1} = γ * z + K_ic / sqrt(π * r_N * ft)
  P_{prop_{N+1}} = P_prop_{N+1} / γ_air
  QL_N = (K_h_air + K_v_air) * [ (P_{N+1} + P_N) / δl ] * [ π * ((r_{N+1})^2 - (r_N)^2) ]
  Q_{N+1} = Q_N - 2 * (QL_N)
  break if P_{N+1} < P_prop_{N+1}
  break if Q_{N+1} ≤ 0
output = Q_{N+1} if Cal=1
output = Q if Cal=2
output = 2 * QL if Cal=3
output = P if Cal=4
output = P_prop if Cal=5
output = P_{N+1} P_prop_{N+1} if Cal=6

```

```

output -- b if Cal=7
output -- r if Cal=8
output

```

```

Bisection(low,up) for N ∈ 0.. 1000
  error --  $\left| \frac{up - low}{up + low} \right| \cdot 100$ 
  middle --  $\frac{(low + up)}{2}$ 
  up -- middle if Constant_Width (low, 1) · Constant_Width (middle, 1) < 0
  low -- middle if Constant_Width (middle, 1) · Constant_Width (up, 1) < 0 otherwise
  break if Constant_Width (low, 1) · Constant_Width (up, 1) = 0
  break if error < 1
middle

```

**APPENDIX F
PARTICULATES TRANSPORT IN A FLUIDIZED SOIL FORMATION
INPUT PARAMETERS FOR THE MODEL**

HANFORD SITE

gas filled porosity (volumetric gas content)		$\phi = 0.34$ [uniform sand; Harr]
pneumatic conductivity	$K = 0.106 \frac{\text{cm}}{\text{sec}}$	$K = 300 \frac{\text{ft}}{\text{day}}$
radial gas permeability (intrinsic)	$k_R = 1.003 \cdot 10^{-6} \cdot \text{cm}^2$	$k_R = 1.08 \cdot 10^{-9} \cdot \text{ft}^2$
vertical gas permeability (intrinsic)		$k_Z = 1.08 \cdot 10^{-11} \cdot \text{ft}^2$
universal gas constant		$R_{\text{air}} = 49709 \frac{\text{ft} \cdot \text{lb}_f}{\text{slug} \cdot \text{R}}$
injection gas temperature		$T = 518.67 \text{R}$
injection mass flow rate		$M = 0.5 \frac{\text{lb}}{\text{sec}}$
unit weight of air		$\gamma_{\text{air}} = 0.08 \frac{\text{lb}_f}{\text{ft}^3}$
dynamic viscosity of air		$\mu_{\text{air}} = 3.74 \cdot 10^{-7} \frac{\text{lb}_f \cdot \text{sec}}{\text{ft}^2}$
ambient air pressure		$P_a = 14.7 \frac{\text{lb}_f}{\text{in}^2}$
average gas molecular weight		$M_{\text{wt}} = 30$
critical entrainment air velocity		$v_{\text{cr}} = 5 \frac{\text{ft}}{\text{sec}}$
depth of injection		$Z_s = 14 \text{ft}$

depth and radius at which pressures and velocities are being determined

$Z_0 = 0 \text{ft}$	$R_0 = 0.25 \text{ft}$
$Z_{\text{incr}} = 1 \text{ft}$	$R_{\text{incr}} = 1 \text{ft}$
$z = 0, 1, \dots, 30$	$r = 0, 1, \dots, 30$
$Z_{z+1} = Z_z + Z_{\text{incr}}$	$R_{r+1} = R_r + R_{\text{incr}}$

$$q = \frac{2 \cdot P_a \cdot R_{\text{air}} \cdot T \cdot M}{\phi \cdot M_{\text{wt}}}$$

$$\alpha_R = \frac{k_R \cdot P_a}{\phi \cdot \mu_{\text{air}}}$$

$$R_{k_r} = \left(\frac{k_Z}{k_R} \right)^{\frac{1}{2}} \cdot R_r$$

Calculating the pressure distribution around the injection well:

$$u_{(z,r)} = \frac{q}{4 \cdot \pi \cdot \alpha_R \cdot \left[R_{k_r}^2 + Z_z + Z_s^2 \right]}$$

$$P_{(z,r)} = \sqrt{P_a^2 - u_{(z,r)} \cdot \frac{\text{ft} \cdot \text{sec}^2}{\text{lb}}}$$

Calculating air velocities in the direction of the co-ordinate axes with the well as the origin

X - direction (radially outward from the well)

$P_{x1} = \text{submatrix}(P, 0, 30, 0, 29)$

$P_{x2} = \text{submatrix}(P, 0, 30, 1, 30)$

$$\text{air_vel}_x = \frac{K \cdot \begin{bmatrix} P_{x1} & P_{x2} \\ \phi & \gamma \text{ air} \cdot R \text{ incr} \end{bmatrix} \cdot \text{lb}}{\text{ft}^2}$$

Y - direction

$P_{y1} = \text{submatrix}(P, 0, 29, 0, 30)$

$P_{y2} = \text{submatrix}(P, 1, 30, 0, 30)$

$$\text{air_vel}_y = \frac{K \cdot \begin{bmatrix} P_{y1} & P_{y2} \\ \phi & \gamma \text{ air} \cdot Z \text{ incr} \end{bmatrix} \cdot \text{lb}}{\text{ft}^2}$$

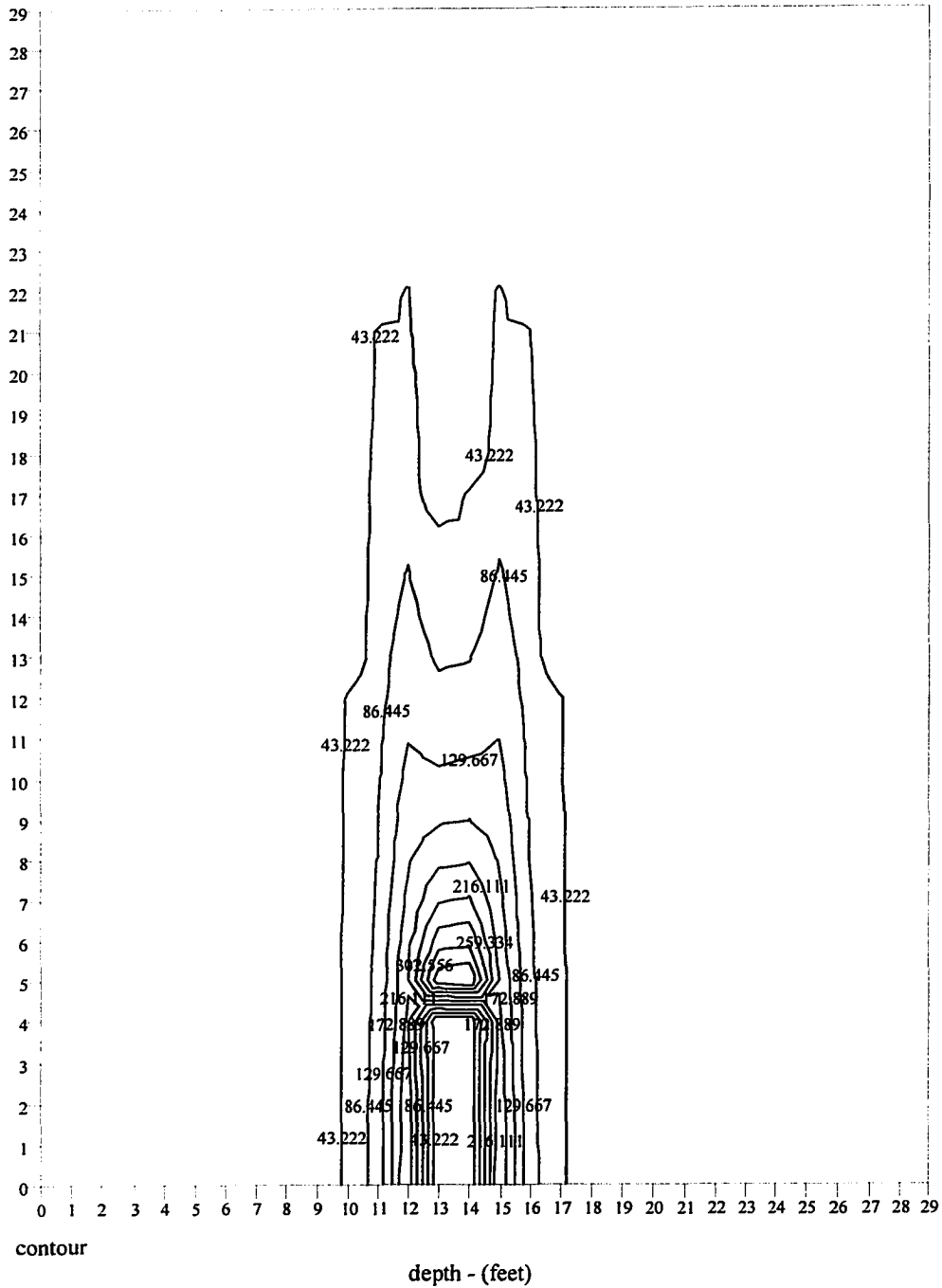
Calculating the resultant velocity vectors around the well

$$\text{air_vel} := \begin{array}{l} \text{for } J \in 0, 1..29 \\ \quad \text{for } K \in 0, 1..29 \\ \quad \quad \text{resultant}_{(J,K)} = \sqrt{[\text{air_vel}_{x(J,K)}]^2 + [\text{air_vel}_{y(J,K)}]^2} \\ \quad \quad \text{resultant} \end{array}$$

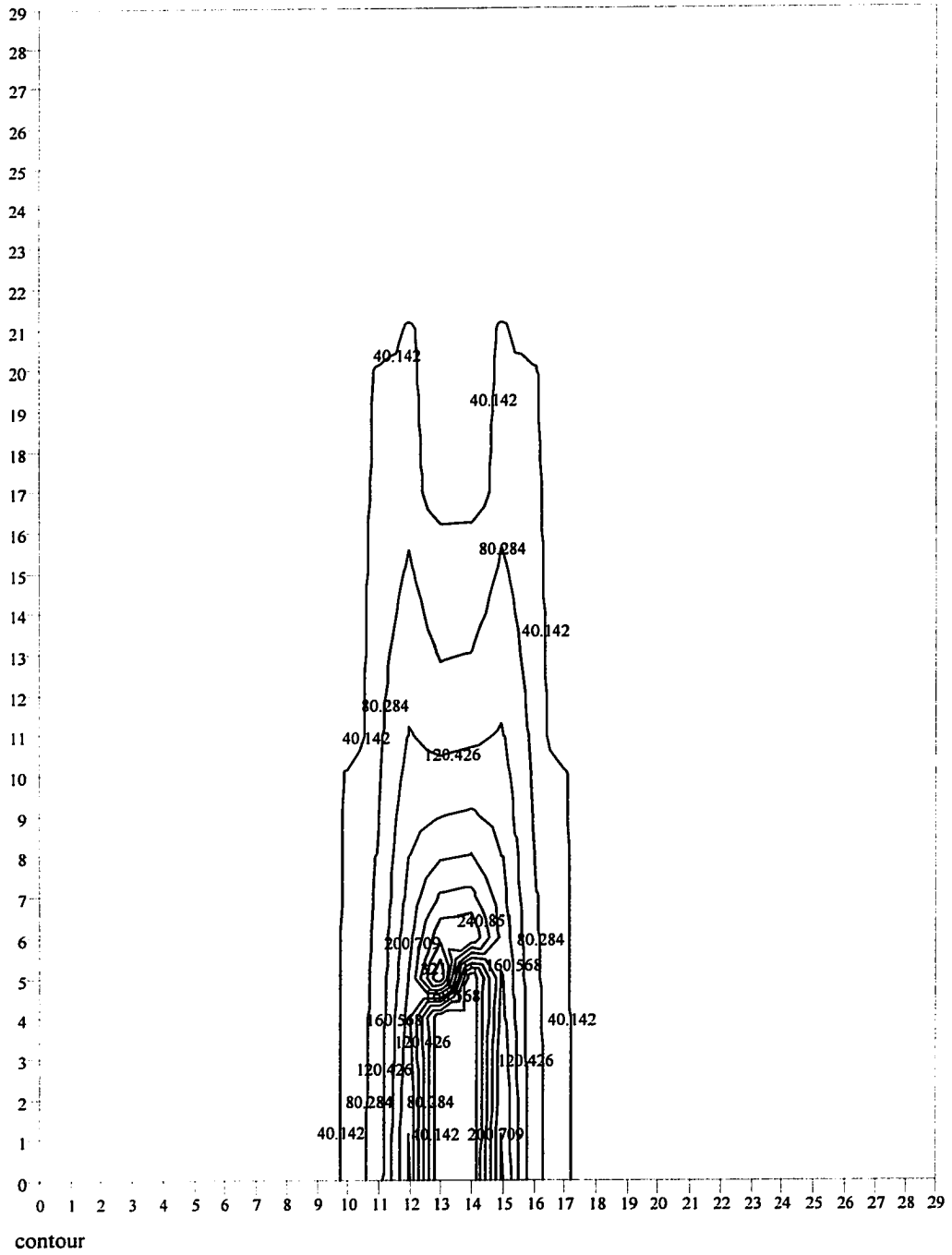
Considering only the velocity vectors whose magnitude is greater than the fluidization velocity

$$\text{fluidization_vel} := \begin{array}{l} \text{for } J \in 0, 1..29 \\ \quad \text{for } K \in 0, 1..29 \\ \quad \quad \left[\begin{array}{l} m \cdot \text{air_vel}_{(J,K)} \\ [\text{air_vel}_{(J,K)} - \text{air_vel}_{(J,K)}] \text{ if } \left(m \cdot \frac{\text{ft}}{\text{sec}} > v_{cr} \right) \\ [\text{air_vel}_{(J,K)} - 0] \text{ otherwise} \end{array} \right] \\ \quad \quad \text{air_vel} \end{array}$$

**APPENDIX F-2
EXTENT OF PARTICULATE TRANSPORT
(North - Quad Nozzle Setting)**

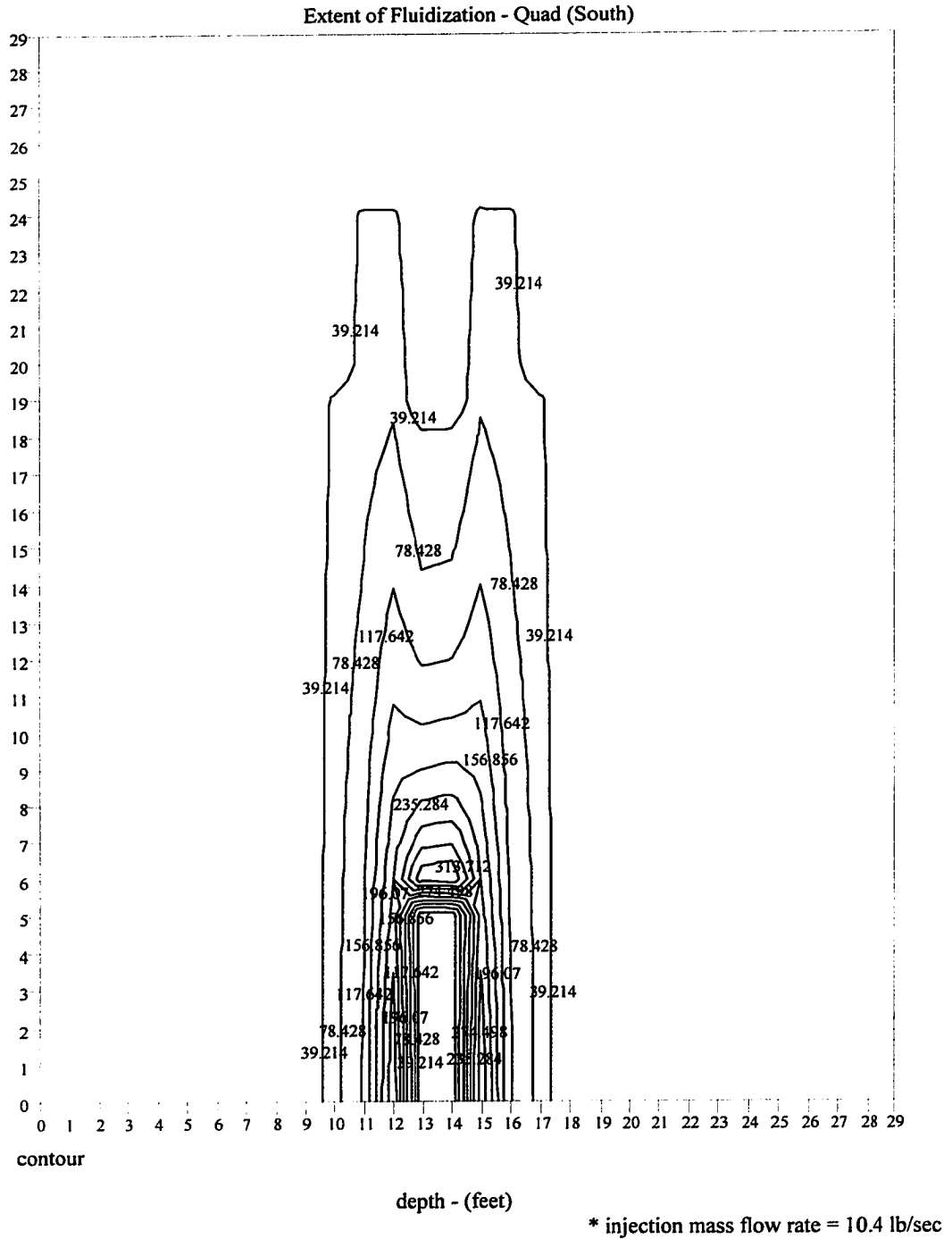


**APPENDIX F-3
EXTENT OF PARTICULATE TRANSPORT
(South - Quad Nozzle Setting)**

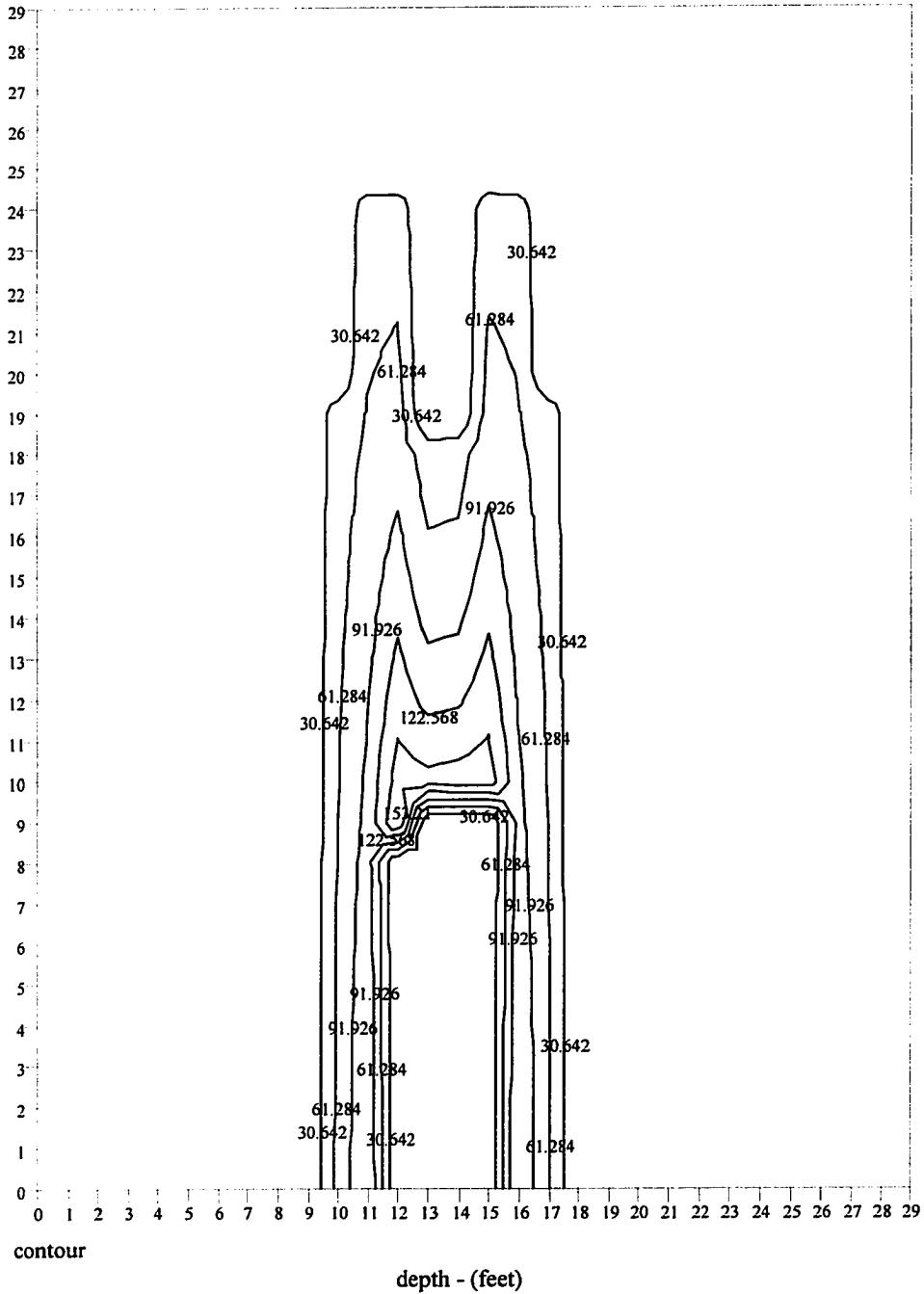


* injection mass flow rate = 7.5 lb/sec

APPENDIX F-4 EXTENT OF PARTICULATE TRANSPORT (East - Quad Nozzle Setting)



APPENDIX F-5 EXTENT OF PARTICULATE TRANSPORT (West - Quad Nozzle Setting)



APPENDIX G

SHAPE FACTORS OF FLOWNETS FOR DIFFERENT FRACTURE GEOMETRIES

R/z	r/R	$K_h = K_v$			$K_h = 5K_v$			$K_h = 10K_v$			Remarks
		N_f	% Q-injected	$\Sigma N_f / \Sigma N_d$	N_f	% Q-injected	$\Sigma N_f / \Sigma N_d$	N_f	% Q-injected	$\Sigma N_f / \Sigma N_d$	
0.14	0.1	1.48	9.3	0.98	1.16	9.9	0.79	1.06	10.9	0.69	No of head drops for all these flownets is 24.0
	0.2	1.59	10.0		1.35	11.5		0.92	9.5		
	0.3	1.5	9.4		1.12	9.6		0.91	9.4		
	0.4	1.64	10.3		1.2	10.2		1.01	10.4		
	0.5	1.6	10.1		1.13	9.6		1.01	10.4		
	0.6	1.74	11.0		1.22	10.4		1.04	10.7		
	0.7	1.8	11.3		1.32	11.3		1.06	10.9		
	0.8	1.91	12.0		1.44	12.3		1.23	12.7		
	0.9	2.63	16.6		1.77	15.1		1.45	15.0		
	1	7.69	48.4		7.28	62.2		7.06	72.9		
0.29	0.1	1.9	6.0	1.32	1.35	6.3	0.89	1.23	6.6	0.77	
	0.2	1.9	6.0		1.69	7.8		1.08	5.8		
	0.3	1.91	6.0		1.43	6.6		1.2	6.5		
	0.4	2.02	6.4		1.4	6.5		1.21	6.5		
	0.5	1.95	6.1		1.42	6.6		1.26	6.8		
	0.6	2.21	7.0		1.62	7.5		1.3	7.0		
	0.7	2.53	8.0		1.69	7.8		1.39	7.5		
	0.8	5.47	17.3		1.64	7.6		1.4	7.5		
	0.9	3.18	10.0		2.18	10.1		1.85	10.0		
	1	8.64	27.2		7.17	33.2		6.63	35.7		
0.43	0.1	1.89	5.8	1.37	1.49	6.3	0.98	1.32	6.6	0.83	
	0.2	2.07	6.3		1.5	6.3		1.27	6.3		
	0.3	2.21	6.7		1.55	6.6		1.37	6.8		
	0.4	2.41	7.3		1.63	6.9		1.24	6.2		

APPENDIX G (Cont.)

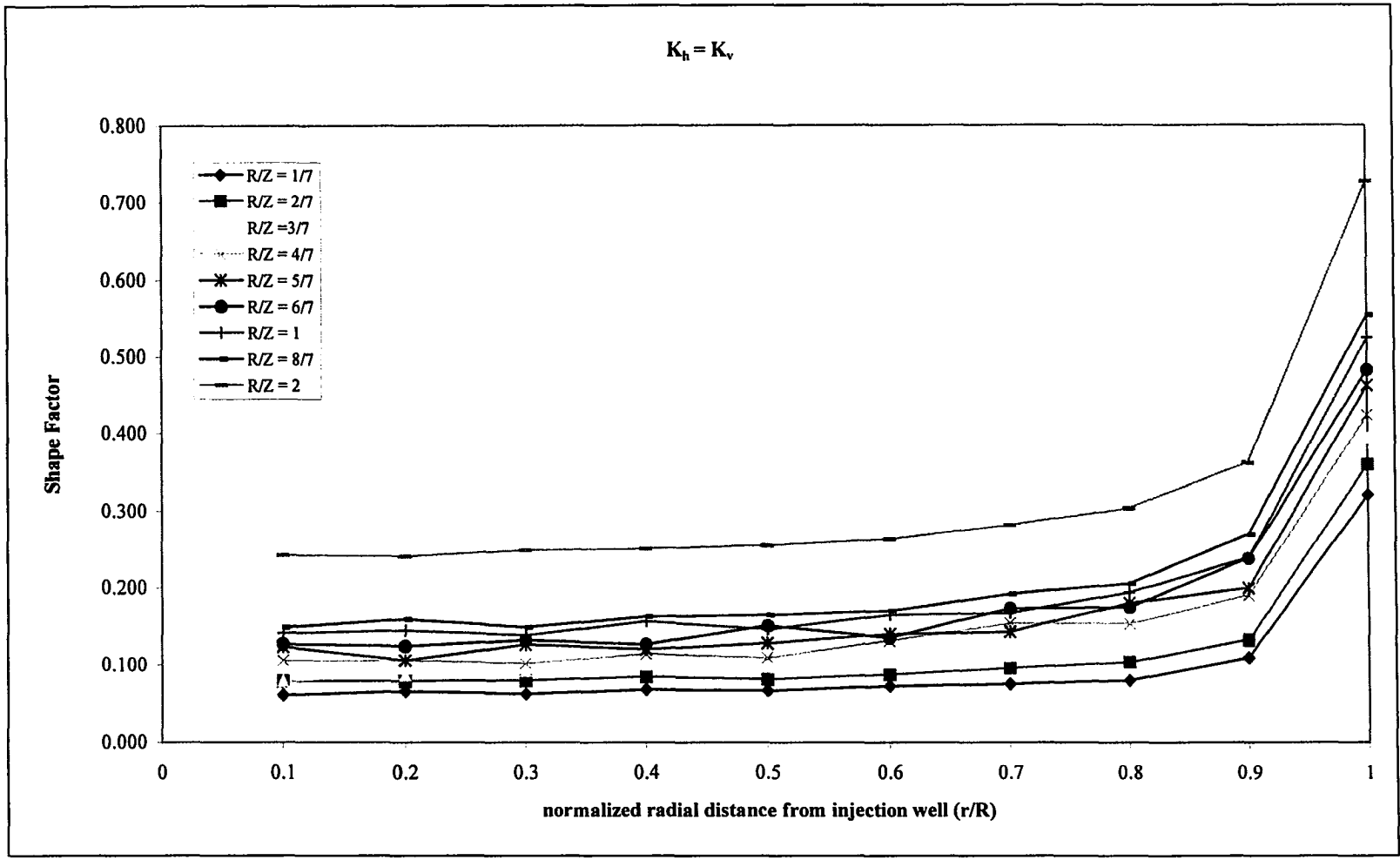
R/z	r/R	$K_h = K_v$			$K_h = 5K_v$			$K_h = 10K_v$			Remarks
		N_f	% Q-injected	$\Sigma N_f / \Sigma N_d$	N_f	% Q-injected	$\Sigma N_f / \Sigma N_d$	N_f	% Q-injected	$\Sigma N_f / \Sigma N_d$	
0.43	0.5	2.38	7.3		1.84	7.8		1.43	7.1		
	0.6	2.68	8.2		1.66	7.0		1.52	7.6		
	0.7	2.76	8.4		1.89	8.0		1.57	7.8		
	0.8	3.11	9.5		2.2	9.3		1.76	8.8		
	0.9	3.84	11.7		2.47	10.4		1.89	9.4		
	1	9.45	28.8		7.43	31.4		6.73	33.5		
0.57	0.1	2.53	6.7	1.56	1.78	7.0	1.06	1.35	6.3	0.89	
	0.2	2.55	6.8		1.6	6.3		1.37	6.4		
	0.3	2.46	6.6		1.63	6.4		1.42	6.6		
	0.4	2.76	7.4		1.74	6.8		1.58	7.4		
	0.5	2.64	7.0		1.86	7.3		1.32	6.1		
	0.6	2.98	7.9		1.89	7.4		1.67	7.8		
	0.7	3.15	8.4		2.16	8.4		1.88	8.7		
	0.8	3.68	9.8		2.34	9.1		1.9	8.8		
	0.9	4.57	12.2		2.9	11.3		2.21	10.3		
	1	10.18	27.1		7.68	30.0		6.79	31.6		
0.71	0.1	2.98	7.2	1.72	1.87	6.8	1.14	1.62	7.2	0.94	
	0.2	2.55	6.1		1.73	6.3		1.44	6.4		
	0.3	3.05	7.3		1.73	6.3		1.53	6.8		
	0.4	2.9	7.0		1.99	7.3		1.69	7.5		
	0.5	3.07	7.4		1.92	7.0		1.42	6.3		
	0.6	3.36	8.1		2.22	8.1		1.8	7.9		
	0.7	3.41	8.2		2.19	8.0		1.74	7.7		
	0.8	4.31	10.4		2.71	9.9		2.33	10.3		
	0.9	4.77	11.5		3.1	11.3		2.17	9.6		
	1	11.1	26.7		7.98	29.1		6.91	30.5		

APPENDIX G (Cont.)

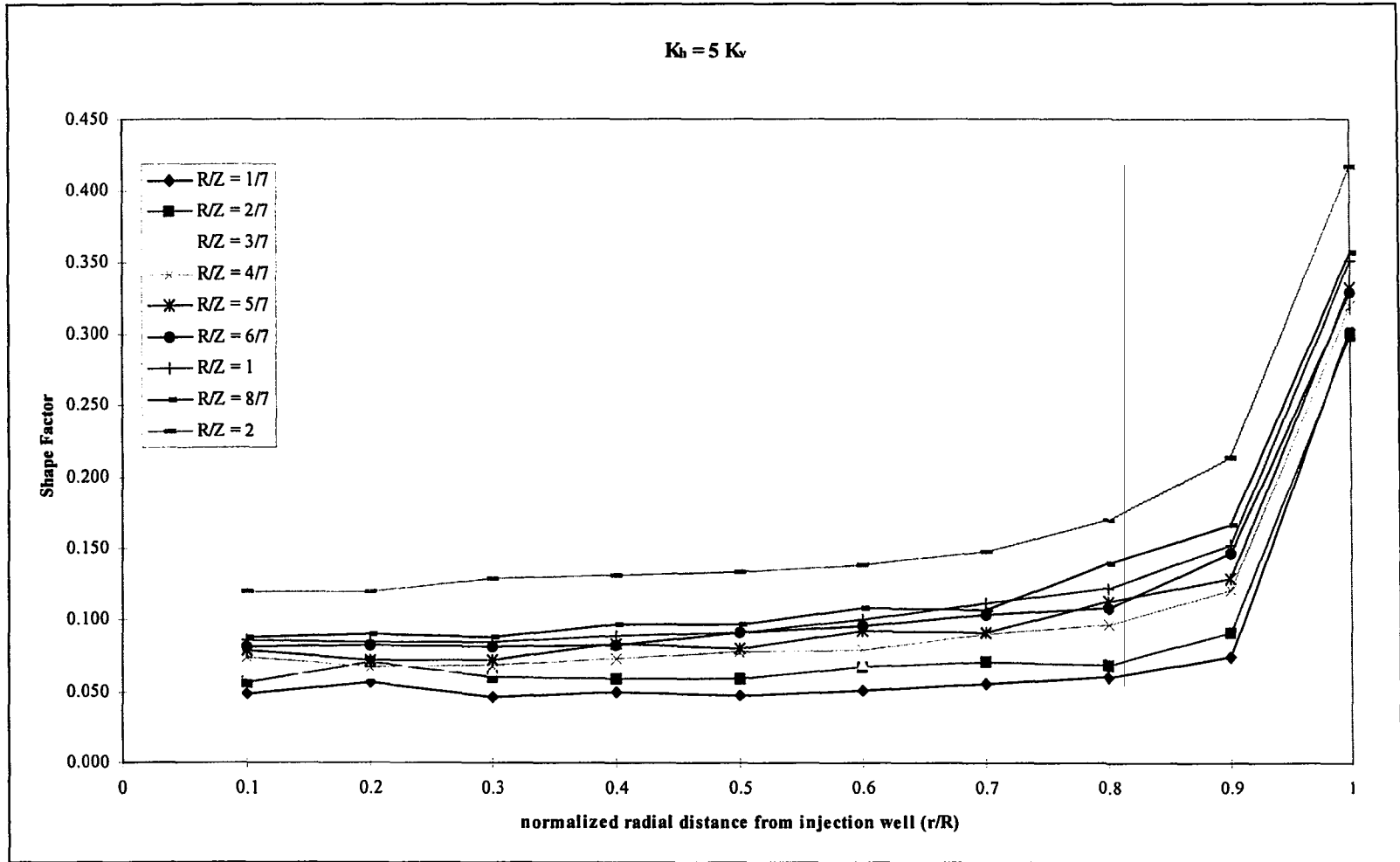
R/z	r/R	$K_h = K_v$			$K_h = 5K_v$			$K_h = 10K_v$			Remarks
		N_f	% Q-injected	$\Sigma N_f / \Sigma N_d$	N_f	% Q-injected	$\Sigma N_f / \Sigma N_d$	N_f	% Q-injected	$\Sigma N_f / \Sigma N_d$	
0.86	0.1	3.06	6.8	1.86	1.95	6.8	1.20	1.42	6.1	0.97	
	0.2	2.99	6.7		1.98	6.9		1.45	6.2		
	0.3	3.17	7.1		1.95	6.8		1.57	6.7		
	0.4	3.05	6.8		1.98	6.9		1.58	6.8		
	0.5	3.61	8.1		2.18	7.6		1.73	7.4		
	0.6	3.23	7.2		2.29	7.9		1.76	7.6		
	0.7	4.16	9.3		2.48	8.6		2	8.6		
	0.8	4.18	9.3		2.59	9.0		2.29	9.8		
	0.9	5.7	12.7		3.53	12.3		2.76	11.8		
	1	11.6	25.9		7.88	27.4		6.75	29.0		
1	0.1	3.39	7.0	2.01	2.05	6.7	1.27	1.47	6.0	1.01	
	0.2	3.46	7.2		2.02	6.6		1.49	6.1		
	0.3	3.32	6.9		2.01	6.6		1.58	6.5		
	0.4	3.74	7.7		2.13	7.0		1.65	6.8		
	0.5	3.5	7.2		2.19	7.2		1.79	7.3		
	0.6	3.94	8.2		2.42	7.9		1.92	7.9		
	0.7	4.01	8.3		2.68	8.8		2.13	8.7		
	0.8	4.65	9.6		2.93	9.6		2.38	9.8		
	0.9	5.72	11.8		3.66	12.0		2.87	11.8		
	1	12.59	26.1		8.43	27.6		7.08	29.1		
1.14	0.1	3.56	6.8	2.17	2.1	6.5	1.33	1.39	5.5	1.05	
	0.2	3.81	7.3		2.16	6.7		1.73	6.8		
	0.3	3.57	6.8		2.11	6.6		1.55	6.1		
	0.4	3.9	7.5		2.32	7.2		1.84	7.3		
	0.5	3.94	7.6		2.32	7.2		1.75	6.9		
	0.6	4.08	7.8		2.61	8.1		2.08	8.2		

APPENDIX G (Cont.)

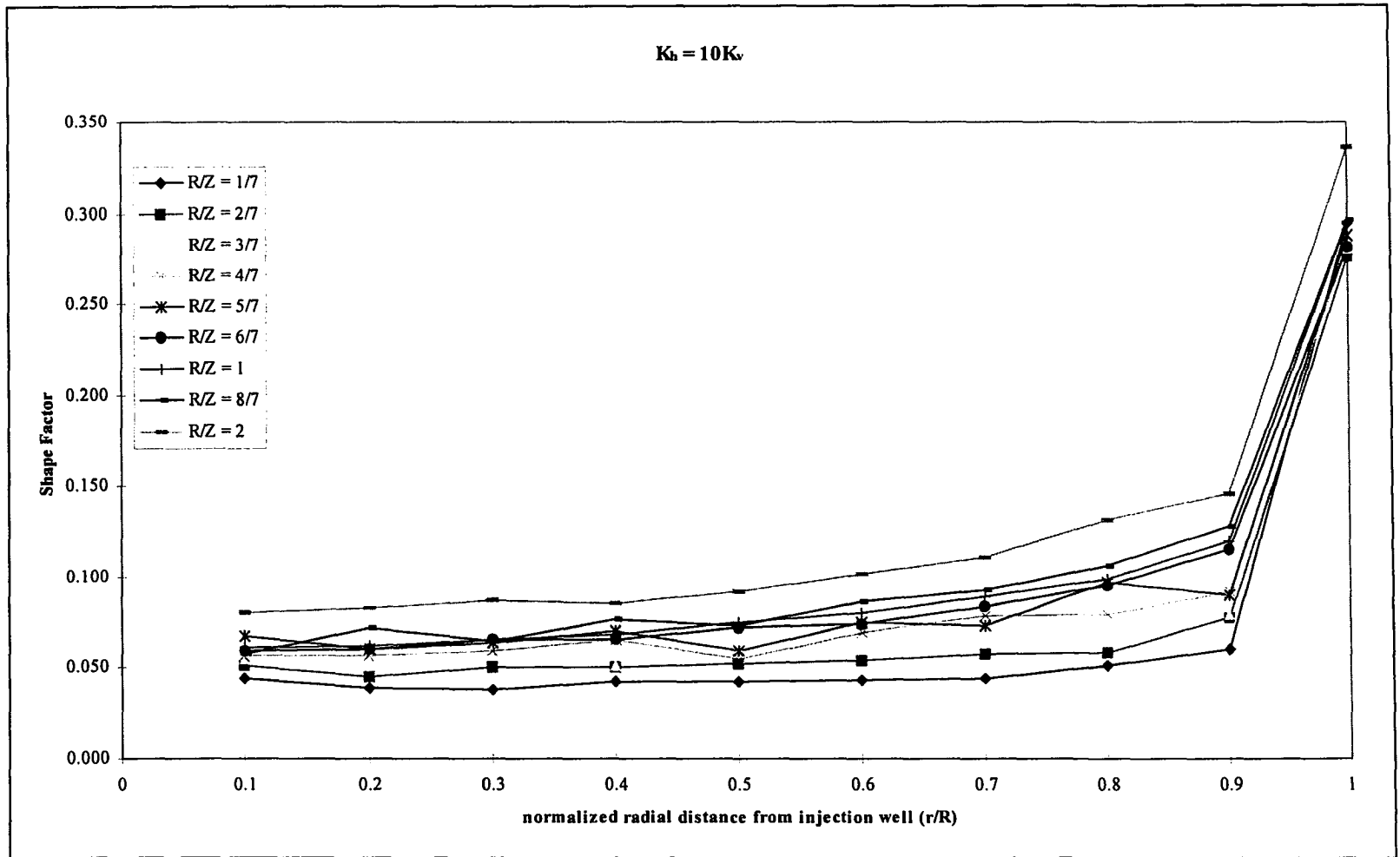
R/z	r/R	$K_h = K_v$			$K_h = 5K_v$			$K_h = 10K_v$			Remarks
		N_f	% Q-injected	$\Sigma N_f / \Sigma N_d$	N_f	% Q-injected	$\Sigma N_f / \Sigma N_d$	N_f	% Q-injected	$\Sigma N_f / \Sigma N_d$	
	0.7	4.59	8.8		2.57	8.0		2.23	8.8		
	0.8	4.92	9.4		3.34	10.4		2.55	10.1		
	0.9	6.46	12.4		3.98	12.4		3.06	12.1		
	1	13.32	25.5		8.57	26.7		7.11	28.1		
2	0.1	5.8	7.6	3.17	2.89	7.0	1.72	1.9	6.4	1.25	
	0.2	5.77	7.6		2.89	7.0		1.99	6.6		
	0.3	5.97	7.8		3.09	7.5		2.1	7.0		
	0.4	6.02	7.9		3.15	7.6		2.06	6.8		
	0.5	6.11	8.0		3.22	7.8		2.2	7.3		
	0.6	6.31	8.3		3.32	8.0		2.45	8.1		
	0.7	6.75	8.9		3.55	8.6		2.66	8.8		
	0.8	7.3	9.6		4.06	9.8		3.16	10.5		
	0.9	8.7	11.4		5.11	12.4		3.5	11.6		
	1	17.47	22.9		10	24.2		8.06	26.8		



Appendix G cont. Variation of flownet shape factor with radial distance from the injection well



Appendix G cont. Variation of flownet shape factor with radial distance from the injection well



Appendix G cont. Variation of flownet shape factor with radial distance from the injection well

APPENDIX H1
FLUID CONDUCTIVITIES OF ROCKS AND SOILS

Material	Intrinsic Permeability k	Hydraulic Conductivity K _{water}	Pneumatic Conductivity K _{air}	Ref
ROCK	S.I.(cm ²)	S.I.(cm/sec)	S.I.(cm/sec)	
Anhydrite	4.08E-16 - 2.04E-11	4E-11 - 2E-6	2.6E-12 - 1.3E-7	T
Basalt	1.93E-14 - 4.81E-10	1.89E-9 - 4.72E-5	1.2E-10 - 3.1E-6	A
Basalt	1.18E-12	1.16E-7	7.6E-9	B
Basalt	2.04E-14 - 4.34E-10	2.00E-9 - 4.25E-5	1.3E-10 - 2.8E-6	C
Basalt, permeable	4.85E-10 - 4.85E-05	4.75E-5 - 4.75	3.1E-6 - 3.1 E-1	B
Basaltic lava and sediments	1.84E-06 - 1.84E-04	1.80E-1 - 18.0	1.2E-2 - 1.2	Q
Basalt	2.04E-14 - 4.28E-10	2.0E-9 - 4.2E-5	1.3E-10 - 2.8E-6	T
Basalt - permeable	4.08E-10 - 2.04E-05	4.0E-5 - 2.00	2.6E-6 - 1.3E-1	T
Carbonate rocks (augmented by tubes tunnels and cavities)	4.86E-13 - 1.16E-06	4.76E-8 - 1.14E-1	3.1E-9 - 7.5E-3	F
Chalk	3.67E-07	3.6E-2	2.4E-3	P
Chalk (fractured)	2.24E-07	2.2E-2	1.4E-3	P
Dolomite	4.34E-14 - 9.62E-14	4.25E-9 - 9.43E-9	2.8E-10 - 6.2E-9	A
Dolomite	1.18E-11	1.16E-6	7.6E-8	B
Dolomite and limestone - fractured	3.06E-06 - 7.14E-06	3.00E-1 - 7.00E-1	2.0E-2 - 4.6E-2	H
Dolomite - fractured	5.10E-07 - 2.55E-06	5.0E-2 - 2.5E-1	3.3E-3 - 1.6E-2	I
Dolomite - fractured	1.16E-10	1.14E-5	7.5E-7	J
Gabbro - weathered	2.36E-09	2.31E-4	1.5E-5	B
Gabbro - weathered	5.10E-10 - 3.88E-09	5.0E-5 - 3.8E-4	3.3E-6 - 2.5E-5	C
Gabbro - weathered	5.61E-10 - 3.88E-09	5.5E-5 - 3.8E-4	3.6E-6 - 2.5E-5	T
Gneiss	2.41E-13 - 2.41E-11	2.36E-8 - 2.36E-6	1.5E-9 - 1.5E-7	A
Gneiss	4.79E-13 - 2.65E-08	4.70E-8 - 2.60E-3	3.1E-9 - 1.7E-4	G
Granite	4.34E-16 - 2.41E-15	4.25E-11 - 2.36E-10	2.8E-12 - 1.5E-11	A
Granite, weathered	1.65E-08	1.62E-3	1.0E-4	B
Granite, weathered	3.37E-09 - 5.30E-08	3.3E-4 - 5.2E-3	2.2E-5 - 3.4E-4	D
Granite, weathered	3.37E-09 - 5.30E-08	3.3E-4 - 5.2E-3	2.2E-5 - 3.4E-4	T
Granite, fractured	3.06E-07 - 9.18E-07	3E-2 - 9E-2	2.0E-3 - 6.0E-3	O
Granite, fractured	1.02E-10 - 1.02E-08	1.0E-5 - 1.0E-3	6.6E-7 - 6.6E-5	O
Greenstone	5.81E-11 - 1.02E-07	5.7E-6 - 1E-2	3.7E-7 - 6.6E-4	G
Hematite	9.62E-16 - 4.28E-12	9.43E-11 - 4.2E-7	6.2E-12 - 2.7E-8	A
Igneous and Metamorphic Rocks	9.59E-13 - 1.94E-09	9.4E-8 - 19.0E-5	6.2E-9 - 1.2E-5	G
Igneous and Metamorphic Rocks - unfractured	3.06E-17 - 2.04E-13	3E-12 - 2E-8	2.0E-13 - 1.3E-9	T

Material	Intrinsic Permeability k	Hydraulic Conductivity K_{water}	Pneumatic Conductivity K_{air}	Ref
ROCK	S.I.(cm ²)	S.I.(cm/sec)	S.I.(cm/sec)	
Igneous and Metamorphic Rocks - Fractured	8.16E-12 - 3.06E-07	8E-7 - 3E-2	5.2x10 ⁻⁸ - 2.0x10 ⁻³	T
Igneous - coarse grained rock (granite, diorite, gabbro)	4.28E-12 - 4.28E-08	4.2E-7 - 4.2E-3	2.8x10 ⁻⁸ - 2.8x10 ⁻⁴	G
Igneous, tight, fine grained rock (rhyolite, trachite, basalt)	6.22E-10 - 1.33E-06	6.1E-5 - 1.3E-1	4.0x10 ⁻⁶ - 8.5x10 ⁻³	G
Igneous, fine grained, cavernous rock	1.18E-06 - 8.28E-05	1.16E-1 - 8.12	7.6x10 ⁻³ - 5.3 x10 ⁻¹	F
Limestone, karst and reef	1.02E-09 - 1.02E-05	1.0E-4 - 1.0	6.6x10 ⁻⁶ - 6.6x10 ⁻²	C
Limestone	4.81E-15 - 9.62E-13	4.72E-10 - 9.43E-8	3.1x10 ⁻¹¹ - 6.2x10 ⁻⁹	A
Limestone	1.11E-08	1.09E-3	7.2x10 ⁻³	B
Limestone (0.16 porosity)	1.39E-09	1.36E-4	8.9x10 ⁻⁶	C
Limestone, karst	2.36E-09 - 4.85E-05	2.31E-4 - 4.75	1.52E-05 - 3.12E-01	B
Limestone, argillaceous	9.87E-13	9.68E-8	6.35E-09	C
Limestone and Dolomite	5.91E-13 - 4.85E-09	5.79E-8 - 4.75E-4	3.80E-09 - 3.12E-05	B
Limestone	1.33E-11 - 1.73E-11	1.3E-6 - 1.7E-6	8.53E-08 - 1.12E-07	K
Limestone	4.79E-09	4.7E-4	3.08E-05	L
Limestone	1.12E-09	1.1E-4	7.22E-06	I
Limestone, fractured	1.84E-07 - 4.85E-06	1.8E-2 - 4.75E-1	1.18E-03 - 3.12E-02	M
Limestone fractured and calcareous sandstone	1.50E-07	1.47E-2	9.64E-04	N
Limestone - karst and reef	1.02E-09 - 2.04E-05	1.0E-4 - 2.0	6.56E-06 - 1.31E-01	T
Limestone and dolomite	1.02E-12 - 6.12E-09	1.0E-7 - 6.0E-4	6.56E-09 - 3.94E-05	T
Quartzite	1.94E-12 - 2.65E-08	1.9E-7 - 2.6E-3	1.25E-08 - 1.71E-04	G
Rock Salt	1.02E-15 - 1.02E-13	1.0E-10 - 1.0E-8	6.56E-12 - 6.56E-10	T
Sandstone	3.37E-12 - 5.51E-08	3.3E-7 - 5.4E-3	2.16E-08 - 3.54E-04	G
Sandstone	1.45E-12 - 1.45E-08	1.42E-7 - 1.42E-3	9.32E-09 - 9.32E-05	A
Sandstone	4.85E-11	4.75E-6	3.12E-07	B
Sandstone - 0.29 porosity	2.37E-08	2.32E-3	1.52E-04	C
Sandstone	3.47E-10	3.4E-5	2.23E-06	E
Sandstone - fine grained	2.36E-09	2.31E-4	1.51E-05	B

Material	Intrinsic Permeability k	Hydraulic Conductivity K_{water}	Pneumatic Conductivity K_{air}	Ref
ROCK	S.I.(cm ²)	S.I.(cm/sec)	S.I.(cm/sec)	
Sandstone - fine	5.10E-12 - 2.32E-08	5E-7 - 2.27E-3	3.28E-08 - 1.49E-04	D
Sandstone - medium grained	3.66E-08	3.59E-3	2.36E-04	B
Sandstone - silty	2.57E-11	2.52E-6	1.65E-07	C
Sandstone - coarse	1.09E-08	1.07E-3	7.02E-05	C
Sandstone (arkosic), siltstone and shale	4.79E-13 - 7.24E-08	4.7E-8 - 7.1E-3	3.08E-09 - 4.66E-04	G
Sandstone	2.45E-09 - 1.43E-07	2.4E-4 - 1.4E-2	1.57E-05 - 9.18E-04	R
Sandstone	3.06E-13 - 6.12E-09	3E-8 - 6E-4	1.97E-09 - 3.94E-05	T
Schist	2.36E-09	2.31E-4	1.52E-05	B
Schist	2.04E-14 - 1.15E-08	2.0E-9 - 1.13E-3	1.31E-10 - 7.41E-05	D
Schist	4.79E-12 - 1.22E-07	4.7E-7 - 1.2E-2	3.08E-08 - 7.87E-04	G
Schist and Gneiss - fractured and crystalline	3.67E-10	3.6E-5	2.36E-06	S
Shale	2.45E-09 - 2.65E-08	2.4E-4 - 2.6E-3	1.57E-05 - 1.71E-04	G
Shale	1.18E-16 - 4.85E-11	1.16E-11 - 4.75E-6	7.61E-13 - 3.12E-07	B
Shale	2.04E-11	2.0E-6	1.31E-07	E
Shale	1.02E-16 - 2.04E-12	1.0E-11 - 2.0E-7	6.56E-13 - 1.31E-08	T
Siltstone	1.02E-14 - 1.45E-11	1.0E-9 - 1.42E-6	6.56E-11 - 9.32E-08	D
Siltstone - Shale	2.04E-11	2.0E-6	1.31E-07	E
Siltstone - Shale	2.86E-12	2.8E-7	1.84E-08	E
Siltstone	1.02E-14 - 1.43E-11	1.0E-9 - 1.4E-6	6.56E-11 - 9.18E-08	T
Slate	4.81E-10 - 1.45E-09	4.72E-5 - 1.42E-4	3.10E-06 - 9.32E-06	A
Slate	9.45E-13	9.26E-8	6.07E-09	B
Tuff	1.45E-13 - 4.81E-09	1.42E-8 - 4.72E-4	9.32E-10 - 3.10E-05	A
Tuff	2.36E-09	2.31E-4	1.52E-05	B
Material	Intrinsic Permeability k	Hydraulic Conductivity K_{water}	Pneumatic Conductivity K_{air}	Ref
SOILS	S.I.(cm ²)	S.I.(cm/sec)	S.I.(cm/sec)	Ref
Calcium kaolinite	2.12E-11 - 1.18E-10	2.08x10 ⁻⁶ - 1.16x10 ⁻⁵	1.36E-07 - 7.61E-07	B,V
Caliche (compacted)	5.08E-14 - 1.01E-12	4.98x10 ⁻⁹ - 9.95x10 ⁻⁸	3.27E-10 - 6.53E-09	B
Caliche (compacted)	2.04E-13 - 1.02E-12	2x10 ⁻⁸ - 1.0x10 ⁻⁷	1.31E-09 - 6.56E-09	V
Caliche (compacted)	5.10E-14 - 1.84E-13	5.0x10 ⁻⁹ - 1.8x10 ⁻⁸	3.28E-10 - 1.18E-09	V
Clay	4.81E-13 - 4.81E-10	4.72x10 ⁻⁸ - 4.72x10 ⁻³	3.10E-09 - 3.10E-06	A
Clay	1.01E-12	9.95x10 ⁻⁸	6.53E-09	B
Clay	1.02E-14 - 4.79E-12	1.00x10 ⁻⁹ - 4.70x10 ⁻⁷	6.56E-11 - 3.08E-08	D
Clay	1.02E-16 - 4.79E-12	1x10 ⁻¹¹ - 4.7x10 ⁻⁷	6.56E-13 - 3.08E-08	T
Clay	< 1.02E-11	< 1.0x10 ⁻⁶	< 6.56E-08	U
Clay	< 1.02E-12	< 1.0x10 ⁻⁷	< 6.56E-09	V

Material	Intrinsic Permeability k	Hydraulic Conductivity K_{water}	Pneumatic Conductivity K_{air}	Ref
SOILS	S.I.(cm ²)	S.I.(cm/sec)	S.I.(cm/sec)	Ref
Clay - montmorillonite	1.04E-20	1.00E-10	6.56E-12	C
Clay - kaolinite	1.04E-18	1.00E-8	6.56E-10	C
Clay - unweathered marine	5.18E-21 - 1.33E-17	4.98E-11 - 1.27E-7	3.27E-12 - 8.33E-09	B
Clay - unweathered marine	8.32E-21 - 2.08E-17	8.0E-11 - 2.0E-7	5.25E-12 - 1.31E-08	T
Clay - silty	4.95E-18 - 9.76E-15	4.75E-8 - 9.38E-5	3.12E-09 - 6.15E-06	B
Clay - sandy	2.65E-20 - 2.65E-15	2.55E-10 - 2.55E-5	1.67E-11 - 1.67E-06	B
Clay - sandy	2.70E-20 - 3.64E-20	2.6E-10 - 3.5E-10	1.71E-11 - 2.30E-11	V
Clay - sandy	7.28E-15 - 2.92E-14	7.0E-5 - 2.8E-4	4.59E-06 - 1.84E-05	V
Clay - lean	2.05E-19 - 2.90E-18	1.97E-9 - 2.78E-8	1.29E-10 - 1.82E-09	B,V
Clay - sodium Boston blue	1.68E-20 - 1.03E-17	1.62E-10 - 9.95E-8	1.06E-11 - 6.53E-09	B,V
Clay - Vicksburg buckshot	3.13E-20 - 1.14E-19	3.01E-10 - 1.10E-9	1.97E-11 - 7.22E-11	B,V
Clay - compacted Boston blue	3.73E-19 - 3.13E-18	3.59E-9 - 3.01E-8	2.36E-10 - 1.97E-09	B,V
Clay - London	1.04E-18	1.0E-8	6.56E-10	W
Clay - Boston blue	1.04E-18	1.0E-8	6.56E-10	W
Clay - loess	4.21E-19 - 5.18E-19	4.05E-9 - 4.98E-9	2.66E-10 - 3.27E-10	B
Sodium montmorillonite	1.90E-18	1.82E-8	1.19E-09	B, V
Sodium montmorillonite	1.04E-18 - 1.04E-19	1.0E-8 - 1.0E-9	6.56E-10 - 6.56E-11	W
Clay -silty (CL-ML)	6.14E-18 - 2.01E-17	5.9E-8 - 1.93E-7	3.87E-09 - 1.27E-08	T
Clay - lean (CL)	5.00E-18 - 1.10E-17	4.8E-8 - 1.06E-7	3.15E-09 - 6.95E-09	T
Clay - fat (CH)	1.04E-18 - 9.99E-18	1.0E-8 - 9.6E-8	6.56E-10 - 6.29E09	T
Clay - quick	2.08E-18	2.0E-8	1.31E-09	W ₁
Clay - Bootlegger Cove clay	2.08E-17	20E-8	1.31E-08	W ₂
Clay -silty, West Branch Dam	1.24E-18 - 6.76E-18	1.2E-8 - 6.5E-8	7.87E-10 - 4.26E-09	W ₃
Cobbles	> 1.97E-10	> 1.89	> 1.24E-01	A
Glacial till	1.03E-20 - 1.20E-14	9.95E-11 - 1.16E-4	6.53E-12 - 7.61E-06	B
Glacial till - NE Ohio	3.98E-18 - 4.46E-16	3.82E-8 - 4.28E-6	2.51E-09 - 2.81E-07	B
Glacial till surficial, Montgomery Co., Ohio	3.98E-18 - 4.46E-15	3.82E-8 - 4.28E-5	2.51E-09 - 2.81E-06	B
Glacial till, buried, Rohrsers Island, Ohio	1.45E-16 - 6.63E-16	1.39E-6 - 6.37E-6	9.12E-08 - 4.18E-07	B
Glacial Till, S.Illinois	4.01E-16 - 3.01E-15	3.85E-6 - 2.89E-5	2.53E-07 - 1.90E-06	B
Glacial Till, S. Dakota	1.45E-18 - 2.41E-15	1.39E-8 - 2.31E-5	9.12E-10 - 1.52E-06	B

Material	Intrinsic Permeability k	Hydraulic Conductivity K_{water}	Pneumatic Conductivity K_{air}	Ref
SOILS	S.I.(cm^2)	S.I.(cm/sec)	S.I.(cm/sec)	Ref
Glacial deposit, outwash	5.18E-12	4.98E-2	3.27E-03	B
Glacial deposit, outwash plains	5.20E-12 - 2.08E-10	5.0E-2 - 2.0	3.28E-03 - 1.31E-01	V
Glacial deposit, esker, Westfield, Massachusetts	1.03E-12 - 1.33E-11	9.95E-3 to 1.27E-1	6.53E-04 - 8.33E-03	B, V
Glacial deposit, delta, Chicopee, Massachusetts	1.03E-12 - 1.56E-10	9.95E-3 - 1.50	6.53E-04 - 9.84E-02	B, V
Glacial till	< 1.04E-14	< 1.0E-4	< 6.56E-06	V
Glacial till - mostly sand	5.90E-14	5.67E-4	3.72E-05	B
Glacial till - mostly gravel	3.61E-12	3.47E-2	2.28E-03	B
Gravel	4.95E-12 - 1.03E-08	4.75E-2 - 99.5	3.12E-03 - 6.53E+00	B
Gravel	3.12E-12 - 3.24E-10	3.0E-2 - 3.12	1.97E-03 - 2.05E-01	D
Gravel - very well sorted	4.32E-09	41.6	2.73E+00	C
Gravel - very fine	3.93E-11 - 5.40E-11	3.77E-1 - 5.19E-1	2.47E-02 - 3.40E-02	A
Gravel - fine	5.40E-11 - 7.85E-11	5.19E-1 - 7.55E-1	3.40E-02 - 4.95E-02	A
Gravel - fine	5.42E-11	5.21E-1	3.42E-02	B
Gravel - medium	7.85E-11 - 1.08E-10	7.55E-1 - 1.04	4.95E-02 - 6.82E-02	A
Gravel - medium	3.25E-11	3.13E-1	2.05E-02	B
Gravel - coarse	1.08E-10 - 1.48E-10	1.04 - 1.42	6.82E-02 - 9.32E-02	A
Gravel - coarse	1.81E-11	1.74E-1	1.14E-02	B
Gravel - very coarse	1.48E-10 - 1.97E-10	1.42 - 1.89	9.32E-02 - 1.24E-01	A
Gravel	3.12E-14 - 3.12E-12	3E-4 - 3E-2	1.97E-05 - 1.97E-03	T
Gravel - well graded (GW)	1.41E-12 - 4.01E-12	1.35E-2 - 3.85E-2	8.86E-04 - 2.53E-03	T
Gravel - poorly graded (GP)	3.02E-12 - 9.88E-12	2.9E-2 - 9.5E-2	1.90E-03 - 6.23E-03	T
Gravel - clean	> 1.04E-10	> 1.0	> 6.56E-02	U
Kaolin	1.04E-17	1.0E-7	6.56E-09	W
Loess	4.91E-15 - 1.48E-13	4.72E-5 - 1.42E-3	3.10E-06 - 9.32E-05	A
Loess	1.04E-13	1.0E-3	6.56E-05	V
Loess	4.16E-19 - 5.41E-19	4E-9 - 5.2E-9	2.62E-10 - 3.41E-10	V
Loess loam	1.04E-14	1.0E-4	6.56E-06	V
Mica powder	1.04E-15	1.0E-5	6.56E-07	W
Peat	6.86E-13	6.6E-3	4.33E-04	B
Quartz powder	1.04E-14	1.0E-4	6.56E-06	W
Rock flour	1.04E-17	1.0E-7	6.56E-09	W
Sand (Beach)	4.91E-13 - 1.97E-12	4.72E-3 - 1.89E-2	3.10E-04 - 1.24E-03	A

Material	Intrinsic Permeability k	Hydraulic Conductivity K_{water}	Pneumatic Conductivity K_{air}	Ref
SOILS	S.I.(cm ²)	S.I.(cm/sec)	S.I.(cm/sec)	Ref
Sand (Beach)	8.26E-07 - 2.01E-06	8.10E-2 - 1.97E-1	5.31E-03 - 1.29E-02	B
Sand (Beach)	8.16E-07 - 2.04E-06	8.0E-2 - 2.0E-1	5.25E-03 - 1.31E-02	V
Sand (Dune)	9.62E-08 - 2.89E-07	9.43E-3 - 2.83E-2	6.19E-04 - 1.86E-03	A
Sand (Dune)	2.36E-07 - 3.07E-06	2.31E-2 - 3.01E-1	1.52E-03 - 1.97E-02	B
Sand (Dune)	1.02E-06 - 3.06E-06	0.1 - 0.3	6.56E-03 - 1.97E-02	V
Sand	4.85E-09 - 1.01E-05	4.75E-4 - 9.95E-1	3.12E-05 - 6.53E-02	B
Sand - very fine	4.81E-09 - 4.81E-08	4.72E-4 - 4.72E-3	3.10E-05 - 3.10E-04	A
Sand - very fine	4.85E-09 - 1.42E-08	4.75E-4 - 1.39E-3	3.12E-05 - 9.12E-05	B
Sand - very fine	9.77E-08	9.58E-3	6.28E-04	C
Sand - very fine and fine	9.57E-09 - 2.84E-08	9.38E-4 - 2.78E-3	6.15E-05 - 1.82E-04	B
Sand - very fine and uniform, uniformity coefficient = 5-2	1.02E-09 - 6.53E-08	1.0E-4 - 6.4E-3	6.56E-06 - 4.20E-04	V
Sand - very fine and uniform, uniformity coefficient = 5-2, Bulls liver, Sixth Ave., N.Y.	1.02E-09 - 5.10E-08	1.0E-4 - 5.0E-3	6.56E-06 - 3.28E-04	V
Sand - very fine and uniform, Uniformity coefficient = 5 Bull's liver, Brooklyn, N.Y.	1.02E-10 - 1.02E-09	1.0E-5 - 1.0E-4	6.56E-07 - 6.56E-06	V
Sand - fine	4.81E-08 - 4.81E-07	4.72E-3 - 4.72E-2	3.10E-04 - 3.10E-03	A
Sand - fine	2.36E-08 - 6.73E-08	2.31E-3 - 6.6E-3	1.52E-04 - 4.33E-04	B
Sand - fine	2.04E-10 - 1.93E-07	2.0E-5 - 1.89E-2	1.31E-06 - 1.24E-03	C
Sand - fine	1.02E-08 - 5.10E-07	1.0E-3 - 5.0E-2	6.56E-05 - 3.28E-03	U
Sand - fine	1.02E-09	1.0E-4	6.56E-06	W
Sand - fine and medium	4.85E-08 - 1.18E-07	4.75E-3 - 1.16E-2	3.12E-04 - 7.61E-04	B
Sand - medium	4.81E-07 - 2.16E-06	4.72E-2 - 2.12E-1	3.10E-03 - 1.39E-02	A
Sand - medium	9.57E-08 - 2.36E-07	9.38E-3 - 2.31E-2	6.15E-04 - 1.52E-03	B
Sand - medium	9.18E-10 - 5.78E-07	9.0E-5 - 5.67E-2	5.90E-06 - 3.72E-03	D
Sand - medium, well sorted	2.57E-06	2.52E-1	1.65E-02	C
Sand - medium and coarse	1.89E-07 - 4.85E-07	1.85E-2 - 4.75E-2	1.21E-03 - 3.12E-03	B
Sand - coarse	2.16E-06 - 3.13E-06	2.12E-1 - 3.07E-1	1.39E-02 - 2.01E-02	A
Sand - coarse	3.90E-07 - 9.57E-07	3.82E-2 - 9.38E-2	2.51E-03 - 6.15E-03	B
Sand - coarse	9.18E-10 - 6.74E-06	9E-5 - 6.61E-1	5.90E-06 - 4.34E-02	C
Sand - coarse, well sorted	3.06E-05	3.00	1.97E-01	C
Sand - clean, coarse	1.02E-07 - 1.02E-05	1.0E-2 - 1.0	6.56E-04 - 6.56E-02	U
Sand (mixture)	5.10E-08 - 1.02E-07	5.0E-3 - 1.0E-2	3.28E-04 - 6.56E-04	U
Sand - coarse and very coarse	7.20E-07 - 1.89E-06	7.06E-2 - 1.85E-1	4.63E-03 - 1.21E-02	B

Material	Intrinsic Permeability k	Hydraulic Conductivity K_{water}	Pneumatic Conductivity K_{air}	Ref
SOILS	S.I.(cm ²)	S.I.(cm/sec)	S.I.(cm/sec)	Ref
Sand - very coarse	3.13E-06 - 3.85E-06	3.07E-1 - 3.77E-1	2.01E-02 - 2.47E-02	A
Sand - very coarse	1.42E-06 - 4.37E-06	1.39E-1 - 4.28E-1	9.12E-03 - 2.81E-02	B
Sand and Gravel	9.57E-08 - 2.36E-06	9.38E-3 - 2.31E-1	6.15E-04 - 1.52E-02	B
Sand - very coarse, and Gravel, very fine	2.84E-06 - 7.20E-06	2.78E-1 - 7.06E-1	1.82E-02 - 4.63E-02	B
Sand - Scituate, Massachusetts	4.13E-08 - 9.68E-08	4.05E-3 - 9.49E-3	2.66E-04 - 6.23E-04	B,V
Sand - Plum Island	1.89E-07 - 2.71E-07	1.85E-2 - 2.66E-2	1.21E-03 - 1.74E-03	B,V
Sand - Fort Peck	1.77E-08 - 2.95E-08	1.74E-3 - 2.89E-3	1.14E-04 - 1.90E-04	B,V
Sand - Ottawa sand	5.76E-08 - 8.62E-08	5.65E-3 - 8.45E-3	3.71E-04 - 5.54E-04	B,V
Sand - Union Falls	4.25E-07 - 1.01E-06	4.17E-2 - 9.95E-2	2.74E-03 - 6.53E-03	B,V
Sand - Franklin Falls	9.21E-09 - 1.53E-08	9.03E-4 - 1.5E-3	5.92E-05 - 9.84E-05	B,V
Sand - from dike	1.53E-09 - 1.84E-08	1.5E-4 - 1.8E-3	9.84E-06 - 1.18E-04	V
Sand - dam filters	1.53E-08 - 1.01E-06	1.5E-3 - 9.95E-2	9.84E-05 - 6.53E-03	B,V
Sand - silty	7.08E-11 - 7.08E-07	6.94E-6 - 6.94E-2	4.55E-07 - 4.55E-03	B
Sand - silty	1.02E-09 - 2.04E-08	1.0E-4 - 2.0E-3	6.56E-06 - 1.31E-04	U
Sand - silty	7.14E-14 - 3.06E-13	7.0E-9 - 3.0E-8	4.59E-10 - 1.97E-09	V
Sand - poorly graded (SP)	> 4.08E-11	> 4E-6	>2.62E-07	T
Sand - coarse	9.18E-10 - 6.12E-06	9E-5 - 6E-1	5.90E-06 - 3.94E-02	T
Sand - medium	9.18E-10 - 5.10E-07	9E-5 - 5E-2	5.90E-06 - 3.28E-03	T
Sand - fine	2.04E-10 - 2.04E-07	2E-5 - 2E-2	1.31E-06 - 1.31E-03	T
Sand -silty (SM)	2.65E-11 - 1.20E-10	2.6E-6 - 1.18E-5	1.71E-07 - 7.74E-07	T
Sand - clayey (SC)	1.02E-12 - 4.90E-12	1.0E-7 - 4.8E-7	6.56E-09 - 3.15E-08	T
Sand - silty and clayey (SC - SM)	1.94E-12 - 1.38E-11	1.9E-7 - 1.35E-6	1.25E-08 - 8.86E-08	T
Silt	4.81E-10 - 4.81E-09	4.72E-5 - 4.72E-4	3.10E-06 - 3.10E-05	A
Silt	9.45E-10	9.26E-5	6.07E-06	B
Silt	9.18E-14 - 7.23E-09	9E-9 - 7.09E-4	5.90E-10 - 4.65E-05	D
Silt	1.02E-10 - 5.10E-09	1.0E-5 - 5.0E-4	6.56E-07 - 3.28E-05	U
Silt - loess	1.01E-12 - 1.77E-08	9.95E-8 - 1.74E-3	6.53E-09 - 1.14E-04	B
Silt - loess	1.02E-12 - 2.04E-08	1.0E-7 - 2.0E-3	6.56E-09 - 1.31E-04	T
Silt - sandy	7.08E-14 - 3.07E-13	6.94E-9 - 3.01E-8	4.55E-10 - 1.97E-09	B
Silt - Boston	1.01E-13 - 2.01E-11	9.95E-9 - 1.97E-6	6.53E-10 - 1.29E-07	B,V
Silt - North Carolina	5.67E-12 - 1.30E-09	5.56E-7 - 1.27E-4	3.65E-08 - 8.33E-06	B,V
Silt (ML)	3.57E-12 - 8.06E-12	3.5E-7 - 7.9E-7	2.30E-08 - 5.18E-08	T
Silt - clayey	1.02E-11	1.0E-6	6.56E-08	W
Silt - clayey, Little Pic River, Ontario	2.04E-10	2.0E-5	1.31E-06	W ₄
Silt - elastic (MH)	5.51E-13 - 2.51E-12	5.4E-8 - 2.46E-7	3.54E-09 - 1.61E-08	T
Till	1.45E-12 - 2.41E-10	1.42E-7 - 2.36E-5	9.32E-09 - 1.55E-06	A
Till	1.02E-15 - 2.04E-09	1.0E-10 - 2.0E-4	6.56E-12 - 1.31E-05	T

References for Formation Conductivity Values

- A) California Department of Water Resources, 1968
- B) C. Daly, Evaluation of the procedures for determining selected aquifer parameters. Prepared for U.S. Army Toxic Hazardous Materials Agency, CR REL Report 82-41, 1982
- C) S. Davis and J.M. DeWeist, Hydrogeology. New York: Wiley, p. 463, 1966.
- D) D. A. Morris and A. I. Johnson, Summary of hydrological and physical properties of rock and soil materials as analyzed by the hydrologic laboratory of the U. S. Geological Survey. USGS Water Supply Paper 1839 - D, 1967.
- E) Golder Associates, Development of site suitability criteria for a high level waste repository. Lawrence Livermore Laboratory Report, UCRL - 13793, 1977.
- F) ---
- G) W. C. Rasmussen, Permeability and storage of heterogeneous aquifers in the U. S. International Association of Scientific Hydrologic Publication 64, pp. 317-325, 1964.
- H) H. C. Classen and E. H. Cordes, Two-well recirculating tracer test in fractured carbonate rock. Nevada Hydrol. Sci. Bull. 20(3), 367-382, 1975.
- I) A. Krefl, A. Lenda, B. Turek, A. Zuber and K. Czuderna, Determination of effective porosities by two-well pulse method. Isot. Tech. Groundwater Hydrol. Proc. Symp., vol.2, pp. 295-312, 1974.
- J) G. B. Walter, Convergent flow tracer test at H-6: Waste Isolation Plant (WIPP) southeast New Mexico (draft), Hydro Geochem, Inc., Tuscon, AZ, 1983.
- K) J. D. Bredehoeft and G. F. Pinder, Mass transport in flowing groundwater, Water Resources Research, 9(1), 144-210, 1973.
- L) P. R. Fenske, Hydrology and radionuclide transport, monitoring well HT-2m, Tatum Dome Mississippi. Proj. rep. NVD-1253-6. Cent. for Water Resources Research, Desert Research Institute, University of Nevada Syst., Reno, 1973.
- M) D. D. Rabinowitz and G. W. Gross, Environmental tritium as a hydrometeorologic tool in the Roswell Basin, New Mexico. Tech. Completion Rep. OWRR:A-037-NMEX, New Mexico, Water Resources Research Institute, Las Cruces, 1972.
- N) G. Segol and G. F. Pinder, Transient simulation of salt water intrusion in southeastern Florida. Water Resources Res. 12(1), 65-70, 1976.
- O) A. Dieulin, Lixiviation *in situ* d'un gisement d'uranium en milieu granitique, Draft Rep. LHM/RD/81/63, Ecole Natl. Super. des Mines de Paris, Fontaineleau, France, 1981.
- P) M. Ivanovitch and D. B. Smith. Determination of aquifer parameters by two-well pulsed method using radioactive tracers, Journal of Hydrol. 36(1/2), 35-45.
- Q) D. B. Grove, The use of Galerkin finite-element methods to solve mass transport equations, Rep USGS/WRD/WRI-78/011. USGS, Denver, CO. (Available as NTIS PB 277-532 from National Technical Information Services, Springfield, VA, 1977.
- R) D. B. Oakes and D. J. Edworthy, Field measurements of dispersion coefficients in United Kingdom. Groundwater Quality, Measurement and Prediction. Reading, England: Water Research Center, pp. 327-340, 1977.
- S) D. S. Webster, J. F. Procter and J. W. Marine, Two-well tracer test in fractured crystalline rock. USGS, Water Supply Paper, 1544-1, 1970
- T) P. A. Domenico and F. W. Schwartz. Physical and Chemical Hydrogeology. New York : Wiley, p. 824, 1990.
- Bureau of Reclamation, 1960.
- U) Milton E. Harr, Groundwater and Seepage. Mineola, N.Y.: Dover Publications, 1991.
- from A. I. Silin-Bekchurin, "Dynamics of Underground Water," p.34, Moscow University, 1958.
- V) T. William Lambe and Robert V. Whitman, *Soil Mechanics*. New York, N.Y.: John Wiley & Sons.
1) K. Terzaghi and R. B. Peck, *Soil Mechanics in Engineering Practice*, 2nd ed. New York, N. Y.: John Wiley and Sons, 1967.
- W) James K. Mitchell, *Fundamentals of Soil Behavior*. New York, N.Y. : John Wiley & Sons, Inc, 1993.

- 1) Bjerrum et al., 1957.
- 2) E. Long and W. George, "Turnagain Slide Stabilization, Anchorage, Alaska," *Journal of Soil Mechanics and Foundation Division, A.S.C.E.*, Vol. 93, No. SM4, pp. 611-627, 1967.
- 3) C. A. Fetzer, "Electro-osmotic Stabilization of West Branch Dam," *Journal of the Soil Mechanics and Foundation Division, A.S.C.E.*, Vol. 93, No. SM4, pp. 85-106.
- 4) L. Casagrande, et al., "Electro-osmotic Stabilization of a High Slope in Loose Saturated Silt," *Proceedings of the Fifth International Conference on Soil Mechanics and Foundation Engineering, Vol. II*, pp. 555-558, 1961.

APPENDIX H2

ANISOTROPIC FLUID CONDUCTIVITIES OF ROCKS AND SOILS

Material	K_v/K_h	Intrinsic Permeability k		Hydraulic Conductivity K_{water}		Pneumatic Conductivity K_{air}		Reference
ROCK		S.I.(cm ²)		S.I.(cm/sec)		S.I.(cm/sec)		
		Horizontal	Vertical	Horizontal Conductivity	Vertical Conductivity	Horizontal Conductivity	Vertical Conductivity	
Anhydrite	0.1	1.02E-17 - 1.02E-15	1.02E-18 - 1.02E-16	1.0E-12 - 1.0E-10	1.0E-13 - 1.0E-11	6.56E-14 - 6.56E-12	6.56E-15 - 6.56E-13	K
Chalk	0.5	1.02E-13 - 1.02E-11	5.10E-14 - 1.02E-12	1.0E-08 - 1.0E-06	5.0E-09 - 1.0E-07	6.56E-10 - 6.56E-08	3.28E-10 - 6.56E-09	K
Dolomite	0.5	1.02E-12 - 1.02E-10	5.10E-13 - 5.10E-11	1.0E-07 - 1.0E-05	5.0E-08 - 5.0E-06	6.56E-09 - 6.56E-07	3.28E-09 - 3.28E-07	K
Limestone	0.5	1.02E-12 - 1.02E-10	5.10E-13 - 5.10E-11	1.0E-07 - 1.0E-05	5.0E-08 - 5.0E-06	6.56E-09 - 6.56E-07	3.28E-09 - 3.28E-07	K
Limestone - fractured and calcareous sandstone	0.002	4.59E-06	9.18E-09	4.5E-01	9.0E-04	2.95E-02	5.90E-05	L
Salt	1.0	1.02E-17	1.02E-17	1.0E-12	1.0E-12	6.56E-14	6.56E-14	K
Sandstone	0.5	5.10E-16 - 1.02E-13	2.55E-16 - 5.10E-14	5.0E-11 - 1.0E-08	2.5E-11 - 5.0E-09	3.28E-12 - 6.56E-10	1.64E-12 - 3.28E-10	K
Sandstone	1.0	3.47E-10	3.47E-10	3.4E-05	3.4E-05	2.23E-06	2.23E-06	J
Shale	0.1	1.02E-17 - 1.02E-15	5.10E-18 - 5.10E-16	1.0E-12 - 1.0E-10	5.0E-13 - 5.0E-11	6.56E-14 - 6.56E-12	3.28E-14 - 3.28E-12	K
Shale	0.5	2.04E-11	1.02E-11	2.0E-06	1.0E-06	1.31E-07	6.56E-08	A
Siltstone - Shale	0.1	2.14E-09	2.14E-10	2.1E-04	2.1E-05	1.38E-05	1.38E-06	A
Siltstone - Shale	0.107	2.86E-10	3.06E-11	2.8E-05	3.0E-06	1.84E-06	1.97E-07	A
Material	K_v/K_h	Intrinsic Permeability k		Hydraulic Conductivity K_{water}		Pneumatic Conductivity K_{air}		Reference
Soil		S.I.(cm ²)		S.I.(cm/sec)		S.I.(cm/sec)		
		Horizontal Conductivity	Vertical Conductivity	Horizontal Conductivity	Vertical Conductivity	Horizontal Conductivity	Vertical Conductivity	
Clay - Boston	0.3 -1.4							B
Clay - marine	0.8							C
Clay - marine	0.95							D

Clay - soft	0.66							E
Clay - varved	0.3 - 0.66							F
Clay - varved	0.66							G
Clay - varved	0.025 - 0.25							H
Clay - varved	0.066 - 0.3							I
Sand, silt and clay	0.1	5.10E-07	5.20E-08	5.0E-2	5.1E-3	3.28E-03	3.35E-04	M
Silt - organic	0.6 - 0.8							A
Varved soil - New Liskeard	0.27 - 0.68	3.47E-13 - 3.43E-12	2.34E-13 - 9.64E-13	3.4E-8 - 3.36E-7	2.29E-8 - 9.45E-8	2.23E-09 - 6.20E-09	1.50E-09 - 6.20E-09	N

References for Formation Conductivity Values

- A) Golder Associates, Development of site suitability criteria for a high level waste repository. Lawrence Livermore Laboratory Report, UCRL - 13793, 1977
- B) Haley and Aldrich, Engineering properties of foundation soils at Long Creek-Fore River areas and back cover. Report No. 1. Maine State Highway Commission, 1969.
- C) P. Lumb and J. K. Holt, Geotechnique, 18, 25-36, 1968.
- D) B. H. Subbaraju, T. K. Natarajan and R. K. Bhandari, Proc., 8th International Conference of Soil Mechanics and Foundation Engineers, Moscow, vol.2.2, pp.217-220.
- E) D. J. Bazzet and A. F. Brodie, Ontario Hydro Research News 13 (4), 1-6, 1961.
- F) H. T. Chan and T. C. Kenny, Canadian Geotechnical journal 10(3) 453-472, 1973.
- G) T. C. Kenny and H. T. Chan, Canadian Geotechnical Journal 10(3) 473-488, 1973.
- H) L. Casagrande and S. J. Poulos, Canadian Geotechnical Journal 6(3) 287-326, 1969.
- I) T. H. Wu, N. Y. Chan and E. M. Ali, J. Geotechnical Engineers Division, American Society of Civil Engineers, vol. 104 no. GT7. Pp. 899-905.
- J) S. I. Tsien, Stabilization of marsh deposit. Highway Research Board Bulletin, 115, 15-43, 1955.
- K) P. A. Domenico and F. W. Schwartz. Physical and Chemical Hydrogeology. New York : Wiley, p. 824, 1990.
- L) G. Segol and G. F. Pinder, Transient simulation of salt water intrusion in southeastern Florida. Water Resources Res. 12(1), 65-70, 1976.
- M) S. S. Papadopulos and S. P. Larson, Aquifer storage of heated water: II. Numerical Simulation of field results, Groundwater 16(4), 242-248, 1978.
- N) H. R. Chan and T. C. Kenney, "Laboratory Investigation of Permeability Ratio of New Liskeard Varved Soil," Canadian Geotechnical Journal, Vol. 10, pp. 453-472, 1973.

APPENDIX H3
YOUNG'S MODULI OF ROCKS AND SOILS

Material	Young's Modulus	Young's Modulus	Reference
ROCK	U.S.(psi)*10 ⁶	S.I.(GPa)	
Amphibolite	13.6 - 17.6	93.8 - 121.4	I ₁
Anhydrite	9.9	68.3	I ₁
Basalt	5.0 - 14.6	34.9 - 100.6	A
Basalt	7.1 - 16.2	49.0 - 112.0	B
Basalt	2.8 - 16.2	19.6 - 98.1	G ₃ , G ₆ , G ₇ , G ₉
Basalt	0.2 - 16.2	48.5 - 111.5	G ₁
Basalt	8.5 - 14.2	58.6 - 98.0	N
Chalk	0.01 - 1.7	0.1 - 12.0	H
Coal	0.2 - 4.3	1.0 - 30.0	H
Coal	1.4 - 2.8	9.7 - 19.3	N
Coal	1.5 - 2.9	10.0 - 20.0	O ₃
Diabase	10.4 - 15.5	72.0 - 107.0	B
Diabase	4.3 - 12.8	29.4 - 88.3	G ₄ , G ₆
Diabase	3.2 - 16.5	22.0 - 114.0	G ₇
Diabase	11.6 - 15.6	80.0 - 107.5	G ₁
Diabase	12.6 - 16.9	86.9 - 116.5	I ₁
Diorite	7.9 - 12.6	55.0 - 87.0	B
Diorite	10.9 - 15.6	75.2 - 107.6	I ₁
Diorite	9.9 - 14.2	68.2 - 98.0	N
Dolerite	11.4 - 15.6	78.6 - 107.6	N
Dolomite	7.1 - 13.5	49.0 - 93.0	B
Dolomite	8.0 - 13.0	55.2 - 89.6	C
Dolomite	2.8 - 12.0	19.6 - 82.4	G ₃ , G ₆
Dolomite	10.3 - 13.5	71.0 - 93.0	G ₇ , G ₉
Dolomite	16.0	110.3 - 121.3	I ₁
Dolomite	5.7 - 11.9	39.3 - 82.0	N
Dunite	21.6 - 26.5	148.9 - 182.7	I ₁
Gabbro	8.5 - 15.7	58.8 - 107.8	G ₃ , G ₆ , G ₇
Gabbro	8.4 - 12.6	58.4 - 87.1	G ₁
Gabbro	12.9 - 18.4	88.9 - 126.9	I ₁
Gabbro	9.9 - 15.6	68.2 - 107.6	N
Gneiss	2.4 - 11.7	16.8 - 81.0	A
Gneiss	2.8 - 8.6	19.6 - 58.8	G ₃ , G ₆
Gneiss	3.6 - 8.6	24.5 - 58.8	G ₉ , G ₁₀
Gneiss (Feldspathic)	12.0 - 17.3	82.7 - 118.6	I ₁
Granite	3.8 - 10.9	26.2 - 75.5	A
Granite	2.5 - 11.0	17.0 - 76.0	B

Material	Young's Modulus	Young's Modulus	Reference
ROCK	U.S.(psi)*10 ⁶	S.I.(GPa)	
Granite	3.7 - 10.0	25.5 - 68.6	G ₃ , G ₆
Granite	3.6 - 7.3	25.0 - 50.0	M
Granite	2.8 - 8.5	19.3 - 58.6	N
microGranite	4.3 - 11.4	29.6 - 78.6	N
Granite (sound)	4.5 - 82.7	31.0 - 57.0	O ₁
Granite (partially decomposed)	1.0 - 2.0	7.0 - 14.0	O ₁
Ice	1.0	7.1	I ₁
Igneous Rock (Coarse grained)	1.2 - 18.1	8.0 - 125.0	H
Igneous Rock (Fine grained)	1.0 - 17.0	7.0 - 117.0	H
Igneous and Metamorphic (sound & intact)	8.3 - 13.9	57.0 - 96.0	O ₃
Limestone	1.1 - 13.3	7.7 - 91.6	A
Limestone	4.2 - 11.9	29.0 - 82.0	B
Limestone	8.0 - 13.0	55.2 - 89.6	C
Limestone	1.4 - 11.4	9.8 - 78.5	G ₆ , G ₉
Limestone	1.2 - 11.4	8.0 - 78.5	G ₁
Limestone (Crystalline)	2.5 - 14.5	17.0 - 100.0	H
Limestone (Porous)	1.5 - 14.5	10.0 - 100.0	H
Limestone	12.6 - 15.6	86.9 - 107.6	I ₁
Limestone	1.4 - 11.4	6.7 - 78.6	N
Limestone	3.1 - 6.9	21.0 - 48.0	O ₁
Limestone (sound & intact)	5.5 - 11.0	38.0 - 76.0	O ₃
Marble	3.4 - 10.5	23.2 - 72.4	A
Marble	4.1 - 12.6	28.0 - 87.0	B
Marble	0.36 - 0.55	2.5 - 3.8	G ₇ , G ₁₀
Marble	0.23 - 0.39	1.6 - 2.7	G ₁
Marble	0.16 - 0.3	1.1 - 2.0	G ₆
Marble	12.6 - 15.6	86.9 - 107.6	I ₁
Marlestone	0.6 - 4.8	4.1 - 33.0	B
Mica Schist	11.5 - 14.7	79.3 - 101.4	I ₁
Mudstone	2.8 - 7.1	19.3 - 49.0	N
Obsidian	9.4 - 11.6	64.8 - 80.0	I ₁
Oligoclasite	11.6 - 12.3	80.0 - 84.8	I ₁
Quartzite	6.1 - 14.5	42.4 - 100.0	A
Quartzite	6.1 - 14.5	42.0 - 100.0	B
Quartzite	3.7 - 12.6	25.5 - 87.0	G ₁₀
Quartzite	4.1 - 12.6	28.0 - 87.0	G ₆
Quartzite	14.1	97.5	G ₁
Quartzite	1.6 - 17.3	11.0 - 119.0	H
Quartzite	11.9 - 14.0	82.1 - 96.5	I ₁
Rock Salt	5.1	35.4	I ₁
Salt	0.7 - 6.4	5.0 - 44.0	H

Material	Young's Modulus	Young's Modulus	Reference
ROCK	U.S.(psi)*10 ⁶	S.I.(GPa)	
Sandstone	0.3 - 5.7	1.9 - 39.2	A
Sandstone	1.4 - 7.3	9.7 - 50.0	B
Sandstone (medium hardness)	2.0 - 4.0	13.8 - 27.6	C
Sandstone (hard, dense)	5.0 - 7.5	34.5 - 51.7	C
Sandstone	7.1 - 12.2	49.0 - 84.3	G ₁₀
Sandstone	6.4 - 7.4	44.1 - 51.0	G ₆
Sandstone	0.2 - 14.5	1.0 - 100.0	H
Sandstone	1.0 - 2.9	7.0 - 20.0	M
Sandstone	0.7 - 11.4	4.8 - 78.6	N
Schist	0.9 - 11.1	5.9 - 76.9	A
Schist	5.8 - 10.2	40.0 - 70.5	G ₁
Schist	0.7 - 14.2	5.0 - 98.0	H
Slate and high durability Shale	1.7 - 13.9	12.0 - 96.0	H
Shale	1.1 - 3.2	7.5 - 21.9	A
Shale	1.7 - 7.5	12.0 - 52.0	B
Shale	1.1 - 4.3	7.8 - 29.4	G ₃ ,G ₇
Shale	1.7 - 6.4	12.0 - 44.0	G ₉
Shale (low durability)	0.3 - 4.4	2.0 - 30.0	H
Shale	0.02 - 2.1	0.2 - 5.0	L
Shale	1.4 - 2.8		N
Shale - weatherd (Bearpaw formation, Cretaceous period, Canada)	0.01	69.0	N ₁
Shale - unweatherd (Bearpaw formation, Cretaceous period, Canada)	0.02	0.14	N ₁
Shale - (Pierre formation, Cretaceous period, So. Dakota)	0.02 - 0.14	0.14 - 1.0	N ₁
Shale - (Ft. Union formation, Tert. period, No. Dakota)	0.01 - 0.06	0.07	N ₁
Shale - (Trinity formation, Cretaceous period, Texas)	0.002 - 0.03	0.01 - 0.21	N ₁
Shale - (Taylor formation, Cretaceous period, Texas)	0.006 - 0.02	0.04 - 0.14	N ₁
Shale - Silty Calyey (Composite Cyclothem of Pennsylvania)	1.0	69	N ₁
Shale - Sandy (Composite Cyclothem of Pennsylvania)	0.5	3.4	N ₁
Shale - (Mauv, calc. Shale formation, Cambrian period, Utah)	2.3	15.9	N ₁
Shale - (Quartzose Sh. formation, Cambrian period, Utah)	2.3	15.9	N ₁
Shale (sound & intact)	1.5 - 5.8	10.0 - 40.0	O ₃
Siltstone	1.9 - 6.4	13.0 - 44.0	B
Siltstone	0.007889 - 0.097750	0.05 - 0.67	E ₁

Material	Young's Modulus	Young's Modulus	Reference
ROCK	U.S.(psi)*10 ⁶	S.I.(GPa)	
Siltstone	0.016430 - 0.498055	0.11 - 3.43	E ₂
Slate	11.5 - 16.3	79.3 - 112.4	I ₁
Syenite	8.5 - 11.4	58.8 - 78.5	G ₃
Syenite	9.1 - 12.5	62.9 - 86.3	G ₁
Syenite	8.5 - 11.4	58.6 - 78.6	N
SOILS	U.S.(psi)	S.I.(Mpa)	Reference
Clay (soft)	250 - 500	1.4 - 3.5	F
Clay (hard)	850 - 2000	5.9 - 14.0	F
London Clay	1450 - 21756	10.0 - 150.0	B
Clay - soft	435	3.0	J
Clay - medium	1015	7.0	J
Clay - hard	2030	14.0	J
Clay - sandy	5221	36.0	J
Clay - very soft	76 - 764	0.5 - 52.7	K
Clay - soft	764 - 3055	52.7 - 210.0	K
Clay - medium	3055 - 7639	21.0 - 52.7	K
Clay - stiff	7639 - 15278	52.7 - 105.3	K
Clay - sandy	3820 - 30555	26.3 - 210.7	K
Clay Shale	15278 - 30555	105.3 - 210.7	K
Clay - Silty	7639 - 15278	52.7 - 105.3	K
Clay - very soft	350 - 1750	2.0 - 15.0	L
Clay - soft	700 - 3500	5.0 - 25.0	L
Clay - medium	2100 - 7000	15.0 - 50.0	L
Clay - hard	7000 - 14000	50.0 - 100.0	L
Clay - sandy	3500 - 35000	25.0 - 250.0	L
Clay - soft (undrained)	208 - 1389	1.5 - 10.0	M
Clay - medium (undrained)	694 - 6944	5.0 - 50.0	M
Clay - stiff (undrained)	2083 - 10417	15.0 - 75.0	M
Clay - soft (drained)	35 - 208	0.3 - 1.5	M
Clay - medium (drained)	69 - 486	0.5 - 3.5	M
Clay - stiff (drained)	174 - 2778	1.2 - 20.0	M
Clay - very soft	50 - 400	0.34 - 2.8	N
Clay - soft	250 - 600	1.7 - 4.1	N
Clay - medium	600 - 1200	4.1 - 8.3	N
Clay - hard	1000 - 2500	6.9 - 17.2	N
Clay - sandy	4000 - 6000	27.6 - 41.4	N
Clay - weak plastic	203 - 580	1.4 - 4.0	O ₁
Clay - stiff plastic	609 - 1160	4.2 - 8.0	O ₁
Clay - semi solid	1000 - 2030	6.9 - 14.0	O ₁
Clay - soft	145 - 435	1.0 - 3.0	O ₂
Clay - stiff	362 - 725	2.5 - 5.0	O ₂
Clay - semi firm	725 - 1450	5.0 - 10.0	O ₂
Clay - solid, boulder clay	4351 - 14504	30.0 - 100.0	O ₂
Clay - soft	290 - 580	2.0 - 4.0	O ₃

SOILS	U.S.(psi)	S.I.(Mpa)	Reference
Clay - stiff	1160 - 2756	8.0 - 19.0	O ₃
Clay - hard	1160 - 2756	8.0 - 19.0	O ₃
Clayey Silt	422 - 3364	2.9 - 23.2	D
Clay - soft	72 - 725	0.5 - 5.0	P
Clay - medium	580 - 1450	4.0 - 10.0	P
Clay - firm	1015 - 2901	7.0 - 20.0	P
Clay - sandy	3626 - 5801	25.0 - 40.0	P
Glacial till (loose)	1400 - 22400	10.0 - 150.0	L
Glacial till (dense)	2100 - 105000	150.0 - 720.0	L
Glacial till (very dense)	70000 - 210000	500.0 - 1440.0	L
Gravel (dense)	14794 - 15084	102.0 - 104.0	O ₁
Gravel (loose)	4206 - 11168	29.0 - 77.0	O ₃
Gravel (dense)	13923 - 27847	96.0 - 192.0	O ₃
Gravel (without sand)	14504 - 29008	100.0 - 200.0	O ₂
Gravel (coarse and sharp edged)	21756 - 43512	150.0 - 300.0	O ₂
Loess	2100 - 8400	15.0 - 60.0	L
Loess	2030 - 8412	14.0 - 58.0	O ₃
Loess	2176 - 7252	15.0 - 50.0	P
Muck	73 - 507	0.5 - 3.5	O ₁
Peat	58 - 290	0.4 - 2.0	O ₂
Sand (unconsolidated to lightly consolidated)	5000 - 15000	34.5 - 24.3	C
Sand (loose)	1500 - 4000	10.4 - 27.6	F
Sand (dense)	5000 - 10000	34.5 - 69.0	F
Sand (screened crushed quartz, coarse, angular and loose)	14.9	103.0	I ₂
Sand (screened crushed quartz, coarse, angular and dense)	28.0	193.0	I ₂
Sand (screened crushed quartz, medium, angular and loose)	18.0	124.0	I ₂
Sand (screened crushed quartz, medium, angular and dense)	27.0	186.0	I ₂
Sand (screened crushed quartz, fine, angular and loose)	17.0	117.0	I ₂
Sand (screened crushed quartz, fine angular and dense)	30.0	207.0	I ₂
Sand (screened, medium, subangular and loose)	20.0	138.0	I ₂
Sand (screened, medium, subangular and dense)	35.0	241.0	I ₂
Sand (Ottawa standard sand, medium, rounded and loose)	30.0	207.0	I ₂
Sand (Ottawa standard sand, medium, rounded and dense)	97.0	669.0	I ₂
Sand (screened Ottawa sand, fine, rounded and loose)	26.0	179.0	I ₂

SOILS	U.S.(psi)	S.I.(Mpa)	Reference
Sand (screened Ottawa sand, fine, rounded and dense)	45.0	310.0	I ₂
Sand (loose)	2.1	15.0	J
Sand (dense)	11.6	80.0	J
Sand and Gravel (loose)	14.5	100.0	J
Sand and Gravel (dense)	21.8	150.0	J
Sand (loose)	1528 - 3819	10.5 - 26.3	K
Sand (dense)	3819 - 15278	26.3 - 105.3	K
Sand and Gravel (dense)	15278 - 30556	105.3 - 210.7	K
Sand - Silty	3819 - 30556	26.3 - 210.7	K
Sand (loose)	1400 - 3500	10.0 - 25.0	L
Sand (dense)	7000 - 11900	50.0 - 81.0	L
Sand - Silty	1050 - 3150	5.0 - 20.0	L
Sand and Gravel (loose)	7000 - 21000	50.0 - 150.0	L
Sand and Gravel (dense)	14000 - 28000	100.0 - 200.0	L
Sand (loose)	1389 - 3472	10.0 - 25.0	M
Sand (medium dense)	2778 - 8333	20.0 - 60.0	M
Sand (dense)	6944 - 13889	50.0 - 100.0	M
Sand (loose)	1500 - 3500	10.3 - 24.1	N
Sand (dense)	7000 - 12000	48.3 - 82.7	N
Sand (Silty)	1000 - 3000	6.9 - 20.7	N
Sand and Gravel (loose)	14000 - 28000	96.5 - 193.0	N
Sand (loose)	1450 - 3046	10.0 - 21.0	O ₁
Sand (dense)	7542 - 12038	52.0 - 83.0	O ₁
Sand (loose)	2900 - 11603	20.0 - 80.0	O ₂
Sand (medium)	7252 - 21756	50.0 - 150.0	O ₂
Sand (dense)	7107 - 11313	49.0 - 78.0	O ₂
Sand (loose)	1450 - 4206	10.0 - 29.0	O ₃
Sand (medium)	4206 - 6962	29.0 - 48.0	O ₃
Sand (dense)	6962 - 11168	48.0 - 77.0	O ₃
Sand (loose)	1305 - 3626	9.0 - 25.0	P
Sand (dense)	6527 - 11603	45.0 - 80.0	P
Sand (Silty)	1015 - 3045	7.0 - 21.0	P
Sand and Gravel (loose)	6527 - 21031	45.0 - 145.0	P
Sand and Gravel (dense)	13053 - 26107	90.0 - 180.0	P
Silt	280 - 2800	2.0 - 20.0	L
Silt	435 - 1450	3.0 - 10.0	O ₂
Silt (soft, silty clayey sea silt)	290 - 725	2.0 - 5.0	O ₂
Silt (soft, strongly clayey silt)	73 - 435	0.5 - 3.0	O ₂
Silt (soft)	580 - 1160	4.0 - 8.0	O ₂
Silt (semi-firm)	725 - 2900	5.0 - 20.0	O ₂
Silt	725 - 2756	2.0 - 19.0	O ₃
Silt	348 - 2901	2.4 - 20.0	P
Miscellaneous Materials	U.S.(psi)*10⁶	S.I.(Gpa)	Reference
Concrete	2.8 - 4.0	0.02 - 0.04	N
Steel	30.0	0.2	N
Wood	1.2 - 1.5	0.008	N

References for Formation Modulus Values

- A) Robert B. Johnson, Jerome V. DeGraff, *Principles of Engineering Geology*. New York: John Wiley & Sons.
- B) Arvid M. Johnson, *Physical Processes in Geology*. San Francisco, CA: Freeman, Cooper & Company.
- C) T. K. Perkins, L. R. Kern, "Widths of Hydraulic Fractures," *J.Petroleum Technology*, 13:pp. 937-949, 1961.
- D) M. C. Canino, "Potential Effects of Pneumatic Fracturing on Existing Structures and Utilities," Master's thesis, Department of Civil and Environmental Engineering, New Jersey Institute of Technology, Newark, NJ, 1997
- E) T. J. Imholte, "Potential Effects of Pneumatic Fracturing on Existing Structures and Utilities," Master's project, Department of Civil and Environmental Engineering, New Jersey Institute of Technology, Newark, NJ, 1996
- F) Braja M. Das, *Advanced Soil Mechanics*. New York: McGraw Hill, 1941.
- G) Alfreds R. Jumikis, *Rock Mechanics*. Trans Tech Publications, 1983.
- 1) F. Birch, "Compressibility, Elastic Constants," *American Institute of Physics Handbook*, 3rd ed. New York, N.Y.: McGraw Hill Book Company, Table 7-15 on Rocks: Elastic Constants, pp. 100-170, 1972.
 - 2) S. P. Clark, Jr., *Handbook of Physical Constants*. The Geological Society of America, Memoir 97, 1966.
 - 3) I. W. Farmer, *Engineering Properties of Rock*. London: E. & F. N. Spon Ltd., 1968.
 - 4) A. A. Griffith, Thermal Expansion of Typical American Rocks. Ames, Iowa: Iowa State College of Agriculture and Mechanic Arts, Iowa Engineering Experiment Station, Vol. 35, No. 19, pp. 19-20, October 7, 1936.
 - 5) J. C. Jaeger and N. G. Cook, *Fundamentals of Rock Mechanics*. London: Chapman and Hall, p. 82, 1969.
 - 6) A. R. Jumikis, *Settlement Tables For Centrally Loaded Rigid Circlar Footings on Multi-layered Soil Systems*. New Brunswick, N.J.: Rutgers University, College of Engineering, Engineering Research Bulletin 54, p.21, 1973.
 - 7) A. R. Jumikis and A. A. Jumikis, *Red Brunswick Shale and its Engineering Aspects*. New Brunswick, N.J.: Rutgers University, College of Engineering, Engineering Research Bulletin 55, p.51, 1975.
 - 8) *Smithsonian Physical Tables*, 7th ed., Washington, D. C.: Vol. 71, No. 1, Publication 2359, p. 229, 1970.
 - 9) K. Szechy, *The Art of Tunnelling*. Budapest: Akademiai Kiado, p. 76, 1966.
 - 10) U. S. Bureau of Reclamation, *Physical Properties of Typical Foundation Rocks*. Concrete Laboratory Report SP39, 1954.
- H) John A. Franklin and Maurice B. Dusseault, *Rock Engineering*. New York, N.Y.: McGraw Hill Publishing Company, p. 301.
- I) T. William Lambe and Robert V. Whitman, *Soil Mechanics*. New York, N.Y.: John Wiley & Sons.
- 1) W. F. Brace, "Elasticity an Rigidity of Rock," *Encyclopedia of Earth Sciences*, R. Fairbridge (ed.), Reinholt.
 - 2) L-S. Chen, "An Investigation of Stress-Strain and Strength Characteristics of Cohesionless Soils by Triaxial Compression Tests," *Proceedings 2nd International Conference on Soil Mechanics and Foundation Engineering*, Vol. 5, p. 35, 1948.
- J) John N. Cernica, *Geotechnical Engineering*. New York, N.Y.: Holt, Rinehart and Winston.
- K) *Technical Engineering and Design Guides as Adapted from the US Army Corp of Engineers, No. 9, Settlement Analysis*, Appendix D. New York, N.Y.: American Society of Civil Engineers, p.89, 1994.
- L) Joseph E. Bowles, *Foundation Analysis and Design*. New York, N.Y.: McGraw Hill Book Company, 1988.
- M) Donald P. Coduto, *Foundation Design - Principles and Practices*. Englewood Cliffs, N.J.: Prentice Hall, 1994.

- N) Hans F. WinterKorn and Hsai-Yang Fang, *Foundation Engineering Handbook*. New York, N.Y.: Van Nostrand Reinhold Company, 1975.
- O) Underwood, 1967.
- P) Jean-Pierre Bardet, *Experimental Soil Mechanics*. Upper Saddle River, NJ: Prentice Hall, p.286, 1997.
 - 1) F. J. Converse, "Chapter 8, Foundations Subjected to Dynamic Forces," *Foundation Engineering*, G.A.Leonards ed., McGraw-Hill, New York, pp. 769 - 825, 1962.
 - 2) M. G. Hallam, N. J. Heaf and L. R. Wootton, "Dynamics of Marine Structures," *Report UR 8, 2nd Edition*, CIRIA Underwater Engineering Group, 1978.
 - 3) R. R. Hunt, *Geotechnical Engineering Techniques and Practices*. New York, N.Y.: McGraw-Hill, p. 134, 1986.
- Q) David F. McCarthy, *Essentials of Soil Mechanics and Foundations*. Upper Saddle River, N.J.: Prentice Hall, p.438, 1997.

REFERENCES

- A. S. Abou-Sayed, C. E. Brechtel, and R. J. Clifton, "In Situ Stress Determination by Hydrofracturing: A Fracture Mechanics Approach," *J. Geop. Res.* 83: 2851-2862, 1978.
- R. E. Babcock, C. L. Prokop and R. O. Kehle, "Distribution of Propping Agents in Vertical Fractures," *Presented at the Spring Meeting of the Mid-Continent District, API Division of Production*, 1967.
- G. I. Barenblatt, "The Mathematical Theory of Equilibrium Cracks in Brittle Fracture," *Advances of Applied Mechanics.* 7: 55-129, 1962.
- L. Bjerrum, J.K.L. Nash, R.M. Kennard and R. E. Gibson, "Hydraulic Fracturing in Field Permeability Testing," *Geotechnique.* 22: 319-332, 1972.
- B.N. Bjornstad, "Moisture Content of Hanford Soils: A Summary," *Geology and Geophysics Group, Earth and Environmental Sciences Center, Pacific Northwest Laboratory, Richland, WA*, 1994.
- Jr. S. Boggs, *Principles of Sedimentology and Stratigraphy*. Ohio: Merrill Publishing Company, 1987.
- R. S. Brodkey, *The Phenomena of Fluid Motions*. New York: Dover Publication, 1995.
- M. C. Canino, "Potential Effects of Pneumatic Fracturing on Existing Structures and Utilities," Master's thesis, Department of Civil and Environmental Engineering, New Jersey Institute of Technology, Newark, NJ, 1997
- R. D. Carter, "Derivation of the General Equation for Estimating the Extent of the Fractured Area," *Appendix to "Optimum Fluid Characteristics for Fracture Extension," by G.C. Howard and C.R. Fast. Drilling and Prod. Prac.*, API: 261-270, 1957.
- S. C. Chapra and R. P. Canale, *Numerical Methods for Engineers*. New York: McGraw Hill Inc., 1988.
- H. Chiou, "Deposition of Particles in a Convergent Channel," Ph.D. dissertation, Department of Mechanical and Industrial Engineering, New Jersey Institute of Technology, Newark, NJ, 1993.
- A. A. Daneshy, "On the Design of Vertical Hydraulic Fractures," *Journal of Petroleum Technology*. Vol. 25, pp. 83-97, 1973.
- J.F. Davidson and D. Harrison, *Fluidization*. New York: Academic Press, 1971.

REFERENCES (Continued)

C. N. Davies, *Aersol Science*. New York: Academic Press, 1966.

Y. Ding, "A Theoretical Analysis of Volatile Contaminant Removal by the Pneumatic Fracturing Process," Ph.D. dissertation, Department of Civil and Environmental Engineering, New Jersey Institute of Technology, Newark, NJ, 1995.

P. A. Druet, and S. J. O'Connor, "High-Energy Gas Fracturing Succeeds in Central Lake Erie," *Oil and Gas Journal*. Dec. 23, 1991, pp. 92-97.

S. Ergun, *Chem. Eng. Progr.* 48, 89, 1952.

N. A. Fuchs, *Mechanics of Aerosols*. London: Pergamon Press, 1964.

J. Geertsma, and F. de Klerk, "A Rapid Method for Predicting the Width and Extent of Hydraulically Induced Fractures," *Journal of Petroleum Technology*. Vol 21, No 12, pp. 1571-1581, 1969.

J. L. Gidley, S. A. Holditch, D. E. Nierode and R.W. Veatch, "Recent Advances in Hydraulic Fracturing," *Society of Petroleum Engineers, Richardson, Texas*, 1989.

J. C. Gottschling, T. N. Royce and L. Z. Shuck, "Nitrogen Gas and Sand: A New Technique for Stimulation of Devonian Shale," *Journal of Petroleum Technology*, May 1985, pp. 901-907.

K. Habibagahi, "Design of Foundations on Cavernous Rocks," *In: Proceedings of Design and Construction of Foundations on the Carbonate Formations of New Jersey and Pennsylvania, New Jersey Institute of Technology, Newark, NJ*. March 27, 1981.

B. G. Haimson and C. Fairhurst, "In-Situ Stress Determination at Great Depth by Means of Hydraulic Fracturing," *Rock Mechanics-Theory and Practice*, 1967, pp. 559-584.

B. Haimson, and E. J. Stahl, "Hydraulic Fracturing and the Extraction of Minerals Through Wells," *In: Proc. 3rd Sym. on Salt, Northern Ohio Geol. Soc., Cleaveland, OH*. 2: pp. 421-432, 1970.

H. A. Hall, "Investigation into Fracture Behavior and Longevity of Pneumatically Fractured Fine-Grained Formations," M.S. Thesis, Department of Chemical Engineering, Chemistry and Environmental Science, New Jersey Institute of Technology, Newark, NJ, 1995.

REFERENCES
(Continued)

- E. M. Harr, *Groundwater and Seepage*. New York: McGraw Hill Publishers, 1962.
- G. C. Howard, and C. R. Fast, *Hydraulic Fracturing, Monograph Series-2*. SPE, Richardson, Texas, 1970.
- T. L. Holzer, T. L. Youd and T.C. Hanks, "Dynamics of Liquefaction During the 1987 Superstition Hills, California Earthquake," *Science*, 244: pp. 56-59, 1989.
- M. K. Hubbert, and G. Willis, "Mechanics of Hydraulic Fracturing," *Trans. AIME*, 210: pp. 153-166, 1957.
- P. J. Huck, M.J. Waller and S. L. Shimondle., "Innovative Geotechnical Approaches to the Remedial *In situ* Treatment of Hazardous Materials Disposal Sites," *In: Proc. Nat. Conf. Control Haz. Mater. Spills, Louisville, KY*, 1980, 421-426.
- P. W. Huntoon and E. M. Shoemaker, "Roberts Rift, Canyonlands, Utah, A Natural Hydraulic Fracture Caused by Comet or Asteroid Impact," *Ground Water*, Vol 33, No. 4, pp. 561-569, July-August 1995.
- S. Hurlburt, "Moving Ahead with Hydrofracing," *Water Well J*, Feb. 1989, pp. 37-40.
- A. M. Johnson, *Physical Processes in Geology*. San Francisco: Freeman, Cooper & Co.
- R. L. Johnson, D. B. McWhorter, R. E. Hinchee and Goodman, "An Overview of In Situ Air Sparging," *Ground Water Monitoring and Remediation*, Fall 1993, pp. 127-135.
- L. R. Kern, T. K. Perkins and R. E. Wyant, "The Mechanics of Sand Movement in Fracturing," *Presented at 33rd Annual Fall Meeting of Society of Petroleum Engineers in Houston, TX*, 1958.
- T. C. King, "Mechanism of Pneumatic Fracturing," M.S. Thesis, Department of Civil and Environmental Engineering, New Jersey Institute of Technology, Newark, NJ, 1993.
- G. V. Last and V. J. Rohay, "Refined Conceptual Model for the Volatile Organic Compounds Arid Integrated Demonstration and 200 West Area Carbon Tetrachloride Expedited Response Action," *PNL-8597, Pacific Northwest Laboratory, Richland, WA*, 1993.

REFERENCES
(Continued)

- L. S. Leung and P. J. Jones, *Proceedings of Pneumotransport 3. BHRA Fluid Engineering Cranfield*, paper D4, 1978.
- D. K. Lowe, and J. L. Huitt, "Propping Agent Transport in Horizontal Fractures," *Presented at AIME Meeting, Denver, Colorado. SPE-1285*, October 3-6 1965.
- J. Luey, and D. K. Seiler, "Application of *In Situ* Vitrification in the Soil Subsurface," *PNL-10485 Pacific Northwest Laboratory, Richland, WA*, 1995.
- S. Matsumoto, S. Harada, S. Saito and S. J. Maeda, "Minimum Transport Velocity for Horizontal Pneumatic Conveying," *Chemical Engineering, Japan*, 7, 425, 1975.
- L. M. McDowell-Boyer, J. R. Hunt and N. Sitar, "Particle Transport Through Porous Media," *Water Resources Research*, 22(13), pp. 1901-1921, 1986.
- S. T. McGonigal, "Integration of Pneumatic Fracturing and *In Situ* Vitrification in Coarse Grained Soils," M.S. Thesis, Department of Civil and Environmental Engineering, New Jersey Institute of Technology, Newark, NJ, 1995.
- D. A. Mendelsohn, "A Review of Hydraulic Fracture Modelling-Part I : General Concepts, 2D Models, Motivation for 3D Modelling," *Journal of Energy Resources Technology*, 106: pp. 369-375, 1984.
- _____. "A Review of Hydraulic Fracture Modelling-II: 3D Modelling and Vertical Growth in Layered Rock," *Journal of Energy Resources Technology*, 106: pp. 543-553, 1984.
- L. C. Murdoch, "The Hydraulic Fracturing of Soil," Ph.D. dissertation, University of Cincinnati, 1991.
- _____. "Hydraulic Fracturing of Soil During Laboratory Experiments Part 1: Methods and Observations," *Geotechnique*, 43-2: pp. 255-265, 1992.
- _____. "Hydraulic Fracturing of Soil During Laboratory Experiments Part 2: Propagation," *Geotechnique*, 43-2: pp. 267-276, 1992.
- _____. "Hydraulic Fracturing of Soil During Laboratory Experiments Part 3: Theoretical Analysis," *Geotechnique*, 43-2: 277, 1992.

REFERENCES
(Continued)

D. Nautiyal, "Fluid Flow Modeling for Pneumatically Fractured Formations," M.S. Thesis, Department of Civil and Environmental Engineering, New Jersey Institute of Technology, Newark, NJ, 1994.

S. Nemat-Nasser, H. Abe, and S. HIRAKAWA, *Hydraulic Fracturing and Geothermal Energy*. Martinus Nijhoff, eds. 1983.

R. H. Nilson, "Gas-Driven Fracture Propagation," *Sandia National Laboratories report, SAND79-2379*, 1981.

R. H. Nilson, W. J. Proffer and R. E. Duff, "Modelling of Gas-driven Fractures Induced by Propellant Combustion Within a Borehole," *International Journal of Rock Mech. Min. Sci. and Geomech. Abstr.*, 22-1: pp. 3-19, 1985.

NJIT (New Jersey Institute of Technology) and ARS (Accutech Remedial Systems), *Integration of Pneumatic Fracturing and ISV technologies: DOE Hanford Facility*. Prepared for Battelle Pacific Northwest Laboratories, Richland, WA, 1994.

R. P. Nordgren, "Propagation of a Vertical Hydraulic Fracture," *Society of Petroleum Engineers Journal*, 12: pp. 306-314, 1972.

T. K. Perkins and L. R. Kern, "Widths of Hydraulic Fractures," *J. Petroleum Technology*, 13: pp. 937-949, 1961.

D. D. Pollard, "Derivation and Evaluation of a Mechanical Model for Sheet Intrusions," *Tectonophysics*, 19: pp. 233-269, 1973.

R. Sakthivadivel, "Clogging of a Granular Porous Medium by Sediment," *Rep. HEL, Hydraulic Engineering Laboratory, University of California Berkeley, CA*, 106, pp 15-17, 1969.

J. R. Schuring, V. Jurka and P. C. Chan, "Pneumatic Fracturing to remove VOCs," *Remediation Journal*, 1991.

J. R. Schuring and P. C. Chan, "Removal of Contaminants from the Vadose Zone by Pneumatic Fracturing," *United States Geological Survey, Department of Interior, Award No 14-08-0001-G1739*, 1992.

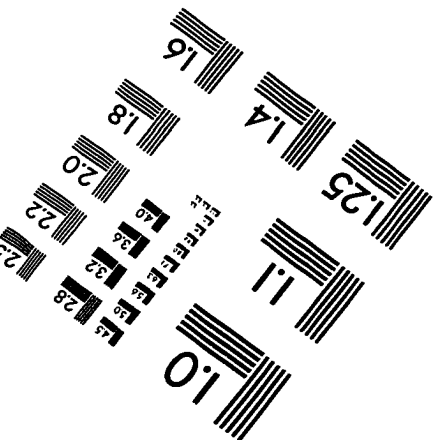
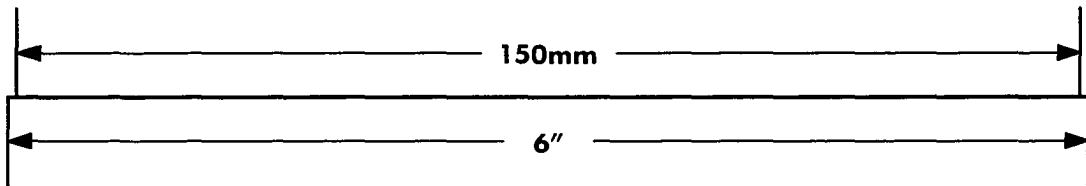
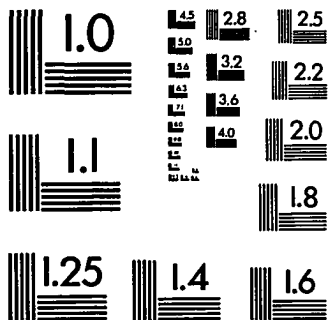
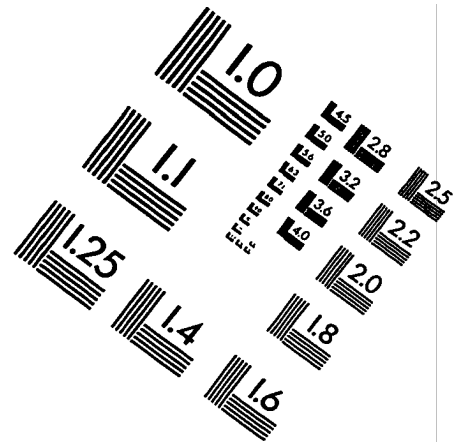
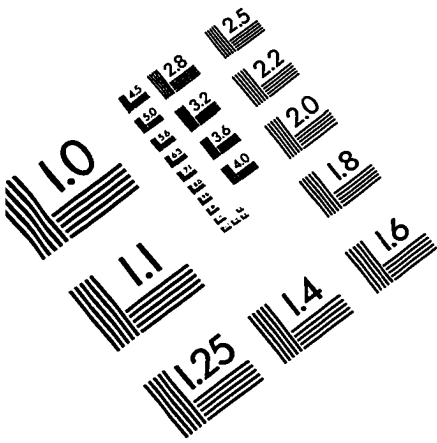
REFERENCES
(Continued)

- C. Shan, R. W. Falta and I. Javandel, "Analytical Solutions for Steady State Gas Flow to a Soil Vapor Extraction Well," *Water Resources Research*, 28(4), pp. 1105-1120, April 1992.
- J. L. Sherard, L. P. Dunnigan, and J. R. Talbot., "Basic Properties of Sand and Gravel Filters," *Journal of Geotechnical Engineering*., 110(6), pp. 684-700, 1984a.
- B. M. Sielski, "Development of Computer and Analytical Models for Subsurface Pneumatic Fracturing and Liquid Injection (in progress) ," Ph.D. dissertation, New Jersey Institute of Technology, Newark, NJ (proposed 1997).
- I. N. Sneddon, "The Distribution of Stress in the Neighbourhood of a Crack in an Elastic solid," *Proceedings, Royal Society of London*, A 187, 229, 1946.
- S. L. Soo, *Fluid Dynamics of Multiphase Systems*. Blaisdell, Waltham, Mass, 1967.
- D. A. Spence, and D. L. Turcotte, "Magma Driven Propagation of Cracks," *Journal of Geophysical Research*, 90-B1: pp. 575-580, 1985.
- G. E. Stewart, "Hydraulic Fracturing of Crystalline Rocks Stimulates Two Wells Drilled in New Hampshire," *Ground Water*, Vol. 12, 1974.
- H. G. Thomas, "Transport Characteristics of Suspensions: Minimum Transport Velocity for Large Particle Size Suspensions in Round Horizontal Pipes," *American Institute of Chemical Engineers Journal*, 7, 423, 1961.
- S. Timoshenko, and J. N. Goodier, *Theory of Elasticity*. Mc Graw-Hill Book Company, Inc, 1951.
- US EPA, RREL, Office of Research and Development, *Accutech Pneumatic Fracturing Extraction and Hot Gas Injection, Phase I*. US EPA SITE Program, Application Analysis Report, 1993.
- US EPA, Office of Research and Development, *Integrating Pneumatic Fracturing and Bioremediation for the In-Situ Treatment of Contaminated Soil*. Prepared by Rutgers, The State University of New Jersey and New Jersey Institute of Technology, 1995.
- United States Patent No. 5,032,042, *Method and Apparatus for Eliminating Non-Naturally Occurring Subsurface Liquid Toxic Contaminants from the Soil*, 1991.

REFERENCES
(Continued)

- L. E. Vallejo, "Shear Stresses and the Hydraulic Fracturing of Earth Dam Soils," *Soils and Foundations*, 33-3: pp. 14-27, 1993.
- R. Wolff, *et al.*, "Stress Determination by Hydraulic Fracturing in Sub-Surface Waste Injection," *Journal of American Water Works Association*, Vol 67, 1975.
- R. G. Wuerker, "Annotated Tables of Strength and Elastic Properties of Rocks," Paper 633-G published as a separate publication by SPE, 1956.
- H. Y. Wong, and I.W. Farmer, "Hydrofracture Mechanisms in Rock During Pressure Grouting," *Rock Mechanics*, 5: 21-41, 1973.
- S. T. Yuster, and J. C. Calhoun, "Pressure Parting of Formations in Water Flood Operations," *The Oil Weekly*, pp. 34-40, March 9, 1945.
- Z. M. Zhang, "Application of Hydrofracture Principles to Grouting in Deep Foundation," *Pile Buck*, 1-12, 1989.

IMAGE EVALUATION TEST TARGET (QA-3)



APPLIED IMAGE, Inc
1653 East Main Street
Rochester, NY 14609 USA
Phone: 716/482-0300
Fax: 716/288-5989

© 1993, Applied Image, Inc., All Rights Reserved

